Physica Scripta

INVITED COMMENT

Nuclear structure features of very heavy and superheavy nuclei—tracing quantum mechanics towards the ‘*island of stability*’

To cite this article: D Ackermann and Ch Theisen 2017 *Phys. Scr.* **92** 083002

IOP Publishing | Royal Swedish Academy of Sciences Physica Scripta

Phys. Scr. **92** (2017) 083002 (83pp) https://doi.org/10.1088/1402-4896/aa7921

Invited Comment

Nuclear structure features of very heavy and superheavy nuclei—tracing quantum mechanics towards the '*island of stability*'

D Ackermann[1,2] **and Ch Theisen**[3]

[1] Grand Accélérateur National d'Ions Lourds—GANIL, CEA/DSM-CNRS/IN2P3, Bd. Becquerel, BP 55027, F-14076 Caen, France
[2] GSI Helmholtzzentrum für Schwerionenforschung, Planckstr. 1, D-62491 Darmstadt, Germany
[3] Irfu, CEA, Université Paris-Saclay, F-91191 Gif-sur-Yvette, France

E-mail: dieter.ackermann@ganil.fr

Received 13 March 2017, revised 19 May 2017
Accepted for publication 13 June 2017
Published 18 July 2017

Abstract

The quantum-mechanic nature of nuclear matter is at the origin of the vision of a region of enhanced stability at the upper right end of the chart of nuclei, the so-called 'island of stability'. Since the 1960s in the early second half of the last century, various models predict closed shells for proton numbers 114–126 and neutron numbers such as 172 or 184. Being stabilized by quantum-mechanic effects only, those extremely heavy man-made nuclear species are an ideal laboratory to study the origin of the strong nuclear interaction which is the driving force for matter properties in many fields ranging from microscopic scales like hadronic systems to cosmic scales in stellar environments like neutron stars. Since the 1950s, experiments on the synthesis of new elements and isotopes have also revealed various exciting nuclear structure features. The contribution of Bohr, Mottelson and Rainwater with, in particular, the development of the unified model played an essential role in this context. Although not anticipated in the region of the heaviest nuclei, many phenomena were subsequently discovered like the interplay of collective features manifesting themselves e.g. in nuclear deformation, ranging from spherical to prolate and oblate shapes with the possible occurrence of triaxial symmetries, and single particle states and their excitation into quasiparticle configurations. The continuous development of modern experimental techniques employing advanced detection set-ups was essential to reveal these exciting nuclear structure aspects in the actinide and transactinide regions since the production cross-section becomes extremely small with increasing mass and charge. Further technological progress, in particular, high intensity stable ion beam accelerator facilities presently under construction, as well as potentially in the farther future radioactive neutron rich ion beams provide a high discovery potential for the basic understanding of nuclear matter.

Keywords: nuclear structure, superheavy nuclei, decay spectroscopy, in-beam spectroscopy *K*-isomers, nuclear deformation

(Some figures may appear in colour only in the online journal)

0031-8949/17/083002+83$33.00

Contents

1. Introduction

This review article will focus on the nuclear structure studies in the region of the heaviest nuclei on both the experimental and the theoretical side. In the first section, we will introduce the basic theoretical and experimental aspects relevant for the heaviest nuclei. We will in particular highlight the contribution of Bohr, Mottelson and Rainwater to the progress in theory. In the course of this review, reference to the literature of these authors will be made whenever the concepts result from their work, thus emphasizing the profound legacy from these pioneers. Nuclear structure studies were historically first performed studying the decay of rare isotopes after their necessary extraction from the large background due to parasitic reactions. This aspect of so-called decay spectroscopy after separation (DSAS) will be discussed in section 2. It is only since the end of the last century that in-beam experiments could be performed for elements with atomic numbers greater than 100. These experiments revealing mainly the collective structure will be developed in section 3. Theory lessons and exotic phenomena will be discussed in section 4. Section 5 will discuss recent and future advances in instrumentation and production techniques as well as future facilities. Open questions and perspectives will be debated in the concluding section.

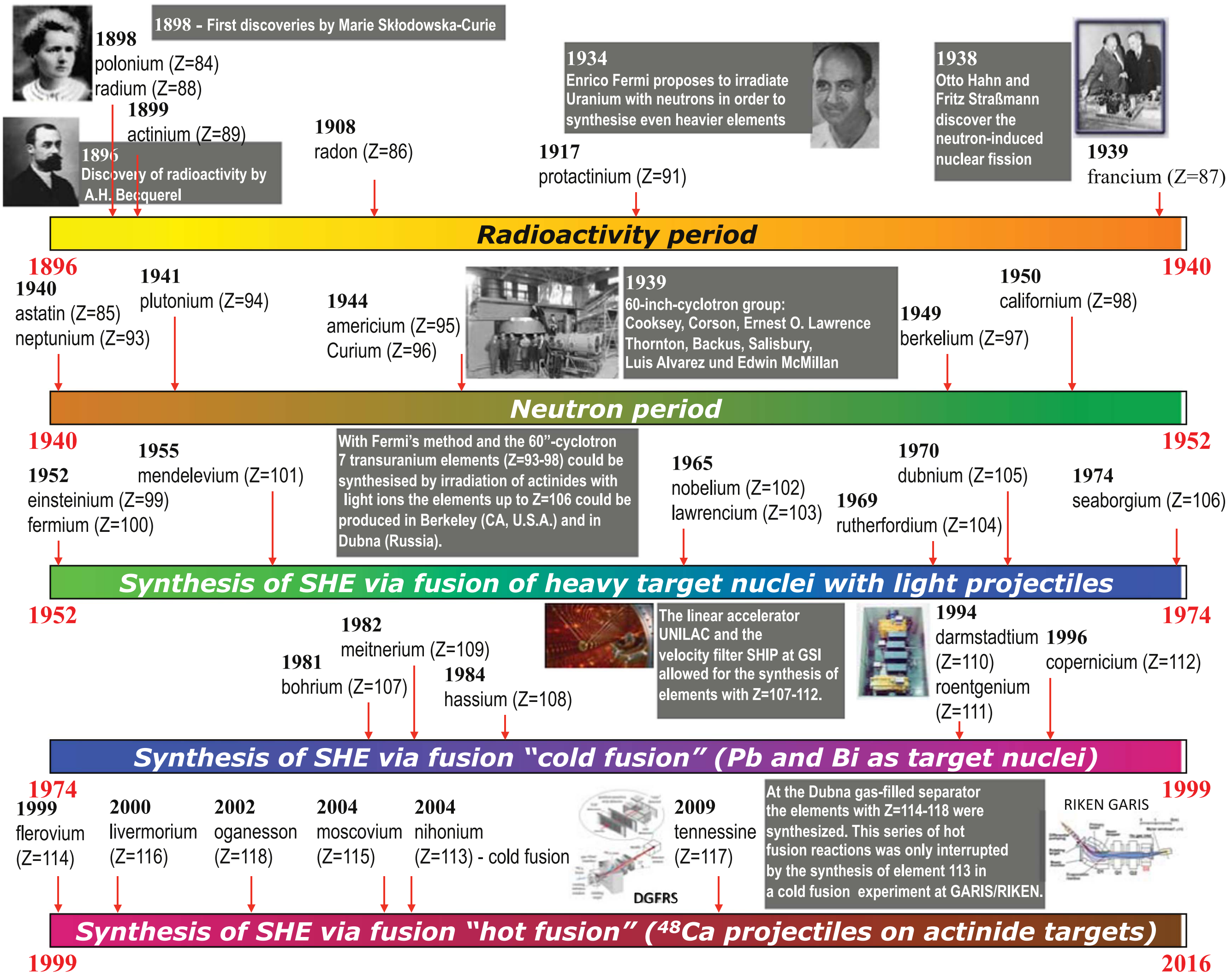

Figure 1. History of discovery and synthesis of heavy and SHEs. The subdivision in periods follows the spirit set by Peter Armbruster in [25].

1.1. Bohr, Mottelson and Rainwater legacy from the superheavy nuclei (SHN) point of view

Since the early times of atomic and nuclear physics, heavy elements have always been at the heart of some of the most fundamental discoveries. Radioactivity, initially referred to as ‘uranic rays’, was discovered in 1896 by Becquerel, who observed that uranium salts unexpectedly produced an image on a photographic plate [1]. This was the beginning of a scientific adventure which should continue for more than a century, motivating generations of scientists to develop ever advancing technology and theoretical models, producing exciting science with the aim to reach the limits of nuclear stability in terms of mass and atomic number. An overview over the episodes experienced so far in this continuing story is illustrated in figure 1. In 1898, Pierre and Marie Curie discovered the new elements Po and Ra in pitchblende ores [2, 3]. In 1899, Rutherford isolated α and β radioactivities from uranium [4]. Alpha radiation was later identified as the emission of helium nuclei by Rutherford and Geiger [5], and β radiation as electrons by Becquerel [6, 7]. In 1899, Rutherford discovered the exponential law of radioactive decay from ‘thorium emanations’ [8]. In 1900, Villard observed a new type of radiation emitted by radium [9], named γ-rays by Rutherford in 1909. In 1911, Bayer, Hahn and Meitner observed a fine structure of the decay of ‘radium B’ and ‘C’ (^{214}Pb and ^{214}Bi) [10]. This turned out to correspond to the internal conversion process, as confirmed by Ellis in 1921, from ‘radium B’ studies [11, 12]. In the same year, Hahn discovered an isomer decay from ‘uranium X2’ to ‘uranium Z’ (^{214}Pa isomer decay) [13] and in 1929, Rosenblum discovered the α-decay fine structure from ‘thorium C’ (^{212}Bi) [14].

Later, in 1938, Hahn, Strassmann and Meitner discovered fission from the bombardment of ^{238}U with neutrons [15, 16]. A theory of fission was rapidly developed by Bohr and Wheeler in a seminal paper [17], in which it was also shown that the stability of the heaviest nuclei against fission is governed by the value of Z^2/A, Z (A) being the number of protons (nucleons). Above the critical value $Z^2/A \approx 48$, nuclei undergo spontaneous fission. As a consequence of this critical value, nuclear matter cannot be extended limitlessly. In their original paper, Meitner and Frisch estimated this limit to be approximately at $Z \approx 100$ [16]. The spontaneous fission of U was then discovered in 1940 by Flerov and Petrjak [18].

Subsequently, the development of nuclear reactors and ion accelerators used as a neutron source lead to the discovery of new elements beyond U ($Z = 92$) up to Cf ($Z = 98$). With ion beams becoming available, the synthesis of heavy nuclei by fusion of first light and later heavier projectiles on heavy target nuclei started. Figure 1 shows this history of discovery and synthesis of heavy and super-heavy elements (SHE) from the discovery of radioactivity in 1986 until today, divided in five periods: (i) During the radioactivity period the gap between bismuth and thorium was filled by revealing the decay products of uranium and thorium; (ii) subsequently neutron irradiation of uranium followed by β decay, turning a neutron into a proton and raising the atomic number by one in this way, lead to the synthesis of heavier elements up to californium; (iii) after the discovery of einsteinium and fermium in the thermonuclear weapon tests, with the advent of the first ion accelerators, the irradiation of heavy target nuclei with light projectiles produced elements up to atomic number 106 seaborgium; (iv) during the 'cold fusion' period the six elements from bohrium to copernicium were produced by the irradiation of lead and bismuth; (v) the period of 'hot fusion' employing the irradiation of actinide target nuclei by ^{48}Ca, with the exception of nihonium ($Z = 113$) being produced still by a 'cold fusion' reaction, saw the synthesis of the heaviest species up to oganesson ($Z = 118$).

The name 'SHE' first appeared in 1955 in a proceeding by Wheeler [19] who postulated, using the liquid drop model and empirical arguments, the existence of heavy nuclei up to $Z \approx 160$–170, $A \approx 600$ with lifetimes in the 10^{-4} s range, see also [20]. Well before the discovery of fission, the concept of these elements is historically connected to the shell structure and occurrence of magic numbers. Beyond the stability concept, speculations concerning the magicity of yet unknown heavy nuclei had actually appeared well before the development of the spherical shell model by Goeppert-Mayer and Jensen in 1948–1949 [21–23]: see [24] for a review of the, sometimes fanciful, speculations on the upper limit of the periodic table.

The development of the deformed shell model by Nilsson [26] in 1955 was an important step toward the description of nuclei throughout the entire nuclear chart. In the above-mentioned conference proceeding by Wheeler, a discussion of fission barrier heights was based on a Nilsson diagram, a representation of single-particle energies for protons and neutrons in the potential of a nuclear system as a function of deformation of the nucleus, but the link to possible new magic numbers above ^{208}Pb was not yet established. In 1957, Scharff-Goldhaber mentioned in a short review article on nuclear physics [27] that *'There may be, for instance, another region of relative stability at the doubly magic nucleus* $_{126}X^{310}$*'* (which corresponds to $Z = 126$, $N = 184$), without, however, entering into further details. There were no further major developments until 1966, when a symposium 'Why and how should we investigate nuclei far from the stability line?' was held in the city of Lysekil in Sweden. This symposium is considered as one of the most important events in the SHE research on both, the theoretical and the experimental side. For reminiscences on the SHE research since the 1960s, we refer to e.g. the reviews by Armbruster and Münzenberg [28], and Herrmann [29]. At the Lysekil conference, Meldner, using shell model calculations, predicted $Z = 114$, $N = 184$ as possible next magic numbers [30]. Several publications followed the same year. Wong using shell model calculations [31] and Sobiczewski *et al* using a Woods–Saxon potential [32], both confirmed $Z = 114$ and $N = 184$, while Myers and Swiatecki calculated a fission barrier of ≈10 MeV for the corresponding nucleus using the liquid drop model [33]. One year later, Strutinsky published his method to calculate potential energy surfaces (PESs) as a function of deformation [34], which was actually presented in an abridged version at the Lysekil conference [35]. Other predictions followed, e.g. by Nilsson *et al* [36–38], Rost [39], Mosel and Greiner [40], and Grumann *et al* [41].

At this time, elements up to $Z = 104$ were discovered using irradiation of actinide targets and relatively light ion beams up to Ne. How the story of SHE synthesis continued, is beyond the scope of this review. We refer the reader to numerous books and articles e.g. [28, 42–56], and to the contribution of Oganessian, Sobiczewski and Ter-Akopian in this focus issue [57]. In a special issue of *Nucl. Phys.* A in 2015 the present status of synthesis, nuclear structure, atomic physics and chemistry of SHE is reviewed in a comprehensive collection of papers [58]. Recent developments and questions can also be found in the proceedings of the NS160 Nobel symposium on Chemistry and Physics of Heavy and SHEs held in 2016 [59].

In the context of this period of the 1950s and 1960s which corresponds to the development of the unified model by Bohr, Mottelson and Rainwater [60–67], it is interesting to review their contribution to the research on the heaviest elements. It is a striking fact that the word 'superheavy' does not appear in the two volumes of the book on nuclear structure published by Bohr and Mottelson in 1969 [68] and 1975 [69], respectively. It should be noted that Bohr, Mottelson and Rainwater actually established the basis of modern nuclear structure and received the Nobel prize in 1975 '*for the discovery of the connection between collective motion and particle motion in atomic nuclei and the development of the theory of the structure of the atomic nucleus based on this connection*'. However, the early times of SHE research were mainly devoted to the search for the heaviest elements and their synthesis. The spectroscopy of the heaviest actinides was marginal, not only because of a lack of interest, but also because the required instrumentation for this kind of high-precision measurements, namely heavy-ion accelerators and e.g. Ge or Si detectors, had not been developed yet. Since the objective of the work of Bohr, Mottelson and Rainwater is nuclear structure, not synthesis, it is a natural consequence that SHEs were not at the heart of their writings. It should be noted that the two volumes [68, 69] develop general properties of the nuclear structure, with some experimental examples serving for illustration purposes, selected among the nuclei known at the time of writing. Thus the heaviest nucleus discussed was ^{244}Cm ([69], p 144), more precisely the decay of its $K^{\pi} = 6^{+}$ isomer, which gives a flavor of the experimental knowledge in the 1970s.

However, the impact of the work of Bohr and Mottelson on the early SHE discussions should not be underestimated. We have found several articles on SHEs where Mottelson is acknowledged. As an example, Meldner in his Lysekil proceeding [30] thanks Mottelson for *'stimulating discussions and encouragement"*. There are other examples, which show that Bohr and Mottelson were interested in SHE issues. In 1974 they gave a contribution at the 27th Nobel symposium 'SHEs —theoretical predictions and experimental generation' held in Sweden, 11–14 June. Their proceedings contribution [70] was not focused on SHEs but the discussion of shell structure clearly mentioned a shell closure for these elements. Let us also quote a part of the introduction of this proceeding: '*The possibility of discovering SHEs is a theme that has strongly captured the imagination and dreams of the nuclear physics community. It is an adventure that involves an expansion of the frontiers of nuclear research in many directions and that has stimulated major developments in the understanding of nuclear dynamics and continues to pose deeply challenging questions.*'

One of the extensions of the unified model is Nilsson's model of deformed nuclei, and it is worth remembering that it was inspired by Bohr and Mottelson. As written in the acknowledgement of the seminal paper by Nilsson *'This problem was suggested by Drs A Bohr and B Mottelson. I want to thank them cordially for all help and suggestions they have generously given me during the course of the work, and the time they have set apart for discussions"* [26]. Obviously, the Nilsson model is essential for the discussion of fission barriers and therefore of the stability of the heaviest elements. As early as 1955 (the same year as Nilsson published his seminal paper), Wheeler illustrated his conference proceeding (where he coined the term 'superheavy') using a Nilsson diagram [19]. Without using the term 'superheavy', Bohr and Mottelson discussed in their book the limits of stability of spherical nuclei using the liquid drop model: see [69, p 161]. On page 226 of the same volume, they discussed, using Nilsson diagrams, equilibrium deformations and noted that '*In the heavy element region, the deformations are expected to increase to a maximum at $Z \approx 100$, while the neutron maximum is passed at $N \approx 150$*' (actually, $N = 152$ is circled on the Nilsson diagram shown on p 225). Although it was not yet a topic of interest, twenty years later this will become the basis of the spectroscopy of deformed nuclei in the No region.

As will be discussed later in this review, almost all concepts needed for the interpretation of the structure of the heaviest elements are already presented in the two volumes of the book by Bohr and Mottelson. Reference to this book will be made whenever we will (re)-introduce these concepts.

1.2. Theoretical background

1.2.1. Limits of stability from the liquid drop model. Although the word 'superheavy' is part of the everyday nuclear physicist's language, there is no scholar or unanimous definition of this category of nuclei or atoms. A generally accepted definition is that of elements that would not exist without shell or quantum effects, which corresponds to region between fermium and rutherfordium ($Z = 100$ and 104) or, using a chemist vocabulary, the transactinides ($Z \geqslant 104$). The nature of nuclear objects is often depicted in terms of macroscopic and microscopic effects, both concepts being historically closely entwined. The next section is devoted to a discussion of shell effects and their consequences on nuclear stability. In the present section, the global (macroscopic) properties of the heaviest nuclei are discussed using the liquid-drop model. We will show in particular how the $Z = 104$ borderline is connected to this model.

The liquid drop model was born in the 1930s to account for the binding energies of nuclei. A first version was proposed by Gamow in 1930 [71]. It was later extended by Heisenberg [72], von Weizsäcker [73] and Bethe [74]. See e.g. [75] for a brief history of the liquid-drop model. Discussions of this model can be found in numerous textbooks, in particular in the two volumes of the book by Bohr and Mottelson ([68, p 141–144], [69, p 365–367, 654–676]).

A detailed discussion of the question whether nuclear matter effectively behaves like a liquid, and why it is so, goes beyond the scope of this article. This is actually a complex issue, related to the nature of the nuclear force and the validity of the mean-field concept. Mottelson addresses briefly this question in a short paper [76] in terms of the 'quantality' parameter.

Within the liquid-drop model, the nucleus is treated as a charged incompressible liquid sphere. Its binding energy $BE(A, Z) = Zm_p c^2 + Nm_n c^2 - M(Z, A)$ can be described using several terms. The bulk properties involve two opposite effects: the Coulomb repulsion between the Z protons, and the binding due to the strong nuclear force between the A nucleons. The attractive term is proportional to the volume, or the number of nucleons A, and is expressed as $a_V A$. The A dependence is related to the limited range of the force (saturation property), which leads to the binding energy per nucleon being almost constant across the nuclear chart (one would expect a $A(A-1)$ dependence, if each nucleon interacted with all others). The repulsive term can be derived from the Coulomb interaction and is given as $-a_C\, Z^2/A^{1/3}$. At the surface of the nucleus, nucleons interact with fewer neighbors, which leads to a deficit of binding energy that is proportional to the surface. The surface term was introduced by von Weizsäcker and is given as $-a_S\, A^{2/3}$. Additional terms are needed to account for the quantum nature of the constituents, and properties of the strong interaction. The asymmetry term (also called symmetry term by some authors) favors equal numbers of protons and neutrons; it is related to the Pauli exclusion principle. It can be derived from the kinetic energy of a Fermi gas, and is given as $-a_A(N-Z)^2/A$. The last term $\delta(N, Z)$ mimics the tendency of nucleons to form pairs. This term, introduced by Bethe and Bacher [74], is attractive for even Z and N ($+\delta_0$), zero for odd Z or odd N and repulsive for both N and Z being odd ($-\delta_0$). δ_0 is proportional to $A^{-1/2}$; however the $-1/2$ exponent has no fundamental basis as discussed e.g. in [68, p 167–171], [77].

The binding energy of a spherical liquid drop according to these considerations is known as the Bethe–Weizsäcker formula:

$$BE(A, Z) = a_V A - a_C Z^2/A^{1/3} - a_S A^{2/3} - a_A (N - Z)^2/A + \delta(A, Z), \qquad (1)$$

with

$$\delta(A, Z) = \begin{cases} +\delta_0 & N \text{ and } Z \text{ even} \\ 0 & A \text{ odd} \\ -\delta_0 & N \text{ and } Z \text{ odd} \end{cases} \qquad (2)$$

and $\delta_0 = a_P\, A^{-1/2}$.

The a_i coefficients should be in principle deduced from first principles: see e.g. [78]. In practice, they are obtained from a fit to experimental masses thus semi-empirical: see e.g. [33] or more recent versions e.g. [79–81]. Using the Bethe-Weizsäcker formula, it is possible to determine the contours of the nuclear chart. The neutron and proton separation energies are defined as:

$$S_n = BE(A, Z) - BE(A - 1, Z), \qquad (3)$$

$$S_p = BE(A, Z) - BE(A - 1, Z - 1). \qquad (4)$$

The limits $S_n = 0$, $S_p = 0$ define the neutron and proton drip-lines, respectively, as shown in figure 2. It is also possible to delineate nuclei, which have the largest binding energy, i.e. being stable against beta decay. Using $\partial BE(A, Z)/\partial Z = 0$, one obtains:

$$Z \approx \frac{A}{2}\left(\frac{1}{1 + \frac{a_C}{4\, a_A} A^{2/3}}\right), \qquad (5)$$

which is also known as the Green approximation of the line of beta stability [82]. This line slowly deviates from $N = Z$ toward the neutron-rich region. Indeed, an extra contribution of the strong force is needed to compensate for the Coulomb repulsion, which is achieved by adding neutrons that act like a sort of glue. From the experimental perspective, the fact that the line of beta stability exhibits this curvature implies that fusion of two beta-stable nuclei will always create a neutron-deficient isotope. It is therefore *a priori* excluded to create a beta-stable super-heavy nucleus (SHN) by fusing two lighter stable nuclei.

As a general rule, the binding energy decreases for heavier nuclei, but this is not the only effect that determines the contours at the top of the nuclear chart. Indeed, strong Coulomb repulsion favors deviations from the spherical shape, which in turn may result in the nucleus being unstable against fission. Hence, deformation of the liquid drop should be taken into account, and stability of such an object as a function of (A, Z) should be considered. The derivation of the relevant expression is rather tedious, and so we shall not give here all details of the calculation. For further details, we propose to consult e.g. the development proposed by Nilsson and Ragnarsson [83, ch 4], which reproduces the arguments of Bohr and Wheeler [17]; see also [69, appendix 6A p 654–676]. As a first approximation, it is possible to consider only the volume, surface and Coulomb terms, since the asymmetry and pairing terms are not relevant for calculating the evolution of liquid-drop energy as a function of deformation.

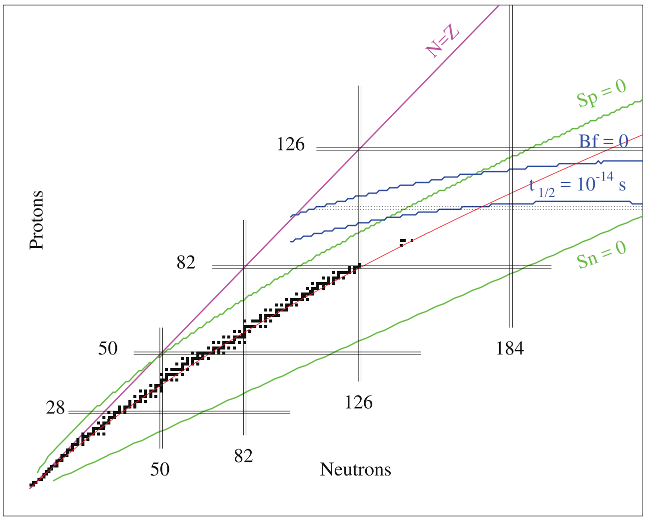

Figure 2. Nuclear chart and its limits of stability deduced from the liquid-drop model. The green lines correspond to the neutron $S_n = 0$ and proton $S_p = 0$ drip lines. The blue lines $B_f = 0$ and $t_{1/2} = 10^{-14}$ s correspond to a vanishing fission barrier and spontaneous fission half-life of 10^{-14} s, respectively. The red line corresponds to beta-stable nuclei (Green line). Besides magic numbers shown by continuous lines, the horizontal dotted line corresponds to $Z = 104$.

As shown by Nilsson and Ragnarsson [83], it is possible to expand the surface E_S and Coulomb E_C terms of the liquid-drop in powers of the β_2 deformation, for example using the convenient parametrization of $a = \sqrt{\frac{5}{4\pi}}\beta_2$. One obtains to the third order:

$$E_C(a) = E_C(0)\left(1 - \frac{1}{5}a^2 - \frac{4}{105}a^3 + ...\right), \qquad (6)$$

$$E_S(a) = E_S(0)\left(1 + \frac{1}{5}a^2 - \frac{4}{105}a^3 + ...\right). \qquad (7)$$

Obviously, the volume term is not supposed to change with deformation. Using $x = E_C(0)/2E_S(0)$, it is possible to calculate the change in the liquid-drop energy as a function of deformation:

$$\begin{aligned} \Delta E &= E_S(a) + E_C(a) - E_S(0) - E_C(0) \\ &= E_S(0)\left[\frac{2}{5}(1 - x)a^2 - \frac{4}{105}(1 + 2x)a^3 + ...\right]. \end{aligned} \qquad (8)$$

For small deformations, the liquid drop is stable if $x < 1$, and fissile if $x > 1$. Using the expressions for the Coulomb and surface terms, x can be expressed as:

$$x = \frac{1}{2}\frac{a_C\, Z^2/A^{1/3}}{a_S\, A^{2/3}} = \frac{a_C}{2\, a_S}\frac{Z^2}{A}. \qquad (9)$$

The stability with respect to spontaneous fission is governed by Z^2/A, x being often known as the fissility parameter. Nuclei with $x > 1$ ($Z^2/A \gtrsim 50$) are those for which the fission barrier vanishes. The corresponding line is shown in

Table 1. Fission barrier and spontaneous fission half-life calculated using the liquid drop model (LDM) compared to experimental values, together with the fissility parameter x. The spontaneous fission half-lives $T_{1/2}$ SF (exp) are taken from [89].

Nucleus	B_f (LDM) (MeV)	B_f(exp) (MeV)	x	$T_{1/2}$(LDM) (s)	$T_{1/2}$SF (exp) (s)
^{238}U	7.76	5.7 [87]	0.77	1.6×10^{21}	0.6×10^{23}
^{240}Pu	5.8	5.6 [87]	0.79	3.6×10^{10}	3.6×10^{18}
^{255}Fm	2.45	5.7 [87]	0.84	1.5×10^{-8}	3.2×10^{11}
^{254}No	1.45	6.6 [88]	0.86	6×10^{-14}	2.9×10^{4}
^{256}Rf	0.85		0.89	3×10^{-17}	6.2×10^{-3}
$^{290}_{184}\mathrm{Fl}^{114}$	0.04		0.96	1.1×10^{-21}	

figure 2. According to this simple formula, $^{298}_{114}\mathrm{Fl}^{184}$ with $Z^2/A \approx 44.81$ should be stable against fission, while $^{310}_{126}\mathrm{X}^{184}$ with $Z^2/A \approx 51$ should not (note that, according to the liquid-drop formula, $^{310}_{126}\mathrm{X}^{184}$ should also be proton-unstable). This is, however, a simplified picture, which does not take into account the barrier penetration.

A further step is to estimate the fission half-life using the Wentzel–Kramers–Brillouin–Jeffreys (WKBJ) semi-classical approximation, leading to:

$$T_{1/2}(\mathrm{s}) = \ln 2 \; 10^{-21} \exp(2\pi B_f / \hbar\omega_f), \tag{10}$$

where B_f is the fission barrier height, and $\hbar\omega_f$ its curvature. Using the expansion in powers of a, the height of the barrier is expressed as:

$$B_f = \frac{98}{15} \frac{(1-x)^3}{(1+2x)^2} Es(0). \tag{11}$$

The barrier curvature can in principle be calculated considering oscillations of the liquid drop, see [84], the discussion in [85, p 22–24] and evaluated data, e.g. [86]. In the region of interest, it is possible to use $\hbar\omega_f \approx 0.5$ MeV as a first approximation. Typical values of the fission barrier, fissility parameter and fission lifetimes are given in table 1.

Figure 3 taken from [53] and figure 4 from [54] show the spontaneous fission half-lives and fission barrier height as a function of the fissility parameter. Experimental values of the half-life drop by about twenty orders of magnitude from U to No, while estimates from the liquid-drop model fall by about thirty orders of magnitude. Moreover, experimental lifetimes and fission barriers are systematically higher than predictions of the liquid drop-model. Swiatecki suggested as early as 1955 that correcting the liquid drop-model for shell structure may improve the description of spontaneous fission half-lives [90]. This point will be discussed in the next section.

On the other hand, one should define how long a nucleus must live to be considered as an existing object. A criterion, related to atomic physics, is used by the International Union of Pure and Applied Chemistry (IUPAC) and International Union of Pure and Applied Physics (IUPAP) for the approval of new elements. This limit is set at 10^{-14} s, which is '*a reasonable estimate of the time it takes for a nucleus to acquire its outer electrons*' [91]. Using this criterion and the liquid-drop estimate, the limit of stability falls at $Z = 104$, as shown in figure 2, which coincides with the chemist's definition of SHE as the transactinides. A definition based on physical features puts the

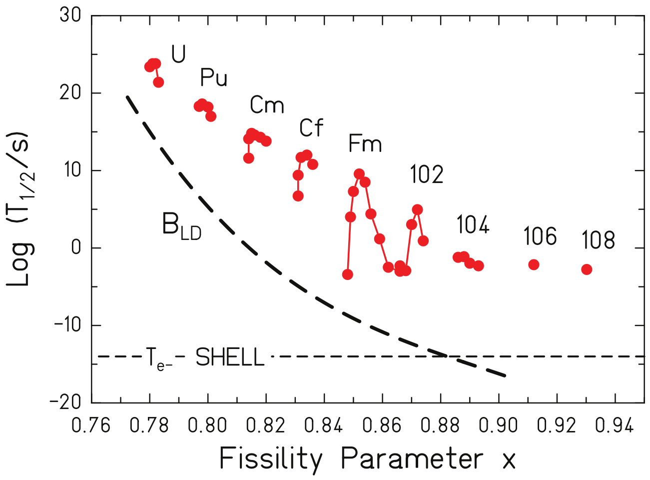

Figure 3. Spontaneous fission half-lives as a function of the fissility parameter. Experimental values are compared to the predictions of the liquid-drop model (dashed black line). Figure taken from [53] (2004). Copyright Springer-Verlag Berlin Heidelberg. With permission of Springer. Original Caption: 'The partial half-lives for spontaneous fission of the doubly even isotopes of the transuranium elements. The dashed curve shows the macroscopic fission half-live.'

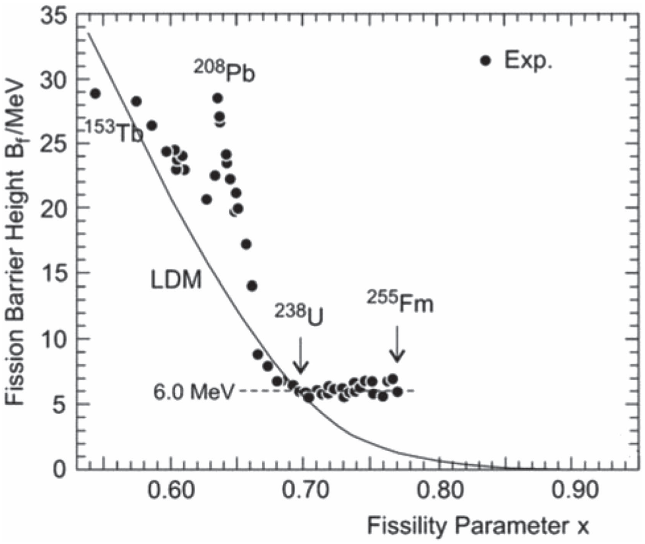

Figure 4. Fission barrier height as a function of the fissility parameter. Experimental values are compared to the predictions of the liquid-drop model. Reproduced from [54]. © IOP Publishing Ltd. All rights reserved.

onset of the region of SHN to nuclei, where the liquid drop fission barrier vanishes. However, fission lifetimes, as also the ones presented here, result from model-dependent estimates, and so the limit drawn in figure 2 can change slightly depending on the liquid-drop parameters used, and moreover it is not constant as a function of the number of neutrons. According to the various models, for a nuclear physicist SHN start then in the region between fermium and rutherfordium.

To be exhaustive on the topics of fission and stability against it, the stability of rotating nuclei should also be discussed. This subject has been extensively addressed by Cohen, Plasil and Swiatecki [92] and it is treated in [69, p 663–666]. We will come back to it later in this review (paragraph 3.5.3), together with a discussion on rotation of very heavy nuclei (VHN) and SHN.

1.2.2. Nuclear structure shell effects. The idea that nuclei have a shell structure goes back to the 1930s with the evidence that nuclei are made of protons and neutrons, by analogy with the atomic shell structure, based on several experimental evidence such as the ‘clustering’ of nuclei when represented as a function of their mass and charge, discontinuities in the binding energies, and abundances of the elements on earth and in meteorites. First attempts to formulate a shell model were made in 1933–1934 by Bartlett [93, 94], Elsasser [95–97], and Guggenheimer [98, 99]. Elsasser pointed out that, contrary to the electrons orbiting around the nucleus, protons and neutrons feel an average field they create themselves (the concept of mean-field), which is a consequence of the Pauli exclusion principle. However, these early calculations were not able to account for several experimental evidence i.e. the special properties observed for specific neutron or proton numbers like 8, 20, 50, 82; numbers who showed ‘magic virtues’ according to Wigner (the notion ‘magic’ reflects that their explanation was mysterious). It is finally using a strong spin–orbit coupling introduced in parallel by Goeppert-Mayer [22, 23] (actually suggested to her by Fermi) and Haxel, Jensen and Suess [21] (evidenced from a plot of the ground-state (g.s.) spin as a function of the number of neutrons/protons), that the magic numbers could be explained.

Besides the first experimental evidence of shell effects mentioned above, other manifestations were later found such as discontinuities in the neutron absorption cross section, magnetic moments, electric quadrupole moments, energy of the first (2^+) excited state, α-decay energy, g.s. spin and parity, isomeric states, asymmetric fission mode, etc. In the heaviest elements, manifestations of shell structure were first observed in lifetime discontinuities and their deviations from the liquid-drop predictions, staggering of odd/even fission probabilities and discontinuities in the decay modes.

Let us draw basic consequences of the nuclear shell structure for the heaviest elements. Using simple arguments derived in part from the periodic orbit theory (POT), Bohr and Mottelson show that the largest main quantum numbers n, l of the harmonic oscillator are of the order $A^{1/3}$: see [69] p 578–587, [100]; see also Strutinsky *et al* [101]. This can be understood considering A nucleons confined in a potential of radius proportional to $A^{1/3}$. Also, the spacing between shells is of the order of $A^{-1/3}$ and the number of particles in a shell of order $A^{1/3}$. Hence for heaviest nuclei, the energy between shells decreases (and so do the energy gaps), and the level density within a shell increases (the total density being proportional to A). In other words, the nuclear structure becomes more complex as a function of mass. Figure 5 taken from [68, p 239] illustrates this point. It is immediately apparent that any modification of the orbital position can possibly result in drastic modifications of nuclear structure.

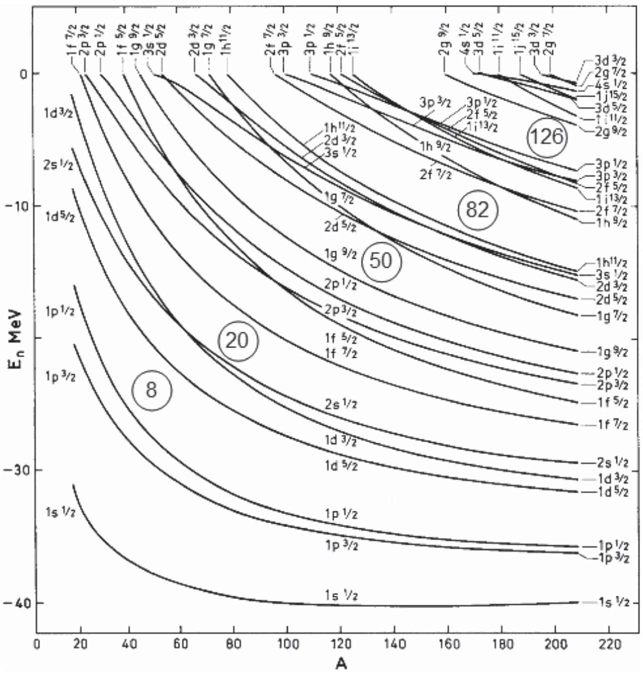

Figure 5. Energy of neutron orbitals as function of the mass A of the nucleus. Figure taken from [68]. Reproduced from Nuclear Structure Volume I, Aage Bohr and Ben R. Mottelson. Copyright 1998. World Scientific.

Early calculations in the SHN region were made using phenomenological potentials of the modified oscillator type [30, 36–38, 40], and of the Woods–Saxon type [31, 32, 39]. These calculations predict $Z = 114$, $N = 184$ as spherical magic numbers, while $Z = 126$ would be expected if the proton and neutron potentials were identical. The fact that $Z = 114$ has no counterpart for the neutrons is certainly one of the most striking features of the SHN region. The opening of the $Z = 114$ shell gap is related to an increased spin–orbit splitting of the $2f_{5/2}$–$2f_{7/2}$ partners for protons. The magnitude of the spin–orbit interaction is itself related to the radial dependence of the potential $(\frac{1}{r}\frac{\partial V}{\partial r})$, which is altered not only for the protons due to the Coulomb repulsion, but more generally due to the filling of orbitals with large angular momentum which tends to push these nucleons towards the surface. Since the number of these orbits increases with mass, the structure of SHN are especially sensitive to the spin–orbit interaction.

Mean-field calculations using an effective interaction is a concept taken from atomic physics which has been developed at the end of the 1920s by Hartree and Fock [102–105]. Although effective forces were developed since the 1950s, like the force derived from a meson field (relativistic mean field: RMF) by Duerr [106] or the Skyrme force [107], the implementation of ‘self-consistent’ calculations could not be made before the 1970s by Vautherin *et al* [108, 109]. While the RMF and Skyrme forces are contact forces (zero range), Gogny introduced in the 1970s a finite range interaction [110]. Several self-consistent mean field calculations have been performed in the 1970s in the SHN region: see e.g. [108, 111–124]. However, these calculations were performed for a limited number of isotopes only, and in particular for $^{298}_{184}114$, sometimes with a simplified interaction, mostly without pairing and for spherical nuclei only. Therefore, although some of them suggested other gaps at $Z = 120$, 126 or 138, these calculations were not really casting doubt on the $^{298}_{184}114$ magicity. In the early 1980s, RMF calculations were performed as well in the SHN region for $^{298}_{184}114$ [125, 126]. On the contrary, calculations using a Gogny force published in 1996 [124], clearly indicate that $Z = 114$ is not a magic number.

There was a renewal of interest for more detailed calculations in the mid 1990s with the increased availability of spectroscopic data and computational power. In a seminal paper, Ćwiok *et al* [127] performed systematic calculations using the SkP and SLy7 Skyrme forces. These calculations turn out to corroborate the magic neutron number $N = 184$, however favor $Z = 126$ contrary to calculations using phenomenological potentials. Even more comprehensive calculations were performed using several Skyrme and RMF forces, for spherical [128] and deformed nuclei [129], and investigating the influence of the spin–orbit force and effective mass [130].

In general, models based on the Skyrme or Gogny interaction favor the spherical magic numbers $Z = 126$, $N = 184$, those based on RMF force favor $Z = 120$ and $N = 172$ while phenomenological models still predict $Z = 114$, $N = 184$.

The reason for such differences is rather complex. It should first be noted that in the SHN region, the proton single-particle energies change significantly with the number of neutrons and vice versa. Therefore shell gaps can appear/disappear in isotopic/isotonic chains. For the sake of simplicity, the discussion will be based on single-particle spectra calculated with various forces for $^{298}_{184}114$: see figure 6 taken from [130].

As shown in figure 6, the $Z = 114$ proton shell gap is correlated with a large spin–orbit splitting of the $\pi 2f_{5/2}$–$2f_{7/2}$ partners. This gap tends to vanish when the spin–orbit splitting decreases, and/or when the $i_{13/2}$ orbital falls in between.

Most calculations based on RMF forces predict $Z = 120$ as a spherical gap, which is related to a lowest spin–orbit splitting of these forces reducing the $Z = 114$ gap. Lowering the $\pi 2f_{5/2}$ orbital together with a reduced spin–orbit splitting of the $\pi 3p_{1/2}$–$3p_{3/2}$ partners opens the $Z = 120$ spherical gap. At the same time, this proton gap is coupled to $N = 172$, which does not appear in figure 6 since the neutron shell structure changes as a function of proton number, especially at $Z = 120$. The opening of this neutron gap is correlated with a reduction of the $\nu 3d_{3/2} - 3d_{5/2}$ spin–orbit splitting. Deformed calculations using the most recent covariant density functionals

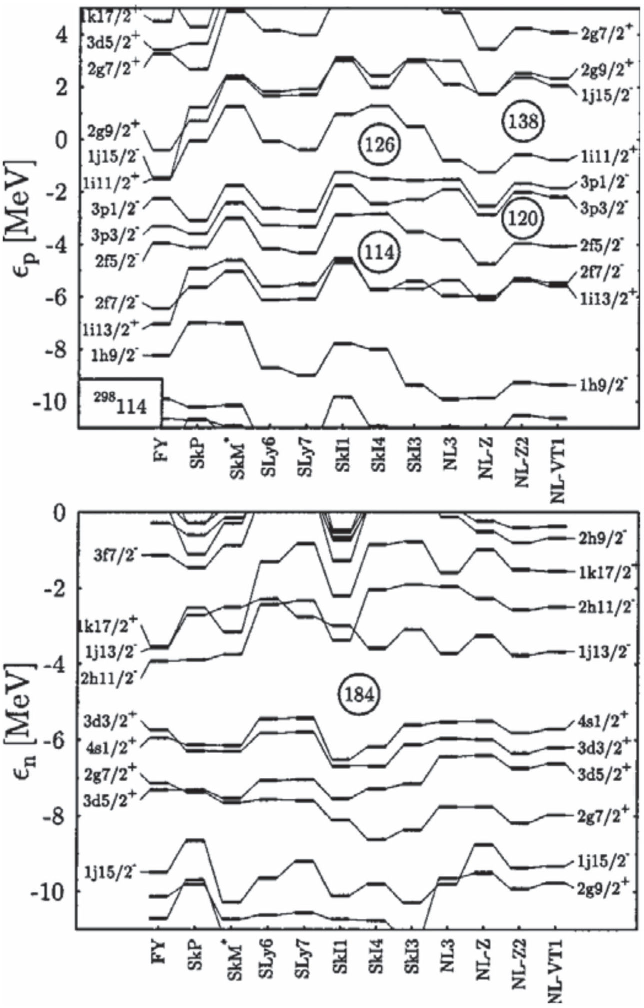

Figure 6. Proton (top) and neutron (bottom) single-particle spectra for $^{298}_{184}114$ using various Skyrme (Sk, SL) and RMF (NL) forces. Reprinted figure with permission from [130], Copyright (1999) by the American Physical Society.

however suggest deformed shapes for $N = 172$ isotones and instead $N = 184$ as a spherical gap [131].

Conversely, calculations based on most Skyrme forces predict $^{310}_{184}126$ as a magic spherical nucleus, which is linked to a reduced splitting of the $\pi 2f_{5/2}$–$2f_{7/2}$ partners and a high position of the $\pi i_{13/2}$ shell. $Z = 126$ is coupled to the $N = 184$ neutron shell gap.

As discussed above, the magnitude of shell gaps is strongly related to the spin–orbit splitting, which is itself related to the radial nuclear density: see for instance the discussion in [132] for the SHN. In extreme cases, the central depression induced by the Coulomb repulsion and the filling of specific high l orbitals leads to the concept of semi-bubble or, for even heavier isotopes, of bubble nuclei having a very low central density as suggested in 1946 by Wilson [133]: see [134–139]. Recently the first evidence for a bubble structure has been discovered in the light nucleus ^{34}Si [140].

Besides modifications of the spin–orbit splitting, the position of high-j orbitals, i.e. $\nu j_{13/2}$, $\pi i_{11/2}$, $\pi i_{13/2}$, $\pi j_{15/2}$, can alter the magnitude of the gap. However, they are often

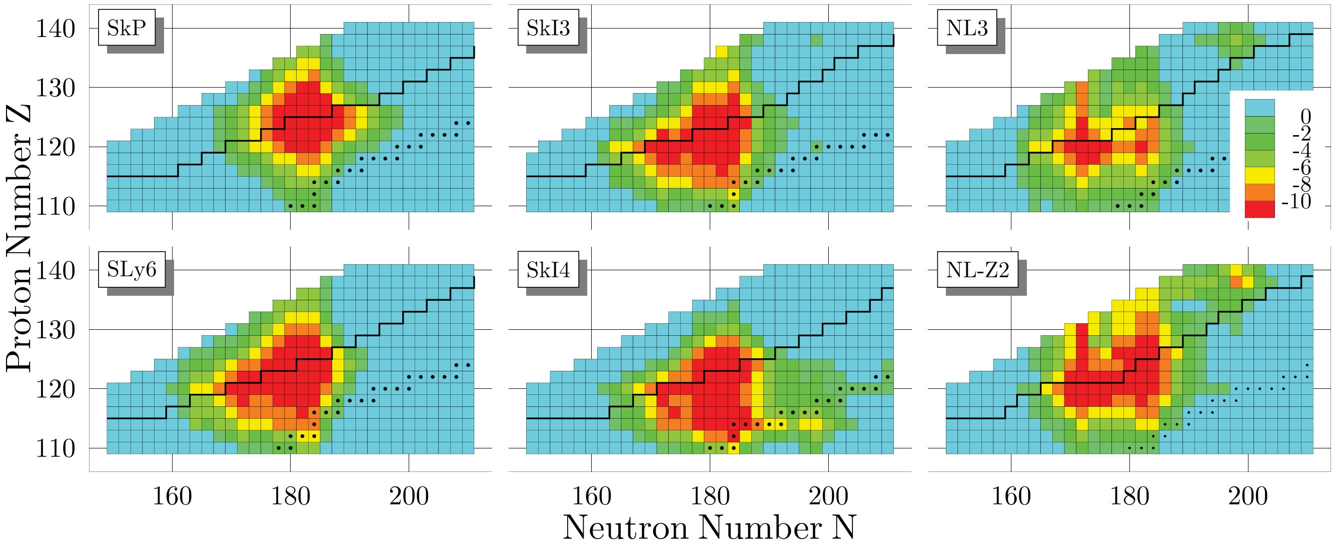

Figure 7. Shell corrections for even–even nuclei around predicted doubly magic numbers. Enhanced stability extends in a large region around magic numbers: the island of stability is soft. Reprinted from [141], Copyright 2001, with permission from Elsevier.

predicted too low in energy, with differences as large as 2 MeV depending on the force used [142].

The differences between the predictions are linked to the rather large level density and large sensitivity to fine details of the models. Indeed, each level of total angular momentum j drawn in figure 6 is $(2j + 1)$-fold degenerate. Orbitals with high j play therefore an increasing role in the level density and therefore in the structure of SHN. Since the gaps are relatively small, the presence of low-j orbitals can significantly alter the gap, however without changing drastically the binding energies and therefore the stability of the nuclei [141]. As a consequence, the magic character in the SHN region is not confined to a single nucleus like for ^{208}Pb or lighter doubly magic nuclei, but spread in a wider region as illustrated in figure 7. A SHN island of stability, if existing, would therefore have rather soft or washed out limits. It has been also suggested that the 'coexistence' of proton gaps in the single-particle diagrams could be interpreted as a magicity spread across $Z = 114, 120, 126$ [56]. It is, however, rather meaningless to combine in one picture predictions of completely different and independent models which are based on different and unrelated approaches.

It is not clear why the different parametrizations lead to so large differences concerning the location and properties of the SHN island of stability. There are certainly many reasons besides the question of the spin–orbit splitting already mentioned: correlations beyond the mean-field or in substance problems with the force are possible routes followed by theoreticians. A detailed discussion on the subject goes beyond this review, not only because of its complexity, but also because those spherical SHN are experimentally still out of reach. More details can be found in numerous publications, see e.g. [127, 130, 132, 141–144]. Moreover, the SHN world cannot be restricted to spherical nuclei.

Deformed nuclei

We have so far discussed the magic character of spherical SHN. However, the heaviest nuclear species for which detailed spectroscopy has been performed (say up to $Z \approx 104$) are deformed. How the spectroscopy of deformed nuclei can help to disentangle the discrepancies between models and gain more understanding of the nuclear structure of the heaviest elements, is the major topic we will develop in this review.

Evidence that some nuclei are not spherical were found in 1935 by Schüler and Schmidt performing atomic (optical) spectroscopy of ^{151,153}Eu [145][4]. Anomalies in the spectra lead the authors to speculate that these nuclei did not have spherical symmetry. In the same year, Casimir proposed that the asymmetry is correlated with an electric quadrupole moment of the nucleus, i.e. that the deformation of the nucleus influences the atomic properties [147], which was actually suggested as early as 1924 by Pauli [148]. In 1939, Bohr and Kalckar suggested that a rotational collective mode could be associated with a finite quadrupole moment [149]. The accumulation of data on electric quadrupole moments (in particular the systematics of Townes *et al* [150]) that could not be explained using the spherical shell model (with or without the proper ingredients provided in 1949–1950) lead Rainwater to propose in 1950 the spheroidal model [60]. This method uses a deformed shell potential in which the orbits are anisotropic. In 1951, excited states corresponding to a rotational band were observed in ^{180}Hf by Burson *et al* [151]. In the same year, Bohr published the foundation of the particle plus rotor model [61], which was an important step toward the development of the unified model. The virtue of this model is to reconcile both collective and single-particle motions. An important justification of the unified model is that the orders of magnitude are different for the collective properties of the volume (A) and surface ($A^{2/3}$) on one side, and shell effects on the other side ($A^{-1/3}$). They can be therefore decoupled, which is also known as the adiabatic condition. This can be phrased differently as the collective

---

[4] See also historical developments in the contribution to this focus issue by Heyde and Wood [146].

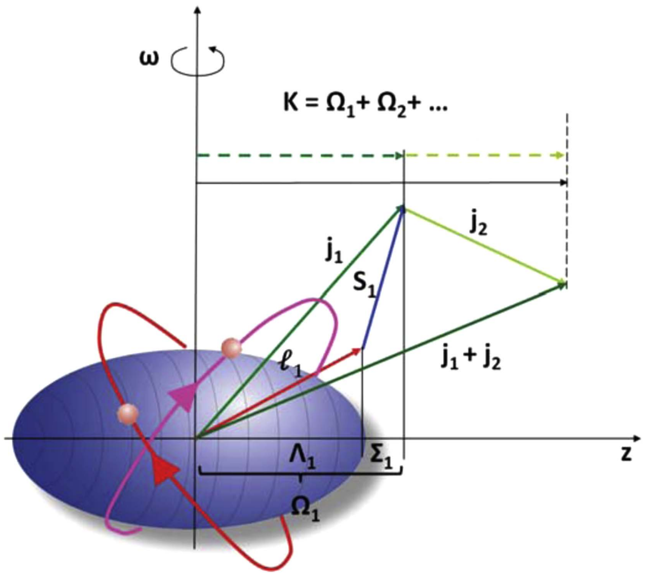

Figure 8. Definition of the K quantum number as the total projection of the sum j_i of the spin of the nucleon S_i and the orbital angular momentum ℓ_i of all excited 2-quasi-particle states onto the symmetry axis of the nucleus.

motion being slow compared to the internal motion of the nucleons inside the nucleus.

In a paper published in 1954, Ghiorso *et al* discuss the evidence for a subshell at $N = 152$, based on systematics of α-decay energies [152]. A modern representation of α-decay energies, more precisely Q_α values, is represented in figure 9. On the basis of publications by Bohr and Mottelson, Ghiorso *et al* suggest that the nature of the $N = 152$ subshell should be fundamentally different compared to major (spherical) closed shells, a possible reason for the difference in the level filling being related to spheroidal deformation. This would soon be confirmed by theoretical developments form of the continuation of the spheroidal model of Rainwater and of the unified model of Bohr and Mottelson, while Nilsson developed the deformed shell model [26] using a deformed modified oscillator. As a consequence of the deformed potential, the spherical single-particle levels are split into $(2j + 1)/2$ orbits which are up- or down-sloping as a function of deformation, Ω being the projection of the total angular momentum j on the symmetry axis as shown in figure 8. The down-sloping orbitals with a small projection Ω of the angular momentum onto the symmetry axis have a density concentration mainly along the symmetry axis, which results in a driving force towards prolate shapes. Conversely, the up-sloping orbitals have a large projection Ω and a density concentration mainly in a plane perpendicular to the symmetry axis, driving oblate shapes. As an example, a proton single-particle diagram, a so-called Nilsson diagram displaying single particle energies as a function of nuclear deformation, taken from [69, p 224], is shown in figure 10 for prolate shapes.

The modification of the shell structure as a function of the deformation generates new shell gaps. As shown in figure 10, $Z = 100$ (Fm) corresponds to a new gap for a deformation parameter ≈ 0.3, associated with a neutron gap at $N = 152$. Deformed shell gaps for $Z = 108$, $N = 162$ (^{270}Hs) would also clearly appear from a Nilsson diagram calculated in this region (see figure 10 for protons and figure 36 for neutrons). In this last nucleus, the shape of the nuclei play a decisive role for its stability: without shell corrections leading to a deformed shape, nuclei would not be stable in this region. This is probably the only region of the nuclear chart were the stability is entirely correlated to its deformed shell structure.

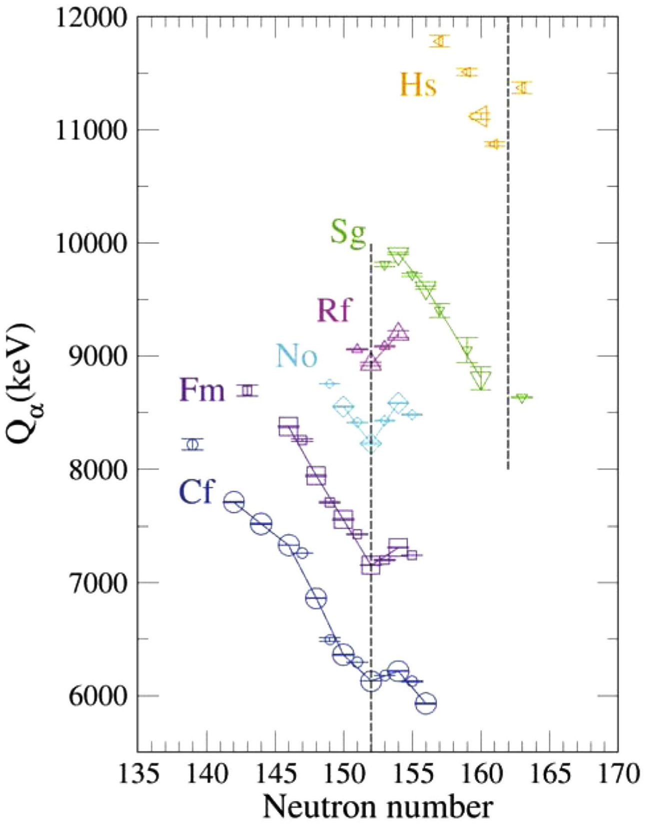

Figure 9. Q_α values for Cf–Hs isotopes. The large (small) symbols correspond to even–even (even–odd) isotopes. The dashed vertical lines correspond to the deformed subshells $N = 152$, 162. Data are taken from [153] and the ENSDF database [154] (cut-off date 27th July 2016).

An interesting aspect of deformed nuclei near ^{252}Fm or ^{270}Hs is that their structure involves low Ω orbitals which are down-sloping with increasing deformation. Some of these orbitals originate from spherical multiplets which close spherical shell gaps, therefore providing insight into the structure of heaviest spherical nuclei. This is for instance the case of the $\nu g_{7/2}$, $\pi h_{11/2}$, $\pi i_{11/2}$, $\pi j_{15/2}$ orbitals in the ^{270}Hs region and the $\pi f_{5/2}$ shell in the ^{252}Fm region. The spectroscopy of deformed nuclei provides therefore a view (definitively partial but nonetheless a view) of heaviest spherical nuclei.

Equilibrium shapes however are not only governed by shell effects: the macroscopic part has to be included in the calculations. Besides evidence of nuclear deformation from

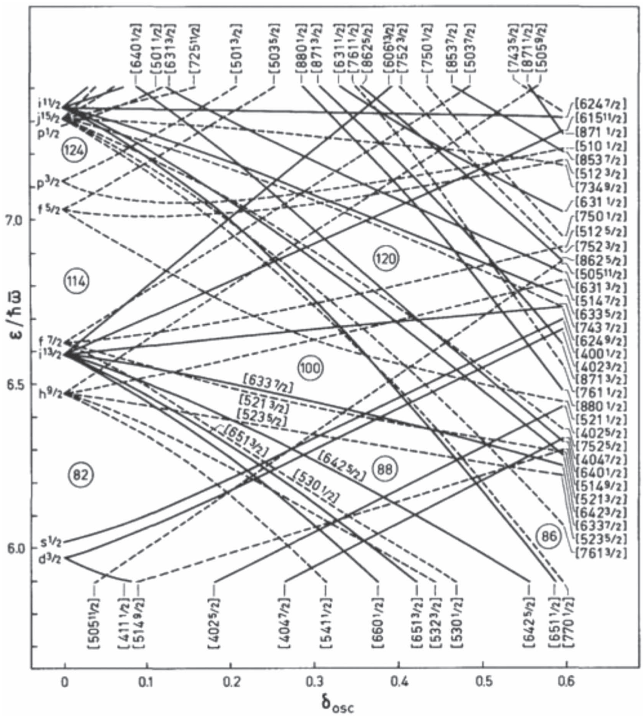

Figure 10. Proton Nilsson diagram for $Z > 82$ and prolate shapes. The figure is taken from [69]. Reproduced from Nuclear Structure Volume I, Aage Bohr and Ben R. Mottelson. Copyright 1998. World Scientific.

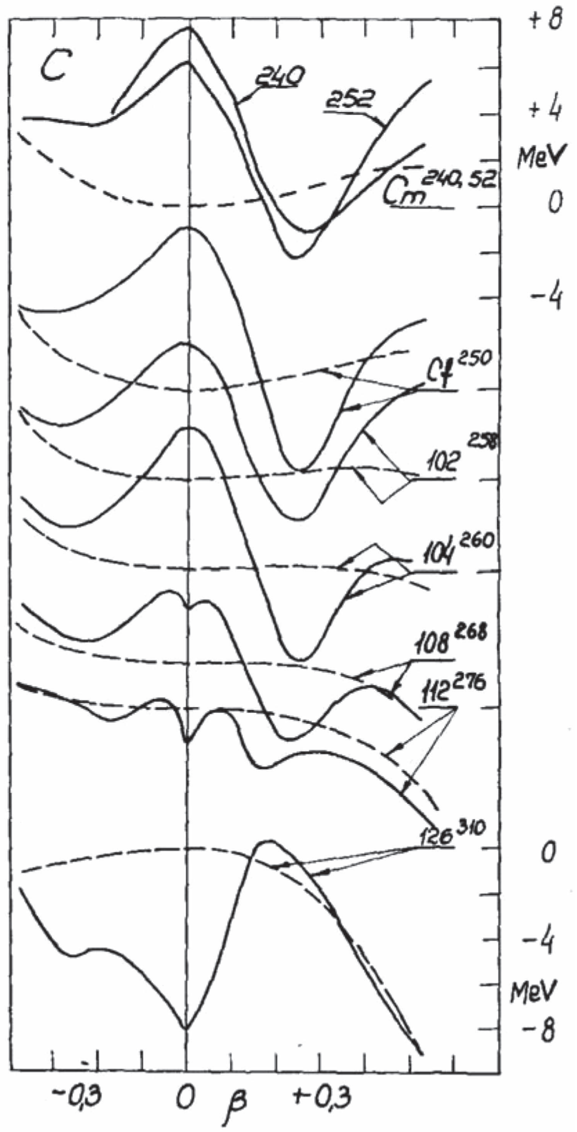

Figure 11. Deformation energy as a function of the deformation from the Strutinsky method (solid lines) compared to the liquid-drop energy (dashed lines). Reprinted from [34], Copyright 1967, with permission from Elsevier.

spectroscopic data, the parallel route of the fission discovery provided evidence for nuclear elongation. The fundamental difference is that in the second case, the process is dynamic from the g.s. to the saddle point and beyond. On the other hand, shell gaps, either deformed or spherical, can be associated to a deformed shape only if the total energy has a minimum as a function of the deformation parameters. The Strutinsky method accounts properly for both microscopic and macroscopic parts (known as microscopic–macroscopic model). The method which enables calculation of the potential energy as a function of shape, can consequently account for equilibrium shapes, and allows calculation of fission barriers. The method developed in 1965 [34, 35] was used since its foundation in the VHN/SHN region as shown in figure 11. The shell correction energies in the SHN region calculated using a Woods–Saxon deformed potential [155] are represented in figure 12, in which the enhanced stability around ^{270}Hs is clearly visible.

A consequence of a deformed g.s. is a narrower fission barrier for these nuclei as compared to spherical nuclei. Therefore for the same barrier height, deformed nuclei have a shorter partial fission lifetime compared to spherical ones. Similar arguments lead to the interpretation of an unusually short fission component of ^{241}Am as corresponding to a fission isomer and to the discovery of very elongated shapes [156], see section 4.2.4. Predictions displayed in e.g. figure 13, show that the partial fission lifetime for the spherical ^{296}Cn is about four orders of magnitude longer compared to the

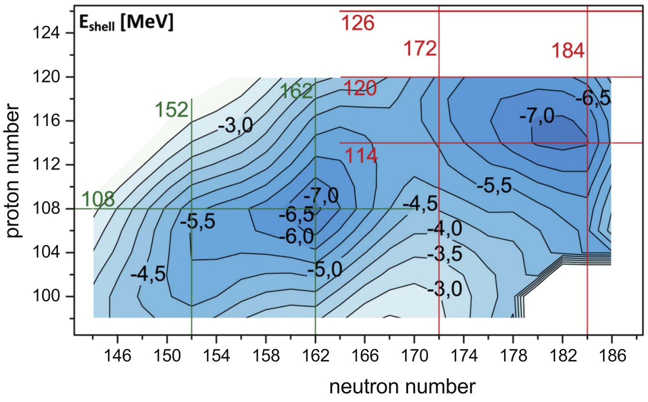

Figure 12. Shell correction energies in the SHN region calculated in a microscopic–macroscopic model approach by Sobiczewski [155]. Two regions of enhanced stability are visible near the deformed ^{270}Hs and spherical ^{294}114 nuclei.

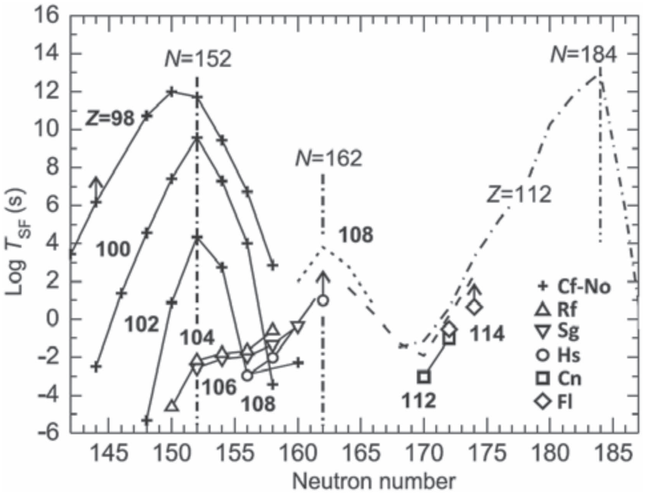

Figure 13. Calculated (dotted, dashed, add dotted–dashed lines) and experimental partial spontaneous fission half-lives. Reprinted from [157], Copyright 2015, with permission from Elsevier.

doubly magic deformed ^{252}Fm. This contrasts strongly to the α-decay process which partial lifetime is less sensitive to the deformation, since the parent and daughter states have a similar structure.

The regions of deformed-stabilized nuclei around ^{252}Fm and ^{270}Hs connect the region of deformed actinides (say around U) to the predicted island of spherical magic SHN, therefore the word peninsula is often used. The spectroscopy of this peninsula has grown considerably since the 1970s using various techniques: decay spectroscopy, particle spectroscopy coupled to direct reactions, γ and conversion-electron spectroscopy, mass measurements, etc. On the theoretical side, microscopic–macroscopic models have been used since the early predictions of SHN. This approach reproduces most of the spectroscopic properties remarkably well: see for instance the thorough works of Chasman *et al* [158, 159] and Ćwiok *et al* [160] using the Woods–Saxon potential. On the other hand, deformed calculations using a energy density functional model (EDF) performed since the 1990s provide more contrasting results. While experimental data (mainly separation energies, Q_α values, single-particle states, lifetimes, etc) clearly indicate that $Z = 100$ and $N = 152$ are indeed deformed magic numbers, all calculations based on a Skyrme or Gogny interactions, or relativistic EDFs systematically fail to simultaneously reproduce these magic deformed numbers: see [142] and references therein. This is nicely illustrated by the shell gap parameter $\delta_{2n} = S_{2n}(N, Z) - S_{2n}(N + 2, Z)$, constructed from precise mass measurements for nobelium and lawrencium isotopes across $N = 152$ in a Penning trap system, compared with various models in figure 14 [161]. Here the macroscopic–microscopic models predictions [79, 162] reproduce the observed trend of the mass values, whereas the self-consistent models fail in describing the data points. A Skyrme–Hartree–Fock calculation [128] shows a much smaller δ_{2n} and a relativistic mean-field calculation using the TW-99 parametrization [163] shows the δ_{2n} peak for the nobelium isotopes (panel A in figure 14) at $N = 154$ instead of 152. Conversely, all microscopic–macroscopic and EDF-based models agree on the magic character of the deformed $^{270}_{162}$Hs. Unfortunately detailed spectroscopy of this isotope is not yet possible due to experimental limitations.

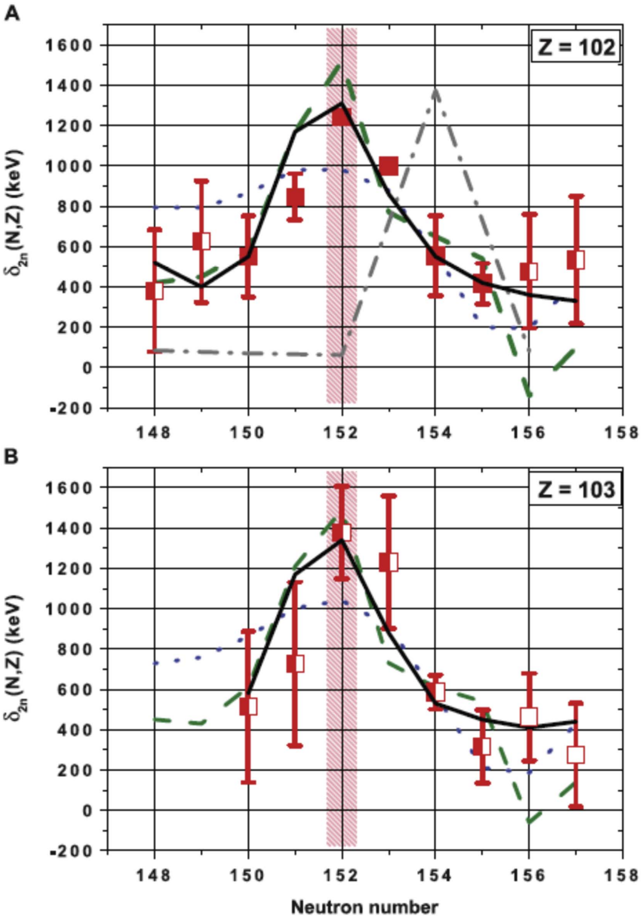

Figure 14. Experimental shell gap parameters $\delta_{2n}(N, Z)$ are shown as an indicator for a possible shell gap in the upper panel for No and in the lower panel for Lr isotopes comparing experimental values with microscopic–macroscopic and self-consistent theory approaches. The microscopic–macroscopic model calculations are plotted as dashed green lines: Möller [79], dotted blue lines: SkM* [128] and black lines: Muntian *et al* [164]. The EDF-based predictions for nobelium isotopes (dashed–dotted gray line: TW-99 [163]) are not reproducing the location of the deformed shell gap at $A = 152$, whereas the other model approaches mainly agree with the experimental values (semi-filled red squares or filled red squares calculated using mass values from [161]; open red squares from AME 2003 [165]). Figure taken from [161]. Reprinted with permission from AAAS.

A promising approach employs on the basis of a RMF ansatz the coupling of quasi-particle vibrations (QVC), consisting in phonons created by quasi-particle excitations, i.e. the creation of particle–hole pairs through the elevation of a nucleon onto a higher single particle level (SPL), leaving a hole in its original position (the concept of particle-vibration coupling had been introduced by Bohr and Mottelson in [69] p 416–447). This model is able to predict nuclear excitation spectra, single particle states and shell gaps for neutrons and protons. In application of this model to the even–even isotopes $^{296-302}120$ ($N = 178$–184), Litvinova shows the local character of the proton and neutron shell gaps, confirming the predicted softness (i.e. the shallow distribution of shell correction energies over a wider range in A and Z rather than sharp shell closures along one specific proton or neutron number) of the island of stability by various other self-consistent models mentioned above [166].

The reason for the differences and discrepancies between the models are undoubtedly complex and at least not yet fully understood. It is the purpose of this review to provide a synthesis of the studies in the VHN/SHN region on the experimental side in connection with theoretical developments.

1.3. Brief review of experimental techniques

The experimental techniques employed to study the heaviest nuclear species always comprise the combination of efficient separation schemes with comprehensive particle and photon detection techniques. In section 2.3 we describe the major separation and detection techniques and instrumentation in detail. The two main approaches, spectroscopy after separation and in-beam spectroscopy, make complementary use of these basic components. In the first case the nuclei of interested are filtered and transported to a decay station where they are identified and where one detects the de-excitation and decay of the implanted nucleus and eventually of their successors. Since the decay process is usually highly selective and obeys selection rules, limiting the change in spin and parity from initial to final state, only low spin states can be accessed. Using in-beam spectroscopy, a prompt array for γ-ray and/or conversion electron (CE) detection is installed around the target. Some angular momentum is transferred to the synthesized nucleus during the collision. Therefore, prompt spectroscopy allows medium to high spin states studies. Using a prompt array limits the beam intensity that can be used, typically to a few tens of pnA[5], which consequently sets limits on cross-sections and nuclei to be studied. On the contrary much higher beam intensity up to several pμA can be used in conjunction with spectroscopy after separation. The methodological and technological details will be discussed together with experimental findings and possible future developments in the sections following this introduction. Here we give an overview of the basic principles of the two approaches.

The nuclear species under investigation are almost exclusively produced in fusion-evaporation reactions. The heavy compound system is formed in the collision of a medium heavy projectile with a heavy target nucleus. The excited nuclear system de-excites then by emission of particles (protons, neutrons and α particles) and γ rays. Due to the high Coulomb repulsion created by the large number of protons in the excited nuclear system, this particle emission has to compete with fission to survive in the g.s. or a metastable or isomeric state. These de-excitation products are called evaporation residues (ER), in analogy to a boiling liquid, cooling down by vapor emission. For the heaviest species typically one to three or four neutrons are emitted to cool down the system. For each neutron evaporation step, the survival probability P_{surv} of the system is defined by the ratio of neutron emission probability Γ_n over the fission probability Γ_f:

$$P_{\mathrm{surv}} = \frac{\Gamma_n}{\Gamma_f}. \tag{12}$$

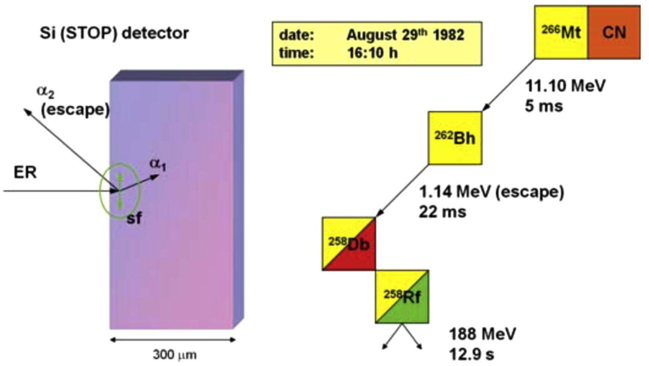

Figure 15. Decay pattern observed for the discovery event of meitnerium, $Z = 109$. The implementation of the evaporation residue ^{266}Mt (ER) into the Si (STOP) detector is followed by its α-decay (α_1). The daughter α-decay (α_2) is recorded only partially as the backward emitted α particle escapes from the detector chip. It populates the grand daughter ^{258}Db whose β-decay is not recorded. The subsequent fission of ^{258}Rf (sf) concludes the decay sequence with the detection of both fragments in the detector [42].

For the synthesis of the heaviest species these reaction products are then separated from the beam using in-flight separators. The major devices in use for SHEs research at various laboratories are in detail described in section 2.3.2. The ERs are then implanted into a silicon detector where they typically decay by sequences of α-decays, β-decays, or spontaneous fission, following decay patterns which are characteristic for the respective isotope. Decay chains formed in this way can be used for determining the isotope at the origin of the sequence in atomic number Z and mass A. As an example, the discovery decay event for meitnerium, $Z = 109$, is shown in figure 15. This decay pattern contains all possible decay features. The implanted nucleus decays by emission of an α particle with deposition of the total energy in the detector, being stopped inside the chip volume. The daughter nucleus decays again by α-decay, this time emitting the α particle in backward direction and releasing only part of its energy in the silicon chip as the range of the heavy ER in material is much shorter than the one of the helium nucleus. This step is then followed by β-decay into the final chain member which disintegrates by fission. This unique decay pattern observed at the velocity filter SHIP at GSI (see section 2.3.1), led to the first successful synthesis and identification of element 109, meitnerium, with a probability of miss-assignment of 2×10^{-18} [42]. This method of correlating the implantation of a reaction product to its subsequent decay, often referred to as 'genetic correlations', is described in detail in section 2.3.2. In figure 16

---

[5] 1 pnA $\approx 6.2 \times 10^9$ particle per second.

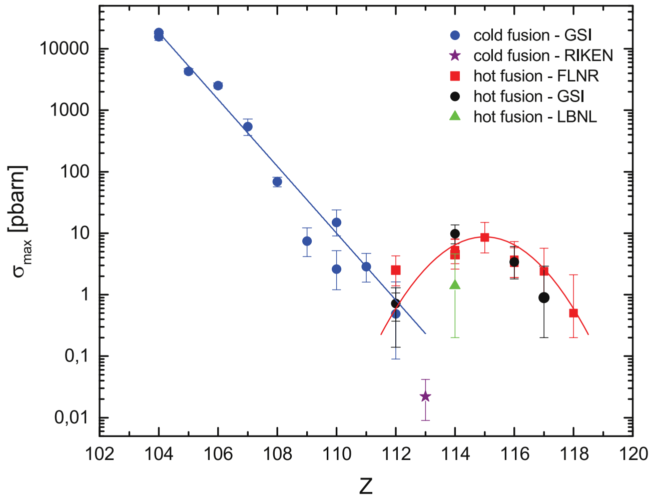

Figure 16. Maximum cross sections for SHE synthesis observed in cold and hot fusion reactions at FLNR in Dubna, Russia [157], at GSI in Darmstadt, Germany [49, 168–172], at RIKEN, Tokyo, Japan [173] and at LBNL, Berkeley, CA, United States of America [626].

the maximum synthesis cross sections obtained in the various laboratories pursuing this research are plotted as function of the atomic number Z. The major production schemes are the so-called 'cold fusion' and 'hot fusion'. In the first case the excitation energy E^* of the compound system is controlled and kept in the range of 10–15 MeV by irradiating the doubly magic ^{208}Pb and the neighboring isotope ^{209}Bi, both being well bound. For the latter reactions, the neutron rich ^{48}Ca, being again double magic, is used to irradiate actinide targets, leading to slightly more excited nuclei with E^* in the range of 30–40 MeV. Note the local maximum near $Z =$ 114–116 for the hot fusion reactions which can be interpreted as enhanced shell effects in the compound/residual nuclei. Indeed, inspection of fusion-evaporation cross section can already provide hints for shell structure.

Alpha-decay, being characteristic in decay energy and time for specific isotopes, is particularly powerful for isotope identification via the connection of a newly produced nuclide to known α emitters. In addition, it provides information on the first excited states of the daughter de-excitation. In combination with the detection of γ-rays, CEs and x-rays, it was used in the past decades to extend our nuclear structure knowledge to the heaviest species, in DSAS employing a comprehensive particle and photon detection array after a separator. Section 2 will discuss this type of investigations in detail.

The progress in developing advanced γ-ray and CE detection arrays at the target position of a separator has enabled in-beam or prompt spectroscopy which made the detection of high spin structure $\geqslant 20\hbar$ possible for heavy nuclei up to ^{256}Rf [167]. This will be discussed in section 3.

2. Decay spectroscopy after separation—DSAS

In contrast to in beam spectroscopy which will be discussed in detail in section 3, DSAS only provides access to the low lying structure features of atomic nuclei, looking at processes surviving the flight time through an ion optical separator or other separation schemes. The method yields clean and often almost background free spectroscopic data by detecting particles and photons with and without coincidence between the correlated decay radiations. Alpha-decay into ground and excited states of the daughter nucleus, isomer decay and fissioning nuclei give insights mainly into the nuclear structure at low excitation energies of the studied species. Isotopic trends of these first excited states as well as development of deformation along isotopic and isotonic chains, and towards the highest atomic numbers can be studied. In comparison with advanced model predictions these experimental trends help to trace structure features towards the region of spherical shell stabilized nuclei, the so-called *island of stability*. The state of the art of DSAS of the heaviest nuclei has been reviewed recently for $100 \leqslant Z \leqslant 109$ in [174] and for $Z \geqslant 110$ in [175].

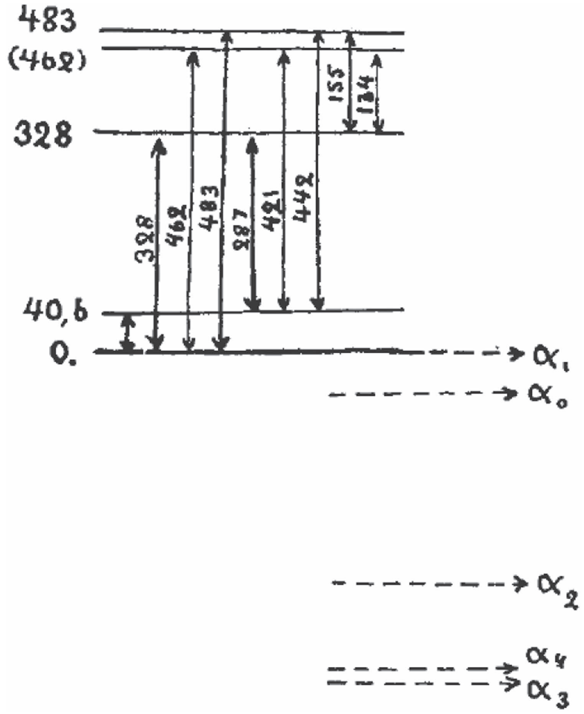

Figure 17. Original level scheme produced by Gamow (Reprinted by permission from Macmillan Publishers Ltd: Nature [176], Copyright (1967) by the American Physical Society) from the α energy differences and γ-rays observed in the decay of 'thorium C' by Rosenblum [14] and Black [177], respectively.

2.1. Historic placement

In the early decades of the last century the potential of α-decay to reveal nuclear structure features of heavy nuclei was discovered. In 1929 Rosenblum [14] had resolved the fine structure of the α-decay of 'thorium C' (^{212}Bi). The five α energies differing by 40.6, −287, −442 and −421 keV were used by Gamow [176] together with γ rays observed for the same species by Black [177] to construct the level scheme of this heavy nucleus (figure 17). These pioneering

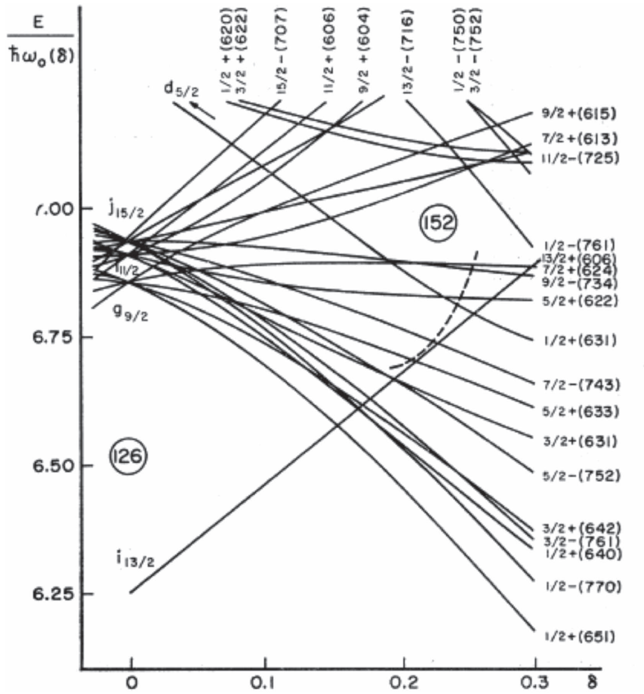

Figure 18. Original figure of the Nilsson diagram for neutron single particle states used by Ahmad and co-workers in 1967 to identify the configuration responsible for the transitions observed in ^{249}Cf [178]. The y-axis denotes the single particle energy drawn as a function of quadrupole deformation δ. Reproduced with permission. Copyright American Physical Society 1967.

investigations were followed by numerous studies of α decaying heavy nuclei pushing nuclear structure investigations towards a region where nuclear deformation played an increasingly decisive role for the stabilization of nuclear matter.

One of the prerequisites for the success of these investigations was effective separation of the isotope of interest from the sometimes overwhelming background of unwanted species. In a series of experiments started in the late 1960s Ahmad and co-workers relied on sophisticated radio-chemical methods of source preparation in combination with efficient particle and photon detection techniques. Studying e.g. excited states in odd-A californium isotopes (^{247,249,251,253}Cf) being populated by α-decay of the fermium mother nuclides [178–181], they could reveal detailed nuclear structure information, construct detailed level schemes and locate the single particle states in the single particle energy E_{sp}-deformation plane, the so-called Nilsson diagram. In figure 18 a Nilsson diagram for neutron single particle states is shown, which had been used by Ahmad *et al* in 1967 to identify the configuration responsible for the observed transitions [178]. The region of low level density for neutron number 152 at quadrupole deformation $\beta_2 = 0.2$–0.3, the so-called deformed shell gap is clearly visible.

In these early studies, comprehensive spectroscopy could already be performed, including the detection of α particles, γ- and x-rays, as well as CEs. While Ahmad and co-workers were using chemical separation methods, the He gas-jet technique was used e.g. by Bemis and co-workers in the pioneering work to establish the Z of element 104 rutherfordium [182] and 105 dubnium [183]. These investigations will be discussed in detail in the next subsection. With the advent of powerful ion optical separation techniques, like velocity filters, gas-filled separators and magnetic mass spectrometers coupled to advanced particle and photon detection systems in the last decades of the 20th century, the door was opened to access the heaviest nuclear species. In conjunction with modern correlation methods, the area of deformed shell stabilized nuclei around $Z = 108$ and between $N = 152$ and 162 moved increasingly towards the focus of decay spectroscopy of heavy nuclei, with the starting point in the fermium–nobelium region [174]. The nowadays available digital signal processing, yielding basically deadtime free data elaboration, allows the investigation of extremely short-lived species. The upper right of the chart of nuclides, sometimes also referred to as the chart of Segré with the spherical shell stabilized nuclei and the *island of stability* beyond $Z = 110$ [175] seems to come closer in reach of nuclear structure investigations. The landscape we are moving on here and which we are exploring in this paper is shown in figure 19.

2.2. X-ray spectroscopy—Z identification for rutherfordium, dubnium and beyond

The identification of the atomic number of a nuclear species is essential, in particular, when isotopes of previously unknown elements are synthesized for the first time. A powerful method is the connection to known decay properties like the correlation to members of an α-decay chain with known α-decay properties, as the α-decay is characteristic for each isotope (see also section 1.3). This method was most successfully applied in SHE synthesis via so-called cold fusion up to $Z = 112$ [49] and $Z = 113$ [173]. In cases, however, where those decay chains end in spontaneously fissioning nuclei with only unknown decays in the chain, alternative methods have to be sought for.

One possibility is offered by the detection of characteristic x-rays. The precise understanding of atomic shell properties leads to an unambiguous prediction of the Z dependent x-ray decay energies for an atomic species. In 1913 and 1914 Moseley first used K and L x-ray measurements to verify a simple linear relation between the measured x-ray frequency ν and the atomic number Z of the emitting atoms up to gold [185, 186].

Alpha-decay of nuclides with odd nucleon numbers often populate excited states in the decay daughter nucleus, due to decay selection rules and the quantum mechanics properties of the involved nuclear states. The de-excitation of these levels can proceed preferentially by internal conversion followed by a cascade of Auger electrons and x-rays.

Detecting characteristic nobelium K x-rays in coincidence with ^{257}Rf ($Z = 104$) α-decays, Bemis and co-workers could prove the observation of (at that time) new element 104 [182]. This granted the group led by Darleen Hoffmann from the Lawrence Berkeley National Laboratory

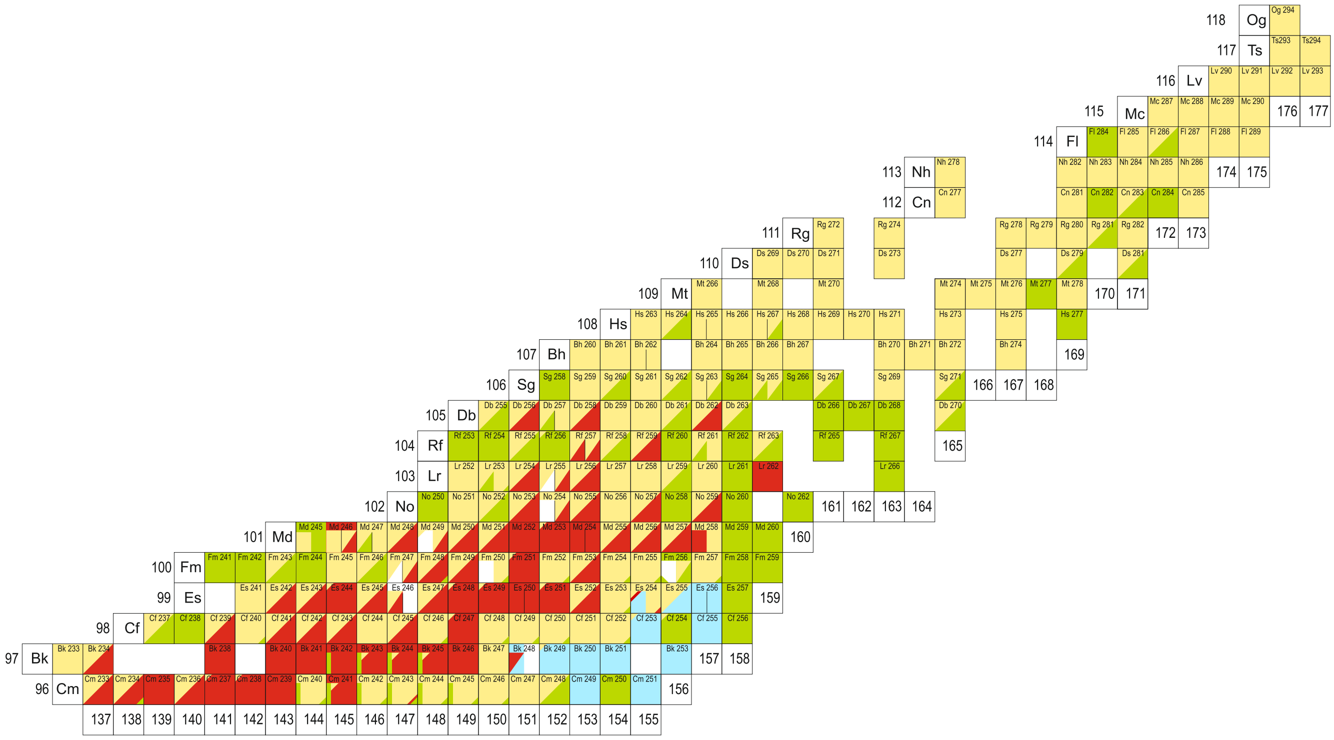

Figure 19. Excerpt of the chart of nuclides showing the heaviest nuclei observed ($Z = 96$–118 and $N = 137$–177). The colors indicate the decay mode and the subdivision in areas of different sizes the relative decay probabilities. Yellow denotes α-decay, green spontaneous fission (SF), red β^+ or electron capture (EC) and blue β^- decay. The scheme is adopted from [184].

(LBNL) the right to name this element rutherfordium. The original spectrum with clear peaks for the K_α radiation and indications with a few counts even at $K_{\beta1}$ and $K_{\beta2}$ energies is shown in figure 20. Later they could apply the same technique successfully to the element with $Z = 105$ [183]. The naming rights, however, were awarded to the Russian competitors from the Flerov Laboratory for Nuclear Reactions (FLNR) in the city of Dubna who named it dubnium.

The heaviest system for which x-ray—α-decay coincidences have been observed is the decay of ^{262}Bh ($Z = 107$) for which three photons with K_α energies of dubnium were observed by Heßberger *et al* [187]. Recently, attempts were undertaken to use x-ray detection in order to establish the atomic number for members of decay chains which were attributed to the first synthesis of isotopes of the element with $Z = 115$.

At the gas-filled separator TASCA of GSI Darmstadt, Germany Rudolph and collaborators irradiated ^{243}Am with ^{48}Ca and observed a total of thirty decay chains. For one of these chains they detected in coincidence with the α-decay of ^{276}Mt, a member of the ^{288}115 decay chain, a candidate for a bohrium x-ray cascade, consisting of two signals which were in agreement with K_α energies [188]. However, Gates *et al* who observed for the same reaction in an experiment performed at the Berkeley gas-filled separator (BGS) a total of forty-six chains, showed that discrete γ transitions are present in the respective x-ray energy range which make an unambiguous detection of x-rays impossible. They could show in a comprehensive analysis, employing detailed simulations, that the photons observed in [188] could be convincingly explained by γ-decay of excited states of ^{272}Bh, which were populated by ^{276}Mt α-decay. The final confirmation of this group of decay data, obtained by the irradiation of actinide targets with ^{48}Ca is still pending. The assignment of the naming rights by the responsible IUPAC/IUPAP committee was recently made, based on indirect proof like the so-called cross bombardment, where the same nuclei are produced in fusion evaporation reactions differing by one α particle in the entrance channel [189, 190].

2.3. Experimental technique

The experimental scheme of DSAS relies on the combination of an efficient separator with a comprehensive detection setup. Various separator types have been employed over the years to separate the wanted species after their production in a target foil from unwanted background particles, which consist mainly of scattered or unreacted projectiles. While the early measurements relied on chemistry and gas-jet techniques, the advent of ion-optical separators made the investigation of the heaviest species possible.

General considerations

When dealing with rare events, there are only few parameters one can play with to reach the best efficiency and selectivity; the ultimate room for improvement being the beam intensity as soon as the 100% detection efficiency limit is approached. In general, however, lowering the spectroscopic limits can be achieved by increasing the efficiency of

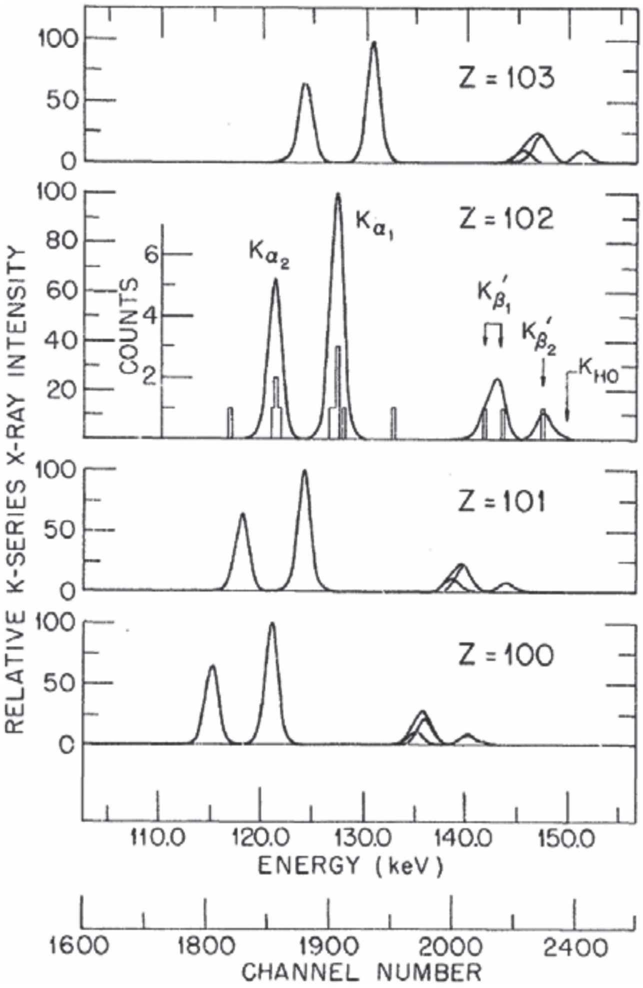

Figure 20. Nobelium x-rays measured in coincidence with α-decays of ^{257}Rf (second panel) compared to theoretical predictions. Calculated spectra for elements 100, 101 and 103, fermium, mendelevium and lawrencium are also shown. Reprinted figure with permission from [182], Copyright (1973) by the American Physical Society.

the decay station, and the transmission of the separator. The detection resolution is also an important parameter contributing to the data quality. Cleanliness is moreover a key aspect to isolate the transitions of interest from the often overwhelming background (this is in particular the case using a prompt array as discussed in section 3). Therefore, improving the efficiency of spectrometers/separators should be also combined with an improvement of the rejection capability. As far as selectivity is concerned, vacuum separators are in principle superior to gas-filled devices, as they can often provide the mass and charge of the recoiling nuclei, but often at the price of a lower transmission. It is important to note that rejection is probably the most difficult quantity to model and parametrize in the design of separators. Indeed, most of the background arises from scattering inside the spectrometer/separator or from beam tail distributions (charge states, emittance). The first aspect is difficult, if not impossible, to be included in simulations. This does not prevent taking some precautions e.g. avoiding beam scattering inside the spectrometer/separator chambers, appropriate design of the beam dump to avoid the transmission of scattered ions, etc. These considerations are extremely important in the design of high-acceptance devices since improving the angular acceptance improves not only the recoil transmission but also the transmission for Rutherford scattered beam, scattered target nuclei, transfer products, etc.

Besides kinematic selection of the implanted nuclei, the decay station should allow an as accurate as possible spectroscopy, taking into account the characteristic decay of SHN, i.e. α, CE, β and γ spectroscopy. The best α energy resolution is needed since α transitions are usually bunched in a narrow energy region. The α energy resolution is however affected by the electron summing effect. In the case of simultaneous α-decay and daughter de-excitation by CE emission, both signals can be summed (at least partially) in the implantation Si detector, consequently producing spurious peaks: see e.g. [174, 191]. In that respect, gas-jet techniques are superior since they are equivalent to spectroscopy using a thin source: see e.g. [174] and references therein. In the case of isomer de-excitation, several simultaneous transitions and subsequent Auger or x-ray transitions can be summed (at least partially) in the implantation detector (DSSD) whose threshold should be as low as possible to exploit the calorimetric technique (see [192]). An overall good granularity is needed to avoid pile-up events although the cascade multiplicity is rather low in decay experiments. Obviously, the best coincidence efficiency is needed which leads to compact arrays with a good transparency of the most central detectors. The time resolution is usually a compromise with energy resolution, but dedicated fast-timing arrays can be considered for measurements of short lifetimes as an alternative to HP–Ge detectors.

The position resolution can be exploited to measure angular correlations and therefore deduce the multipolarity of the transitions, as done since the 1950s in e.g. 'ThC′' (^{212}Bi), 'ThC″' (^{208}Tl) decay [193]. More recent exploitation of the method can be found in e.g. [194–196].

2.3.1. *Separation methods.*

While the early measurements were relying on chemistry, mass separation and gas-jet techniques, the advent of ion-optical separators made the investigation of the heaviest species with lowest production cross sections possible.

Chemical separation, mass separation and gas-jet techniques

In [174] a comprehensive overview of the various types of studies is given. The einsteinium, fermium and mendelevium isotopes which were produced by long-term neutron irradiations in high flux nuclear reactors, by αxn and multinucleon transfer reactions (MNTs), were investigated by offline detection methods, performing α, γ and electron (from internal conversion) spectroscopy. The chemistry of actinides and transactinides, which is the basis for the separation techniques applied for a given species, is described in a comprehensive review in [197].

Gas-jet techniques are used to transport short-lived species for which the slower chemical methods are not

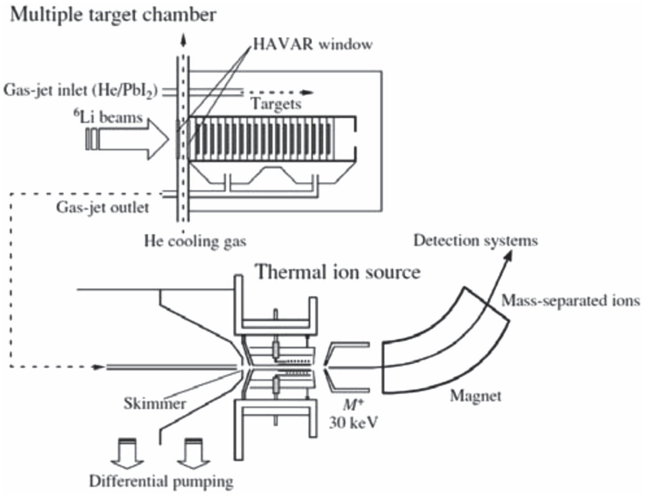

Figure 21. Gas-jet set-up of the JAEA Tandem Facility in Tokai, Japan [198, 199]. Figure taken from [199](2003). Copyright © MAIK 'Nauka/Interperiodica' 2003. With permission of Springer. Original Caption: 'Schematic view of the gas-jet coupled JAERI-ISOL'.

applicable to a detection system remote from the irradiation site after they have been stopped in a gas volume. As an example the gas-jet setup used at the JAEA tandem facility in Tokai, Japan is shown in figure 21 [198, 199]. Here the projectiles (in the shown case ^{6}Li) are sent onto a multiple target station. The reaction products are then slowed down in the gas. The gas, a mixture of He and an aerosol to which the products attach, is then sent through a capillary to the detection station which includes a thermal ion source and a magnetic mass separation stage. An isotope separation online (ISOL) system provides an efficient separation of the species of interest. Asai *et al* used this set-up to identify e.g. spin, parities and single-particle configurations of ^{257}No and its α-decay daughter ^{253}Fm [200].

The techniques described here have been applied to isotopes up to element hassium ($Z = 108$). In particular gas-jet and chemistry instrumentation has been used also in combination with ion-optical separators [201].

Ion-optical separators

Ion optical separators have been employed to study the heaviest nuclear species, produced mainly in fusion evaporation reactions. These heavy nuclides which move under 0° with respect to the beam direction are effectively separated from the many orders of magnitude more intense projectile beam and efficiently transported to a detection station located in the separator's focal plane. Two major types of separators are in use and under continuous development, gas-filled and vacuum separators.

Gas-filled separators

Gas-filled separators exploit the fact that the ions recoiling out of the reaction target undergo multiple charge changes due to many collisions with the gas atoms through a gas volume with pressures of the order of a mbar of typically helium or hydrogen. A gas-filled separator was first used in the late 1950s by Cohen and Fulmer as a fission fragment separator [202]. In the magnetic fields of the instrument, the ions follow the trajectory of the average charge state scattering around this path according to their magnetic rigidity $B\rho = mv/q_{\text{av}}$. Assuming that the atomic electrons having a velocity smaller than the ions will be stripped, Bohr suggested that the average charge state can be approximated to $q_{\text{av}} = (v/v_0)Z^{1/3}$, with v_0 being the Bohr velocity [203] (in practice, more accurate parametrizations based on experimental data are used). Hence the magnetic rigidity is given as $B\rho \approx 0.0227A/Z^{1/3}$ (Tm), which does not depend on velocity or gas pressure. This leads to 'charge focusing' and a substantially narrower spatial distribution as compared to the wide charge state distribution in vacuum. In this way this separator type gains in transmission with respect to vacuum separators, in particular, for more asymmetric reactions, where the difference in charge leads to larger spatial distributions for the slower recoils: see e.g. [204, 205] and references therein. Quite a number of these instruments are used for SHEs research such as the DGFRS of the FLNR, in Dubna [206] which is shown as an example in figure 22, GARIS at RIKEN, in Tokyo, Japan [207], BGS at LBNL, Berkeley, USA [208], RITU of JYFL, in Jyväskylä, Finland [209, 210] which is shown in figure 23, SHANS at IMP in Landzou, China [211] and TASCA at GSI, Darmstadt, Germany [212]. TASCA was initially motivated by the necessity of additional separation for chemical studies of superheavy single atom experiments. It was subsequently

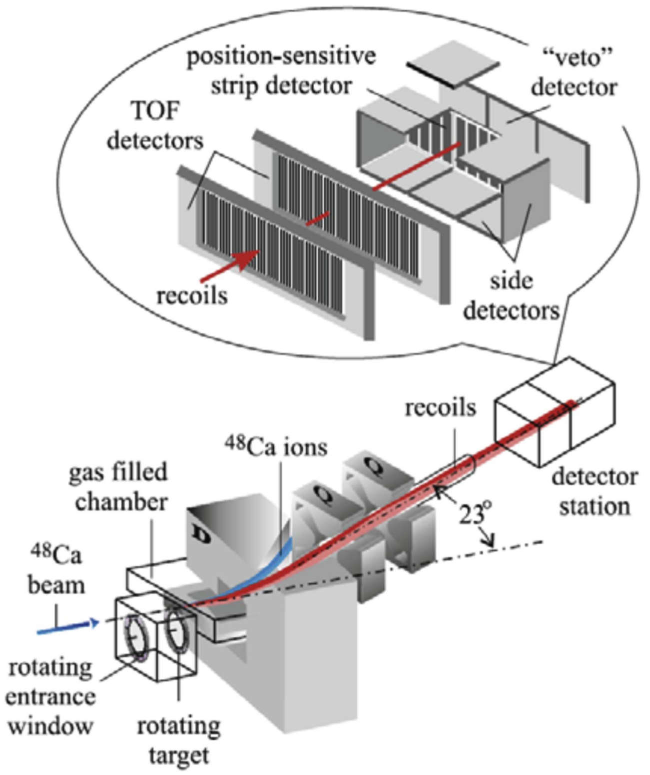

Figure 22. The Dubna gas-filled separator DGFRS together with its particle (ERs, αs and SF fragments) detection system in the focal plane and the rotating wheel holding the target foils. The well separated trajectories of projectiles (typically ^{48}Ca) and recoil nuclei are also shown. Reprinted from [157], Copyright 2015, with permission from Elsevier.

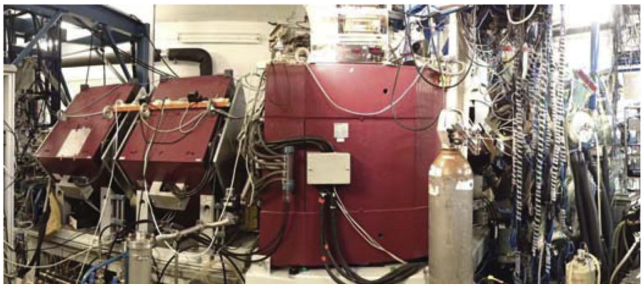

Figure 23. Panoramic view of RITU. The SAGE array for prompt spectroscopy is on the right, where the beam comes from. The optics elements of RITU are from right to left: dipole and two quadrupoles. These elements are preceded by one more quadrupole, not visible in the picture. Part of the GREAT focal plane is visible on the left.

successfully used for SHE synthesis and decay spectroscopy studies. Similar to the DGFRS, it is composed of one magnetic dipole followed by two quadrupoles. A list of spectrometers and separators in operation or under construction is given in table 2, where the magnetic/ion-optic configurations and technical specifications are shown.

Vacuum separators and spectrometers

The group of vacuum devices is itself subdivided in separators and spectrometers. While separators mainly separate exploiting ion-optic parameters sensitive to electromagnetic forces on moving charged particles, spectrometers provide in addition spectrometric information, typically on the mass of the species under investigation. The velocity filter SHIP (see figure 24) e.g. exploits the velocity difference of projectiles and reaction products of fusion reactions [213]. It was successfully employed to synthesize the elements with $Z = 107$–112. Equipped with a comprehensive focal plane detection system, it was used throughout the last one to two decades to collect a wealth of decay spectroscopic information on the low lying structure of heavy and superheavy nuclei from the nobelium region up to ^{270}Ds for which the heaviest K-isomer was discovered at this set-up. As with SHIP the velocity filter of the LISE spectrometer of GANIL in Caen, France, is used in FULIS mode [214] to perform decay spectroscopy for heavy species.

The vacuum separator of the FLNR/JINR in Dubna, Russia, VASSILISSA, has recently been upgraded to Separator for Heavy Elements Spectroscopy (SHELS) [215–217] with the purpose of increasing the transmission in particular for very asymmetric reactions, and to extend the kinematic range: see figure 25. The central separation unit, originally being an energy filter consisting of electric fields only, has been transformed into a velocity filter by substituting the electrostatic separation section by a combination of electric and magnetic field components. The optics has a Q^3EDDEQ^{3}D scheme, the electric deflectors being characterized by movable plates to optimize the electric field for different reaction kinematics.

Exploiting the mass-over-charge selectivity of magnetic fields a class of ion-optical arrangements are used as mass spectrometers. In the mid-eighties of last century Spolaore and Lawson had developed the RMS a configuration of combined electric and magnetic fields which was then built at the Laboratori Nazionali di Legnaro LNL in Legnaro (Padua), Italy [218]. It consisted of a quadrupole triplet after the target for focusing the products onto the focal plane detector, followed by a magnetic dipole which was surrounded by a electric dipole plus sextupole and a sextuple plus electric dipole arrangement (QQESDSE). Though this was never used for SHN research it was the model for a number of sometimes slightly modified copies, such as the fragment mass analyzer (FMA) at ANL [219], which has been used in combination with particle and γ detector arrays for an extended nuclear structure research program of in beam and DSAS including the investigation of SHN. In comparison to the RMS of Legnaro, for the FMA sextuples were omitted but a quadrupole doublet was added at its exit allowing a better beam spot control in the focal plane.

A similar approach though more compact has been implemented recently at the University of Jyväkylä. The new MARA recoil mass separator [220] of QQQED configuration has been optimized for the study of $A < 150$ nuclei using mostly symmetric reactions although it will be adapted to more symmetric cases albeit with lower transmission for VHN/SHN compared to RITU. However, its vacuum mode and M/q resolving power may be beneficiary for lifetime measurements using the charge-state plunger technique [221] or the recoil shadow method coupled to conversion-electron measurement [222]: see section 5.2.2.

In section 5.1 in the context of future facilities for SHN research new separator and spectrometer concepts are presented, for example the planned pre-separator for the Dubna SHE-factory or the separator-spectrometer combination S^3 presently under construction at the new SPIRAL2 facility of GANIL. In the spirit of new concepts we will discuss in the following the use of ion traps and laser spectroscopy methods for the investigation of heavy and superheavy nuclei in recent years.

Ion traps and laser spectroscopy

Recently, new techniques such as laser spectroscopy and mass measurements in ion traps, developed for the neighboring discipline of atomic physics, have in turn aided SHN and VHN research.

At the SHIPTRAP Penning trap set-up precise masses have been measured for the heaviest nuclides so far with nobelium and lawrencium isotopes [228, 229]. Together with Q_α values obtained from α decay studies at SHIP [230] masses and binding energies could be established up to the even–even superheavy nucleus ^{270}Ds, providing benchmark values for model calculations close to these very extreme values of high Z and A. In addition to providing precision mass measurements, being a highly selective separator, its use for trap assisted spectroscopy is envisaged, by coupling particle and photon detector systems (see section 2.3.2) similar to the ones in use with the separators discussed earlier to it.

Radioactive decay-detected resonance ionization spectroscopy (RADRIS) was applied to samples of radioactive material produced in high-flux thermo-nuclear reactors. Therefore, it was limited to species having sufficiently long life-times with fermium isotopes being the limit. Recently the technique has been developed to a stage in which it is now possible to extend its application beyond fermium [231].

Table 2. List of spectrometers and separators in operation or being built for the spectroscopy or synthesis of VHN/SHN.

Name	Optics	Acceptance msr	Dipole(s) angle deg.	$B\rho_{\max}$ Tm	$E\rho_{\max}$ MV	Resolution	Length m
Vacuum devices							
SHIP [213]	QQQEDDDDEQQQD	3	6, 12, 12, 6	1.2	20	$\nu/\Delta\nu = 50$	12
SHELS [215]	QQQEDDEQQQD		22, 22, 8				12
RMS [218]	QQESDSE	10	40	1	12	$M/\Delta M = 280$	8.2
FMA [219]	QQEDEQQ	8	40	1	18	$M/\Delta M = 350$	8.2
MARA [220]	QQQED	9	40	1	14	$M/\Delta M = 250$	7
S^3 [223]	Q^{3}DQ^{3}Q^{3}DQ^3– Q^{3}EQ^{3}Q^{3}DQ^3	9	22, 22, 22	1	1.8	$M/\Delta M = 300$	30
LISE [214] (FULIS)	QQQ(E×D) (E×D)QQQD	4	n.a.	3.0	n.a.		11.5
Gas-filled devices							
DGFRS [224]	DQ$_h$Q$_v$	10	23	3.1	n.a.	n.a.	4.3
DGFRS-II [224]	Q$_v$DQ$_v$Q$_h$D		30, 10	3.2	n.a.	n.a.	6.3
GARIS [207]	DQ$_h$Q$_v$D	22	45, 10	2.2	n.a.	n.a.	5.75
TASCA [212]	DQ$_h$Q$_v$	13	30	2.4	n.a.	n.a.	3.5
RITU [225]	Q$_v$DQ$_h$Q$_v$	8.5	25	2.2	n.a.	n.a.	4.7
BGS [208]	Q$_v$D$_h$D	45	70	2.2	n.a.	n.a.	4.6
SHANS [211]	Q$_v$DDQ$_v$Q	25	52	2.9	n.a.	n.a.	6.5
HYRA GF [226]	QQDQDQQ	28		2.25	n.a.	n.a.	
AGFA [227]	Q$_v$D	44@40 cm 22@80 cm	38	2.5	n.a.	n.a.	3.9 4.2
VAMOS-GFS [563]	Q$_v$Q$_h$D	70 max	20-60	2.2	n.a.	n.a.	7.6-8

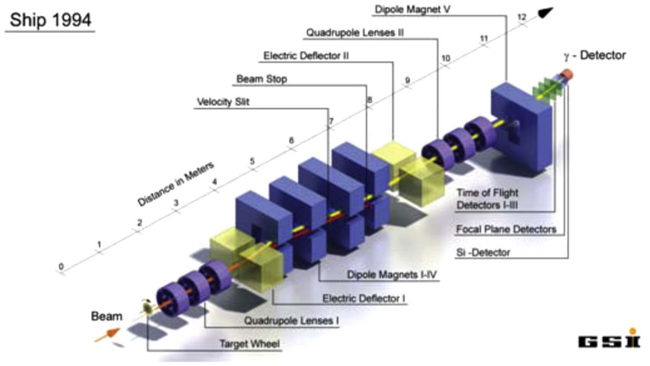

Figure 24. The velocity filter SHIP of GSI in its version from 1994. In addition to the original version [213], apart from focal plane detection development, a magnetic dipole for further background suppression had been added at the end of the ion-optical system [49]. (Graphics: Maurer. Reproduced with permission from J. Maurer.)

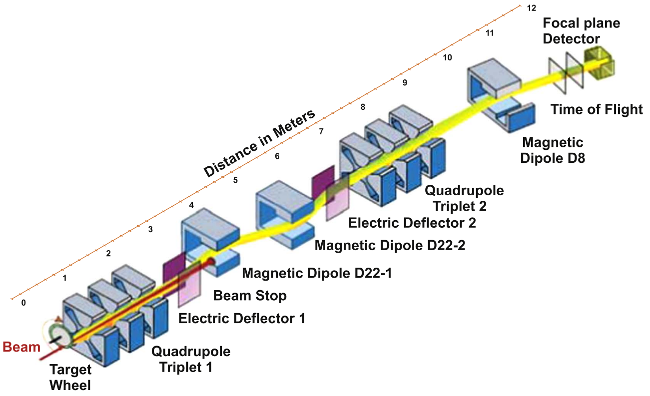

Figure 25. The SHELS separator at Dubna. Reprinted from [217], Copyright 2015, with permission from Elsevier.

In a pioneering experiment, Laatiaoui and co-workers used reaction products from heavy ion fusion-evaporation reactions separated from the beam by the velocity filter SHIP [232]. In a cycle procedure the positively charged heavy ions were stopped after SHIP in a gas volume, then attracted by a filament polarized to a negative electric potential and subsequently released into the gas volume again by heating the filament to a controlled temperature. Shining lasers of characteristic frequencies on the now neutral nobelium atoms, they were ionized and transported to a solid state detector, where they were identified by their characteristic α decay.

Scanning a specific frequency range with lasers in a two-step excitation scheme the experimenters succeeded in locating the resonance for the $^1S_0 \rightarrow {}^1P_1$ g.s. transition in ^{254}No for the first time in a transfermium nuclide [232], opening up the possibility to study this nucleus in detail by laser-spectroscopic means. With the observation of a first series of Rydberg states they were able to establish an upper limit for the ionization potential of the nobelium atom. A continuation of these experiments will provide a firm establishment of this value [233]. Using the different technique of surface ionization, the ionization potential of lawrencium ($Z = 103$) has been recently measured in conjunction with the gas-jet technique at JAEA, Tokai, Japan [234].

The potential of the RADRIS method, moreover, promises the detailed study of atomic levels as well. Via the interaction of electrons in the atomic shells and the nucleus, it is possible to investigate nuclear properties like gyromagnetic factors and quadrupole moments of the nucleus by measuring isotope shifts and hyperfine structure. Being highly selective in separating the species of interest almost background free, RADRIS adds a new detection tool to classic detection schemes of DSAS which will be presented in the following section.

2.3.2. Particle and photon detection. Since the 1960s devices have been developed to identify the nuclei using their characteristic α decay, correlate the subsequent parentage decays and eventually measure lifetime and spectroscopic data. After a physical separation using either a gas-jet or separator/spectrometer technique, still parasitic nuclei can be implanted, preventing a clear parentage identification. Moreover, decay sequences of several nuclei of interest can temporally overlap. Therefore the device needs to provide some granularity in order to avoid decay entanglement. Ghiorso *et al* developed in the early 1960s an original method based on the transport of nuclei to be identified in several sequential independent measurement stations. The device known as the vertical wheel (VW) is displayed in figure 26 in an upgraded version [235]. Nuclei are implanted into the surface of the wheel which moves at regular time intervals to a series of seven decay stations. At each position the wheel faces a Si detector who can measure α-decay which can be therefore correlated in time to its implantation. A subsequent α from the same implantation can be detected in a next decay station. Alpha-decay, γ or conversion-electron emission can also eject the daughter nucleus from the wheel to the facing Si detector. As shown in the inset of figure 26, this detector moves on a regular basis off the wheel to face another Si detector to measure daughter decay or eventually collect ejected daughter nuclei. At the same time, a second movable detector substitutes the position facing the wheel. The VW has been used in particular for the identification of elements $Z = 104$–106.

Using a similar principle, arrays based on a tape device playing the same role as the wheel have been developed.

As an alternative to the wheel cycle for the separation of decay generations, the application of position correlations had been developed. The granularity obtained by the mechanical transport of the nuclide has been replaced in the late 1970s by position-sensitive Si detectors. The technique often known as 'genetic correlations' is illustrated in figure 27. After separation, recoils are implanted into a position sensitive detector at time t_0, position (X_r, Y_r). A subsequent decay with energy $E_{\alpha 1}$ occurs at time $t_{\alpha 1}$ and position $X_{\alpha 1}$, $Y_{\alpha 1}$ nearby the implantation. The process continues with the decay of the daughter, the granddaughter, etc. The technique correlates in position and time the implant (X_r, Y_r) and the subsequent decays ($E_{\alpha i}$, $t_{\alpha i}$, $X_{\alpha i}$, $Y_{\alpha i}$) to isolate a decay chain which provides the nucleus identification, lifetime measurement and eventually spectroscopic data through the α-decay fine structure and coincident γ and conversion-electron measurement. The genetic correlations technique is credited to S. Hofmann *et al* with the α-decay study of very neutron-deficient isotopes of Hf, Ta, W and Re at SHIP [236].

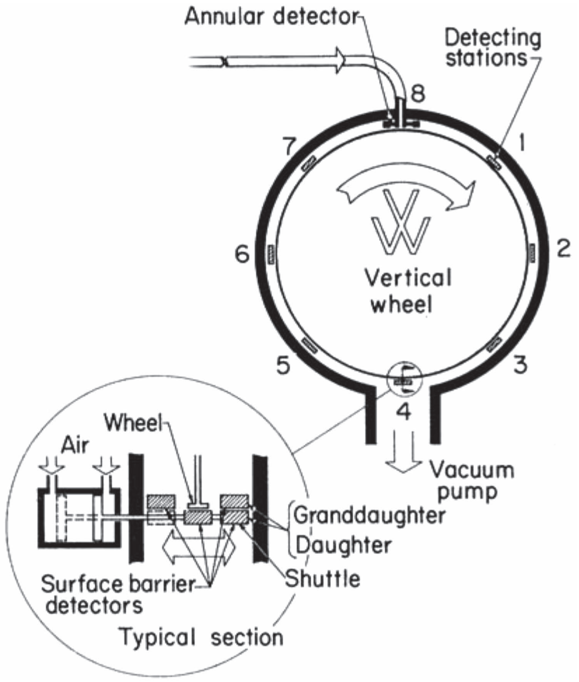

Figure 26. Vertical wheel used by Ghiorso *et al* to measure implantation correlations between the implantation and alpha decay. See text for details. Reprinted figure with permission from [235], Copyright (1974) by the American Physical Society.

An early example is the comprehensive arrangement of particle and photon detectors used at SHIP in the 1980s [237] (see figure 28). A silicon detector array, consisting of a central implantation unit and two backward wings for escaping particles, mainly α particles and fission fragments, was at that time already combined with a germanium unit for x-ray and γ-ray detection, looking from behind at the implantation unit. The silicon detectors were still composed of small single units: seven position sensitive Si-chips of $9 \times 27\,\mathrm{mm}^2$ for the implantation array and 4 quadratic ($10 \times 10\,\mathrm{mm}^2$) Si-chips without position sensitivity for each backward wing. Each of the implantation units was position sensitive in vertical direction by charge division in a resistive surface electrode. The Ge crystal of 36 mm length and 46 mm diameter provided a relative detection efficiency of 12%, which is defined as in comparison to the reference efficiency of a $3'' \times 3''$ NaI detector at 25 cm distance from the source, which is $\epsilon_{\mathrm{NaI}} = 1.2 \times 10^{-3}\,cps/Bq$. The analog electronic system was still relatively modest with a total of 22 parameters treated, recording energies and positions for two different amplification ranges with $E_{\max} = 320$ and 32 MeV. It had the capability of measuring the kinetic energies of fission fragments, ERs and α particles at the same time. Together with the photon detection and the implemented event timing, this set-up provided the basic functionality for a

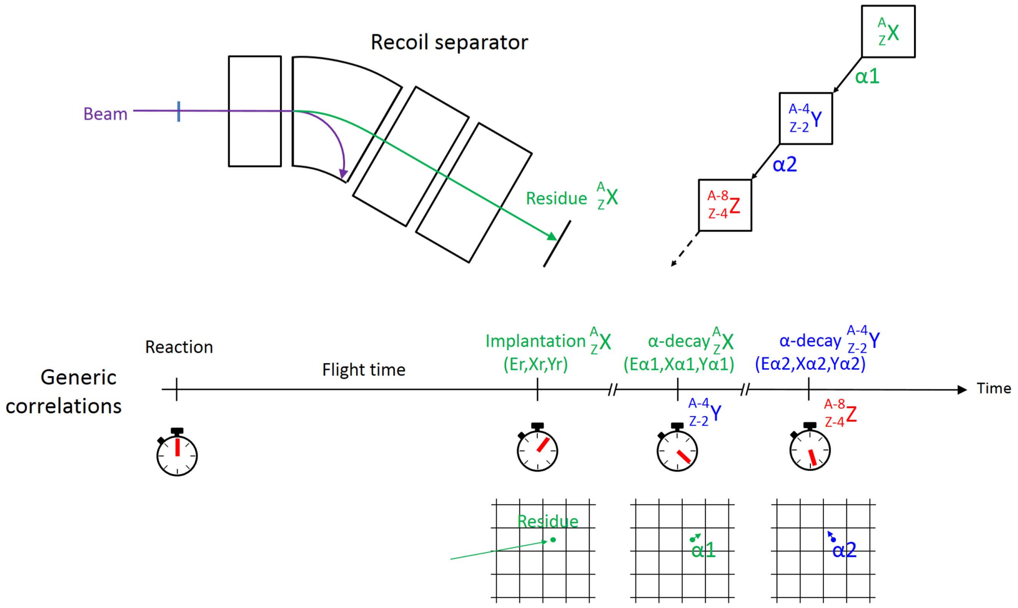

Figure 27. Illustration of the genetic correlations technique. After the separator, the recoiling nucleus ${}^{A}_{Z}X$ is implanted in a position-sensitive detector at position (Xr, Yr). It subsequently decays via alpha emission in its neighborhood at position $(X\alpha 1, Y\alpha 1)$ to the daughter nucleus ${}^{A-4}_{Z-2}Y$ which itself decays to the granddaughter ${}^{A-8}_{Z-4}Z$ at position $(X\alpha 2, Y\alpha 2)$. The technique allows correlations in time and position of the implantation and subsequent decays.

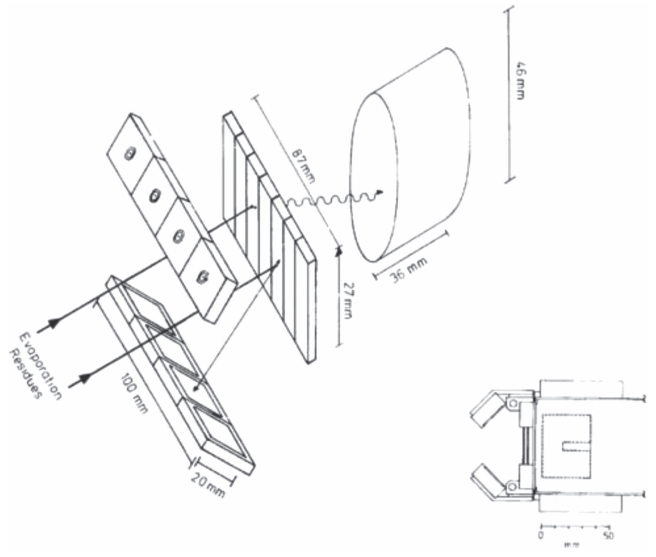

Figure 28. Early implementation of the detector system in the focal plane of SHIP for particle and photon detection. Reprinted from [237], Copyright 1984, with permission from Elsevier.

decay spectroscopy set-up allowing particle-photon correlations to be reconstructed.

Technical developments over the last three decades have refined the instrumentation, improving efficiency and resolution in energy, position and time. We will illustrate this history following the development at SHIP. There the next step was the construction of a new silicon array now based on a single larger wafer of 35 × 80 mm^2 subdivided by resistive surface electrodes into 16 strips of 5 mm width each [49]. Seven of these units built a box configuration with an implantation ('stop') detector surrounded upstream by 6 units of the same type forming a box for backward detection. The system was equipped with two planar and a larger single crystal germanium detectors for x-ray and γ-ray detection, mounted in close configuration behind the stop detector. Two transmission detectors for time-of-flight and anti-coincidence purposes based on micro-channel plates in front of the 'box' and a veto detector behind the 'stop' for the detection of light particles passing the silicon-chip completed the array. The number of parameters to be handled by the data acquisition electronics in terms of analog-to-digital conversion was still limited to $\approx$50. Given the need of treating substantially more signals than 50, adopted strategies like multiplexing had to be used in the analog part to overcome this bottleneck.

The advent of so-called digital electronics modules employing fast sampling analog-to-digital converters, flash ADCs, opened new horizons towards a high number of electronics channels and, in particular, in terms of pulse shape analysis, yielding e.g. higher count rate capabilities and the access to short decay times. Sampling rates of up to GHz with nanosecond timing granularity make it easily possible to investigate short-lived processes as they are expected for decay of heavy and superheavy nuclei. A number of modern detection arrays employ this technology. A mobile decay spectroscopy set-up with a compact mechanical mounting (MoDSS; see figure 29), facilitating its use at and transportation to different separator installations [238], has recently been constructed and used in first experiments at SHIP [239] as well as at the LISE separator of GANIL [214, 240]. The set-up is similar to the TASiSpec array [241] produced earlier. It accommodates up to five large volume Ge- detectors around a cube shaped housing with thin aluminum γ windows of 1.5 mm thickness. The heart of the array is the double-sided

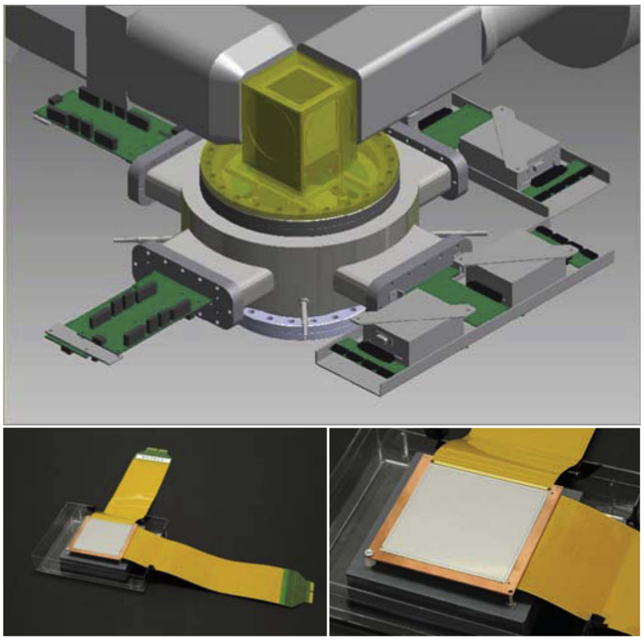

Figure 29. Mobile decay spectroscopy detection array (MoDSS) developed for the use after separators [238]. The set-up consists of a compact cube like arrangement in a thin aluminum housing which can be surrounded by up to five large volume γ detectors. The double-sided silicon strip detector directly glued to the copper support for better cooling with the integrated signal lines on flex-PCB is shown in the lower panel. (Graphics: Maurer; Photography: Otto. Reproduced with permission from J. Maurer.)

silicon strip detector (DSSD). On either side of a $60 \times 60\,\mathrm{mm}^2$ wafer, 60 strip electrodes are placed perpendicular to each other creating a pixelized position sensitivity of $1\,\mathrm{mm}^2$ spatial resolution. The chip is glued directly onto a copper frame allowing a better cooling and it is directly connected to the signal conductor produced as an insulator-copper sandwich construction with an integrated ground plane and grounded copper lines in between each signal line to shield against external noise and internal cross talk. The data readout by a sampling ADC arrangement with 50 MHz sampling frequency and 14 bit ADC resolution can accommodate up to 256 channels extracted from the compact vacuum chamber and additional signals from the Ge-detectors and other auxiliary equipment like time-of-flight detectors or timing sources. In this way it is well suited for the comprehensive detection of all ingredients needed for advanced decay spectroscopy, including ERs, α particles, fission fragments, electrons, γ-rays and to some extent x-rays. As most of the modern DSAS set-ups it provides high detection efficiencies (ER $\approx$100% (intrinsic; total efficiency depends mainly on the separator transmission), $\alpha \approx 80\%$, fission fragments $\approx$100% and $\gamma \approx 40\%$).

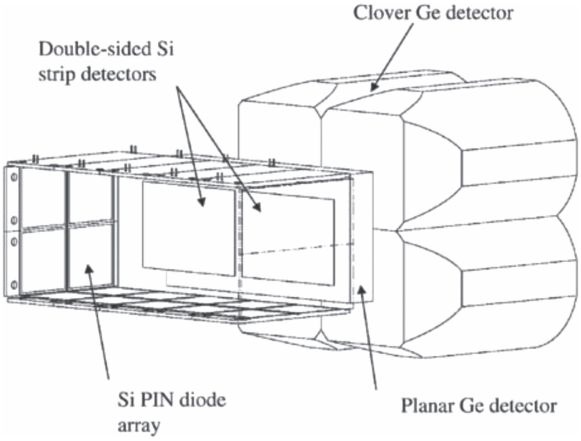

Figure 30. The GREAT spectrometer for DSAS mounted in the focal plane of the gas-filled separator RITU of JYFL. Reprinted from [242], Copyright 2003, with permission from Elsevier.

A number of set-ups of this type are presently in operation at various places. One of the first devices for particle and photon detection for the detection of heavy and superheavy nuclei is the gamma recoil electron tagging (GREAT) set-up built in the focal plane of the gas-filled separator RITU at the cyclotron laboratory of the University of Jyväskylä [242]. The composition of GREAT is shown in figure 30. Two DSSDs, having an active area of $60 \times 40\,\mathrm{mm}^2$ with a strip width of 1 mm, serve for the detection of implantation and subsequent particle decays. Twenty-eight silicon PIN diodes are mounted in the backward hemisphere of the DSSDs to detect α particles escaping from the DSSD and CEs. To increase their electron detection efficiency their thickness is 500 μm, larger than the 300 μm typically used for the implantation detectors. The latter thickness value is sufficient to cover the ranges of reaction and decay products from some 10 μm for the heavy reaction products up to $\leqslant$100 μm for α particles and fission fragments, whereas electrons of several hundreds of keV can pass through several hundred μm of silicon. For the photon detection a planar germanium strip detector with an active area of $120 \times 60\,\mathrm{mm}^2$, 15 mm thickness and a strip pitch of 5 mm for x-ray detection is followed by a Ge-clover detector consisting of four large volume crystals ($70 \times 70 \times 105\,\mathrm{mm}^3$ with 15° tapering of the first 30 mm) for γ-ray detection.

Other arrays with arrangements very similar to the MoDSS set-up have been constructed to be used in the focal plane of various separators like the before mentioned TASiSpec [241] for the gas-filled separator TASCA of GSI or the digital high-granularity implantation-decay station at the FMA recoil mass spectrometer of the Argonne National Laboratory (ANL) [227]. A geometrically slightly different arrangement was chosen for the cube corner clover array at the BGS [243]. Here three $64 \times 64\,\mathrm{mm}^2$ DSSDs with 32×32 strips form a corner of a cube with its corner pointing in beam direction. The Si-detectors are surrounded by three large volume germanium clover detectors. This configuration is saving detector instrumentation efforts by minimizing the loss of efficiency in comparison to a full cube geometry. In Dubna, the SHELS separator is equipped with a focal plane detection system known as GABRIELA (Gamma Alpha Beta Recoil Investigation with the Electromagnetic Analyzer) [244] which is continuously upgraded to improve its performances. Recently a highly-efficient Compton-suppressed Ge detector known as CLODETTE [245] has been added.

Having this advanced instrumentation available enables a comprehensive decay spectroscopy including all decay processes like α emission, fission, β and γ decay, x-ray and CE emission to be performed, with access to the heaviest nuclear species ever. The next section illustrates the features which can be accessed.

2.4. Accessible processes

DSAS is a powerful tool to study the lowest excited states of nuclei by a number of different processes. The major limitation is the flight time through the separator which is of the order of 1 μs. Therefore, studies can only be performed on produced nuclei which have decay times of $\gtrsim$1 μs. One of the major advantages of DSAS is the efficiently reduced background due to the separation of the species under investigation from the beam and to some extent from unwanted reaction products. In addition, correlations between various decay modes, like e.g. α-decay or fission and γ emission, and the ER implantation signal provide additional background reduction and identification of the decaying species. Another advantage is that the implantation of the activity into a solid state detector provides a stopped and well localized source. Therefore, no Doppler corrections have to be applied as in the case of fast moving radiation sources as with in-beam spectroscopy. The efficiency of the photon detection profits very much from spatially well confined implantation spots of a few cm^2, which can be covered easily by a large volume germanium detector like the ones discussed in the preceding section on the detection instrumentation, providing near 2π solid angle coverage. With additional detector modules surrounding the implantation wafer in the backward hemisphere, up to $\approx$40% total efficiency at photon energies of 100–200 keV can be achieved [246].

The processes accessible by DSAS as shown schematically in figure 31 are mainly α-decay and the decay of isomeric states. The detected radiation is then the emission of α particles, γ- and x-rays, and CEs. In addition nuclear fission and beta-decay are investigated.

Alpha-decay

Alpha-decay is often described by the combination of two processes: (i) the formation of an α particle inside the nucleus and (ii) the penetration through the Coulomb barrier (see. e.g. [69]; p 115ff). In the beginning of last century Geiger and Nuttal established a regular relation of α half-life $T_{1/2}$ and total decay energy (Q_α) by a Z-dependent parametrization (parameters A and B):

$$\log T_{1/2} = A(Z)Q_\alpha^{-1/2} + B(Z), \tag{13}$$

leading to a robust linear behavior for each isotopic chain [247] which is illustrated in figure 32, showing the logarithmic decay time as a function of the range R, which is proportional to the velocity and therefore the kinetic energy of the α particle. The $Q_\alpha^{-1/2}$ dependence of the half-life was first explained with the tunneling of the α particle through the nuclear potential as the inverse process of α-decay in 1929 by Gamow [248], analyzing the experimental findings for α-decay from various emitting sources being absorbed by different light nuclei [249, 250]. The Q_α is itself a function of the mass and charge of the emitting nucleus. As can be seen in e.g. figure 9, the Q_α energy is increasing with the atomic number Z and decreasing as a function of the mass A for an isotopic chain. This trend can be inferred from the liquid-drop model, but can also be seen somewhat differently: the first effect (Z dependence) is related to the kinetic energy gained by the α particle due to the Coulomb repulsion during the daughter and α separation. The second effect (mass) is due to the increased radius of the nucleus which lowers the Coulomb separation energy.

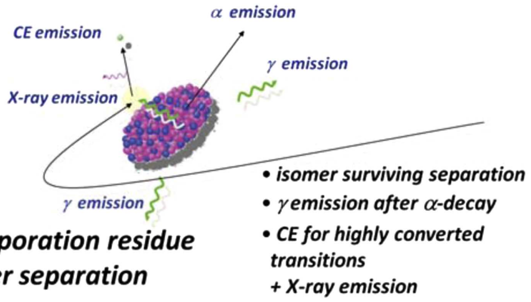

Figure 31. Overview over processes accessible for decay spectroscopy after separation and implantation into a comprehensive focal plane particle and photon detection array. Reprinted from [175], Copyright 2015, with permission from Elsevier.

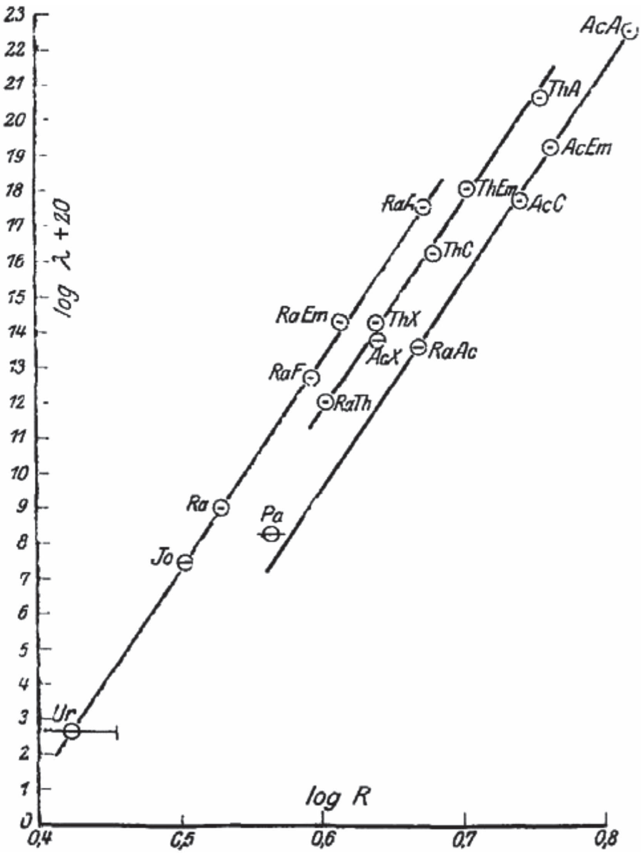

Figure 32. The Geiger–Nuttal law: relation between the decay time and the range in matter of α particles emitted from various isotopes. Original figure taken from [251] (1922). Reproduced with permission from Springer.

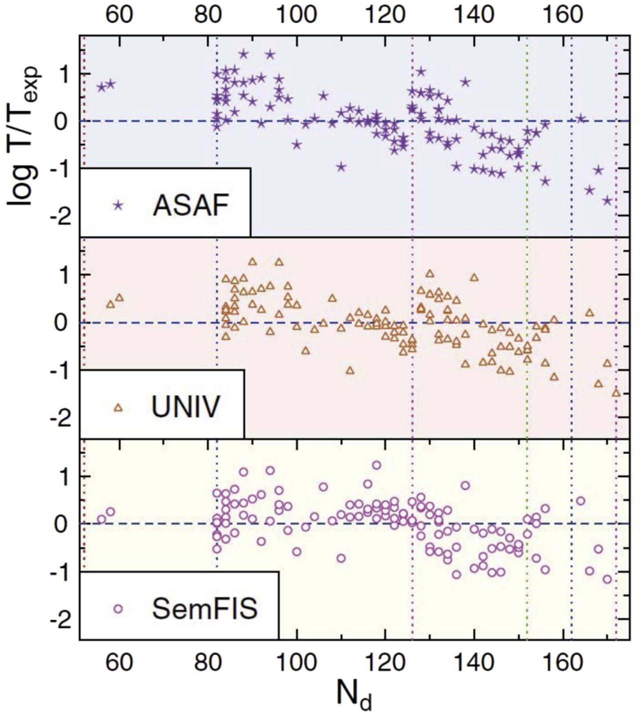

Figure 33. Comparison of calculated and experimental half-lives as a function of the neutron number N_d of the decay daughter nucleus for various parametrizations. Reproduced from [252]. Copyright © EPLA, 2007. All rights reserved.

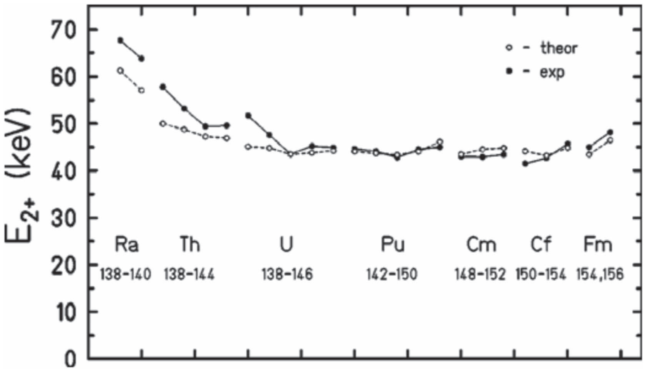

Figure 34. comparison of experimental excitation energies of the first excited 2^+ states for even Z isotopes from Ra ($Z = 88$) to Fm ($Z = 100$) with the results of microscopic–macroscopic calculations by Sobiczewski *et al*. Reprinted figure with permission from [255], Copyright (2001) by the American Physical Society.

Only recently a deviation from this linear behavior had been observed for light polonium isotopes [253] for which the $\log_{10}$ dependence of $T_{1/2}$ is no longer valid. In the same paper the authors explain the reason for that newly observed feature analyzing the dependence of the α cluster formation probability in isotopic chains as a function of neutron number, in particular, in the vicinity of the closed $N = 126$ neutron shell where they find a strong discontinuity. They identify the origin of the parameters A and B in (13) by modeling the tunneling process (A) and taking account of α formation (B), respectively.

In order to reproduce the relation of decay times and energies for a wide range of nuclei, substantial effort has been put in developing parametrizations of the Geiger–Nuttal relation by various groups. Poenaru *et al* developed a set of parametrizations adapted to various mass regions, in particular also for the region of the heaviest α-emitters [252]. Figure 33 shows the improvement of three generations of parametrizations, employing different fission models, with the discontinuity at the $N = 126$ shell closure almost vanishing for the 'SemFIS' parameter set (lowest panel in figure 33). Despite these efforts, the accuracy is sometimes exceeding an order of magnitude. Nevertheless, this approach is a valid tool to reveal decay retardation and confirm in this way a possibly metastable, isomeric character of the emitting state. This retardation is mainly due to the quantum mechanics properties of the emitting and receiving state in the mother and decay daughter nucleus, respectively, which is not taken into account in the above-mentioned model. It is often quantified using a so-called hindrance factor HF which is defined as the ratio between theoretical and experimental half-lives:

$$\mathrm{HF} = \frac{T_{1/2}^{\mathrm{theo}}}{T_{1/2}^{\mathrm{exp}}}, \tag{14}$$

or more complicated derivations of this basic relation. One typically applies a rule-of-thumb validation of the hindrance factor which can provide arguments in the process of establishing spins and parities of the involved states: see [254]. The hindrance factor is close to 1 when the initial and final states are similar. Its value increases as the wave function differs in the following order: initial and final spin projection parallel with parity unchanged, initial and final spin projection parallel with parity changes, spin flip and change of parity.

Alpha fine structure measurements populating or depopulating excited states of heavy nuclei can yield nuclear structure properties by establishing properties such as spin, parities and excitation energies of those states. In particular collective rotational 2^+ states in even–even nuclei are populated with a rather high probability of 20%–50% depending on the mass and deformation. Thus experimental excitation energies of 2^+ states in even–even nuclei can trace deformation via the relation between E_{2^+} and the moment of inertia $\mathcal{J}$ (see e.g [155, 255]):

$$E_{2^+} = \frac{\hbar^2 \ell(\ell + 1)}{2\mathcal{J}}, \quad \ell = 2. \tag{15}$$

In figure 34, Sobicweski *et al* compare the results of their microscopic–macroscopic calculations with experimentally established 2^+ energies for even Z isotopes from Ra ($Z = 88$) to Fm ($Z = 100$) [255]. The theoretical values, obtained in a cranked approximation using a large seven-dimensional deformation space, reproduce the experimental values very well and underline the reliability of the model concerning the prediction of nuclear deformation. Extending these calculations towards heavier nuclei, the authors of [255] can reproduce the deformed doubly magic character at $Z = 100$ and $N = 152$, and at $Z = 108$ and $N = 162$ as minima in E_{2^+}.

Alpha-decay competes in general with other decay processes like spontaneous fission, β decay and in case of excited states also with γ decay and internal conversion. The observed half-lives for the disintegration of a nucleus is the convoluted value of the partial half-lives of the competing decay modes, with the inverse ratio in decay time determining the branching ratio between those modes.

Fission

For heavy, high Z nuclei with increasing Coulomb repulsion forces between the increasing number of protons in the system, the probability of rupture into two fragments increases. As introduced in section 1.2.1, this trend is proportional to the square of the proton or atomic number Z and inversely proportional to the atomic mass A. The so-called fissility of a nucleus is described by the ratio between these parameters. Under reasonable assumptions on the basis of a liquid drop concept of the atomic nucleus, one can establish a critical value for which fission wins over the confining nuclear potential: $Z^2/A \gtrsim 50$. The barrier against spontaneous fission, however, is modified by quantum mechanics effects. As can be seen from figure 19 it sets-in in the fermium ($Z = 100$) region. Following even Z isotopic chains, like e.g. for rutherfordium ($Z = 104$) and seaborgium ($Z = 106$), a distinct pattern can be observed for the onset of spontaneous fission. Theoretical efforts to model the process of a nucleus breaking apart, using the one-dimensional WKBJ approximation for the solution of the Schrödinger equation and a static fission path on a PES of deformation parameters, initially failed [256]. A dynamic approach using an effective inertia along the fission path, based on an inertia tensor $B_{\alpha_i\alpha_j}$ in the cranking approximation [155]:

$$B_{\alpha_i\alpha_j} = 2\hbar^2 \sum_{\nu\nu'} \frac{\langle|\partial H/\partial\alpha_i|\partial H/\partial\alpha_j|\nu\rangle}{(E_\nu + E_{\nu'})^3}(u_\nu v_{\nu'} + u_{\nu'} v_\nu)^2 + P^{ij}, \tag{16}$$

was more successful in describing experimental findings. Here α_i and α_j are the deformation parameters spanning the plane for the PES, H denotes the single particle Hamiltonian, u_ν and v_ν are the BCS variables taking into account nucleon pairing, and E_ν the quasi-particle energy related to the single-particle state $|\nu\rangle$. The collective motion is described by P^{ij}. The comparison of the trajectory obtained with this dynamic approach is compared to the static case in figure 35.

Spontaneous fission half-lives calculated with the same model approach are shown in figure 13 for the heaviest even-Z isotopic chains compared to experimental data for $Z = 98$–114. Here, the onset of nuclear structure dependent effects is indicated by the disappearance of the symmetric isotopic distribution of T_{SF} at $Z = 104$. The increasing values for $Z = 112$ toward $N = 184$ reflect the closed proton and neutron shells, $Z = 114$ and $N = 184$, predicted by this macroscopic–microscopic model.

A closer look at figure 19 reveals another interesting feature of nuclear fission. At its onset it seems to be more probable for even neutron numbers (see e.g. the rutherfordium and seaborgium isotopic chains) and proton numbers (compare e.g. Lr, Rf, Db, Sg in figure 19). The reason for this is the so-called specialization energy occurring for single occupations of the Nilsson levels, as shown in figures 10 and 36. The SPL occupied by the odd particle in that mass region typically increases the fission barrier by ≈1 MeV compared to its even–even neighbors. In the fission path from the equilibrium shape to the saddle point the projection Ω remains constant. While in even–even nuclei the states with $\Omega = 0$ are often the lowest at each deformation, the situation is different in odd nuclei: the state having the same Ω projection as the g.s. is usually not the lowest lying at the saddle point (see e.g. [256], ch 2.4.4). This concept was introduced by Wheeler in 1955 [20]. For decay spectroscopy, the detection of fission can be used to select decay preceding fission, in particular from isomeric states, for a specific nucleus.

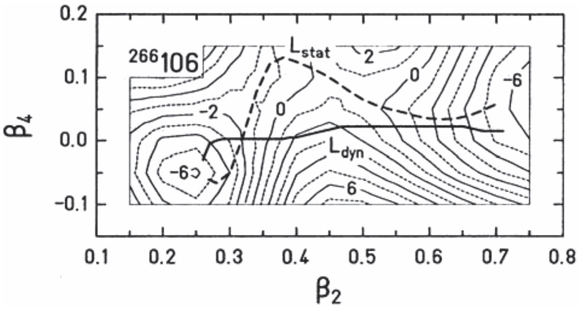

Figure 35. Potential energy surface of ^{266}Sg for which the dynamic and static spontaneous fission trajectory are calculated. For detail see text and [257], from which this figure is reprinted with permission, Copyright (1995) by the American Physical Society.

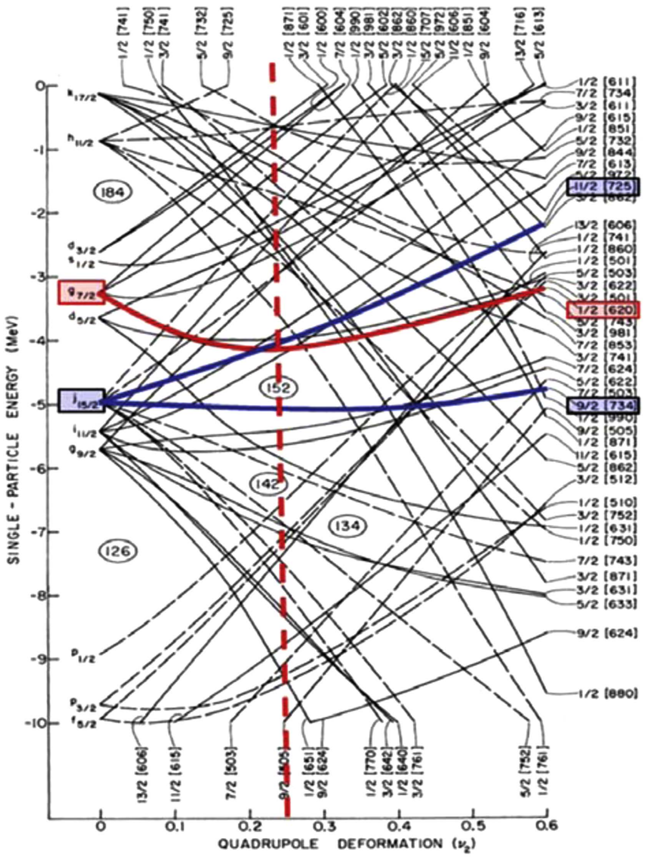

Figure 36. Neutron single particle energies as a function of quadrupole deformation from a momentum-dependent Woods–Saxon model by Chasman *et al*. Reprinted figure with permission from [158], Copyright (1977) by the American Physical Society.

More details on the spontaneous fission properties of the heaviest nuclei can be found in the recent review by Heßberger [258].

Electromagnetic and β-decay

Similar to coincidences with emitted α particles or fission fragments, electrons from β-decay or internal conversion can also be used in decay spectroscopy. The electrons stemming from these processes are investigated using the particle detectors described in section 2.3.2. The spectroscopy of electrons, thanks to the development of efficient electron detection set-ups, is nowadays effectively used also in in-beam spectroscopy. The spectroscopic techniques applied for their investigation is described in detail together with γ ray spectroscopy in section 3.4. The exploitation of the processes described in this chapter for DSAS will be treated in the following section 2.5.

Isomeric states

Phil Walker and George Dracoulis introduced the various types of metastable states in nuclei [259]; see also the contribution of Walker and Xu in this focus issue [260]. Apart from spin traps and from shape isomers presented there, K-isomers are a central feature to be studied in the region of deformed heavy and superheavy nuclei. This type of isomer is caused by large differences in the K quantum number in the initial and final state including possibly a parity change, which leads to a retardation of the decay of high-K states. For an early estimate of the relation of the decay hindrance factor, and the difference in K for initial and final state, see [261]. In a recent comprehensive review Dracoulis, Walker and Kondev report on the present state of research dealing with nuclear metastable states [262]. For a detailed description of this feature see section 2.5.2, where we discuss the investigation of such states.

2.5. Features to be investigated

The experimental capabilities developed throughout the last decades concerning separators and detection technology, the latter including more and more complex and comprehensive systems for particle and photon spectroscopy (see section 2.3), made the collection of an impressive body of data possible, investigating the processes presented in section 2.4 in terms of DSAS. In particular, the properties of SPLs can now be extended along isotopic and isotonic chains from the fermium–nobelium region well towards the center of the shell-stabilized deformed nuclei around the subshell closure at $Z = 108$ and between the closed neutron subshells at $N = 152$ and 162. In 2008 Herzberg and Greenlees reviewed the state of the art of the nuclear structure knowledge in that region obtained by in-beam and decay spectroscopy of transfermium nuclei [263]. The progress regarding DSAS has been revisited by Asai *et al* in their contribution to the special issue of *Nucl. Phys.* A 944 [174]. They report mainly on the trends for even-Z/odd-A, along the $N = 151$, 153 and 155 isotonic chains. We will summarize their report by discussing some examples, illustrating the objective of these nuclear structure studies with an emphasis on their relations to their heaviest species in section 2.5.1. In this context the present experimental knowledge regarding the first excited states will be discussed as well as some examples for even–even species in that area of the chart of nuclei. Some of the findings for those provide links to the heavier nuclei, in particular regarding K-isomeric states observed up to ^{266}Hs and ^{270}Ds, the heaviest nuclei for which K-isomers have been discovered up to now. This topic will be elaborated on in section 2.5.2.

2.5.1. Trends of single particle energies. Asai *et al* compare in their review experimental SPLs which have been established by investigating decay properties in terms α, α–γ and α-electron spectroscopy with the predictions of various models [174]. For a detailed description we advise the interested reader to consult this comprehensive paper. Here, we focus on some striking features which are related in particular to the connection of these findings to possible shell closures expected for higher atomic charges Z and masses A in the region of the island of stability of SHN. This is intimately connected to the deformation of those nuclei as can been seen from the Nilsson representation of single particle energies as a function of the quadrupole deformation parameter shown in figure 10 for protons and figure 36 for neutrons. The SPLs which are at the Fermi surface of the nuclei discussed here with their quadrupole deformations around 0.25 evolve and reorder towards sphericity, decisive for the definition of the predicted shell gaps at $Z = 114$ and $N = 184$. Following the development of those SPL towards higher Z and A is a promising concept to refine the predictions for the superheavy nuclei and the location and properties of long sought for island of stability.

Asai *et al* consider the major theoretical approaches including microscopic–macroscopic models, as well as self-consistent calculations in terms of Hartree–Fock–Bogoliubov (HFB) and relativistic mean-field calculations with various parametrizations. In figure 36 three SPLs are indicated, which play a major role for the definition of the gap at neutron number 152 at the here relevant quadrupole deformation of 0.25. In figure 37 experimental data for SPLs below 700 keV for the even $N = 151$ isotones from plutonium ($Z = 94$) to hassium ($Z = 108$) are compared with results from various model calculations. All models predict the $\nu 9/2^-[734]$ SPL as the g.s. of all six isotones. The experimental trend of the $\nu 1/2^+[620]$ is qualitatively well reproduced by the microscopic–macroscopic approaches of Ćwiok *et al* [160] (figure 37(d)), Parkhemenko and Sobiczewski [266] (figure 37(e)), and Asai *et al* [267] (figure 37(f)). A second single particle state, originating from the $j_{15/2}$ spherical state, the $\nu 11/2^-[725]$, is evident at ≈600 keV in experiment and in some of the model predictions. In the Nilsson diagram (figure 36) it crosses the $\nu 1/2^+[620]$ SPL exactly at a deformation value of 0.25. This state appears in two of the three microscopic–macroscopic calculations (figures 37(d) and (f)). The self-consistent approaches by Zhang *et al* [264] (cranked shell model (CSM); figure 37(b)) and Bender *et al* [265] (HFB+SLy4 Skyrme interaction; figure 37(c)) do not

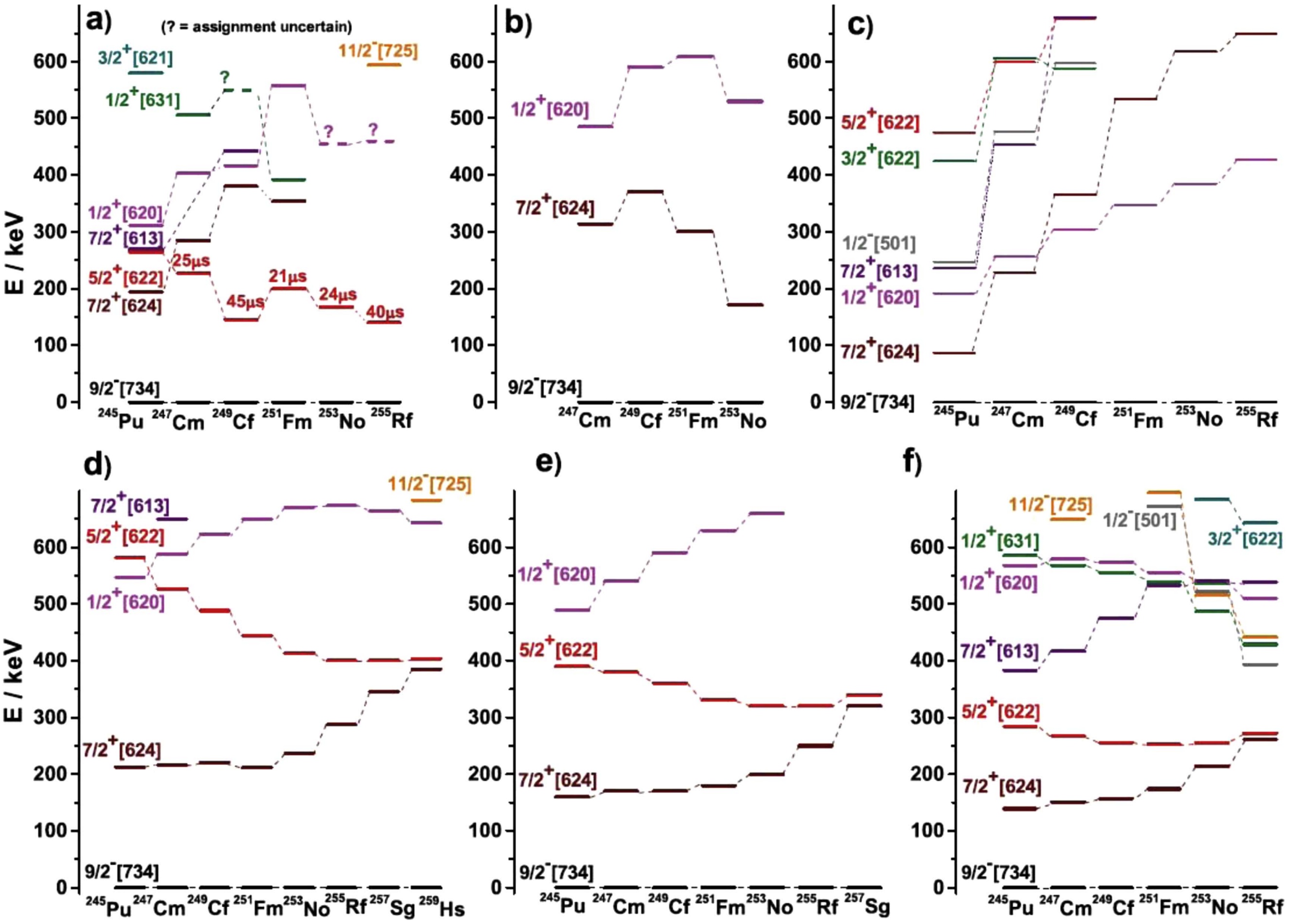

Figure 37. Reprinted from Asai *et al* [174] (Copyright 2015, with permission from Elsevier): comparison of experimental single particle levels (a) below 700 keV for the even $N = 151$ isotones from plutonium ($Z = 94$) to rutherfordium ($Z = 104$) to results from various model calculation; (b) Zhang *et al* [264], (c) Bender *et al* [265], (d) Ćwiok *et al* [160], (e) Pharkhomenko and Sobiczewski [266] and (f) Asai *et al* [267]. Reproduced with permission. Copyright Elsevier 2015.

show it, although for the latter model approach most of the experimentally assigned levels are present with the correct trend as a function of Z in some cases, like e.g. the here discussed $\nu 1/2^{+}[620]$ SPL. While the $\nu 9/2^{-}[734]$, stemming from the $j_{15/2}$ spherical multiplet, defines the lower limit of the $N = 152$ shell gap, the $\nu 1/2^{+}[620]$ is located at its upper limit, coming down from the $g_{7/2}$ spherical multiplet which is lying above the $j_{15/2}$ at sphericity (see figure 36). As can be clearly seen here, it will be very important to localize the $\nu 1/2^{+}[620]$ SPL in the heavier $N = 151$ isotones (^{253}No and ^{255}Rf) and the $\nu 11/2^{-}[725]$ in the next lighter ones up to ^{255}Rf in order to qualify the theoretical predictions. However further development seems obviously needed for the self-consistent models here.

Across the $N = 152$ shell gap looking now at the isotonic chain $N = 153$ from ^{249}Cm to ^{259}Sg for experiment and up to ^{261}Hs for some of the models, figure 38 shows again a experiment-theory comparison by Asai *et al* [174]. Here, the g.s. is now assigned as $\nu 1/2^{+}[620]$ and the $\nu 11/2^{-}[725]$ SPL has come down to excitation energies of ≈ 400 keV for the lightest isotones and eventually forms the g.s. for ^{259}Sg in the level schemes deduced from experimental data. The macroscopic–microscopic models again reproduce the trend qualitatively, however predicting the $\nu 11/2^{-}[725]$ SPL to become the g.s. for higher atomic numbers beyond ^{261}Hs. The self-consistent models (figures 37(b) and (c)) again do not show this particular structure feature. Hence it becomes again obvious how theory and experiment interact in improving the understanding of the complex structure of these heavy nuclear species.

In this spirit, an attempt towards the detection of the $\nu 11/2^{-}[725]$ SPL in ^{253}No investigating the decay of ^{257}Rf had been undertaken by Heßberger *et al* [268]. In a short irradiation of ^{208}Pb with ^{50}Ti projectiles ^{257}Rf had been produced in the one neutron evaporation channel of a fusion reaction. By means of α, CE and γ-ray spectroscopy a new state, the $\nu 7/2^{-}[743]$ SPL, and its decay into the $\nu 5/2^{+}[622]$ excited level in ^{253}No was tentatively assigned. For this an α-decay originating from the $\nu 11/2^{-}[725]$ state which is isomeric in ^{257}Rf was observed: see figure 39. The population of this level in ^{253}No could however not be observed in this short experiment. Settling this important issue requires a longer irradiation run.

Going one step further in neutron number, up to 155, Asai *et al* discuss the development of the level ordering as obtained by theory again for the isotonic chain from

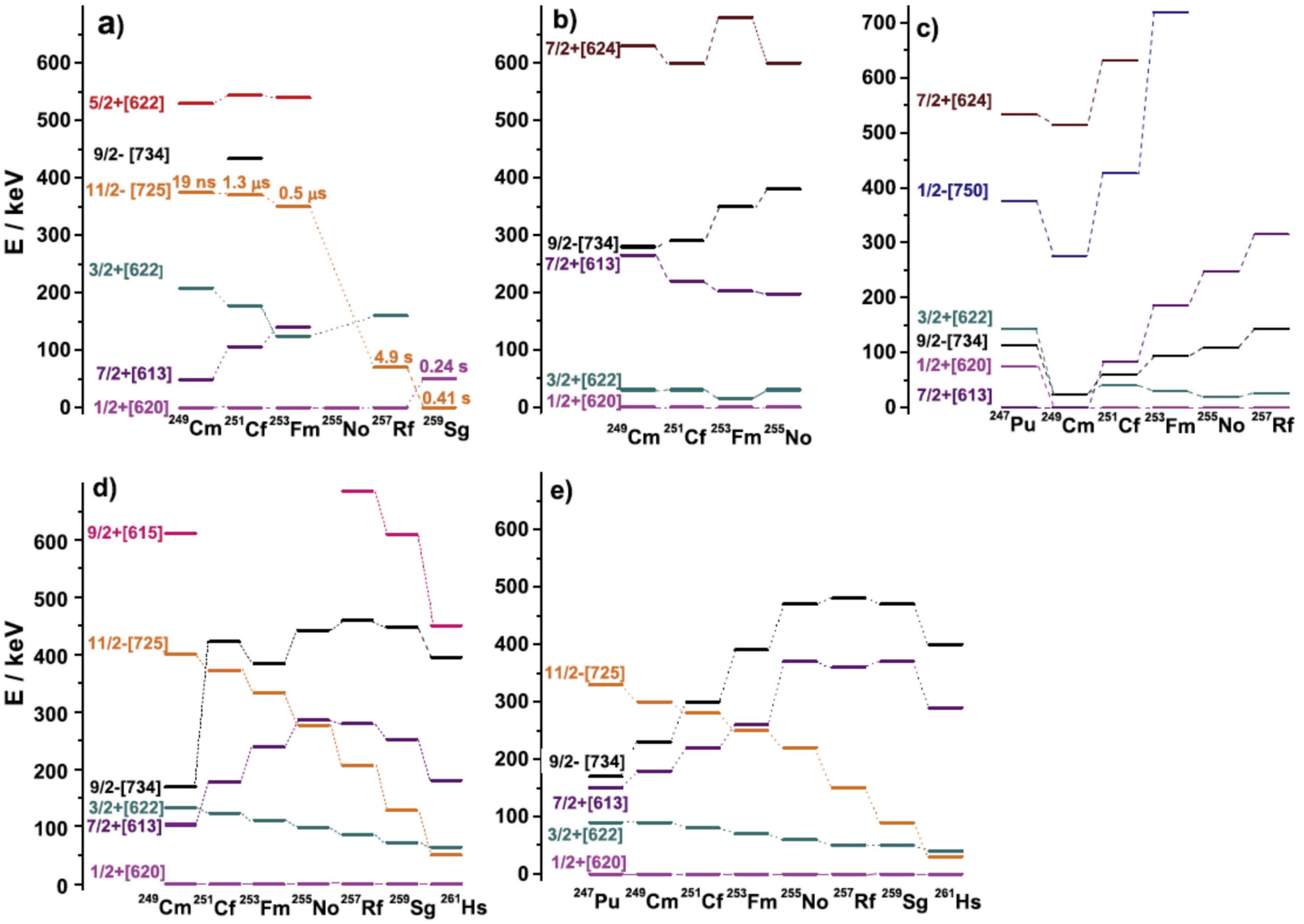

Figure 38. Reprinted from Asai *et al* [174] (Copyright 2015, with permission from Elsevier): comparison of experimental single particle levels (a) below 700 keV for the even $N = 153$ isotones from plutonium ($Z = 94$) to seaborgium ($Z = 106$) to results from various model calculation; (b) Zhang *et al* [264], (c) Bender *et al* [265], (d) Ćwiok *et al* [160] and (e) Pharkhomenko and Sobiczewski [266]. Reproduced with permission. Copyright Elsevier 2015.

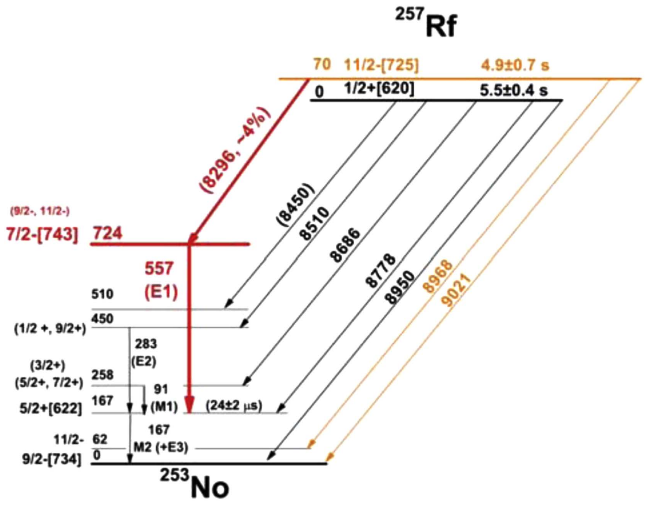

Figure 39. Decay scheme of ^{257}Rf established in a recent measurement at SHIP. Figure taken from Heßberger *et al* [268]. (2016). © SIF, Springer-Verlag Berlin Heidelberg, 2016. With permission of Springer. Original Caption: 'Enhanced decay scheme of ^{257}Rf based on the data reported in [4, 8] and measured in the present study. For better presentation transitions from ^{257}Rf are drawn in black, previously reported transitions from ^{257m}Rf in orange, and the ones from this study in red.'

plutonium to hassium as illustrated in figure 40. Again, the three SPL discussed above are involved in the low lying structures of those nuclei while now the g.s. for the lighter isotones is formed by the $\nu 7/2^{+}[613]$ SPL which is competing, going towards higher isotones with the $\nu 11/2^{-}[725]$ and $\nu 1/2^{+}[620]$ states exhibiting a crossing at $Z = 100$, fermium. We do not want to go into detail here and rather refer the interested reader to the review paper by Asai *et al* [174].

To establish systematic decay networks in order to trace the development of the relevant structure features and compare the findings to theory is essential and is the only promising approach to extend our knowledge of the nature of high Z and high A nuclear matter towards the limits of existence. As an example we want to briefly introduce up to date knowledge concerning the odd–even isotopes in the region from einsteinium ($Z = 99$) to dubnium ($Z = 105$). In figure 41 the complete knowledge in this region is shown as decay properties and in particular the first excited states of the involved nuclei. The investigated species comprise 15 nuclei and span a region from ^{243}Es ($Z = 99$ and $N = 144$) to ^{263}Db ($Z = 105$ and $N = 158$). From the collected data systematic trends can be exploited to shed light onto some striking features.

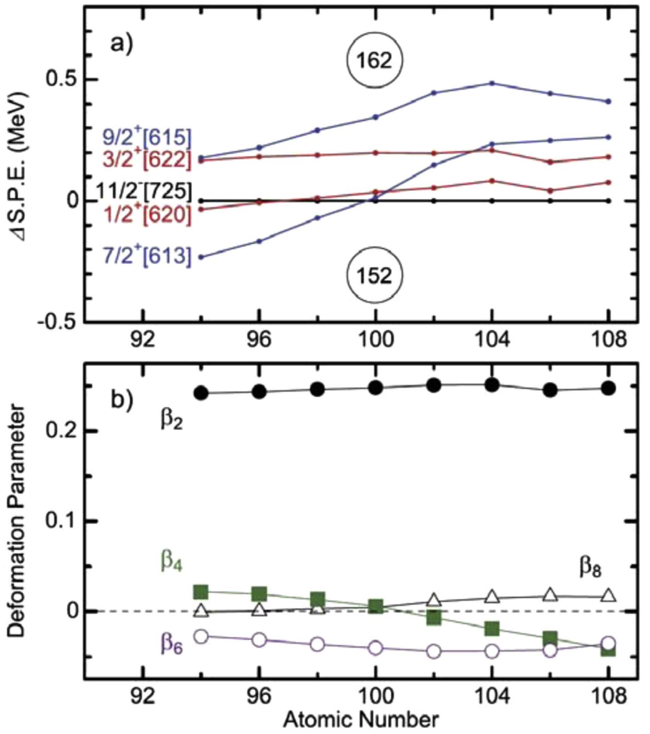

Figure 40. Reprinted from Asai *et al* [174] (Copyright 2015, with permission from Elsevier): calculated [174, 269] single particle levels relative to the $\nu 11/2^-$ (a), and β_2 and β_4 deformation parameters (b) for the $N = 155$ isotones from plutonium ($Z = 94$) to hassium ($Z = 108$). Reproduced with permission. Copyright Elsevier 2015.

Following Heßberger *et al*, we compare as one example in figure 42 the experimental energy differences of two low lying states $\pi 7/2^-[514]$ and $\pi 7/2^+[633]$ in the einsteinium isotopes with deformation values obtained for the same nuclei by the microscopic–macroscopic model of Parkhomenko and Sobiczewski [282]. The striking feature we observe here is that the energy differences peak at the same nucleus, ^{251}Es for which the quadrupole deformation predicted by theory is largest. We remind here that tracing deformation is one of the key issues to proceed from the deformed nuclei investigated here towards the island of superheavy nuclei which are predicted to be spherical by most models.

Figure 41 includes a variety of features for which details can be found in the literature which is cited in the figure caption. Here we want to highlight only a few of them like the situation around the gap opening in the SPL structure at around a quadrupole deformation of 0.25–0.3 (see figure 10) at $Z = 100$. The g.s. assignment for the einsteinium isotopes ($Z = 99$) is hampered by the fact that the two states which define the lower limit of this gap, the $\pi 3/2^-[521]$ and $\pi 7/2^+[633]$, are very close in energy. For the mendelevium isotopes ($Z = 101$) the g.s. $\pi 7/2^-[514]$ which is approached by the $\pi 1/2^-[521]$ state sloping down from some 200 keV at ^{247}Md, where it forms an isomer with a 25.5% fission branch, to 50–60 keV in ^{251}Md and ^{253}Md. Similar conclusions on deformation as drawn above for the einsteinium isotopes seem possible here, as well as on a possible level crossing for heavier mendelevium isotopes, as suggested by the Nilsson diagram for protons (see figure 10).

The occurrence of isomeric states in ^{247}Md, ^{253}Lr and ^{255}Lr promises further insight in the nuclear structure peculiarities in this region. These metastable states are particularly interesting as they often provide a tool for the revelation of nuclear structure properties which are responsible for their retarded decay. One type of isomer decay is particularly intriguing as it is directly connected to the deformation of the nucleus: K isomers. The following section will introduce this field of research and discuss the heaviest nuclei for which K isomers have been observed.

2.5.2. K-isomers—a tool to scan the region of deformed SHN.

Among the most interesting features to be studied for SHN is the observation of K-isomeric states (see e.g. [259, 261]). The definition of the K quantum number is illustrated in figure 8. It is the total sum of the projection Ω_i of the orbital angular momentum Λ_i and the spin Σ_i of one or more (n) nucleons onto the symmetry axis of a deformed nucleus:

$$\Omega = \Lambda + \Sigma,$$
$$K = \sum_{i=1}^{n} \Omega_i. \qquad (17)$$

A particle–hole pair is created by a two-quasiparticle (2qp) excitation of a proton or a neutron into an excited SPL. Thereby high values of the K quantum number can be generated, which can require a large difference in spin and possibly a parity change to de-excite into the next accessible level. This results in a retardation of the decay with hindrance factors HF (14) of up a few thousand as compared to unhindered decays. The excitation energy of 2qp states reads

$$E_{2\mathrm{qp}} = \sqrt{(E_{\mathrm{sp1}} - \lambda)^2 + \Delta^2} + \sqrt{(E_{\mathrm{sp2}} - \lambda)^2 + \Delta^2} \qquad (18)$$

which depends on the pairing gap Δ (having an empirical value of $12/A^{1/2}$, see [69] figure 2.5), and on the single-particle energy E_{sp} with respect to the Fermi energy λ. The excitation energy of a 2qp state is approximately twice the pairing energy, plus extra energy needed to promote particles across the gap. In the $A \approx 250$ mass region, the lowest high-K 2qp states are at ≈1 MeV excitation energy. Since there are several high-K states around the Fermi level, 2qp configurations frequently carry a high-K value as mentioned above. The de-excitation of high-K states is strongly hindered by selection rules. The lifetime is empirically related to the degree of forbiddeness $\nu = |\Delta K - \lambda|$, with λ being the multipolarity of the transition. From the Löbner systematics [261], the hindrance factor $f_\nu = [t_{1/2}^{\mathrm{Exp}} / t_{1/2}^{\mathrm{Weisskopf}}]^{1/\nu}$ increases by a factor of ≈100 for each degree of forbiddeness. In addition, high-K states are generally rather pure, i.e. little mixing with other configurations, which is demonstrated by their long lifetimes related to large hindrance factors. Comparison with models or other configurations is therefore of high relevance with little bias. In such studies, the

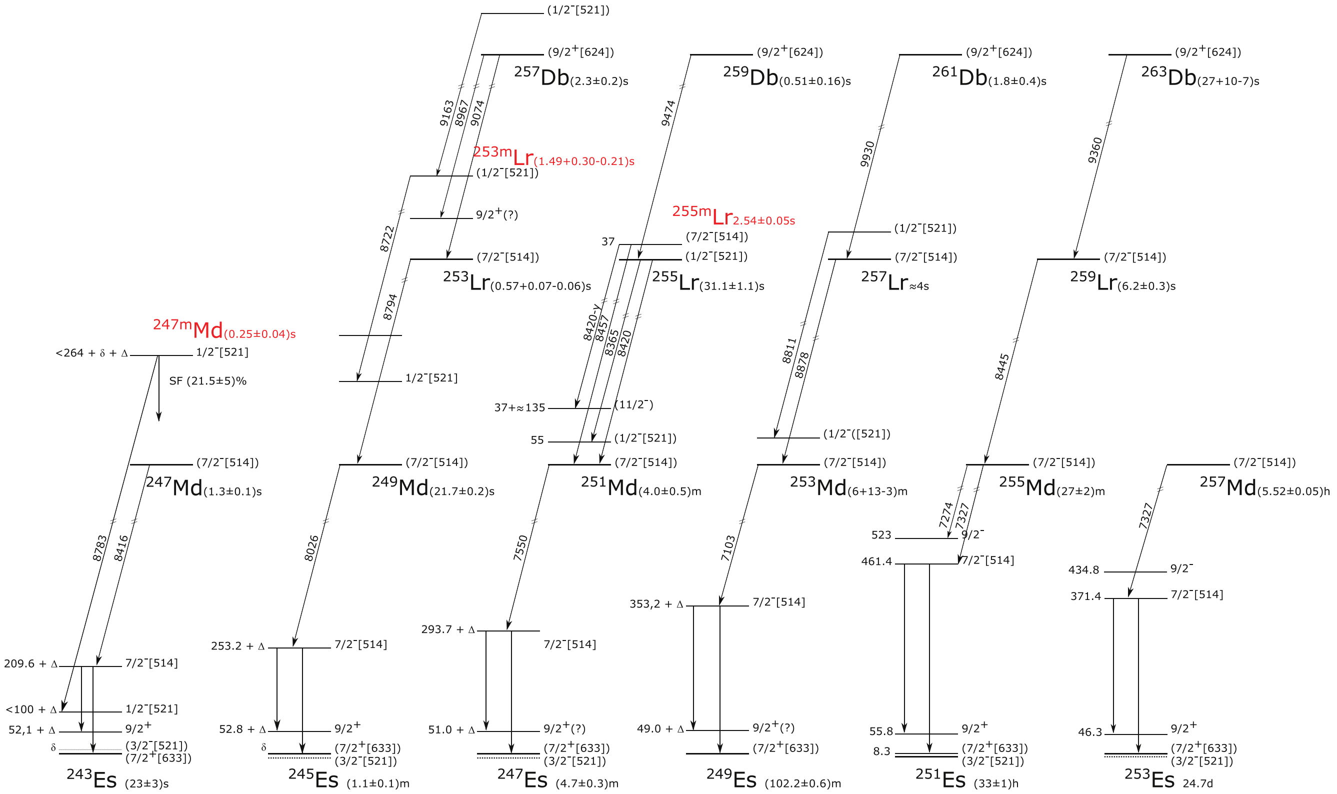

Figure 41. Decay scheme for odd-Z isotopes from einsteinium to dubnium in the vicinity of the $N = 152$ closed shell. Data are taken from [268, 270–281]. For the g.s. assignment for ^{243}Es, the presentation of Antalic *et al* has been chosen who propose two possible scenarios [280]. For the shown case with the $\pi 7/2^{+}[633]$ Nilsson level being the g.s., δ would be the excitation energy of the $\pi 3/2^{-}[521]$ level and $\Delta = 0$. For the opposite assignment Δ would be the excitation energy of the $\pi 7/2^{+}[633]$ state. For the other einsteinium g.s. assignments the representation of [276] has been adopted here.

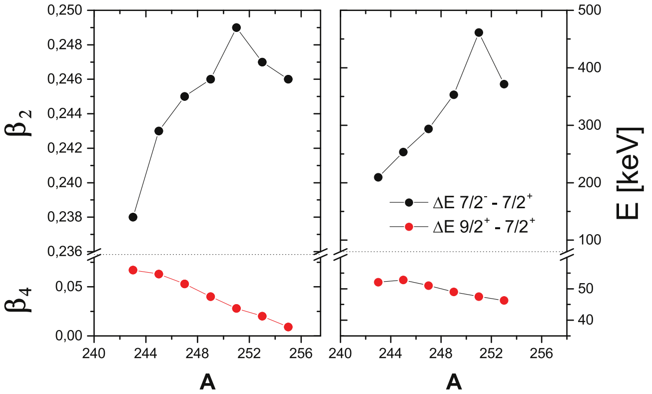

Figure 42. Comparison of the energy differences of the lowest levels in the isotopes ^{243}Es to ^{253}Es (see figure 41) in the right panel with quadrupole β_2 and octupole deformation β_4, obtained by a macroscopic–microscopic model calculation [282], in the left panel. See also Heßberger *et al* [281].

decay of high-K isomers toward the g.s. proceeds at the focal plane of a spectrometer/separator via a high ΔK, high-multipole, highly converted transition, followed by several transitions with a high internal conversion probability. These transitions are emitted by nuclei that have been implanted into the implantation detector, possibly occurring subsequent to an α-decay. Since the range of low-energy electrons in silicon is small (≈100 μm for 100 keV electrons), this leads to a substantial energy of up to several hundreds of keV deposited in the same pixel into which the ion was implanted. This is the idea of the 'calorimetric technique' suggested by Jones [192] and first implemented for the study of high-K states in ^{254}No [283, 284]. In some cases these metastable states can have longer lifetimes than the g.s., a feature which is observed also for the heaviest nuclei observed to exhibit K-isomerism. For nuclei in the region around $Z = 108$ and between $N = 152$ and 162 the formation of those metastable states are expected to occur as a general feature. Xu *et al* predict high K states for the whole region from $Z = 100$ to 108 and $N = 150$–168 at excitation energies of 1–2.5 MeV [285].

The major ingredient for the formation of high K states is nuclear deformation which can be investigated in in-beam studies, which we discuss in section 3, by investigating so called rotational bands. For ^{252}No and ^{254}No the g.s. band structure had been investigated in pioneering experiments at ANL and JYFL [88, 299–304], see details in section 3. For ^{254}No two isomeric states were observed in decay spectroscopic studies [283, 284, 305, 306] at excitation energies of 1293–1297 keV and ≈2.5 MeV with half-lives of 265 ms and 184 μs, respectively. The configuration of the second, higher lying isomers is still under debate and experiments with higher statistics are mandatory to settle this question, the options being four-quasiparticle configurations either with $K^{\pi} = 16^{+}$ [283, 306] or 14^{+} [284]. Additional information could be gathered at SHIP where Heßberger *et al* could

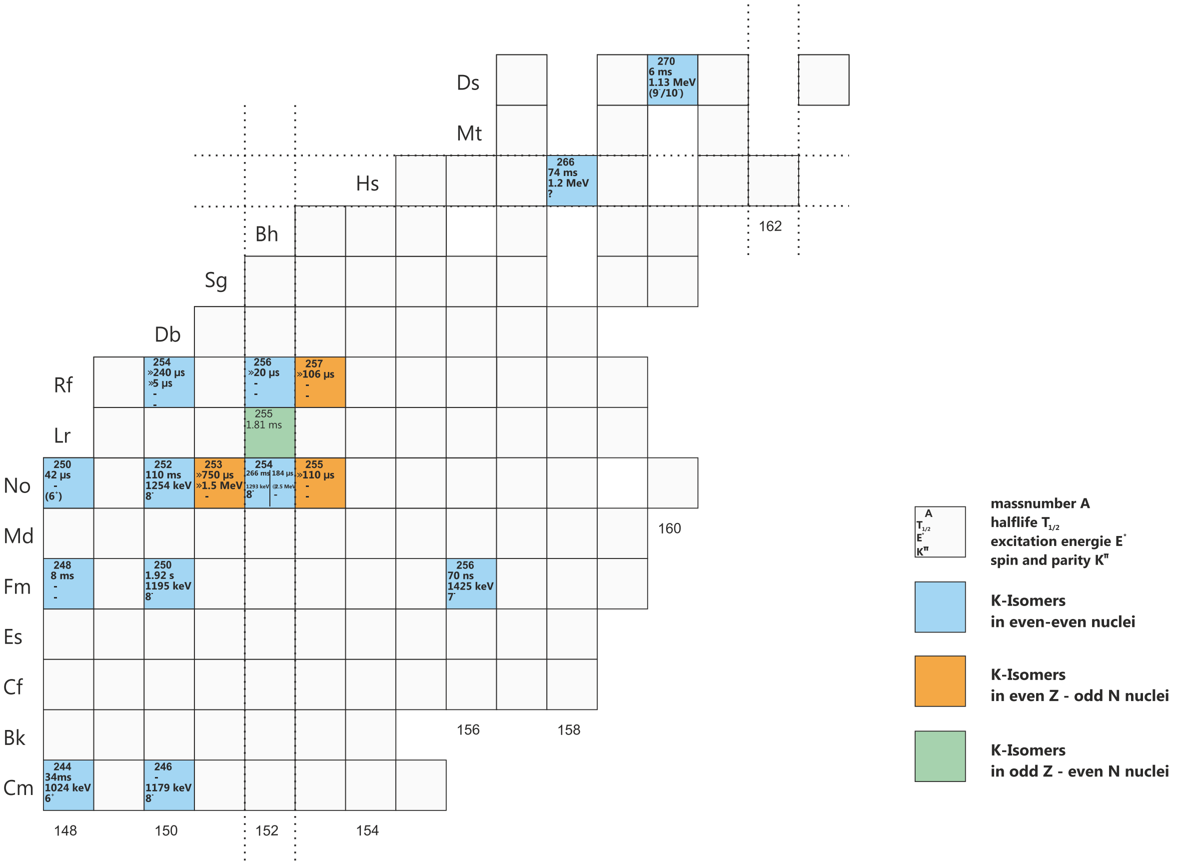

Figure 43. Excerpt of the chart of nuclides indicating the K-isomers observed for heavy nuclei in the region $Z \geqslant 96$. Half-life, decay energy, spin and parity values are given for K-isomers only.

observe the band structure between the two isomers as well as its link to the g.s. rotational band [305]. For the lighter nobelium isotope ^{252}No Sulignano *et al* observed a K-isomer with a half-life of 110 ± 10 ms and an excitation energy of 1254 keV [294]. A total of 16 nuclei for which K isomers have been observed, are shown in figure 43, the heaviest nucleus where such a state was found being ^{270}Ds [298]. Revisiting this nucleus the earlier findings could be confirmed with higher statistical significance [230]. In addition a K isomer and a new fission branch with unexpectedly high sf-α branching ratio could be established for the daughter ^{266}Hs [296]. The decay chain observed in this new experiment could be extended and the α-branch in the granddaughter ^{262}Sg could be observed. In a very recent experiment investigating the decay of ^{258}Db, the last missing member of the chain was detected with the α-decay of ^{258}Rf populated by β-decay of ^{258}Db [307]. This α-decay connects the chain to ^{254}No for which precise mass measurements were performed at SHIPTRAP [228]. From this experimental masses were established for all members of the chain deducing the mass differences between the chain members from the measured α-decay energies and the related Q_α values. The heaviest mass for an even–even nucleus with 110 protons is a very valuable information to use for the adjustment of theoretical models, in particular, in view of predictions for the heavier species approaching the island of stability of SHN.

In table 3 we show the list of K isomers in even–even isotopes in the region from curium to darmstadtium as given in [175] as an update of the one from [263]. Apart from K isomers in nuclei with even nucleon numbers where level densities are lower and the gaps are present which are necessary to cause high decay energy and spin differences, they were found also in even–odd and odd–even isotopes in this region such as e.g. ^{251}No [308], ^{253}No [309, 310], ^{255}No [311], and ^{255}Lr [277, 278].

As mentioned initially in this section, Xu *et al* had investigated high K states from a theoretical point of view, employing configuration constrained PES calculations. They pointed out that high-spin K-isomerism has consequences for the fission barrier and α-decay, which could lead to a higher stability and longer lifetimes of the isomer as compared to the g.s. for a certain class of superheavy nuclei [285], a fact which had been found for the heaviest isotopes mentioned above ^{266}Hs [296] and ^{270}Ds [230]. Other examples for such an isomer-g.s. lifetime inversion are the neutron deficient ^{250}No [293] and ^{254}Rf [312].

In a comprehensive investigation employing again configuration constrained PES calculations [290], Liu, Walker and Xu study K-isomers in nuclei up to copernicium isotopes. They find good agreement with measured excitation energies and half-lives for the K isomers observed in ^{252,254}No and ^{270}Ds which gives a certain confidence in their predictions of four-quasiparticle states, formed by two-

Table 3. Update of the table of known *K*-isomers in even–even nuclei in the heavy and SHEs from [263]. Reprinted from [175], Copyright 2015, with permission from Elsevier.

Nucleus	K^π	$T_{1/2}$	E_x	Decay mode	Configuration	References
^{244}Cm	6^+	34 ms	1.040 MeV	γ	$5/2^+[622]_\nu \otimes 7/2^+[624]_\nu$	[286, 287]
^{246}Cm	8^-	—	1.179 MeV	γ	$7/2^+[624]_\nu \otimes 9/2^-[734]_\nu$	[288]
^{248}Fm	(6^*)	$\simeq$8 ms	—	γ		[289, 290]
^{250}Fm	8^-	1.92 s	1.195 MeV	γ	$7/2^+[624]_\nu \otimes 9/2^-[734]_\nu$	[291]
^{256}Fm	7^-	70 ns	1.425 MeV	γ, SF	$7/2^+[633]_\pi \otimes 7/2^-[514]_\pi$	[292]
^{250}No	(6^+)	42 μs	—	SF, γ?	$(5/2^+[622]_\nu \otimes 7/2^+[624]_\nu)$	[293]
^{252}No	8^-	110 ms	1.254 MeV	γ	$7/2^+[624]_\nu \otimes 9/2^-[734]_\nu$	[294]
^{254}No	8^-	266 ms	1.293 MeV	γ	$7/2^-[514]_\pi \otimes 9/2^+[624]_\pi$	[283, 284]
^{254}No	—	184 μs	$\simeq$2.5 MeV	γ		[283, 284]
^{254}Rf	6,7	4.7 μs	$\simeq$? MeV	e^-	Two-quasiparticle	[312]
^{254}Rf	6,7	247 μs	$\simeq$? MeV	e^-	Four-quasiparticle	[312]
^{256}Rf	6,7	25 μs	$\simeq$1.12 MeV	e^-	—	[295]
^{256}Rf	10^+	17 μs	$\simeq$1.4 MeV	e^-	$(9/2^-[734]_\nu \otimes 11/2^-[725]_\nu)$	[295]
^{256}Rf	—	27 μs	2.2 MeV	e^-	—	[295]
^{266}Hs	—	74 ms	$\simeq$1.2 MeV	α	—	[296, 297]
^{270}Ds	9^-, 10^-	6 ms	$\simeq$1.13 MeV	α	$11/2^-[725]_\nu \otimes 7/2^+[613]_\nu$ $11/2^-[725]_\nu \otimes 9/2^+[615]_\nu$	[230, 297, 298]

quasiproton combined with two-quasineutron states, with spin and parity from $13^+/14^-$ for nobelium and rutherfordium isotopes to 20^+ for the darmstadtium and copernicium isotopes.

As an outlook to what might be possible in future with more advanced instrumentation as presented in section 5, we look into model predictions in the region of the heavier deformed closed neutron shell at $N = 162$. With higher beam intensities and better separators, theoretical predictions could be tested for nuclei in that region which suffer from low production probability. Such a prediction on the basis of relativistic energy density functionals for two-quasiparticle excitations in the axially deformed Rf, Sg, Hs, and Ds isotopes with neutron number $N = 160$–166 had been recently undertaken by Prassa *et al* [313]. They find that the $N = 162$ deformed-shell closure has a striking effect on the excitation of two-quasiparticle states. The proton two-quasiparticle states are elevated to higher excitation energies for the $N = 162$ nuclides of the four isotopic chains they study, resulting in a characteristic difference of the excitation scheme of those isotopes with respect to their neighbors. This effect is shown in figure 44 taken from [313] from which one can also see that many high *K*-states are formed in those nuclei which makes the occurrence of *K* isomeric states very probable. Those two nuclei would be accessible via the reactions ^{248}Cm(^{26}Mg, 4n)^{270}Hs and ^{208}Pb(^{70}Zn, 4n)^{272}Ds + α, both having production cross sections of $\approx$0.5 pb which result in an observation of only about one event per week with nowadays technology. This demands clearly for advanced experimental technology like high intensity heavy ion accelerators and powerful separators. There are presently two facilities under construction with the SHE factory at FLNR/JINR, Dubna, Russia and LINAG of SPIRAL2 at GANIL, Caen, France, as detailed in section 5.1. The example given here is only one among a number of many others which will serve as stepping stones to eventually set foot on the island of stability discovering the nature of this exotic nuclear matter which already fascinates a few generations of scientists.

3. In beam spectroscopy

While decay spectroscopy mainly reveals single-particle properties of nuclei, prompt spectroscopy is an ideal tool to study collective states. This aspect is not related to the experimental technique itself, but to the production mechanism: α-decay populates low-spin, low excitation-energy states, while transfer reactions, Coulomb excitation or fusion-evaporation reactions may also populate medium to high-spin states. In the regions of shell-stabilized deformed nuclei around ($Z = 100$, $N = 152$), ($Z = 108$, $N = 162$), collectivity emerges through appearance of rotational structures, which can reveal many facets of nuclear structure.

As detailed in section 2.4, decay spectroscopy provides a certain insight into collectivity through energies of 2^+ excited states in even–even isotopes, but the information concerning deformed states is rather limited and often difficult to decipher, in particular for odd nuclei, where collective and single-particle excitations lie in the same energy range. More information can be obtained from studies of higher-spin states, which are accessible only in prompt spectroscopy. Obviously, the borders between decay and prompt spectroscopy, single-particle and collective properties are not sharp: e.g. the decay of high-*K* isomers (see section 2.5.2) can populate collective states at moderate spin which are therefore possible to be observed at the focal plane of a separator. Both techniques can also be combined in that case, as will be detailed below.

One of the recent highlights of prompt spectroscopy in the VHN/SHN region is the observation of deformed rotating systems with up to 104 protons, surviving rotation up to angular momenta of more than 20 $\hbar$. The study of such heavy unstable nuclei is possible thanks to continuous technical developments. However, the major highlight and outstanding breakthrough in the VHN/SHN region were prompt γ-ray studies of ^{254}No performed in 1998 at ANL [299] and the Department of Physics, University of Jyväskylä (JYFL) [300]. These experimental studies are striking in many respects, the most remarkable feature being the huge gap that separates ^{254}No from nuclei previously studied at moderate to high spin. In order to evaluate this experimental gap, we will first review the status before the ^{254}No breakthrough. We will then depict the ^{254}No story both from the experimental and theoretical point of view. We will then give an overview of further experimental studies and discuss various phenomena studied during the last two decades in the deformed region around the semi-magic shell gaps $Z = 100$, $N = 152$.

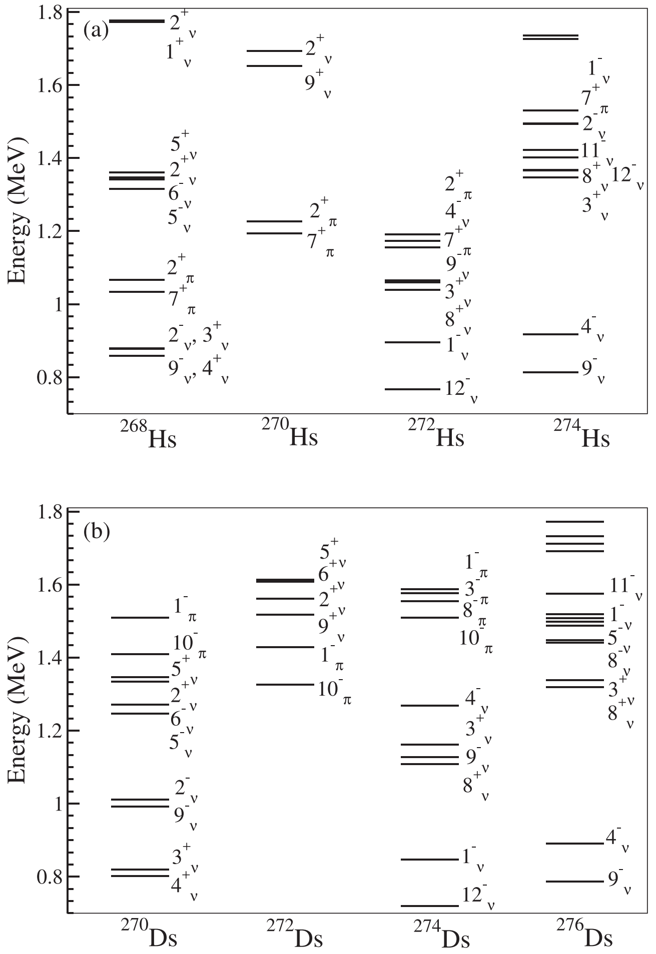

Figure 44. Lowest two-quasiparticle states obtained by REDF in Hs (upper panel) and Ds (lower panel) isotopes with neutron numbers $N = 160$–166. The 2qp states correspond to axially symmetric solutions obtained with the relativistic functional DD-PC1 and a pairing force separable in momentum space. The calculation includes time-reversal symmetry breaking. Reprinted figure with permission from [313], Copyright 2015 by the American Physical Society.

3.1. Global properties of rotational bands

We briefly remind the reader in this paragraph of the basic properties of rotational bands and the consequences they have for the instrumentation, analysis and interpretation in the region of the heaviest nuclei.

The energy of an axially symmetric nucleus, rotating around an axis (x) perpendicular to its symmetry axis (z), is given as

$$E(I) = \frac{\hbar^2}{2\mathcal{J}}\{I(I+1) - K^2 + \delta_{K,1/2}\, a\, (-1)^{I+1/2}(I+1/2)\} + E_K, \qquad (19)$$

where $\mathcal{J}$ is the moment of inertia, K the projection of the spin I on the symmetry axis (z) and E_K the excitation energy of the band head: see e.g. [69] pp 33–39.

In the specific case of g.s. rotational bands of even–even nuclei, only the first term remains. Because the nucleus is invariant with respect to rotation of one π around the x axis, only the spin sequence 0^+, 2^+, 4^+ is allowed. In case of odd nuclei (or, more generally, $K \neq 0$), the odd particle(s) break(s) the time-reversal symmetry, hence rotational structures are split into two signature partner bands. The signature α is related to the eigenvalue r of the rotation operator $R_x = \exp(-\mathrm{i}\pi J_x)$: $r = \exp(-\mathrm{i}\pi\alpha)$. In the formalism of the unified model of Bohr and Mottelson, α is a good quantum number when the rotation axis is perpendicular to the symmetry axis z. The total angular momentum is then $I = \alpha + 2n$, with n being any integer. As a consequence, spins $I = K, K + 1, K + 2,$ are allowed (see [69] paragraph 4.2 for details) and two signature partner bands appear, each consisting of $\Delta I = 2$ $E2$ stretched transitions. Both partner bands are connected by $\Delta I = 1$ transitions of a predominant $M1$ character. Eventually, the two signature partner bands can split with increasing rotation, the orbitals with large angular momentum j and low K being more sensitive to the rotation.

It should be noted that, in the general case, the signature α is not a good quantum number, since for example the rotation axis may not be exactly perpendicular to the symmetry axis, or the nucleus not perfectly axially symmetric. However, the relation $I = \alpha + 2n$ and the concept of signature partners are still used for convenience in the discussion of rotational bands.

In the special case of $K = 1/2$, the mixing of $\Delta K = 1$ states leads to the last additional term $\delta_{K,1/2}\, a\, (-1)^{I+1/2}(I + 1/2)$: the unfavored signature partner is shifted upward ($a > 0$) with respect to the favored one, the intensities in the former being in consequence larger.

The relative intensity of $E2$ and $M1$ transitions is a function of the electric quadrupole moment Q_{20} and of the magnetic dipole moment μ. Usually the gyromagnetic moment g_K is used instead of μ, being related to it by the following equation:

$$\mu = \left[g_R I + (g_K - g_R)\frac{K^2}{I+1}\right]\mu_N, \tag{20}$$

(see [69] equation (4.87)), with $g_R \approx Z/A$ being the rotational gyromagnetic factor, and $\mu_N = \frac{e\hbar^2}{2Mc}$ being the Bohr magneton.

For a single particle (the case of an odd nucleus) g_K itself can be written as a function of the nucleon spin g_s and the orbital gyromagnetic factor g_l: $g_K = \frac{1}{K}\langle K|g_s s_z + g_l l_z|K\rangle$: see e.g. [69], p 203. This expression can be approximated using the Nilsson labels:

$$g_K = \frac{1}{K}(g_s\Sigma + g_l\Lambda), \tag{21}$$

from which magnetic properties can be estimated in a simple way, without referring to detailed theoretical calculations. For neutrons and protons, one has $g_s^n = -3.83$, $g_s^p = 5.59$, $g_l^n = 0$, $g_l^p = 1$. Because of spin polarization effects, g_s is usually attenuated by a factor of 0.6. In the case of multi-particle excitations, the total gyromagnetic factor g_K is the sum of contributions of individual particles.

From these equations, it becomes apparent that the g_K factor differs from one Nilsson configuration to another, and from neutrons to protons. This property can be exploited to assign configurations of single-particle excitations in odd nuclei and, more generally, can be applied to multi-particle excitations.

Electromagnetic moments are related to reduced transitions probabilities using the following equations ([69] equations (4.68*b*) and (4.87)):

$$B(M1, I \rightarrow I-1) = \frac{3}{4\pi}\,(g_K - g_R)^2\,K^2\,\langle IK10|(I-1)K\rangle^2\,(\mu_N^2), \tag{22}$$

$$B(E2, I \rightarrow I-2) = \frac{5}{16\pi}\,e^2 Q_{20}^2\,\langle IK20|(I-2)K\rangle^2\,(e^2\mathrm{fm}^{-4}). \tag{23}$$

It should be noted that a more complex formalism is needed for $K = 1/2$: see e.g. [69, p 57]. Finally, the radiative transition rates are expressed as ([68], p 382):

$$T_\gamma(M1) = 1.76\ 10^{13}E^3B(M1)\ (\mathrm{s}^{-1}), \tag{24}$$

$$T_\gamma(E2) = 1.59\ 10^{9}E^5B(E2)\ (\mathrm{s}^{-1}). \tag{25}$$

Typically, it is the intensity ratio $R = T_\gamma(M1)/T_\gamma(E2)$ that is determined experimentally. It may be expressed by the above quantities, in particular g_K, which in turn can be compared to model predictions. It should be noted that, in principle, the $M1/E2$ mixing ratio of $\Delta I = 1$ transitions has to be taken into account: see e.g. [314].

Since the nuclei are not rigid, their moments of inertia may change with increasing rotation. To study the response of nuclei to rotation, one usually introduces the kinematic $\mathcal{J}^{(1)}$ and dynamic $\mathcal{J}^{(2)}$ moments of inertia and investigates their behavior as a function of the rotational frequency ω. These quantities are defined in numerous textbooks, and ω is expressed for $I^i \rightarrow I^f$ $\Delta I = 2$ transitions as:

$$\hbar\omega = \frac{E_\gamma(I^i \rightarrow I^f)}{I_x^i - I_x^f}, \tag{26}$$

with

$$I_x = \sqrt{I(I+1) - K^2} \tag{27}$$

being the projection of the angular momentum on the rotation axis.

For $I > K$ and $\Delta I = 2$ transitions, one has: $\hbar\omega \approx E_\gamma/2$.

The kinematic $\mathcal{J}^{(1)}$ and dynamic $\mathcal{J}^{(2)}$ moments of inertia correspond to the inverse of the first and second derivative of the excitation energy with respect to the spin squared:

$$\mathcal{J}^{(1)} = \frac{\hbar^2}{2}\left(\frac{\mathrm{d}E}{\mathrm{d}I^2}\right)^{-1} = I\hbar^2\left(\frac{\mathrm{d}E}{\mathrm{d}I}\right)^{-1}, \tag{28}$$

$$\mathcal{J}^{(2)} = \hbar^2\left(\frac{\mathrm{d}^2E}{\mathrm{d}I^2}\right)^{-1} = \hbar\frac{\mathrm{d}I}{\mathrm{d}\omega}. \tag{29}$$

$\mathcal{J}^{(2)}$ also corresponds to the change of spin with the rotational frequency, thus highlighting the alignment process.

The kinematic moment of inertia can be expressed as a function of transition energies:

$$\mathcal{J}^{(1)}(I) = \hbar^2\frac{2I-1}{E(I+1) - E(I-1)}. \tag{30}$$

Since this quantity depends on the spin of the states involved, and therefore implies that K is known, it is usually more convenient to use the dynamic moment of inertia:

$$\mathcal{J}^{(2)} = \hbar^2\frac{4}{E_\gamma(I+2 \rightarrow I) - E_\gamma(I \rightarrow I-2)} \tag{31}$$

$$= \hbar^2\frac{4}{\Delta E_\gamma}. \tag{32}$$

3.2. The pre-^{254}No era

The prompt spectroscopy of transfermium elements took off in 1998 with two experiments performed in an interval of about one month at ANL and at the University Jyväskylä. For the purpose of tracing the progress of prompt γ-ray spectroscopy, we believe it is valuable to briefly review these studies, which dealt with the heaviest elements investigated at that time.

3.2.1. Coulomb excitation. Coulomb excitation is one of the oldest techniques for nuclear spectroscopy of collective states. In the 1950s, Bohr and Mottelson were among the pioneers of this technique, as co-authors of the 1956 seminal paper by Alder *et al* [315]. It is not our purpose to provide here a detailed description of this method, as it can be found in numerous review articles. In brief, in this technique the electromagnetic field interacting between target and projectile

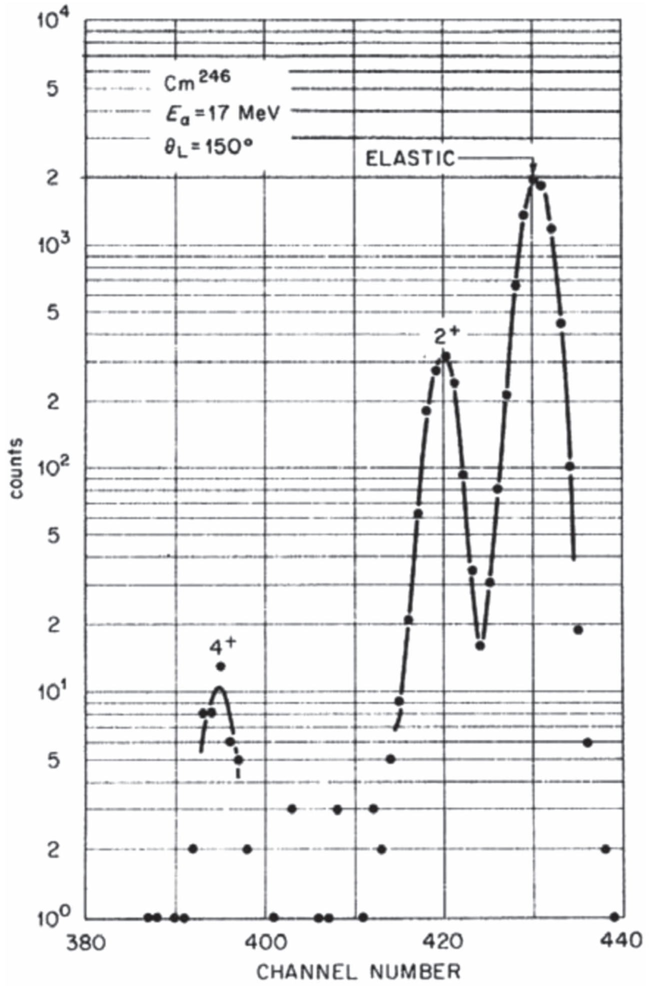

Figure 45. Alpha spectrum measured with an Enge split-pole spectrograph following excitation of a ^{246}Cm target by an α beam. Reprinted figure with permission from [316], Copyright (1971) by the American Physical Society.

nuclei populates excited nuclear states in the collision partners. Energies below the Coulomb barrier are usually chosen, to avoid the competition with excitation via nuclear mechanisms. Coulomb excitation can be employed either for the purpose of precision measurements of electric moments, or as a tool to efficiently populate high-spin states in order to study their spectroscopic properties.

Transitional electric quadrupole moments Q_{20} have been measured in actinide nuclei since the 1960s. A series of 13 actinides ranging from ^{230}Th to ^{252}Cf were studied using Coulomb excitations by Ford *et al* [316]; see also the detailed analysis of the same data by Bemis *et al* [317]. The experiments were performed at the Oak Ridge National Laboratory using a 16–17 MeV α beam. A direct measurement of the de-excitation of Coulomb excited nuclei was not possible because of the large internal conversion of the $2^+ \rightarrow 0^+$ transition at ≈45 keV, and because of the high target activity. In consequence, the inelastically scattered α particles were measured at the focal plane of an Enge split-pole spectrograph using position sensitive detectors: see figure 45 as an example.

The reduced transition probabilities $B(E2, 0^+ \rightarrow 2^+)$ could be deduced from the α spectra, and they could be further related to the electric quadrupole moments Q_{20} using the equation:

$$B(E2, 0^+ \rightarrow 2^+) = 5 \cdot B(E2, 2^+ \rightarrow 0^+) = \frac{5}{16\pi} Q_{20}^2. \quad (33)$$

As an example, the deduced $B(E2, 0^+ \rightarrow 2^+) = 14.99 \pm 0.19\ e^2\mathrm{b}^2$ for ^{248}Cm [317] is still adopted in recent evaluations: see [318–320]. It should be noted here that measured Coulomb excitation cross sections depend not only on transition probabilities, but also on spectroscopic quadrupole moments of populated states. In the analysis of Bemis *et al* [317] these were assumed to be related to $B(E2, 2^+ \rightarrow 0^+)$ using the rotational model formula for a prolate-deformed axial shape.

The nuclear quadrupole deformation β can be inferred from the Q_{20} electric quadrupole moment using model-dependent formulae, i.e. for axially symmetric nuclei:

$$Q_{20} = \frac{3}{\sqrt{5\pi}} Z R_0^2 \beta \left(1 + \frac{2}{7}\sqrt{\frac{5}{\pi}}\beta\right) (e\mathrm{fm}^2), \quad (34)$$

with $R_0 = r_o A^{1/3}$. Relations taking into account higher-order deformations can also be used: see e.g. [321 p, 144], [69, p 139], [322, p 91]. Note that it is also possible to deduce the reduced transition probability $B(E2)$ and subsequently the electric quadrupole moment from lifetime measurements: the transition rate is related to reduced transition probability by (25).

The electric quadrupole moments Q_{20}, deduced from Coulex experiments, correspond to lifetimes of 2^+ collective states at the level of ≈100 ps. Note that this value is corrected for the internal conversion effect using $t_\gamma = t_{\mathrm{total}}(1 + \alpha)$, or $\lambda_{\mathrm{total}} = \lambda_\gamma(1 + \alpha)$, α being the internal conversion coefficient, and that in the absence of this effect the collective 2^+ lifetimes would be ≈1000 times longer, i.e. in the 100 ns range, and therefore isomeric. Measuring such lifetimes in heavy nuclei is extremely challenging using prompt spectroscopy techniques, as discussed in paragraph 5.2.2. However, decay spectroscopy combined with fast electron detection (using a plastic scintillator) allows high-precision lifetime measurements in actinides. This technique was used almost 50 years ago to measure the 2^+ lifetimes in ^{228}Th, ^{234,236}U, ^{238,240}Pu and ^{248}Cm [323]. In the last nucleus, the measured value $t_{1/2} = 120 \pm 10$ ps still represents the only direct measurement; the adopted value 122.5 ± 2.5 ps [324] actually results from analysis of Coulex data and is therefore deduced from the measured $B(E2)$.

The second possible application of Coulomb excitation is for a more spectroscopic purpose, as opposed to multipole moment measurement. It is in this case advantageous to use the heaviest beam possible (highest atomic number Z) in order to maximize the induced electric field, and in consequence the energy and angular momentum transfer. Such experiments have been made possible with the advent of very heavy ion accelerators, for example at GSI, where a series of Coulomb excitation experiments using various actinide targets and a ^{208}Pb beam at ≈5 MeV/A was performed in the 1980s: ^{232}Th

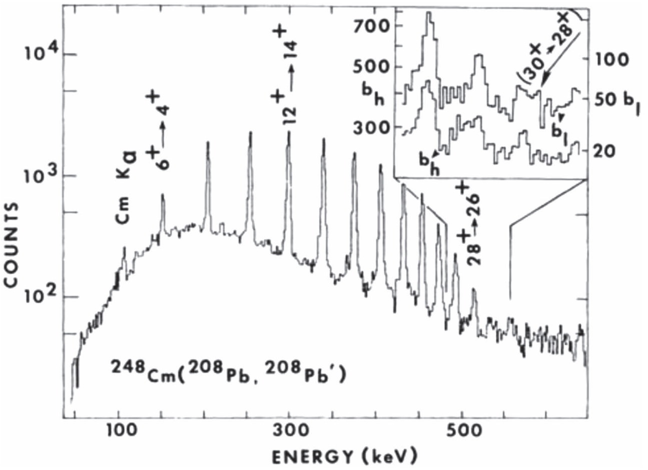

Figure 46. Ground-state rotational band of ^{248}Cm populated in Coulomb excitation using a ^{208}Pb beam at 5.3 MeV/u. Reprinted figure with permission from [329], Copyright (1981) by the American Physical Society.

[325, 326], ^{234,236}U [325] ^{238}U [327], ^{242,244}Pu [328] and ^{248}Cm [329]. Prompt γ-ray transitions were detected using Ge(Li) detectors. In order to select events corresponding to the highest probability of multi-step excitation and consequently, to enhanced population of high-spin states, the de-excitation γ-rays were registered in coincidence with scattered projectiles and target recoils detected in parallel plate avalanche counters (PPACs). The information from these detectors was also used to perform the Doppler correction. Figure 46 shows the resulting γ-ray spectrum in the case of ^{248}Cm [329], corresponding to a rotational band populated up to spin $I = 30\hbar$. This is the heaviest nucleus, for which a high-spin rotational band had been known prior to the ^{254}No studies performed in 1998. High-spin states of ^{248}Cm have not been revisited so far. Similar experiments were performed in the same period at the LBNL, e.g. Coulex of a ^{248}Cm target using a ^{136}Xe beam [330]. Besides energies of γ-ray transitions, the reduced transition probabilities $B(E2)$ were also deduced up to $I = 22\hbar$. The fit procedure included the lifetime of the 2^+ state measured by Ton *et al* [323]. No similar measurement could be yet performed for the heaviest nuclei.

In the series of articles mentioned above, a rise in the moment of inertia was observed. It was discussed as resulting from the alignment of the high-j orbitals $\pi i_{13/2}$, $\nu j_{15/2}$. A backbending was observed for the first time in this region in ^{244}Pu [328]. The evolution of the moment of inertia was compared to results of a cranked HFB calculation performed with some simplifications to circumvent computational difficulties which did not allow in the 1980s for 'full' calculations in this region. From this calculation, it was concluded that the alignment was due to the breaking of a $\pi i_{13/2}$ pair. However, the question of a competition between the $\pi i_{13/2}$ and $\nu j_{15/2}$ pairs in the description of upending and backbending is a longstanding problem which is still under debate 40 years after, as discussed in paragraph 3.7.

For completeness, let us also mention in the same spirit more recent Coulex experiments on ^{248}Cm and ^{240}Pu using a thick target ($\approx$50 mg cm^{-2}), in which new negative-parity side bands have been observed [331].

3.2.2. Transfer reactions. While Coulomb excitation allows only access to nuclei that can be provided as a target or as a beam, MNTs allow to explore nuclei in a broader neighborhood of the target or beam. Compared to Coulomb excitation measurements, where only the inelastic and fission channels are open (at least for sub-barrier experiments), the experimental conditions are more demanding for MNT studies. In order to perform prompt γ-ray studies one has to (i) identify the MNT products in (A, Z); (ii) detect the angle and velocity for Doppler correction, since the products are characterized by a large momentum and angular dispersion. These requirements can be fulfilled in lighter mass regions using e.g. a PPAC [332, 333], a $\Delta E - E$ telescope for light fragment identification [334], or an annular Si detector [335]. These techniques are, however, difficult to adapt to highly active targets. Moreover, the most interesting channels usually correspond to several transferred nucleons, and so the relevant cross sections drop rapidly. The techniques mentioned above do not provide an unambiguous (A, Z) identification of the heavy products. A mass separator would not necessarily address the difficulties: a separator/spectrometer at the grazing angle would intercept only a small fraction of the differential cross section and therefore would lower the observation limit (provided that a sufficient (A, Z) resolution would be obtained). The question whether the differential cross section remains non-negligible around zero degrees and therefore whether a zero degree separator could be used is largely debated and we will come back to this subject in section 5.2.1.

Experimental difficulties have been overcome only recently using e.g. the ^{248}Cm(^{18}O,^{16}O)^{250}Cm reaction [386]. A light beam was selected in order to keep a sufficient (A, Z) identification of the ejectile, however it resulted in observation of transitions at low spin only, which did not allow to fully probe alignment phenomena. An alternative to event-by-event ion identification using a particle detector is to rely on high-fold γ^n or X–γ^n coincidences to pin down the decay cascades of interest. A highly efficient and selective γ-ray detection array is therefore needed. Since particles are not detected, one has to use a thick target (or a thin target on a backing) to minimize the Doppler broadening. This works only if the time needed for the ion to be fully stopped in the target material is shorter than the lifetimes of the states of interest, which turns out to be the case, since typical stopping times are of the order of a picosecond, comparable to the time needed to emit a few γ-rays at high spin[6].

This technique using a thick ^{232}Th target and large Ge arrays has been applied by Cocks *et al* in a series of experiments performed at JYFL, ANL and LBNL [336]. In the experiment using the ^{136}Xe (833 MeV) + ^{232}Th reaction and GAMMASPHERE, high-spin states of ^{218,220,222}Rn

---

[6] Take as an example the $30^+ \to 28^+$ transition at 520 keV in ^{232}Th. From (34): $Q_{20} = 1321\ e\text{fm}^2$ assuming $\beta = 0.3$. Then from (23): $B(E2) = 56\times10^3\ e^2\text{fm}^4$ and finally from (25): $t_{1/2} = 1/T(E2) = 0.4$ ps.

^{222,224,226,228}Ra, ^{228,230,234}Th were studied [337]. Spectra were analyzed using γ^3 coincidences, i.e. the full power of GAMMASPHERE was needed to unravel the rotational bands in the most exotic isotopes. In 1998, ^{234}Th was the heaviest nucleus for which high-spin states were investigated using a transfer reaction. The technique will be further revisited using heavier Cm and Cf targets, as discussed in section 3.5.2.

3.2.3. Fusion-evaporation reactions. The third γ-ray spectroscopy method uses fusion-evaporation reactions to populate high spin states in nuclei of interest. In this case, one has to face a large background of parasitic reactions. The fusion-evaporation cross section is maximum close to the Coulomb barrier, but at such energies the compound nucleus has an excitation energy of several tens of MeV, therefore the fission probability is huge as compared to the fusion-evaporation channel. At best, the fusion-evaporation cross section is at the μb level, compared to a typical total fusion cross section at the b level. Other competing channels are Coulex (up to several b for deformed nuclei), incomplete fusion or transfer. Under such circumstances, the selectivity of the most powerful Ge arrays is not sufficient to tag the channel of interest, not to mention prompt electron spectroscopy which has to face the additional large atomic background resulting from the collision. As fusion-evaporation reactions are strongly forward-peaked, the only alternative is to use a zero-degree in-flight separator. The techniques applied to select the channel of interest are therefore extensions of those used in decay-spectroscopy studies discussed in section 2, the substantial difference being the presence of an array for prompt spectroscopy placed around the target.

There are several variants of the selection technique using a zero-degree separator, the simplest one being the recoil tagging (RT), illustrated in figure 47. After separation, the recoils are selected using kinematics conditions from focal plane measurements: e.g. E versus ToF, ΔE versus ToF contours. Since the dispersion of the residues time-of-flight through the separator is low, it is consequently possible to associate the measured prompt radiation to an implanted nucleus. It is important to note that there is a fundamental difference between the genetic correlations technique and RT. In the former case it is advantageous to use the highest beam intensity, within the limits given by the target resistance to heat, which translates into several μA or even higher intensities. In the latter case, a severe restriction comes from the prompt γ-ray detection array, which has counting rate limitations. In practice, the counting rate of a typical Ge detector positioned at $\approx$20 cm from the target, for a $\approx$10 pnA beam intensity and a $\approx$500 μg cm^{-2} target is about 10 kHz, which is an acceptable limit in terms of preserving good energy resolution and low pile-up probability when conventional analog electronics is used. This limit can be raised up to several tens of kHz, hence several tens of pnA, using digital signal processing.

The RT technique was pioneered at the end of the 1980s at Daresbury, applied to the $A \approx 130$ mass region [338]. In this study, the spectroscopy of the ^{108,109}Te α emitters was performed using the Daresbury recoil mass separator (RMS) and EUROGAM I consisting of 45 HPGe detectors. In this particular case, the RMS was used to select in (A, Z) different evaporation channels, fission not being an issue. The R(D)T technique was further implemented in the beginning of the 1990s at ANL with the FMA [219].

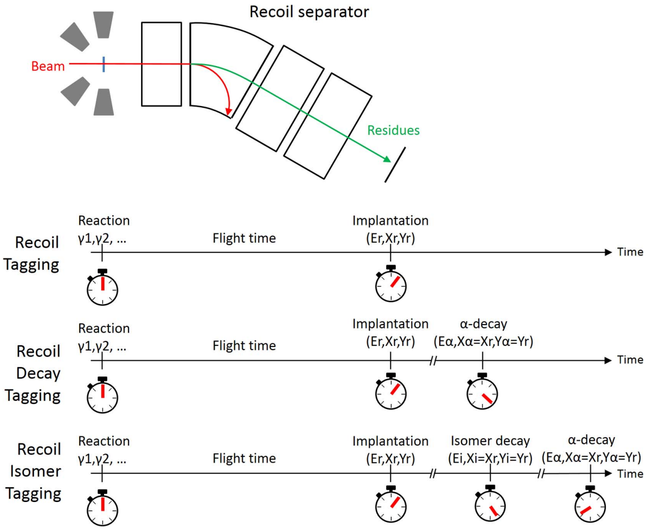

Figure 47. Illustration of the recoil tagging, recoil decay tagging and recoil isomer tagging techniques. See text for details.

When several fusion-evaporation channels are open, and when an (A, Z) resolution cannot be achieved with a separator, it is possible to exploit a characteristic decay of the implanted nuclei in order to reach the required selectivity. The technique is known as the recoil decay tagging (RDT) and its concept is presented in figure 47. The basic idea behind RDT is to correlate the nucleus implantation with its characteristic decay (typically α-decay). Since the lifetime of the nuclei can be longer than the time between implantations (leading to background mis-identified as recoils), position correlations are introduced, like in the genetic correlations technique discussed in section 2.3.2. The RDT technique has therefore similar limitations in terms of counting rate and lifetime of the nuclei under study, in order to preserve unambiguous identification. Also, the RDT efficiency depends on the α detection efficiency ($\approx$50%) and on the α branching ratio. The RDT technique was pioneered in the mid 1980s by Simon at GSI using SHIP and an array of NaI modules known as the CRYSTAL BALL [339]. Prompt γ-rays from ^{180}Hg were observed in the radiative capture reaction ^{90}Zr+^{90}Zr having a cross section of $\approx$40 μb, compared to the total fusion-evaporation cross section of $\approx$2 mb. Tagging on the $T_{1/2} = 2.6$ s α-decay of ^{180}Hg was therefore mandatory to select the channel of interest. Note that the term RDT was coined by Paul in the mid 1990s [340].

The RDT technique was further developed in several laboratories, including ANL with the FMA, and JYFL with the recoil ion transport unit (RITU) gas-filled separator [225] commissioned in 1994: see figure 23. Depending on the decay mode of the nuclei of interest, different variants of the RDT technique can be used, employing proton, β, fission or isomer tagging. These last two cases will be discussed below.

Since its early days, RITU has been coupled to Ge arrays for prompt spectroscopy, which efficiencies increased over the years. The first of them was the JUROSPHERE array, consisting of 12 EUROGAM-type Phase I and 10 TESSA-type HPGe with anti-Compton shields, installed at RITU in 1997 ($\epsilon_\gamma \approx 1.3\%$ at 1.3 MeV). In parallel, the GAMMASPHERE array consisting of ≈100 HPGe detectors, being among the most advanced γ-ray detection setups of these times along with its European counterpart EUROBALL, was installed end of 1997 at ANL at the FMA, providing a larger γ-ray efficiency of ≈10% at 1.3 MeV. RITU and JUROSPHERE have been used, for example, in the region of VHN to study octupole deformation in ^{226}U using the fusion-evaporation reaction ^{208}Pb(^{22}Ne,4n)^{226}U having a cross-section of ≈6 μb [341]. This was at that time the heaviest nucleus ever studied using a fusion-evaporation reaction in conjunction with the R(D)T technique.

3.3. The ^{254}No breakthrough

In 1998 the situation concerning VHN was the following: Coulex studies were performed in the 1980s up to ^{248}Cm using a few Ge detectors and PPACs for kinematic selection and reconstruction. MNTs were exploited up to ^{234}Th using thick targets. Highly efficient γ-ray detection arrays, available since the late 1990s, were used to pin down the cascade of interest. These techniques, however, imposed strong limitations on the nuclei that could be accessed. In parallel, the R(D)T technique in conjunction with fusion-evaporation reactions was ramping up, opening a possibility to access a broader range of isotopes.

It is striking how huge a leap across the nuclear chart has been achieved with the spectroscopy of ^{254}No. Since this nucleus can only be synthesized (at least easily) using a fusion-evaporation reaction, the gap separating it from ^{226}U, the previous record achieved by using this technique, is of 10 atomic numbers. We will try in the following to depict how the idea of these measurements emerged and became a reality.

On the experimental side, the gap in terms of difficulty is not as spectacular as the gap in mass and charge. An important motivation for studying ^{254}No instead of one of its neighbors (in particular the magic deformed ^{252}Fm) is the unusually high cross section of ≈2 μb for the reaction ^{208}Pb(^{48}Ca, 2n)^{254}No [342–344]. This high cross-section is due to the doubly-magic character of both reactants leading to a low excitation energy at the barrier, and therefore a large survival probability (additional enhancement is due to the proximity of the reaction product ^{254}No to the $N = 152$, $Z = 100$ subshell closures), as compared to other systems. For comparison, the cross-section for the reaction ^{238}U(^{22}Ne, 6n)^{254}No is only 15 nb [345].

It should be noted that the 2 μb cross-section is not far from the fusion-evaporation cross section of 6 μb for the reaction ^{208}Pb(^{22}Ne, 4n)^{226}U previously studied at RITU, and by far not an obstacle as compared to even more difficult experiments successfully performed with RITU in this period, such as the in-beam study of ^{198}Rn using the reaction ^{166}Er(^{36}Ar, 4n)^{198}Rn with a cross section of only ≈180 nb [346], or the production of ^{245}Fm using the reaction ^{208}Pb(^{40}Ar, 3n)^{245}Fm [204] with a cross section of ≈18 nb. Challenging experiments were made as well with the FMA at ANL. However, the coupling of the FMA with a prompt γ-ray detection array, namely GAMMASPHERE, which represented the state of the art in the USA, dates back to the end of 1997, while more experience was gained at RITU with various prompt γ-ray arrays like JUROSPHERE I, an assembly of HPGe detectors from different European countries. After this last array had been dismounted at the end of 1997, it was replaced by SARI, an array of 4 HPGe clovers, 3 of which being electrically segmented. Although SARI consisted of a smaller number of crystals compared to JUROSPHERE I, the increase in efficiency was estimated to exceed a factor of ≈4, in part due to the placement at a closer distance from the target made possible by the segmentation.

Table 4. Experimental conditions for the spectroscopy of ^{254}No for the measurements performed at JYFL and ANL in 1997. Here $E_{\rm beam}$ denotes the kinetic energy of the projectiles, $d_{\rm Target}$ the target thickness, $I_{\rm beam}$ the beam intensity, $\epsilon_{\rm ER}$ the probability for a ^{254}No to pass the respective separator and to be detected in the focal plan silicon detector, and ϵ_γ the detection efficiency for a γ-ray of 1.3 MeV.

	$E_{\rm beam}$ (MeV)	$d_{\rm Target}$ (μg/cm^2)	$I_{\rm beam}$ (pnA)	$\epsilon_{\rm ER}$	ϵ_γ
JYFL	216	250–700	10	≈25%	≈1.7%
ANL	215	500	9	≈7%	≈10%

On the theoretical side, the absence at this period of any calculations of high-spin properties of ^{254}No and nuclei around is striking. There were actually several theoretical calculations carried out for ^{254}No before the experiments, but they were limited to the g.s. fission properties [347–350] or to the first low-spin collective states in the context of α-decay spectroscopy [351]. As we will discuss later, theoretical calculations concerning higher spin states, e.g. moments of inertia, appeared only after the experimental results.

Clearly, there was no strong theoretical support, on which a proposal could be based. A point, which was frequently discussed, was related to stability against rotation: could ^{254}No survive to high spin? This concern was certainly justified in the context of fusion-evaporation reactions, which feed nuclei with substantial excitation energy. Nevertheless, Coulex measurements performed in the 1980s in e.g. ^{248}Cm [329, 330] show that $A \approx 250$ nuclei can rotate up to at least $I \approx 30\hbar$. We will come back to this point later in section 3.5.3.

The first experiment was performed in July 1998 at ANL, followed in August 1998 by that at JYFL. The experimental conditions are summarized in table 4. The γ-ray spectra obtained in both experiments are of similar quality: see figure 48 for the ANL results; the lower efficiency of SARI as compared to GAMMASPHERE was compensated by a higher

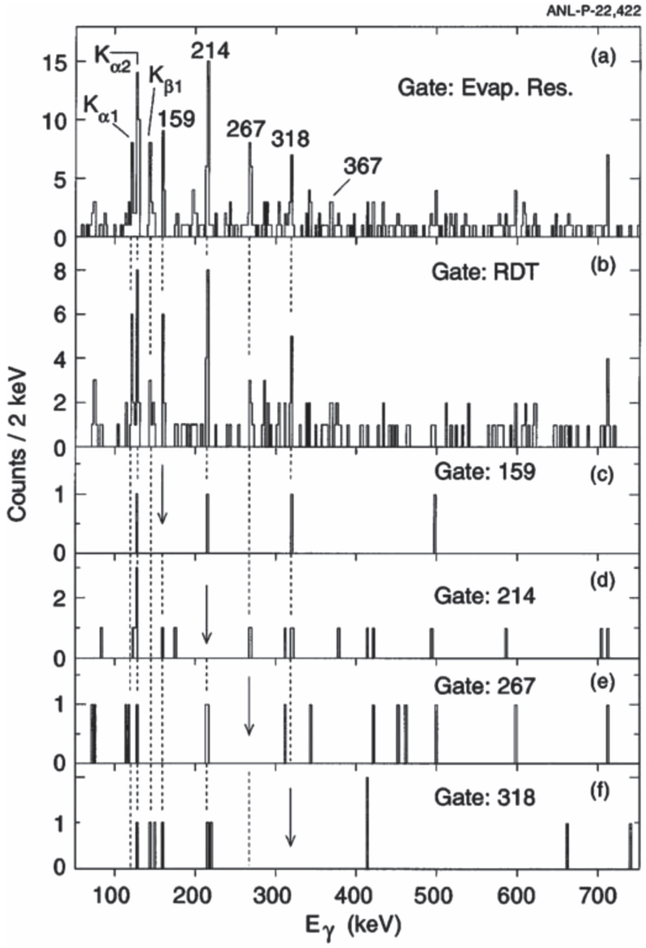

Figure 48. ^{254}No spectra obtained at ANL in 1998. (a) and (b): RT and RDT spectrum, respectively. (c)–(f): spectra resulting from γ–γ coincidences. Reprinted figure with permission from [299], Copyright (1999) by the American Physical Society.

transmission of RITU as compared to the FMA. The γ-ray spectrum obtained at JYFL exhibits higher background, since the HPGe detectors were not surrounded by anti-Compton shields, suppressing Compton background by a veto condition on the detection of scattered γ-rays. For the energies of interest this is, however, not such a large handicap. The observed γ-rays correspond to a rotational band populated up to $I = 14^+$ and 16^+ in the ANL and JYFL experiment, respectively. Spins were attributed using the so-called 'Harris' fitting procedure, to which we will come back in section 3.6. This procedure also allows obtaining from extrapolation the $E(2^+ \rightarrow 0^+)$ and $E(4^+ \rightarrow 2^+)$ transition energies of 44 keV and 102 keV, respectively, which could not be observed due to high internal conversion and low γ-ray detection efficiency at these energies. As will be discussed later in paragraph 3.6, a deformation parameter $\beta_2 \approx 0.27$ can be deduced from the 2^+ excitation energy. This value is in good agreement with theoretical predictions of microscopic–macroscopic models or EDF calculations, which span a range of 0.25–0.30 (see [299, 300] and references therein). It should be noted that comparison of the experimental moments of inertia $\mathcal{J}^{(1)}$ or $\mathcal{J}^{(2)}$ with theoretical predictions could not be made since they were not yet available, although Reiter *et al* [299] refer to unpublished calculations of Muntian *et al* performed using a Woods–Saxon potential.

Theoretical calculations were indeed published later. Just to cite the first ones: in 2000 by Egido and Robledo (HFB with Gogny D1S force) [352], in 2001 by Duguet *et al* [353], Laftchiev *et al* [354] (both HFB with a Skyrme force), Zajac *et al* (collective Hamiltonian) [355], and Sobiczewski *et al* (Woods–Saxon potential, however only 2^+ and 4^+ states were calculated in the context of α-decay studies) [255]. Comparison with theoretical calculations will be made below in paragraph 3.7.

The ANL and JYFL ^{254}No experiments of 1998 represent a significant achievement in the spectroscopy of the heaviest elements, which paved the way for considerable experimental and theoretical progress, as discussed subsequently in this chapter. Before proceeding with the discussion of further results, we will open a parenthesis on the prompt spectroscopy techniques, which are key ingredients in the developments made in the transfermium region.

3.4. Prompt spectroscopy techniques

In this paragraph we will give an overview over prompt spectroscopy techniques and devices relevant for studies of the heaviest nuclei. For a more detailed discussion of γ-ray arrays, we refer the reader to the reviews of Lee *et al* [356], Eberth and Simpson [357], and to the contribution of Riley *et al* in this focus issue [358].

3.4.1. Gamma-ray spectroscopy. Semi-conductor detectors are the only conventional devices providing a resolution at the level of single digit percent values, which is needed for high-resolution γ-ray spectroscopy. The time resolution of these detectors remains nonetheless in the modest 5–10 ns range. Ge is preferred to Si or C because of a larger photoelectric absorption cross section (it is a function of Z^{4-5}), and since crystal-growing technologies allow production of larger volume detectors. The crystals are operated at the LN_2 temperature (77 K) to minimize excitation across the band gap and hence achieve a good energy resolution. The introduction of high-purity Ge detectors (HPGe) in the late 1970s opened up the possibility of using rather compact, reliable and easier to operate detectors. Although large crystals of $\approx$300 cm^2 can be grown, this volume is still not sufficient to fully absorb $\approx$1 MeV photons. The cross section for Compton scattering at such energies exceeds that for the photoelectric absorption by a factor $\approx$100, hence there is a large probability that a photon escapes from the crystal after the first of a multiple Compton scattering sequence. In consequence, the corresponding peak-to-total (P/T) ratio is modest. This problem may be overcome by surrounding the Ge crystals by high-absorption active material. If a coincidence between the Ge crystal and its anti-Compton shield occurs, the hit is rejected. This typically improves the P/T ratio to 50%. For anti-Compton shields, BGO or NaI scintillators have been widely used since the 1980s. Heavy metal (tungsten alloys) collimators are added in front of the shields to prevent their direct exposition to the source. This technology allowed the development of large multidetector arrays. The important criteria for the design are:

- Minimization of the Doppler broadening effect which is maximum at 90° with respect to the velocity vector of the emitting nucleus: $\Delta E_\gamma = E_0\ \beta\ \sin\theta\ \Delta\theta$, where $\Delta\theta$ is the opening angle of the detector, and θ the angle between the velocity vector of the emitting nucleus and that of the detected γ-ray.
- Minimization of pile-up probability, which basically leads to minimization of the solid angle covered by each crystal.
- Maximization of the photopeak efficiency and of the coincident γ^n efficiency which may be fulfilled by using a large number of detectors covering a maximal total solid angle.

A compromise to fulfil these sometimes contradictory conditions typically leads to implementation of arrays consisting of ≈100 crystals positioned at 20–25 cm from the target. The total solid angle covered by the Ge crystals is at best ≈50%, the remaining part being occupied by the anti-Compton shields.

The most powerful arrays of such design were developed in the 1990s. Because of the cost of HPGe detectors, they were constructed within large collaborations, and shared between different host laboratories. GAMMASPHERE in the USA with its 110 crystals [359] (see figure 49) and EUROGAM-EUROBALL in Europe [360] were the most advanced Compton-suppressed arrays with photopeak efficiencies culminating at ≈10% at 1.3 MeV γ energy. GAMMASPHERE was installed at the LBNL from 1993 to 1997, then at ANL from 1997 to 2001, back at LBNL in 2001–2003, and finally returned to ANL in 2003, where it remained since then. During the ^{254}No experiment, GAMMASPHERE consisted of 101 coaxial HPGe detectors. As mentioned above, heavy-metal collimators are usually placed in front of the anti-Compton shields. It is also possible to perform measurements without collimators, and in this way to use the array as a calorimeter, deducing the total energy and multiplicity emitted in a cascade using unfolding procedures.

Increasing the granularity (in order to minimize Doppler broadening and pile-up probability) can be achieved using smaller crystals, but the consequence is a decrease of the photopeak efficiency. The EUROGAM-EUROBALL collaboration developed a method to pack several crystals in the same endcap, sharing the same cryostat. This lead to the introduction of ‘clover’ detectors, consisting of four crystals tapered to a rectangular shape [361], and ‘clusters’, consisting of 7 encapsulated hexagonal tapered crystals [357].

In GAMMASPHERE, the choice of electrically segmented crystals was made, with the two-fold segmented coaxial crystals behaving like two ‘D’ shaped detectors. The segmentation concept was also implemented in clover detectors, where crystals are 4-fold segmented each, leading to the granularity of 16 for each assembly. These detectors resulted from EUROGAM-EUROBALL developments and were predecessors of EXOGAM detectors, which are based on the same concept, but use, however, larger crystals [362].

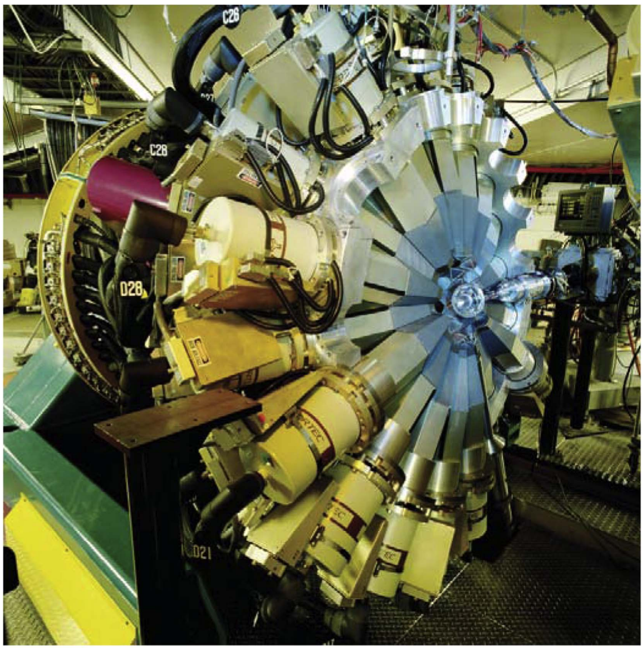

Figure 49. GAMMASPHERE in open position; only half of the array is visible. Photo courtesy of Lawrence Berkeley National Laboratory/Roy Kaltschmidt. Copyright 2010 The Regents of the University of California, Lawrence Berkeley National Laboratory http://photos.lbl.gov/.

With the upgrade of EUROGAM-EUROBALL, 15 available tapered detectors (Phase I) were coupled with 10 smaller TESSA-type crystals (see e.g. [363]) to form the JUROSPHERE I array ($\epsilon_\gamma \approx 1.5\%$ at 1.3 MeV) that operated at JYFL in 1997 (for e.g. γ-ray studies of ^{226}U mentioned above). In 1998, when coaxial detectors left JYFL for other campaigns, the segmented array at RITU (SARI), an array consisting of 4 clovers, 3 of them being segmented, was installed at JYFL. The segmentation allowed using the detectors at a rather close distance of 15 cm, leading to $\epsilon_\gamma \approx 1.7\%$ at 1.3 MeV. Unfortunately, no anti-Compton shields were available, which resulted in a modest P/T ratio. SARI was used to perform the ^{254}No spectroscopy in August 1998 [300]. Subsequently, different variations of JUROSPHERE (II–III–IV) were constructed for experimental campaigns between 1999 and 2001 [364]. The array evolved into JUROGAM I, which was operational in 2003–2007 and consisted of 43 tapered detectors (phase I) giving $\epsilon_\gamma \approx 4\%$ at 1.3 MeV. It was followed by JUROGAM II in 2008, using 24 clovers that were a part of EUROBALL until the collaboration was dissolved in 2003, and 10 tapered (Phase I) HPGe detectors, reaching $\epsilon_\gamma \approx 5.5\%$ at 1.3 MeV. The latest detection array at JYFL, in operation between 2010 and 2017, is known as SAGE (Silicon And GErmanium [365]). It combines JUROGAM II and an array for CE studies that will be discussed in paragraph 3.4.2.

In parallel to the increase of efficiency, efforts were made to increase the electronics and data acquisition throughput and counting rate capabilities. The first step was made at JYFL in

2002 with the TDR 'Total Data Readout' [366], a concept where all channels are read independently without any global trigger, hence overcoming the issue of common dead time. Each channel is time-stamped using a common 100 MHz clock, and events are subsequently software-reconstructed. Since no hardware coincidence or conditions are set, the TDR also provides unfiltered data and therefore more flexibility in the data analysis.

When using analog electronic chains, the counting rate has to be kept below the 10 kHz limit to avoid pile-up and to maintain a good energy resolution. This translates into beam intensity limitations and, consequently, cross section observation limits. An improvement can be made by replacing conventional analog electronics by digital flash ADCs and, eventually, by reset preamplifiers to push the counting rate up to at least 50 kHz/channel. Since 2007, 100 MHz 14 bit flash ADCs have been implemented at JYFL, bringing the limits down to the level of a few tens of nb, as demonstrated by e.g. ^{246}Fm [367] or ^{256}Rf studies [167]. Similarly, the 'Digital Gammasphere' project at ANL aims at the implementation of digital electronics, based on GRETINA developments [368].

With the generation of HPGe anti-Compton shielded detectors, limits in terms of efficiency and sensitivity have been reached. In order to go further, completely new solutions need to be implemented. The latest generation of Ge arrays based on the concept of γ-ray tracking will be discussed in section 5.1.5.

3.4.2. Conversion electron spectroscopy. In the even–even nuclei of the $A \approx 250$, $Z \approx 100$ region, the $2^+ \rightarrow 0^+$ and $4^+ \rightarrow 2^+$ $E2$ transitions in collective rotational bands have low energy and are strongly converted. For example, for Fm isotopes they are equal to ≈100 and ≈45 keV, respectively, with corresponding internal conversion coefficients of ≈25 and ≈1200, respectively. These transitions, therefore, have a very low γ-ray emission intensity. The same problem appears for $M1$ interband transitions in odd nuclei and $K \neq 0$ 2qp bands in even–even isotopes. As an example, the internal conversion coefficients for $M1$ transitions of 60, 100 and 150 keV in Fm isotopes are equal to 46.5, 10.5 and 14.3, respectively. It is therefore important to detect CEs for the heaviest elements and, ideally, combine γ and electron spectroscopy.

It should be reminded that the probability of internal conversion (i) increases with atomic number like Z^3, (ii) increases with the multipolarity of the transition, (iii) is higher for magnetic compared to electric transitions, and (iv) decreases very rapidly with transition energies (dependence like $1/E^{L+5/2}$ for EL and $1/E^{L+3/2}$ for ML transitions). Since spectra have in addition the tendency to be compressed for heavier nuclei i.e. transitions energies are getting lower (for both collective and single-particle states) it is of utmost importance to detect CEs emitted by heavy isotopes. This, however, is a tremendously difficult task for several reasons discussed in the following.

Besides CEs, nuclear collisions generate atomic δ electrons ejected from the target and consequently forward-focused, with cross sections of several barn see e.g. [369]. Their energy increases with the atomic number of the projectile to Z^4_{target} and may overlap with the internal-conversion transitions of interest. It is therefore advantageous to detect the electrons at backward angles, and to suppress the low energy part of the continuous spectrum of δ electrons, ideally without sacrificing the efficiency. This is achieved traditionally using two different types of devices.

The first category consists of a permanent magnet placed between the target and the electron detector. The magnetic field and position of elements shall be such that the electrons having the kinetic energy of interest are focused on the detector. Such devices introduced in the 1970s [370] are known as (mini-)orange spectrometers because of their characteristic shape. Their compact geometry allows coupling with large Ge arrays, like e.g. cluster detectors [371], ICEMOS at SARI [372], ICEBALL at GAMMASPHERE [373], SPICE at TIGRESS [374], etc.

The second category of electron spectrometers is based on solenoids focusing the electrons toward a Si detector. The suppression of low-energy electrons is obtained by an electrostatic barrier placed inside the solenoid. Compared to orange spectrometers, the efficiency curve of such devices is less sharp as a function of electron energy. However, because of the radius of the solenoid (≈20 cm), they cannot be easily coupled to a Ge array. There are few solenoids working in combination with a large Ge array and a recoil spectrometer or a separator. One can mention here the GAREL+ setup installed in the 1990s at IRES (now IPHC) in Strasbourg, which consisted of 14 coaxial (Phase-I) HPGe, the BETATRONC [375] solenoid placed perpendicularly to the beam axis, and of the recoil filter detector [376]. The second example, SAGE, will be detailed below.

For mini-orange as well as solenoid spectrometers, the electron detection consists of a few mm thick Si or Si(Li) detectors, cooled in order to achieve a resolution of few keV below ≈500 keV. In consequence, a good vacuum of 10^{-6} mbar or better has to be maintained, which is at the first glance in contradiction with a gas-filled device. In that case, the Si detector and electrostatic barrier (if any, since it also requires a good vacuum) has to be separated from the gas region using a thin carbon window. This introduces a second contradiction, since presence of any material between the target and the detector induces straggling and deteriorates the energy resolution.

All things considered, electron spectroscopy is much more challenging compared to γ-ray spectroscopy, in particular for heavy-element studies and when coupled to a separator or a spectrometer. Another complication is due to the potential overlap of different CE lines from different transitions e.g. K and L shell peaks stemming from different transitions can have a similar energy, which complicates the interpretation of CE spectra.

A variant of the solenoid and array for conversion electron detection (SACRED) array [378] based on a solenoid, has been designed to be coupled to RITU: see figure 50 [377]. An elegant solution was applied to place the electron detector

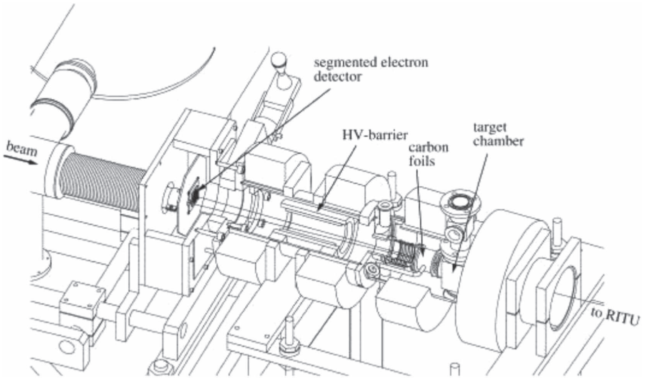

Figure 50. The SACRED array for prompt conversion-electron studies. Reprinted from [377], Copyright 2004, with permission from Elsevier.

at backward angles: it is designed in a near-collinear geometry, the beam passing through the solenoid before reaching the target. The emitted electrons are backward focused by the solenoid tilted at 2.5° with respect to the beam axis. The segmented Si detector is located 56 cm from the target, 25-fold segmented and cooled to ≈ -20 °C to provide energy resolution of 3–4 keV for electron energies of 320 keV. The efficiency is $\approx 10\%$ at 200 keV. SACRED has been used in the $Z \geqslant 100$ region for the prompt spectroscopy of ^{253}No [379], ^{254}No [303] and ^{250}Fm [380].

It is obviously desirable to perform simultaneously prompt γ-ray and conversion-electron spectroscopy, which was not easy with SACRED. Consequently, the SAGE array (silicon And germanium) has been developed [365, 381]. It follows the concept of SACRED, still in a near-collinear geometry, but with a more compact shape, which allows combination with JUROGAM II. The solenoid is tilted at 3.2° with respect to the beam axis. The 1 mm thick Si detector is 90-fold segmented with a concentric ring structure. Is is cooled to $\approx -20°$ C to provide energy resolution of typically ≈ 6 keV for electron energies of 320 keV. The efficiency for electron detection is $\approx 6\%$ at 150 keV. All SAGE detectors are equipped with digital electronics. SAGE is installed since 2010 at RITU and has so far been used for the spectroscopy of the $Z \geqslant 100$ nuclei ^{249,251}Md, ^{253,254}No and ^{255}Lr. Results on ^{253}No have been recently published [382].

3.5. Recent achievements

The ^{254}No experiments of 1998 triggered several prompt spectroscopy studies in the vicinity of this nucleus using fusion-evaporation reactions. At the same time, the improvement of techniques and device performances resulted in revisiting transfer and inelastic scattering reactions on actinides up to californium.

3.5.1. Transfer reactions using light beams. Transfer reactions using light beams such as αs or deuterons have been widely used to study single-particle states in heavy nuclei. Most of the studies up to the 1970s were performed using a spectrograph to detect the ejectile and consequently to deduce the excitation energy spectra and the spectroscopic factors used for spin, parity and Nilsson label assignments. Although very fertile and powerful for studies at low spin, the technique does not allow accessing collective high-spin states. Since the mid-2000s several experiments have been performed at the JAEA-Tokai tandem accelerator facility using mostly an ^{18}O beam impinging on ^{238}U, ^{244}Pu, ^{248}Cm and mixed ^{249,250,251}Cf targets [383–388]. Reaction channels were identified using a set of four $\Delta E - E$ telescopes allowing a precise (A, Z) identification of the ejectiles, while coincident γ-rays were measured using 6 Ge detectors. The target thickness was chosen such that the residual nuclei (target-like) were stopped in it, while the ejectiles could reach the telescopes. Hence, there was no need to measure the direction of the residual nucleus for Doppler correction, a task which would have been challenging in the highly radioactive environment (e.g. 1.4 MBq in the case of the mixed Cf target). Setting different coincidence gates on the $\Delta E - E$ scatter plots allowed selecting different Q values of the reaction corresponding to different reaction channels and residual nuclei.

Using the 2-neutron transfer reaction i.e. the (^{18}O,^{16}O) channel, rotational bands could be established for the first time in ^{246}Pu, ^{240}U and ^{250}Cm up to spin 12^+ [383, 385, 386]. Collective states in ^{248,250,252}Cf resulting from various transfer channels were observed up to spin 10^+, 12^+, 10^+, respectively [388]. The two-proton transfer reaction (^{18}O, ^{20}Ne) was also used to study collective states in ^{236}Th and ^{242}U [389]. The odd nuclei ^{249}Cm and ^{245}Pu were measured as well [385, 387].

These experiments allowed extending the systematics of moments of inertia and 2^+ energies (extrapolated, if needed) in order to study the occurrence and evolution of deformed shell gaps near $N = 152$, $Z = 100$, as discussed further in section 3.6. A sample spectrum for ^{250}Cm is shown in figure 51.

3.5.2. Inelastic scattering and transfer reactions using Pb and Bi beams. As mentioned in paragraph 3.2.1, Coulomb excitation of various actinide targets has been performed in the 1980s using a Pb beam to transfer high angular momentum to the target nuclei. Using heavy beams can also allow high-spin studies of neighboring isotopes after few-nucleon transfer reactions. However, there is no straightforward method to identify ejectiles or residual nuclei in A and Z. For instance, $\Delta E - E$ telescopes cannot provide the required resolution in the Pb–Bi region, contrary to the ^{18}O case. As discussed in section 3.2.2, a solution to circumvent these experimental difficulties is to use a thick target, no heavy ion detection, and exploit the full power of large γ-ray arrays to pin down the cascades of interest. After having been applied at GAMMASPHERE to isotopes up to Th in the 1990s, the technique was recently revisited, also at GAMMASPHERE, using various targets of ^{237}Np, ^{241}Am, ^{240,244}Pu, ^{248}Cm, ^{249}Cf and $^{249-251}$Cf mixture. From these experiments, rotational bands could be observed in ^{236,237}Np, ^{241,242}Am, $^{240,244-246}$Pu, $^{246-250}$Cm and $^{248-251}$Cf [390–396].

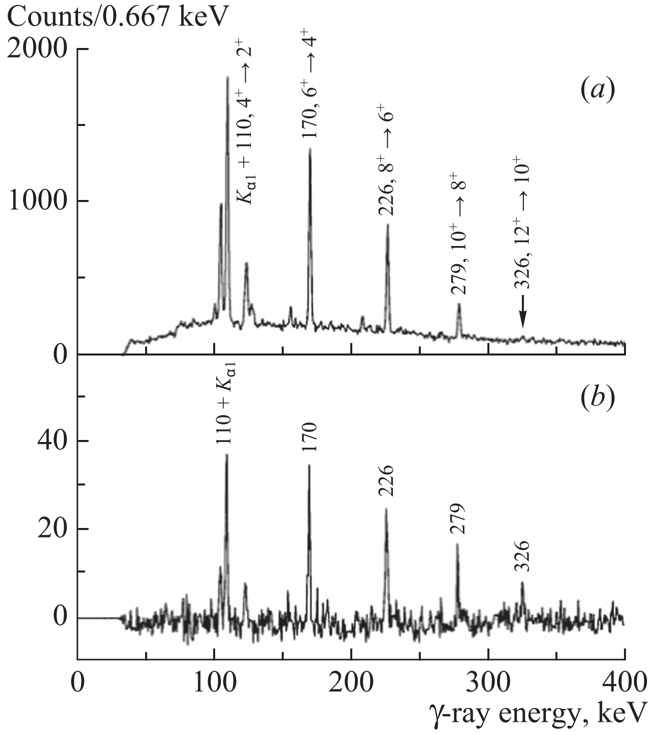

Figure 51. Prompt γ-ray spectra of ^{250}Cm obtained using the ^{248}Cm(^{18}O, ^{16}O) reaction, resulting from (a) gate on the ^{18}O ejectile (b) γ–γ coincidences. Figure taken from [386] (2007). © Pleiades Publishing, Ltd 2007. With permission of Springer. Original Caption: '(a) γ-ray spectrum of ^{250}Cm, obtained by setting the gate on ^{16}O indicated by the enclosed area in Fig. 1; (b) γ-γ coincidence spectrum for the ground-state band transitions in ^{250}Cm,obtained by the sum of spectra incoincidence with 170-, 226-, and 279-keV γ-rays.'

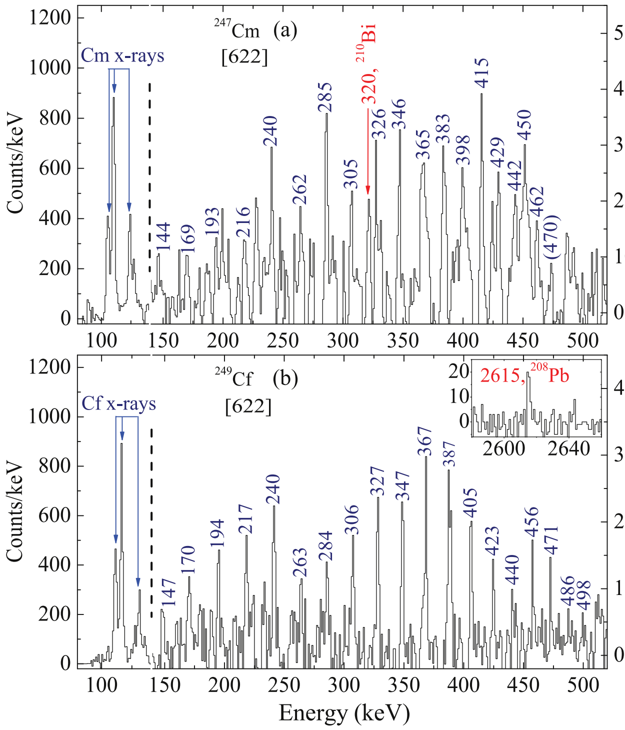

Figure 52. Prompt γ-ray spectra of ^{247}Cm and ^{249}Cf obtained using transfer reactions on a ^{248}Cm target, and inelastic scattering on a ^{249}Cf target, respectively. Reprinted from [393], Copyright 2014, with permission from Elsevier.

Note that in these experiments recoils were not stopped in the target itself, but in a Au backing.

Inelastic cross sections can be as large as 100 mb while transfer reactions cross sections decrease by at least one order or magnitude for each transferred nucleon. These yields are still sufficiently high to collect large statistics and coincident events that are mandatory to select weaker channels, i.e. by γ^2, γ^3, X–γ, by cross-coincidences with the reaction partner, or by gating on the sum energy or total multiplicity. Examples of ^{247}Cm, ^{249}Cf spectra taken from [393] are shown in figure 52. The observation of rotational bands up to spin $\approx 24\hbar$ allows, in particular, to track the backbending phenomenon along isotopic chains, which provide invaluable information on the respective role of $\pi i_{13/2}$ and $\nu j_{15/2}$ orbitals, as discussed in section 3.7.

3.5.3. Fusion evaporation reactions. The ^{254}No experiments, performed at ANL with GAMMASPHERE and the FMA, and at Jyväskylä with RITU and SARI, mark the beginning of a series of $Z \geqslant 100$ studies exploiting fusion-evaporation reactions. So far, these two laboratories have monopolized these prompt studies.

ANL had so far focused their experiments on the ^{253}No and ^{254}No isotopes using the RT and RDT techniques. Thanks to the possibility of using GAMMASPHERE in a calorimetric mode, entry distribution measurements providing insight into fission barriers were performed for ^{254}No. A wider range of isotopes has been studied at JYFL using successive Ge arrays and conversion-electron spectrometers. Different tagging techniques have been developed besides RT and RDT: the recoil fission tagging (RFT) for nuclei predominantly fissioning, and the isomer tagging method to tag rotational bands built on an isomeric (high-K) state. The list of isotopes studied at JYFL includes ^{246,248,250}Fm, ^{251}Md, ^{252,253,254}No, ^{255}Lr and ^{256}Rf. Both in ANL and JYFL, all isotopes have been populated using cold fusion reactions with a ^{40}Ar, ^{48}Ca or ^{50}Ti beam and Hg, Tl, Pb, Bi targets.

Ground-state bands of even–even isotopes

After the successful ^{254}No study, it became clear that reactions with lower cross sections could be used. The first on the list was ^{252}No, for which spectroscopy was performed using RITU, JUROSPHERE II and the fusion-evaporation reaction ^{206}Pb(^{48}Ca,2n)^{252}No, with a production cross section of $\sigma \approx 500$ nb. The dataset was analyzed using the RT and RDT techniques by Herzberg *et al* [302] and complemented by Leppänen *et al* [304] using the RFT technique which can be implemented for this isotope, since spontaneous fission represents $\approx$30% of the total decay [397]. In this case, the recoil implantation is correlated in time and position with subsequent fission, often leaving only part of its energy in the Si focal-plane detector since one of the fragments can escape with a finite probability, as the recoil implantation depth into the DSSD ($\approx$5 μm) is smaller than the range of the isotropically emitted fission fragments in silicon.

The experiment to study the spectroscopy of ^{254}No has been repeated several times at JYFL in order to increase the

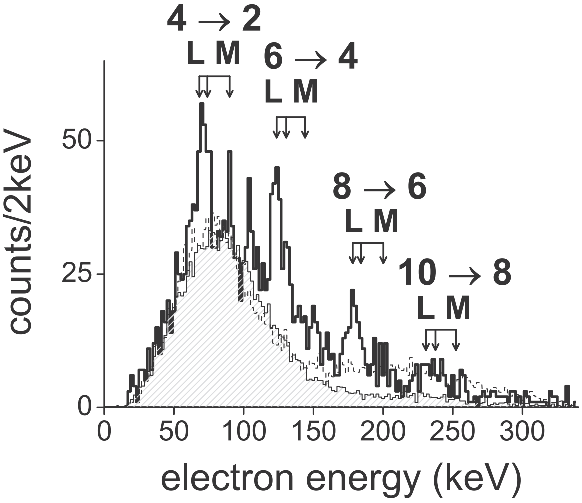

Figure 53. Conversion electron spectrum of ^{254}No obtained with RITU and SACRED. The grey area results from a simulation of de-excitation of high-K rotational bands. Reprinted figure with permission from [303], Copyright 2002 by the American Physical Society.

statistics for e.g. high-K states studies (see below in this section). It was also the first transuranium nucleus, for which prompt electron spectroscopy has been carried out using a fusion-evaporation reaction: the experiment was performed with SACRED, described in section 3.4.2. The corresponding conversion-electron spectrum, taken from [303], is shown in figure 53 (see also [398]). The L and M conversion lines of the transitions from $4^+ \rightarrow 2^+$ up to $10^+ \rightarrow 8^+$ are observed, extending the rotational band to lower angular momenta. The continuous background below the discrete lines is interpreted as corresponding to $M1$ cascades from the de-excitation of high-K (2qp and higher) rotational bands.

The g.s. bands of ^{246,248,250}Fm were studied at JYFL using RITU. ^{250}Fm was populated using the fusion-evaporation reaction ^{204}HgS(^{48}Ca, $2n$)^{250}Fm with a cross-section of $\approx$1 μb [380]. Gamma rays were detected with JUROSPHERE IV, and the reaction channel was selected using RT and RDT methods. A second experiment was devoted to prompt electron spectroscopy of this nucleus using SACRED. Gamma-ray transitions were measured from $6^+ \rightarrow 4^+$ up to $18^+ \rightarrow 16^+$, complemented by electron transitions from $4^+ \rightarrow 2^+$ up to $10^+ \rightarrow 8^+$. Thanks to electron spectroscopy, it has been possible to confirm that the transitions are of $E2$ character using the measured $(L_{\rm I} + L_{\rm II})/L_{\rm III}$ intensity ratios. ^{248}Fm was studied using the reaction ^{202}HgS(^{48}Ca, $2n$)^{248}Fm ($\sigma \approx 120$ nb) with JUROGAM. Details of the rotational band observed up to $I = 18^+$ are reported in the PhD Thesis of Ketelhut [399]. ^{246}Fm was populated using the reaction ^{208}Pb(^{40}Ar, $2n$)^{246}Fm with a cross section of only $\approx$11 nb. At this level of production cross sections, limitations of the RT technique start to appear, since the rate of background events is comparable with that of the nuclei of interest. Therefore the RDT technique has been used to extract unambiguously the rotational band up to $I = 16^+$ [367]. The experiment was made possible since digital electronics was implemented to cope with counting rates up to 40 kHz per crystal, corresponding to a beam intensity up to $\approx$70 pnA. A rotating target was needed, since cooling with the He gas of the separator was not sufficient.

The prompt spectroscopy of ^{256}Rf was performed using the ^{208}Pb(^{50}Ti, $2n$)^{256}Rf reaction with a cross section of 17(3) nb [167]. This experiment, performed in 2011, required large experimental efforts, in particular the introduction of digital electronics for JUROGAM II, and development of the Ti beam using the MIVOC method [400]. Since ^{256}Rf decays almost exclusively via spontaneous fission, the RFT technique was needed to extract the data of interest from the unwanted background, since, like in the ^{246}Fm case, RT alone was not sufficient. From 2210 fission-correlated events, the γ-ray spectrum shown in figure 54 was obtained, revealing a rotational band observed up to $I = 18^+$. ^{256}Rf is the heaviest isotope, for which spectroscopy was studied using prompt techniques. Ground-state bands of even–even isotopes populated by fusion-evaporation, Coulex and transfer reactions will be further discussed in section 3.6.

Fission-barrier measurements

A fission barrier is a fundamental quantity governing the stability of actinide and transactinide nuclei. More generally, fission properties, together with other quantities such as Q_β, Q_α, neutron separation energies, etc are key ingredients in nuclear reactor simulations or calculations of stellar nucleosynthesis abundances in the r-process [401, 402]. It is well known that spontaneous fission lifetimes are extremely sensitive to the barrier height. Changing its value by 1 MeV corresponds to a lifetime difference of up to several orders of magnitude (see paragraph 1.2.1). Fission rates are also a key ingredient in the fusion-evaporation cross-section predictions. In the context of prompt γ-ray spectroscopy, the stability of nuclei against rotation is, to a large extent, governed by the evolution of the fission barrier with angular momentum, although it is more complex in the case of fusion-evaporation reactions which introduce other limitations as we will discuss later. On the theoretical side, fission is probably one of the most complex phenomena in nuclear physics, being a dynamical process during which the nucleus explores several degrees of freedom. Depending on whether they are included or not, the outcome of the calculations may change dramatically. As an example, accurate calculations of fission-fragment yields using microscopic models are still in an early stage of development, see e.g. [403–405]. At the most basic level, there is a large spread in fission barrier heights calculated using different models and forces, see e.g. [406] and references therein.

Measurements of fission barriers are therefore fundamental. In principle, a fission barrier can be determined by measuring the fission probability as a function of the excitation energy. This has been done traditionally using transfer (d, p) or neutron-induced reactions, for which the excitation energy of the compound nucleus can be deduced. The fission barrier height and possibly its curvature are consequently deduced from the fission probability under assumptions resulting from statistical model calculations (e.g.

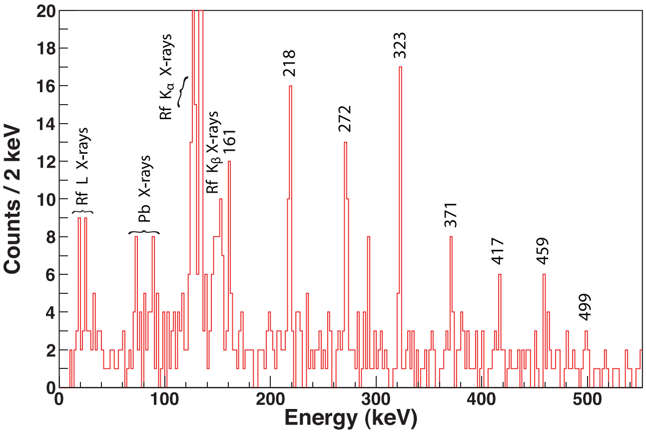

Figure 54. Prompt γ-ray spectrum of ^{256}Rf showing a rotational band populated up to $I = 18^{+}$. Reprinted figure with permission from [167], Copyright 2012 by the American Physical Society.

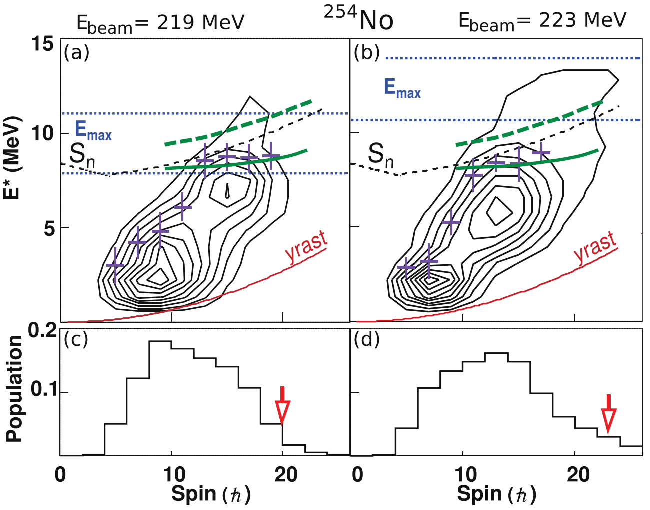

Figure 55. Entry distribution of ^{254}No measured with GAMMASPHERE and the FMA for beam energies of 219 MeV (left) and 223 MeV (right). The top panels (a) and (b) represent the total spin versus energy entry distributions. Panels (c) and (d) correspond to the spin projection of the distribution. The red arrows indicate 10% of the maximum. See text for further details. Reprinted figure with permission from [88], Copyright (2014) by the American Physical Society.

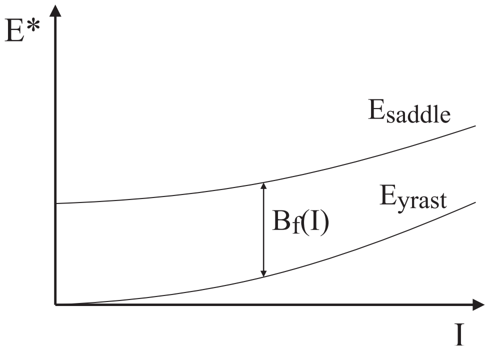

Figure 56. Illustration of the fission barrier $B_f(I)$, yrast and saddle energies.

level densities). Obviously, such measurements are limited to cases for which the required target can be produced. Fission barriers have been measured up to ^{255}Fm [407] (using direct reactions $^{A}Z(^{3}\mathrm{He}, d)sf$). For more details on theoretical or experimental aspects of fission, the reader can refer to the books or reviews [85, 87, 256, 406, 408–410].

Fission barriers can also be deduced using fusion-evaporation reactions from entry distribution measurements. After evaporation of the last neutron, the only channels open are fission and de-excitation to the g.s. The fission probability is then expressed as $P_f(E) = 1 - P_\gamma(E)$, where $P_\gamma(E)$ is the probability to de-excite via γ-ray emission. Using statistical model calculations, it is possible to deduce from $P_f(E)$ the fission barrier or, more precisely, the saddle energy. Compared to direct reactions, a complication arises from the fact that the residual nucleus is fed in a large angular momentum range.

The entry distribution is a measure of the total energy and angular momentum released by the nucleus. It is deduced from the total energy H and multiplicity K measured using a prompt γ-ray detection array. After a rather complex unfolding procedure, correction for undetected high energy statistical and low energy converted transitions, and application of assumptions concerning the multipolarity of the transitions and the spin removed by particle evaporation, the (E^*, I) entry distribution can be obtained. Such measurements were performed for ^{254}No using GAMMASPHERE in a calorimetric mode by Reiter *et al* in the late 1990s [301] at $E_{\mathrm{beam}} = 215$, 219 MeV, and, more recently, at higher energies $E_{\mathrm{beam}} = 219$, 223 MeV by Henning *et al* [88], see figure 55.

For each entry angular momentum I, the E^* distribution of the surviving nuclei provides information on the fission barrier. Another way of putting it is that above the saddle point fission dominates, hence few nuclei contribute to the entry distribution, contrary to what happens below the saddle point. For each angular momentum it is possible to determine the energy $E_{1/2}$, for which the entry distribution drops to $1/2$ of its maximum value (i.e. $P_\gamma(E_{1/2}) = P_f(E_{1/2}) = 50\%$). These points are represented with purple crosses in figure 55. Note that the region $E^* \lesssim 6$ MeV should be omitted in the discussion, since it is interpreted as corresponding to the feeding of isomers, hence with an incomplete (H, K) measurement. $E_{1/2}$ is not exactly the saddle energy, but both these quantities can be related using a statistical model calculation which provides a correction

$$\Delta(I) = E_{1/2}(I) - E_{\mathrm{saddle}}(I). \tag{35}$$

E_{saddle} is related to the fission barrier $B_f(I)$ using

$$E_{\mathrm{saddle}}(I) = B_f(I) + \frac{\hbar^2}{2\mathcal{J}_{\mathrm{yrast}}} I(I+1) \tag{36}$$

$$= B_f(0) + \frac{\hbar^2}{2\mathcal{J}_{\mathrm{saddle}}} I(I+1), \tag{37}$$

as shown in figure 56. Using (35) and (37), it is possible to deduce not only the fission barrier $B_f(0)$, but also the saddle moment of inertia. The analysis yields $B_f(0) = 6.6 \pm 0.9$ MeV, $\mathcal{J}_{\mathrm{saddle}} = 125 \pm 60\ \hbar^2\mathrm{MeV}^{-1}$. More details can be found in [88].

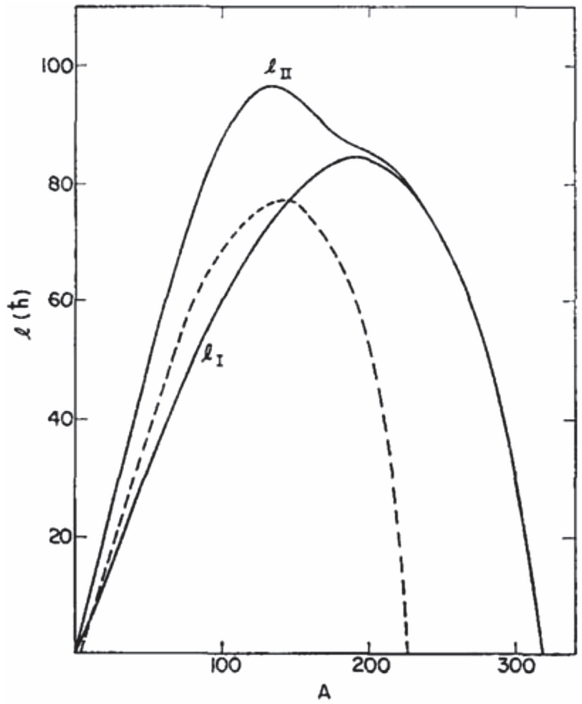

Figure 57. Maximum angular momentum that a nucleus can withstand calculated using the liquid drop model. The l_{II} line corresponds to the maximum angular momentum of a rotating liquid drop as a function of the mass A. The region between the l_I and l_{II} lines corresponds to triaxial shapes. The dashed line corresponds to a fission barrier of 8 MeV. Reprinted from [92], Copyright 1974, with permission from Elsevier.

From figure 55, it can be seen that for $E_{\text{beam}} = 219$ MeV, the $E_{1/2}(I)$ points fall inside the region $E_{\max}$ (delimited by dotted blue lines), corresponding to the maximum possible excitation energy transferred to the residual nucleus during the fusion-evaporation process, which biases the result without a proper data modelling. In the first experiment of Reiter *et al* [301] the measurements were made at $E_{\text{beam}} = 215$ and 219 MeV, which did not allow to fully map the entry distribution above the saddle energy. Consequently, only a lower limit of the fission barrier ($B_f > 6$ MeV) could be obtained.

The fission barrier deduced by Henning *et al* represents an important benchmark for theory. Theoretical predictions for the fission barrier in ^{254}No indeed span from 6 to 12 MeV [299, 352, 353, 404, 411–415].

A recurrent discussion concerns the maximum angular momentum that can be withstood by a rotating nucleus in the No mass region. From macroscopic considerations, the potential energy as a function of deformation β and angular momentum I writes:

$$E(\beta, I) = E(\beta, 0) + \frac{\hbar^2}{2\mathcal{J}(\beta)} I(I+1). \tag{38}$$

For a rigid body, the moment of inertia can be written as:

$$\mathcal{J}(\beta) \approx \mathcal{J}_{\text{sphere}}(1 + 0.3\ \beta), \tag{39}$$

with $\mathcal{J}_{\text{sphere}} = \frac{2}{5}\ A^{5/3}\ M\ r_o^2$.

The evolution of the fission barrier as a function of the angular momentum writes:

$$\begin{aligned} B_f(I) &= E(\beta_{\text{saddle}}, I) - E(\beta_{\text{yrast}}, I) \\ &= B_f(0) + \hbar^2 I(I+1)\left(\frac{1}{2\mathcal{J}_{\text{saddle}}} - \frac{1}{2\mathcal{J}_{\text{yrast}}}\right) \\ &= B_f(0) + \hbar^2 I(I+1)\frac{1}{2\mathcal{J}_{\text{sphere}}}\left(\frac{1}{1 + 0.3\ \beta_{\text{saddle}}}\right. \\ &\quad \left. - \frac{1}{1 + 0.3\ \beta_{\text{yrast}}}\right) \\ &= B_f(0) + \frac{\hbar^2}{2} I(I+1)\ \frac{2}{5} A^{-5/3}\ \frac{1}{M}\ \frac{1}{r_o^2} \\ &\quad \left(\frac{1}{1 + 0.3\ \beta_{\text{saddle}}} - \frac{1}{1 + 0.3\ \beta_{\text{yrast}}}\right). \end{aligned}$$

From the A dependence, it turns out that the heavier a nucleus is, the less the fission barrier $B_f(I)$ is sensitive to the rotation. In other words, for the same static fission barrier, a heavier nucleus can be cranked to higher spins as compared to a lighter nucleus before the fission barrier vanishes. This apparent contradiction is however largely compensated by a decrease of the fission barrier with the fissility parameter x. The full macroscopic treatment is presented in the seminal paper of Cohen *et al* [92]. Figure 57 taken from this paper shows that nuclei with $A \approx 250$ can rotate up to $I \approx 70\hbar$ before the fission barrier vanishes. However, fission will compete with γ-ray de-excitation when lifetimes of the collective states will be at the ps level, i.e. at lowest angular momenta.

Microscopic calculations by Duguet *et al* using Skyrme forces [353] and by Egido and Robledo using the D1S Gogny force [352] confirm that the fission barrier survives up to very high angular momenta, see figure 58 taken from [352]. At $I = 60\hbar$, the barrier height is still ≈2 MeV.

The maximum angular momentum observed in fusion-evaporation reactions is much lower than the value expected from the inspection of fission barriers. The limitation observed actually results mainly from the fusion-evaporation process, not from the structure of the nucleus. For the reaction ^{48}Ca+^{208}Pb at 220 MeV, the excitation energy of the compound nucleus is ≈24 MeV and its critical angular momentum calculated using the Bass barrier parametrization from [416, 417] is ≈53ħ, which is already below the maximum angular momentum for which the fission barrier vanishes as shown in figure 57. At $E^* = 24$ MeV, the nucleus has an extremely high probability to fission since this energy is well above the fission barrier. During the cooling process leading to the residual nucleus ^{254}No, only nuclei with the lowest angular momentum have a chance to survive, as shown by the entry distribution measurement and statistical model calculations performed by Henning [418] using the Kewpie2 [419] or NRV models [420]. These calculations show that the final spin distribution is not correlated with the fission barrier of the residual nucleus. Similarly, the study of the population of g.s. bands using the statistical model and quantum diffusion approaches reproduce well the experimental

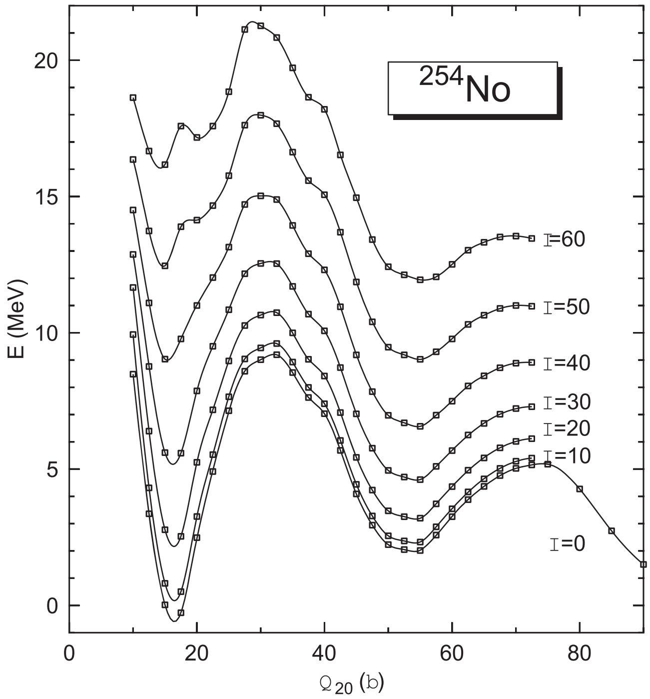

Figure 58. Fission barrier, calculated with a HFB model and the D1S force, as the function of the angular momentum. Reprinted figure with permission from [352], Copyright (2000) by the American Physical Society.

intensity distributions for the g.s. bands of ^{250}Fm and ^{252,254}No [421], the main dependence being due to the capture cross section of the compound nucleus and the survival probability, and not due to the angular momentum dependence of the fission barrier.

Similar arguments can be given for Coulomb excitation experiments. In the Coulex of ^{248}Cm using a ^{208}Pb beam at 5.3 MeV/A, states up to 30^+ (tentatively 32^+) were observed as shown in figure 46 [329]. Calculations using the GOSIA code [422, 423] and taking into account the experimental conditions, show that the measured intensity profile can be entirely correlated with a drop of the Coulex cross section at spin $\approx 30\hbar$ [424]. This shows again that the limit of angular momentum due to fission is not yet reached at $I \approx 30\hbar$, in agreement with the predictions of the liquid drop model and macroscopic calculations.

Odd nuclei

In comparison to even–even isotopes, the experimental spectra of odd nuclei are more complex due to the presence of several single-particle states at low excitation energy, on top of which rotational bands can built up; therefore the flux of de-excitation transitions is more fragmented. In consequence, the spectroscopy of odd isotopes requires more statistics, γ–γ coincidences to unravel the complex spectra and ideally CE spectroscopy to extract the $\Delta I = 1$ transitions connecting the signature partners. Prompt spectroscopy has been performed so far for only 3 isotopes in the $Z \geqslant 100$ region: ^{251}Md, ^{253}No and ^{255}Lr.

The prompt spectroscopy of ^{253}No was first performed by Reiter *et al* [425] at ANL using GAMMASPHERE, FMA and the fusion-evaporation reaction ^{207}Pb(^{48}Ca, 2*n*)^{253}No with a cross section of ≈500 nb. The spectrum features γ-ray lines forming two characteristic signature partner bands de-exciting by *E*2 transitions, but without evidence for interband $\Delta I = 1$ transitions. From decay spectroscopy, it has been established that the g.s. corresponds to the $\pi 9/2^-[734]$ Nilsson orbital, and that the first excited states at 124 and 379 keV correspond to the Nilsson orbitals $\pi 5/2^+[622]$ and $\pi 7/2^+[624]$, respectively [426]. The gyromagnetic factors g_K of these 3 orbitals are equal to −0.24, −0.38 and +0.28, respectively. In the two first cases strong *M*1 transitions are expected, since the $|g_K - g_R|$ value is large. The absence of *M*1 transitions in the experimental data [425] was therefore interpreted as evidence for the $\pi 7/2^+[624]$ configuration (small $|g_K - g_R|$ value) as the band-head.

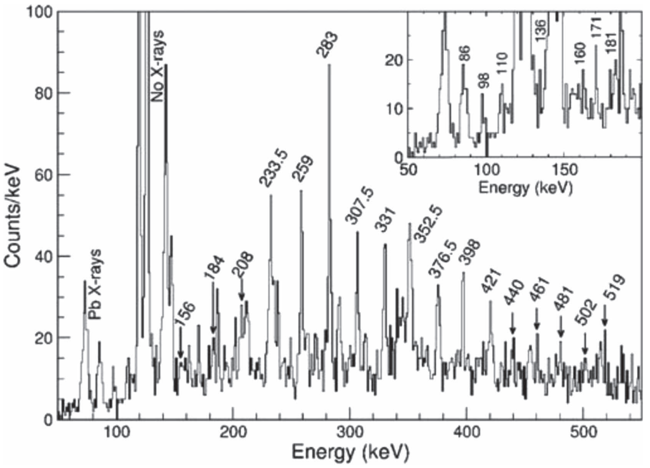

Figure 59. Prompt γ-ray spectrum of ^{253}No. *E*2 transitions are marked in the main panel, while *M*1 transitions are marked in the inset. Figure taken from [379](2009).© SIF, Springer-Verlag Berlin Heidelberg, 2009. With permission of Springer. Original Caption: 'Gamma-ray spectrum of ^{253}No obtained with JUROGAM. The low-lying *M1* transitions linking the two signature partners are clearly visible (see inset).'

In the same period, an electron spectroscopy measurement of ^{253}No was performed using SACRED and RITU [427]. The resulting spectrum did not provide a clear evidence for discrete lines, however, simulations of de-excitation of the rotational band gave a strong support to the $\pi 9/2^-[734]$ g.s. assignment, in contradiction to the interpretation of [425]. The doubts were removed in a subsequent experiment performed at JYFL in 2005, in which $\Delta I = 1$ transitions linking the signature partners were observed [379], see figure 59. The intensity ratio $I(\Delta I = 1)/I(E2)$ was only compatible with a $\pi 9/2^-[734]$ g.s. assignment. This has been confirmed additionally in decay experiments performed more recently at SHIP, that demonstrated that the low-spin part of the rotational band is fed by de-excitation of an isomeric state [310]. Very recently, the combined prompt γ-ray and conversion-electron spectroscopy has been performed at the University of Jyväskylä using SAGE coupled to RITU. The internal conversion coefficient has been deduced for several intraband and interband transitions, from which the configuration based on the $\pi 9/2^-[734]$ orbital was firmly demonstrated [382]. As an example, a prompt tagged electron

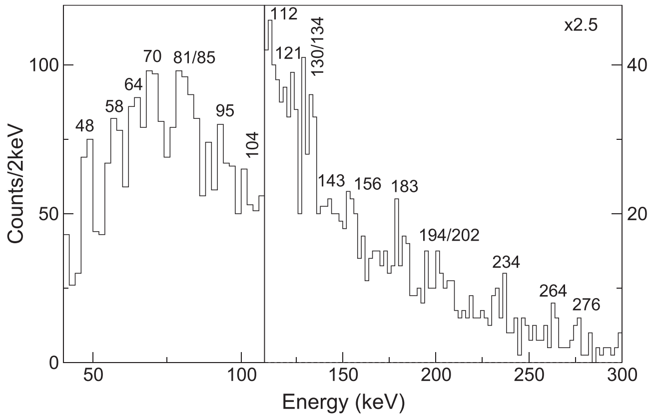

Figure 60. Prompt conversion-electron spectrum of ^{253}No. Reproduced from [382]. CC BY 4.0.

spectrum is shown in figure 60. ^{253}No is the only odd-neutron $Z \geqslant 100$ isotope studied so far using prompt spectroscopy.

The proton-odd transfermium nuclei ^{251}Md and ^{255}Lr were investigated using prompt γ-ray spectroscopy at JYFL. ^{251}Md was studied in 2003 using Jurogam, RITU and the fusion-evaporation reaction ^{205}Tl(^{48}Ca, $2n$)^{251}Md with a cross section of $\approx$1 μb [428]. Since the single recoil-gated γ-ray spectrum displays a plethora of peaks, from which regularly spaced transitions do not clearly emerge, γ–γ coincidences were essential to construct the collective sequence. A single rotational band without evidence for its signature partner was found, which is characteristic for a $K = 1/2$ configuration. Decay spectroscopy studies show that there is a $K = 1/2$ state at 55 keV, corresponding to the $\pi 1/2^{-}[521]$ orbital, while the g.s. is based on the $\pi 7/2^{-}[514]$ configuration [275, 429]. The experiment was repeated in 2012 using SAGE and brought evidence for a rotational band based on the g.s. [430]. Because the favored signature partner of the $K = 1/2$ band concentrates the vast majority of the de-excitation flux, the peak intensities turn out to be larger than those of the $K = 7/2^{-}$ g.s. band, which flux is spread over the two signature partners. The electron spectroscopy was first attempted in 2002 with SACRED [431] without any conclusive results. In contrast, the 2012 SAGE experiment provides meaningful information [430] first partially reported in [432].

The spectroscopy of ^{255}Lr was part of the early prompt γ-ray spectroscopy program at JYFL, included with ^{254}No in the same the SARI-JUROSPHERE-RITU proposal. The first attempt was made with JUROSPHERE in 1999, using the fusion-evaporation reaction ^{209}Bi(^{48}Ca, $2n$)^{255}Lr ($\sigma \approx 300$ nb), but only x-rays could be observed, indicating strong internal conversion. The experiment was repeated in 2005 using RITU and the JUROGAM array [433]. As for ^{251}Md, no rotational band could be unambiguously constructed using single γ-ray spectra, nor were γ–γ statistics large enough to clearly disentangle the de-excitation sequences. Advantage was therefore taken of the characteristic α-decay of ^{255}Lr. It was previously established that ^{255}Lr decays mainly via two α branches: either from the $1/2^{-}$ g.s. to the $1/2^{-}$ first excited state of ^{251}Md, or from the $7/2^{-}$ isomeric state at 37 keV to the g.s. of ^{251}Md [275] (see also figure 41 and discussion in section 2.5.1). Tagging the γ-ray spectrum separately by each of these decay channels therefore highlights either the band based on $\pi 1/2^{-}[521]$ or that built on the $\pi 7/2^{-}[514]$ band head, as shown in figure 61.

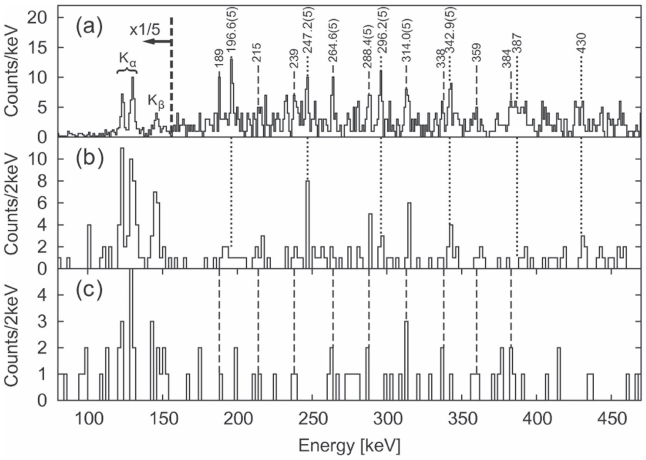

Figure 61. Prompt γ-ray spectra of ^{255}Lr. (a): RT spectrum. (b), (c): RDT spectra tagged by αs emitted from the $1/2^{-}$ and $7/2^{-}$ states, respectively. Reprinted figure with permission from [433], Copyright 2009 by the American Physical Society.

The $K = 1/2$ band is very similar to that of ^{251}Md with only the favored signature band observed, while the band resulting from tagging by the α-decay from $K = 7/2^{-}$ displays two signature partners. It should be noted that a gyromagnetic factor $g_K \approx 0.7$ is predicted for the $\pi 7/2^{-}[514]$ configuration, corresponding to a low $|g_K - g_R|$ value and consequently low intensity of $\Delta I = 1$ transitions; this is consistent with the experimental spectrum. The opposite is expected for the $\pi 7/2^{+}[633]$ configuration ($g_K \approx 1.3$). Additionally, low-spin members of a rotational band based on the $\pi 9/2^{+}[624]$ and $\pi 1/2^{-}[521] \otimes 7/2^{-}[514] \otimes 9/2^{+}[624]$ configurations were found in α-decay studies [434]. The assignment has been made by comparing $I(\Delta I = 1)/I(E2)$ intensity ratios to model predictions.

^{255}Lr was again investigated in 2012, using prompt γ-ray and electron spectroscopy with SAGE. New transitions, complementing the highly-converted low-spin transitions in the $K = 1/2^{-}$ bands have been observed [435, 436]. This experiment shows that a combined prompt γ and conversion-electron spectroscopy is feasible down to the $\approx$300 nb level in an odd isotope.

High-K rotational bands

Rotational bands based on two-quasi-particle states in even–even nuclei have features similar to rotational bands in odd nuclei: as a result of $K \neq 0$, the collective structure consists of two signature partner bands connected by $\Delta I = 1$ interband transitions of intensity depending on the magnetic moment (or gyromagnetic factor). They therefore carry information on single-particle states and their influence on collectivity, while such effects are smoothed in the g.s. band because pairing correlations strongly mix the configurations. As discussed in section 2.5.2 high K values can be generated by 2qp excitations. These 2qp states are more robust with respect to rotation than g.s. rotational bands. Because of the blocking, pairing correlations are less pronounced, therefore the moment of inertia is larger and more stable with respect to the rotational frequency. The created isomeric states provide at the focal plane a strong experimental signal that is extremely valuable to tag the rotational bands built on the 2qp configuration.

When rotational states, built on a high-K isomeric state are studied, the technique is known as recoil isomer tagging, as depicted in figure 47. Selecting high-K bands from γ^n coincidences only would require high statistics and is beyond reach in transfermium isotopes. Even in the lightest actinide studies using inelastic scattering and GAMMASPHERE, it has been possible to establish a rotational band built on 2qp excitations only in ^{244}Pu [437]. High-K isomeric states were first observed in ^{250}Fm and ^{254}No by Ghiorso *et al* in the 1970s [438, 439]. It is only ≈40 years later that a detailed level scheme has been established in ^{254}No using decay spectroscopy at JYFL [283] and ANL [284] (see also section. 2.5.2). However, no rotational band built on the $K^\pi = 8^-$ isomer could be observed so far, which is not yet fully understood. In subsequent experiments performed at JYFL, rotational bands built on $K^\pi = 8^-$ isomeric states could be observed in ^{250}Fm [291] and ^{252}No [440]. The decay of the isomer was deduced from the decay spectroscopy performed jointly with the prompt γ-ray measurement. The spin and parity of the isomer were deduced from the level scheme, shown in figure 62 for ^{250}Fm. However, this is not sufficient to establish its exact configuration. There are two likely possibilities to build a $K^\pi = 8^-$ state in the $A = 250$ mass region: either a $\pi 7/2^-[514] \otimes 9/2^+[624]$ or a $\nu 7/2^+[613] \otimes 9/2^-[734]$ excitation. A firmer assignment can be made from the electromagnetic properties of collective transitions, in a similar manner as in odd nuclei.

In the case of 2qp states, the gyromagnetic factor can be approximated by the sum of gyromagnetic factors of the two particles. According to the Gallagher–Moszkowski rule [441], coupling of particles with anti-parallel spins is favored, which is the case for the proposed $K^\pi = 8^-$ neutron or proton configurations. In this case, the spin gyromagnetic factor cancels, the remaining part being $g_K = \frac{1}{K}(g_l(\Lambda_1 + \Lambda_2)) = g_l$, equal to 1 for protons and 0 for neutrons. The analysis of $I(\Delta I = 1)/I(E2)$ intensity ratios clearly favors a neutron 2qp configuration for ^{250}Fm and ^{252}No. The 2qp states, as well as the behavior of rotational bands built on these isomeric states, will be discussed in section 3.7.

Figure 63 summarizes the status of high-spin spectroscopy in the Cm–Rf region. The structure of nuclei in this region will be discussed in the next paragraphs.

3.6. Deformation and deformed shell gaps

In the absence of direct measurements of nuclear deformation or electric quadrupole moments, it is possible to estimate these quantities from the 2^+ excitation energy in even–even nuclei with a rather good accuracy, as will be discussed below. However, the $2^+ \rightarrow 0^+$ transitions in heavy nuclei cannot be measured using γ-ray spectroscopy because of their high internal conversion probability. Even with electron spectroscopy, the low energy nature of these transitions results in challenging conditions to extract meaningful information. For a 45 keV $E2$ transition, most of the conversion involves the L shell, leading to electron energies of ≈20 keV, still challenging to be detected in in-beam experiments. The 2^+ energy has to be therefore deduced from extrapolations, the most common being based on the 'Harris' parametrization [442]. In this technique, the $\mathcal{J}^{(1)}$ kinematic and $\mathcal{J}^{(2)}$ dynamic moments of inertia are fitted using:

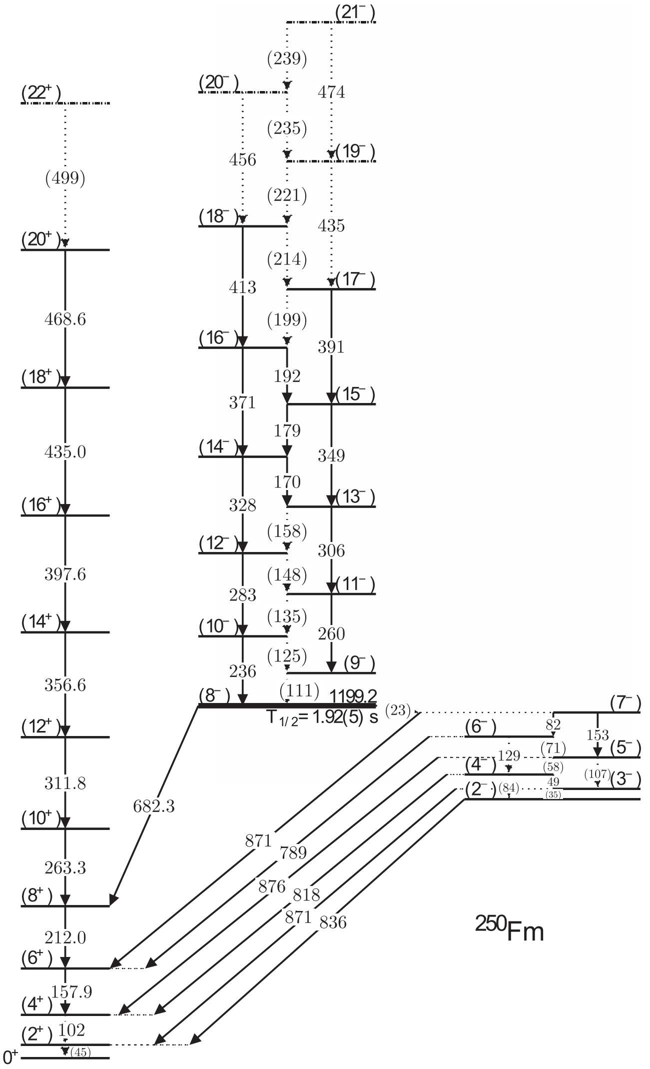

Figure 62. Level scheme of ^{250}Fm from combined prompt and decay spectroscopy. The rotational band built on the $K^\pi = 8^-$ isomeric state has been observed via tagging on the highly converted delayed transitions corresponding to the $K^\pi = 2^-$ structure shown on the right. Reprinted figure with permission from [291], Copyright (2008) by the American Physical Society.

$$\mathcal{J}^{(1)} = \mathcal{J}_0 + \mathcal{J}_1\omega^2, \tag{40}$$

$$\mathcal{J}^{(2)} = \mathcal{J}_0 + 3\mathcal{J}_1\omega^2. \tag{41}$$

As soon as the $\mathcal{J}_0$ and $\mathcal{J}_1$ parameters are obtained, it is possible to extrapolate the rotational frequencies of unobserved transitions using:

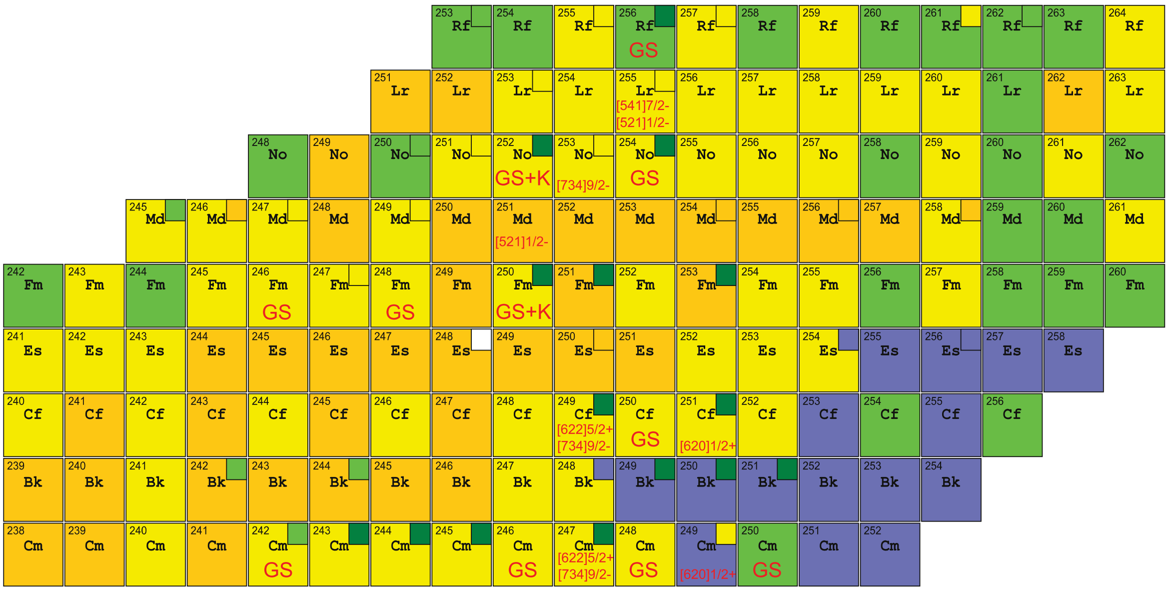

Figure 63. Sample of the nuclear chart in the Cm–Rf region showing the known high-spin rotational bands. In even–even nuclei, g.s. bands are labeled GS, while *K* refers to high-*K* rotational bands. For odd nuclei, the Nilsson configuration of the band head is given. References are provided in the text.

$$I = \mathcal{J}_0\omega + \mathcal{J}_0\omega^3 + 1/2, \tag{42}$$

where I is the initial spin of the transition. This formula is restricted to the case of g.s. bands of even–even nuclei, namely $K = 0$, and no initial alignment. The 'Harris' procedure in a more general form is sometimes used to deduce spins in rotational bands, e.g. in odd nuclei or in superdeformed bands, but it has been shown that the solution does not have to be unique, which may result in a wrong spin assignment [443].

An alternative to the 'Harris' fit is to use the 'ab' parametrization [444]:

$$E(I) = a[\sqrt{1 + b(I + 1)} - 1]. \tag{43}$$

As soon as the $E(2^+)$ energy is deduced, it is possible to estimate the lifetime of the corresponding 2^+ state using the 'Grodzin' estimate [445]. Grodzin made a fit of the known lifetimes as a function of the 2^+ energy and obtained the following relation:

$$\tau_\gamma = (2.74 \pm 0.91)\ 10^{14}\ E^{-4}\ Z^{-2}\ A\ (\text{ps}), \tag{44}$$

where E is expressed in keV.

There is no straightforward (if any) justification of this parametrization. As pointed out by Grodzin, the irrotational flow model of Bohr and Mottelson leads to a different dependence on A, as demonstrated in the following: the transition probability $T(E2)$ is proportional to $E^5\ B(E2)$ (25), while $B(E2)$ is proportional to Q_{20}^2 (23) and Q_{20}^2 is proportional to $ZR_0^2\ \beta$ to first order (34). Therefore $T(E2) \propto E^5\ Z^2\ R_0^4\ \beta^2$. From the irrotational flow model (see [69] p 406), the moment of inertia of an irrotational fluid is: $\mathcal{J}_{\text{irrot}} = 2/5\ A\ R_0^2\ \beta^2$. Using $E = \frac{\hbar^2}{2\mathcal{J}_{\text{irrot}}} I(I + 1)$, one obtains:

$$T(E2) \propto \frac{1}{\mathcal{J}_{\text{irrot}}}\ E^4\ Z^2\ R_0^4\ \beta^2, \tag{45}$$

$$\propto E^4\ Z^2\ A^{-1/3}, \tag{46}$$

which differs from (44) in the A exponent.

After Grodzin's study, another fit of the $E(2^+)$ energies has been performed by Raman *et al* with a larger set of data [318, 446], leading to a dependence of $E^{-4}\ \ Z^{-2}\ \ A^{0.69}$, which is closer to (46). Another refinement of the fit was performed by Herzberg *et al* [302] and the following relation was obtained:

$$\tau_\gamma = (2.9 \pm 1.5)\ 10^{12}\ E^{-3.807\pm0.023}\ Z^{-2}\ A^{1.237\pm0.065}(\text{ps}) \tag{47}$$

(with E given in keV), the A exponent, being very far from what is given by the irrotational flow model. Raman *et al* [318] discussed the relevance of (44) and pointed out that since the energy has more weight in the fit than the mass, the A exponent is of no particular importance; see also the discussion in [447].

Using a local fit for $A > 200$ nuclei, another expression was suggested by Herzberg *et al* [302] that is more accurate, but only locally valid:

$$\ln(\tau Z^2) = 65.15 - 4.017\ln(E) - 5.23\ln(A), \tag{48}$$

with τ expressed in ps and E in keV.

Combining this relation, with (25) and (33), it is possible to estimate the electric quadrupole moment Q_{20}^2 from the $E(2^+)$ energy. Finally, it is also possible to infer the deformation using (34).

In the case of ^{254}No, an energy of 44 keV can be deduced from the 'Harris' fit. Then from (48) one obtains $\tau_\gamma = 1.25\times 10^5$ ps, and consequently $B(E2, 2^+ \to 0^+) = 3.95 \times 10^4\ e^2\ \text{fm}^4$, $Q_{20} = 1409\ e\text{fm}^2$ (14.09 eb) and $\beta = 0.29$.

These values can be compared to theoretical predictions. Using the SLy4 force, Duguet *et al* obtained a mass quadrupole moment of 32.8 b [353], which corresponds to an electric quadrupole moment of 1317 $e\mathrm{fm}^2$. Using the Gogny D1S force, Egido and Robledo [352] give an approximate value of 16 eb. Delaroche *et al* report, still with the D1S Gogny force [412], $B(E2, 2^+ \rightarrow 0^+) = 0.350\ 10^5\ e^2\mathrm{b}^2$ corresponding to $Q_{20} = 1326\ e\mathrm{fm}^2$. The calculations of Laftchiev *et al* [354] (HFB + SLy4), result in mass quadrupole moments which vary between 32.9 and 32.7 b along the rotational band ($Q_{20} = 1321 - 1313\ e\mathrm{fm}^2$). Theoretical calculations provide more frequently the β_2 deformation parameter assuming, however, different relations between the quadrupole moment and the β_2 deformation parameter, and not always that of (34). In some cases e.g. [412] the quadratic term in β_2 is omitted. From Zajac *et al* [355], the value $\beta_2 \approx 0.265$ is obtained, from Bender *et al* [448] (HFB + SLy4): $\beta_2 = 0.28$, and from Stone *et al* [449] (quark-Meson coupling model): $\beta_2 \approx 0.27$. In other cases, higher-order deformations are used: Ćwiok *et al* [160] (Woods–Saxon potential) give $\beta_2 = 0.252$, $\beta_4 = 0.014$ and $\beta_6 = -0.053$. Warda and Egido, [415] (HFB + Gogny D1S), give $\beta_2 = 0.334$, $\beta_4 = -0.017$, $\beta_6 = -0.028$, and Sobiczewski *et al*, [255] (Woods–Saxon potential), $\beta_2 = 0.252$, $\beta_4 = 0.013$, $\beta_6 = -0.054$, $\beta_8 = 0.007$, etc. Comparison with models for a larger range of nuclei is moreover limited by the absence of systematic calculations.

The laser spectroscopy of odd nuclei provides, with the measurement of the hyperfine splitting, a nuclear-model independent value of the magnetic dipole and electric quadrupole moments. Such experiments are being made at GSI using the RADRIS technique at SHIP, in particular for ^{253}No [450]. Since the deformation of this odd nucleus is expected to be similar compared to its even–even neighbors, this will provide an important benchmark in the $N = 152$, $Z = 100$ region.

Thus discussions of systematics from both experimental and theoretical points of view are frequently done in a model-independent way using simply the $E(2^+)$ energy, or the Harris parameter $\mathcal{J}_0$, which can be approximated to $\mathcal{J}_0 \approx 3\hbar^2/E(2^+)$. These quantities have been discussed in the $N = 152$ region by Ishii *et al* [383] and later, using larger data sets, by Ketelhut [399], Theisen *et al* [432], Dobaczewski *et al*, [142]. Figure 64 taken from [432] shows the systematics of 2^+ states in even–even nuclei from Pu to Rf as a function of the neutron number and charge. The $E(2^+)$ energy displays a minimum at $N = 152$ for Fm $Z = 100$ isotopes and at $Z = 100$ for $N = 152$ isotones. The $N = 152$ minimum seems to be still present for No $Z = 102$ isotopes, although information for $^{256}_{102}\mathrm{No}^{154}$ is missing. However, the Cf chain only presents a slope change at $N = 152$. Similarly, it is not possible to draw any conclusions about a minimum at $Z = 100$ for the $N = 154$ chain. It is, however, clear that the $E(2^+)$ energy for the $N = 150$ isotones shows a minimum at $Z = 98$, not $Z = 100$.

Magic spherical or deformed shell gaps can be inferred from inspection of Q_α, proton or neutron separation energies, see e.g. [451] and graphs p 1851, 1834, 1842 in the 2012 atomic mass evaluation [153]. For magic nuclei, Q_α displays a minimum, while the slope of isotopic (isotonic) S_{2n} (S_{2p}) changes. To magnify this effect, it is possible to use the derivative δ_{2n} (δ_{2p}) of the neutron (proton) separation energies S_{2n} (S_{2p}), see e.g. [432].

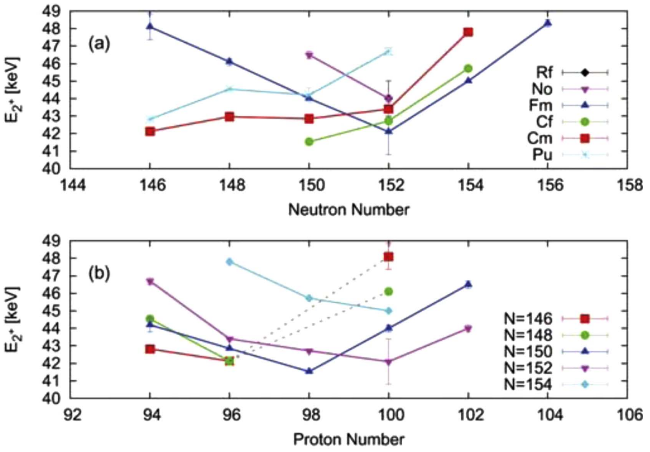

Figure 64. Systematics of $E(2^+)$ energies in the Pu–Rf region as a function of the neutron (top) and proton number (bottom). Reprinted from [432], Copyright 2015, with permission from Elsevier.

Another clear signature comes from inspection of the spontaneous fission lifetime [89] which is directly related to the fission barrier height and therefore to the magnitude of shell effects, see figure 13. All the above-mentioned quantities corroborate $N = 152$, $Z = 100$ as a magic deformed number. Systematics of spontaneous fission lifetimes shows a maximum at $N = 152$ for Fm and No isotopes, which is shifted to $N = 150$ for Cf isotopes. δ_{2n} (Q_α) exhibit a maximum (minimum) at $N = 152$ for all isotopic chains from Cm to No. No conclusions can be drawn for $Z < 96$ and $Z > 102$, as data is still missing for these nuclei.

Similarly, δ_{2p} values display a maximum at $Z = 100$ for $N = 152$ isotones. In the same way as $E(2^+)$ energies show a minimum at $Z = 98$ for $N = 150$ isotones, the same is found for δ_{2p}. As discussed in [142, 432], there is no explanation why the Cf isotopes represent an exception from this rule.

Magic numbers are associated to energy gaps, which in particular are visible in Nilsson diagrams. The presence of these energy gaps lowers the pairing correlations, resulting in an increase of the moments of inertia and reduction of the $E(2^+)$ energies. Microscopic–macroscopic models are known to reproduce well the $N = 152$, $Z = 100$ deformed gap. Calculations using the Woods–Saxon potential by Sobiczewski *et al* [255] indeed reproduce rather well the trend of $E(2^+)$ energies discussed above (see figure 34 and the discussion in [399]) with, however, the exception of the minimum at $Z = 98$ for $N = 150$ isotones.

In contrast, models based on EDFs systematically fail to reproduce the ^{252}Fm magicity and the $E(2^+)$ trend. As discussed by Dobaczewski *et al* [142], calculations based on the SLy4, UNEDF2, D1S, D1M or NL1 EDFs favour gaps at $Z = 98$, $Z = 104$, $N = 150$ and/or $N = 152$, while NL3* force favors gaps at $Z = 102$, $N = 148$. These gaps are clearly visible in the Nilsson diagrams calculated with these forces, as shown in figures 1–3 of [142], and induce corresponding maxima in the kinematic moment of inertia $\mathcal{J}^{(1)}$ or δ_{2n} and δ_{2p} plots: see figures 11–14 of [142].

The problem of the reproduction of the deformed magic numbers $N = 152$, $Z = 100$ and related observables is a key issue for EDF-based calculations (see e.g. [129, 143, 452]) and subject of several on-going studies. Attempts to find better EDF parametrizations have been undertaken by e.g. Kortelainen *et al* [453, 454], Yue Shi *et al* [455], Bender and Heenen [452], but with no current success, which may suggest that the current generation of EDFs has reached their limits. As discussed in section 4.1, the current trend is to include beyond-mean-field effects, such as particle-vibration coupling, which has been shown to improve the single-particle spectra: see e.g. [166, 456–458]. For a detailed discussion we refer to [142] and references therein.

On the other hand, the fact that microscopic–macroscopic models reproduce better the experimental results may be understood as being due to the adjustments of their parameters to specific regions (as has been done e.g. by Chasman *et al* [158, 159]), which may implicitly mimic beyond-mean-field effects.

3.7. Evolution of moments of inertia, alignment and pairing

Even–even nuclei

While the $E(2^+)$ energy or the $\mathcal{J}_0$ Harris parameter (moment of inertia in absence of rotation) provide information on the pairing correlations and deformed shell gaps, the behavior of rotational bands as a function of the angular momentum can provide more subtle information on pairing, occupancy of specific orbitals, and their position with respect to the Fermi level, and possibly other degrees of freedom like octupole correlations.

In the limit of a perfect rigid rotor, rotation would be a fully collective motion. Pairing correlations are in contradiction with this concept. Nucleons forming a pair have their angular momenta pointing in opposite directions, hence in a classic view they are rotating in opposite directions. Indeed, one of the paired nucleons (that with angular momentum pointing in a direction opposite to the rotation) counteracts the collective motion. In 1960, Mottelson and Valatin [459] predicted a transition phase from superfluid (all nucleons paired) to a normal-fluid phase, when pairs break under the effect of rotation. This can be viewed classically as the effect of the Coriolis force aligning the nucleon angular momenta along the rotation axis. The nuclear fluidity analogy is actually not entirely appropriate, since pairing is essentially active for nucleons around the Fermi level (or at the surface of the nucleus, to use another analogy).

The breaking of pairs under the effect of rotation has been confirmed experimentally in the early 1970s in the rare-earth region by Johnson *et al* in ^{160}Dy and neighboring ^{158}Dy and ^{162}Er [460, 461] at Stockholm (see also the contribution of Riley, Simpson and Paul in this focus issue [358]). This phenomenon was discussed by Stephens and Simon [462] as the alignment of a few nucleon pairs. The alignment can be seen as the crossing of the g.s. band with a 2qp band, having a pair aligned (sometimes referred to as an S band, 'superband' or 'Stockholm'). The crossing is possible, since the 2qp band is more collective and therefore has a larger moment of inertia but higher excitation energy at low spin, as shown in figure 65. The crossing therefore results in a rise of the moment of inertia, or alignment with respect to a smooth rotor behavior. When the alignment occurs rapidly, the moment of inertia (and alignment) plotted as a function of the rotational frequency displays a step backward curve.

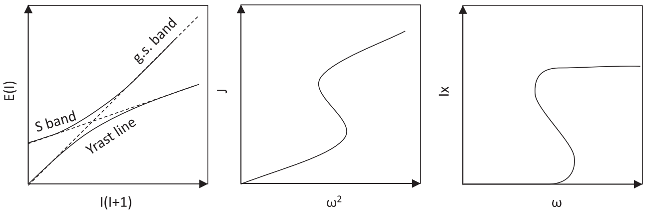

Figure 65. Illustration of the backbending phenomenon and its experimental manifestations.

A backbending is a manifestation of an important rearrangement of the nuclear structure, which provides rich information on pairing correlations and their evolution with rotation, and on the presence of specific orbitals. In fact, the pairs which are most subject to alignment are those with the highest orbital momentum j and low K (by analogy with the Coriolis force). In the rare-earth region, backbending is mostly related to the alignment of $\nu i_{13/2}$ orbitals, see the discussion by Bengtsson and Frauendorf in [463].

In the early 1980s, spectroscopy of actinide nuclei up to ^{248}Cm has been made possible by accelerator and detection advances. A rise of the moment of inertia was observed in e.g. ^{248}Cm [329] and discussed by Diebel and Mosel using cranked HFB calculations as an alignment of the $\pi i_{13/2}$ or $\nu j_{15/2}$ orbitals [464]. The question of possible backbending in the actinides naturally arises. Using the CSM, Egido and Ring predicted backbending in ^{238}U and ^{248}Cm at $I \approx 30\hbar$ due to the sudden alignment of $j_{15/2}$ neutrons [465]. From Woods–Saxon calculations, Dudek *et al* suggested backbending in the neutron deficient ^{224}Th and ^{222}Ra, with competing $\pi i_{13/2}$ and $\nu j_{15/2}$ alignments [466]. Finally, the first experimental observation of backbending in the actinide region was reported by Spreng *et al* in ^{244}Pu [328], not precisely where previously predicted.

The evolution of the moment of inertia of rotational bands subsequently observed in the transuranium region is explained by invoking the high-j orbitals $\pi i_{13/2}$ or $\nu j_{15/2}$ in a large number of publications, see [143, 264, 302, 328, 329, 352, 353, 390, 391, 393, 394, 412, 448, 455, 467–475], etc.

The $\pi i_{13/2}$ and $\nu j_{15/2}$ orbitals are of special interest not only because of their interplay with pairing and rotation dynamics, but also because their position at sphericity is especially poorly predicted by EDF-based calculations. As pointed out by Dobaczewski *et al* [142], the position of the $\nu j_{15/2}$ orbital changes by almost 2 MeV between calculations based on the SLy4 and the UNEDF2 force. While the position of the $\nu j_{15/2}$ orbital has consequences for the predictions of deformed nuclei in the $A \approx 250$ mass region, the position of the $\pi i_{13/2}$ orbital also impacts the possible opening of the presumed $Z = 114$ shell gap.

Experimental studies of the alignment/backbending and their relation to the $\pi i_{13/2}$, $\nu j_{15/2}$ orbitals are therefore highly instructive. The underlying problem is complex, being not only a matter of pairing and shell structure, but also of the interplay between them, as soon as the nucleus rotates. For example, the alignment frequency depends on the magnitude of pairing correlations which tend to delay the alignment. Pairing correlations are themselves related to the magnitude of shell gaps which in turn depend on the position of specific orbitals which may align more or less as a function of their orbital momentum j and projection K. Figure 66 taken from [476] is a survey of rotational bands in even–even transuranium isotopes. A sharp alignment or backbending is clearly present in ^{242,244}Pu, ^{246,250}Cm and ^{250}Cf. It is not observed in $N < 146$ isotopes, but high-spin data are missing in $Z \geqslant 100$ isotopes to draw conclusions. From the survey, it is not possible to identify systematic trends. As an example, ^{248}Cm ($N = 152$, $Z = 98$) does not display backbending, while ^{250}Cf with $N = 152$ and ^{246}Cm ($Z = 96$) do exhibit the phenomenon. Moreover, backbending predicted in Th, U and light Pu isotopes, here in the case of NL3* EDF, is systematically not observed.

Inspection of the experimental alignment can provide arguments in favor of proton or neutron alignment since its magnitude is different for $\pi i_{13/2}$ or $\nu j_{15/2}$ pairs, as discussed in [467]. Other studies do not use this argument, or are more evasive in that respect. One could indeed express some concerns about the relevance of inspecting the magnitude of the alignment in that particular context if, as predicted by a large number of calculations, protons and neutrons align at a similar frequency.

It is nonetheless possible to establish trends in the theoretical interpretation of observed backbending in $Z \leqslant 98$ nuclei: there is a common agreement that it is mostly due to the $\pi i_{13/2}$ orbital. While alignment of $\nu j_{15/2}$ is most often predicted at the same frequency, it is more sharp, see e.g. [264, 391, 470, 471].

The non-observation of alignment in e.g. Th, U and light Pu isotopes has been interpreted as being due to the presence of octupole correlations which delay the alignment to higher frequencies. More precisely, stable octupole deformation is proposed to be present at high spin in $^{238-240}$Pu [467]. As discussed in [477], these correlations delay the alignment. An alternative interpretation invokes octupole phonon condensation [390], as proposed in [477].

In heavier nuclei the picture is more complex and debated, because of the competition between the $\pi i_{13/2}$ and $\nu j_{15/2}$ alignment, and because rotational bands populated after fusion-evaporation reactions are observed up to rotational frequencies that are slightly lower as compared to those reached in Coulex and inelastic scattering. Therefore upbending/backbending may occur above experimental limits. In the Fm–Rf region, one has to look for more subtle effects in the evolution of moments of inertia, still below the possible alignment.

The upper panel of figure 67 (taken from [167]) shows the moment of inertia $\mathcal{J}^{(1)}$ for the $N = 150$ isotones ^{250}Fm and ^{252}No and $N = 152$ ^{254}No and ^{256}Rf. As discussed above, the magnitude of $\mathcal{J}^{(1)}$ at low frequency can be related to the magicity at $N = 152$, $Z = 100$. At $Z = 100$, ^{250}Fm has the highest $\mathcal{J}^{(1)}$ followed by the $N = 152$ isotones ^{254}No and ^{256}Rf. ^{252}No, with no deformed magic nucleon number, and therefore reduced pairing correlations, has the lowest $\mathcal{J}^{(1)}$. The evolution of $\mathcal{J}^{(1)}$ as a function of the rotational frequency is related to both pairing correlations and possible alignment of high-j pairs. It can be seen in figure 67 that the lines corresponding to the evolution of $\mathcal{J}^{(1)}$ in $N = 150$ isotones on one hand, and in $N = 152$ on the other hand, are parallel. A convenient way to amplify the effect of alignment is to normalize the dynamic moment of inertia $\mathcal{J}^{(2)}$ to its smoothly behaving value resulting from the 'Harris fit', as shown in the lower panel of figure 67. It is possible to observe a rise of $\mathcal{J}^{(2)}$ for $N = 150$ isotones at $\hbar\omega \approx 0.15$ MeV, which is delayed to $\hbar\omega \approx 0.22$–0.25 MeV for the $N = 152$ isotones. As in lighter nuclei, the alignment can be discussed in terms of $\pi i_{13/2}$ or $\nu j_{15/2}$ pair alignment.

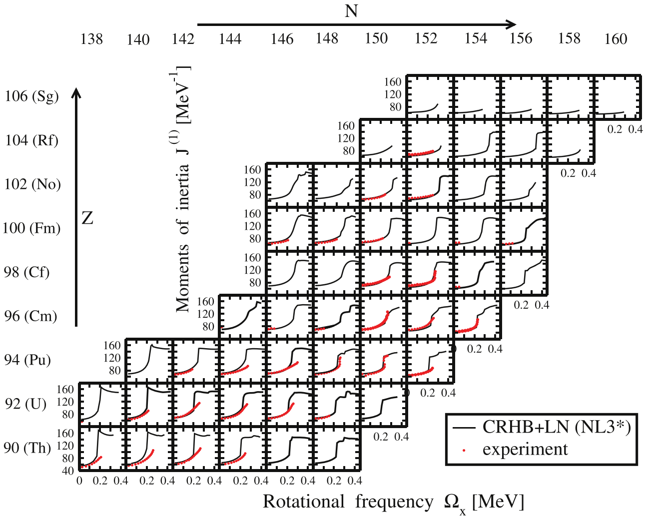

Figure 66. Kinematic moment of inertia of even–even Th–Sg nuclei. Experimental data (red dots) are compared with predictions of the relativistic mean-field model using the NL3* force (black lines). Reprinted from [476]. © IOP Publishing Ltd. All rights reserved.

Figure 68 shows the single-particle configurations for the four discussed isotopes. In the $N = 150$ isotones, the $\nu j_{15/2}$ $9/2^-[734]$ orbital is just above the Fermi surface, being therefore partially occupied. In the $N = 152$ isotones, this orbital is filled, but the deformed shell gap delays the neutron alignment in ^{254}No and ^{256}Rf, as compared to ^{250}Fm and ^{252}No. Additionally it is possible to break the $\pi i_{13/2}$ $7/2^+[633]$ pair, which is below the $Z = 100$ gap, therefore both neutrons and protons can contribute to the alignment. Furthermore, the $\pi i_{13/2}$ $9/2^+[624]$ orbital is near the Fermi surface only for Rf, which may explain the earlier alignment of ^{256}Rf as compared to ^{254}No. The question has been investigated in several theoretical studies, but no consensus has been reached yet, and some contradictions are present. From microscopic–macroscopic models [264, 468, 470, 472, 474], it becomes apparent that the $\pi i_{13/2}$ and $\nu j_{15/2}$ alignments compete for the four nuclei discussed here. EDF-

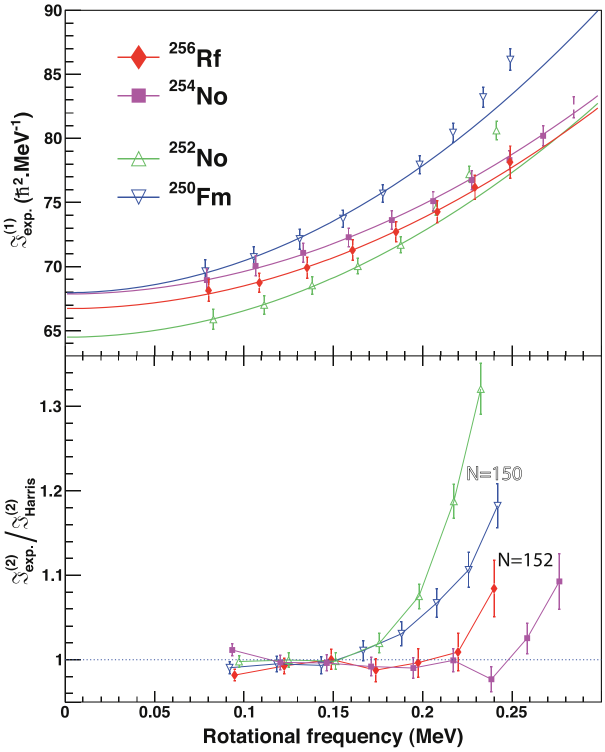

Figure 67. Top: kinematic moment of inertia of ^{250}Fm, ^{252,254}No, ^{256}Rf. In the bottom part, the dynamic moment of inertia normalized to that resulting from the 'Harris' fit is shown for the same nuclei. Reprinted figure with permission from [167], Copyright 2012 by the American Physical Society.

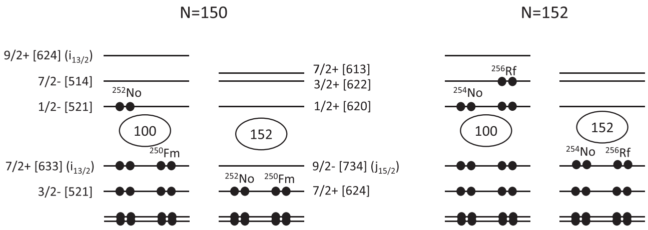

Figure 68. Schematic single-particle configurations of the ^{250}Fm, ^{252,254}No, ^{256}Rf nuclei. In each diagram, the protons (neutron) states are on the left (right).

based models also discuss the alignment in terms of competition between the same orbitals [143, 352, 353, 448, 473]. One might, however, ask, whether in this context discussing details of alignment of specific orbitals is relevant, while the predicted deformed shell gaps do not match the experimental evidence. Moreover, limitations of the cranking model in the crossing region may explain some discrepancies with experimental data and may require utilization of beyond mean-field techniques [476, 478].

Odd nuclei

While the situation is still puzzling in even–even nuclei, additional information can be obtained in odd nuclei. It is only recently that high-spin spectroscopy of odd nuclei has been performed in $N \approx 152$ isotopes using transfer reactions (^{245}Pu, ^{247,249}Cm, ^{249}Cf) or fusion-evaporation reactions. Figure 69 shows the kinematic moment of inertia in the $N \approx 152$ region from low up to high spin for the following nuclei with their respective population schemes and references: ^{245}Pu transfer reactions [385, 393]; ^{247}Cm transfer reactions [393, 479]; ^{249}Cf transfer [393] and α-decay [178]; ^{251}Fm α-decay [267]; ^{253}No fusion-evaporation [379]; ^{249}Cm transfer [387, 394, 479]; ^{251}Cf α-decay [480] and transfer [481]; ^{253}Fm α-decay [200] and electron capture [310]; ^{245}Am α and β-decay [482]; ^{247}Bk transfer, electron capture and α-decay [483–485]; ^{251}Md fusion-evaporation [428]; ^{249}Bk α and β-decay [179], transfer [486]; ^{251}Es electron capture and transfer [487]; ^{255}Lr fusion-evaporation [433]. Bands based on 3qp or higher excitations are not shown.

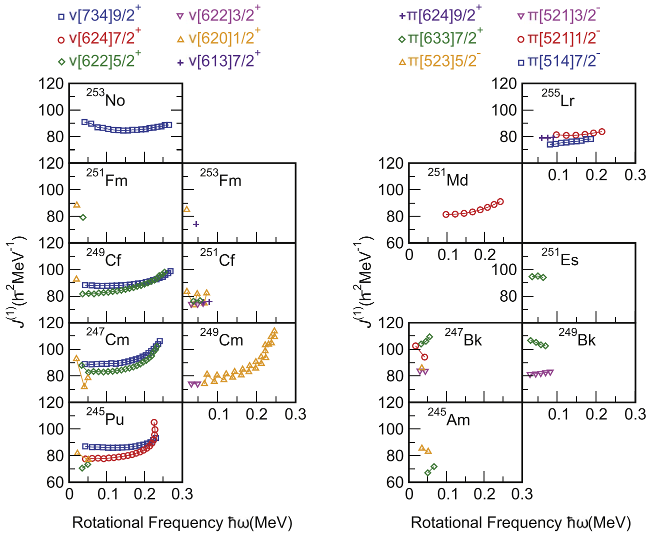

Figure 69. Kinematic moment of inertia for odd nuclei in the $N \approx 152$ region.

As discussed in paragraph 3.1, the single-particle assignment can be made for high-spin states by comparing to the predictions the intensity ratio $T(\Delta I = 1)/T(E2)$ of interband/intraband transitions. It should be noted that for odd nuclei, using the 'Harris' extrapolation to deduce the spins of observed states should be taken with care, since the solution is not unique because of the unknown parameter K. This can be phrased differently: for the same set of transitions, the moment of inertia $\mathcal{J}^{(1)}$ changes according to the K hypothesis. A higher K leads to higher $\mathcal{J}^{(1)}$ values. In other words, differences in $\mathcal{J}^{(1)}$ do not necessarily reflect an underlying physics. Also, the predicted $\mathcal{J}^{(1)}$ values for different s.p. configurations are usually very similar in a given isotope; therefore they are not frequently used. However, a comparison between different isotopes, as for even–even isotopes, provides valuable information on the alignment process. There is, moreover, a fundamental difference between even–even and odd isotopes: in essence, the filling of a specific orbital blocks its alignment. If an alignment is still observed when only one particle occupies the orbital, it is then necessarily due to other orbitals. By comparing the $\mathcal{J}^{(1)}$ slope or, even better, the alignment of rotational bands in a given region, it is therefore possible to infer the orbitals responsible for the alignment. Another consequence of the blocking is that pairing correlations are reduced, therefore the rotation is more collective and the moment of inertia is higher compared to their even–even neighbors. Overall, investigation of the behavior of rotational bands in odd nuclei has a better potential to determine the contribution of single-particle states (or, on the contrary, to exclude some contributions).

The alignment of the $N = 151$ isotones ^{245}Pu, ^{247}Cm and ^{249}Cf is shown in figure 70 taken from [393]. The g.s. bands in all these isotopes (and also in ^{253}No not shown here) are based on the $\nu 9/2^{-}[734]$ Nilsson orbital originating from the $\nu j_{15/2}$ spherical shell, of which alignment is therefore blocked. The alignment of the first excited state based either on the $\nu 7/2^{+}[624]$ (^{245}Pu) or on the $\nu 5/2^{+}[622]$ (^{247}Cm, ^{249}Cf) orbital is also shown. Regardless of the neutron configuration, the alignment does not change noticeably in a given isotope, and is observed for the $\nu j_{15/2}$ $9/2^{-}[734]$ configuration. This proves that another orbital must be involved in the alignment, thus the $\pi i_{13/2}$ orbital. Likewise, the same orbital aligns in ^{244}Pu. This is corroborated by the theoretical analysis of Hota *et al* [393] using cranked Woods–Saxon calculations, and of Zhang *et al* [471] using particle number conserving-cranked-shell model (PNC-CSM) calculations. The onset of alignment in ^{247}Cm and its absence in ^{249}Cf (also in ^{253}No) can be interpreted as a delayed alignment, due to the proximity of the $Z = 100$ deformed shell gap. It would be valuable to complete this picture with a measurement of rotational bands in ^{251}Fm and excited band(s) in ^{253}No.

^{249}Cm is so far the only $N = 153$ isotone for which high-spin states have been observed [394]. Like for other $N = 153$ isotones in this region, the g.s. band is based on the $\nu 1/2^{-}[620]$ Nilsson orbital from the $2g_{7/2}$ spherical shell (see section 2.5.1). Its moment of inertia and alignment reveal a clear but smooth upbend at $\hbar\omega \approx 0.22$ MeV, see figure 69. Both proton $\pi i_{13/2}$ and neutron $\nu j_{15/2}$ alignments are possible for this rotational band, therefore it is not possible to conclude which of them is the case without other measurements in e.g. ^{251}Cf, ^{253}Fm or ^{255}No.

There are only two proton-odd isotopes in the discussed region where rotational bands have been observed at high spin: ^{251}Md [428] and ^{255}Lr [433]. The g.s. band of ^{255}Lr and the excited band of ^{251}Md are built on the $\nu 1/2^{-}[521]$ Nilsson orbital from the $2f_{5/2}$ spherical shell. The excited band in ^{255}Lr and the recently observed g.s. band in ^{251}Md [430] are based on the $\nu 7/2^{-}[514]$ Nilsson orbital from the spherical $1h_{9/2}$ shell. None of these bands display an upbending nor involve the high-j $\pi i_{13/2}$ single-particle configuration. It might be therefore instructive to observe a rotational band based on the $\pi 7/2^{+}[633]$ Nilsson orbital derived from this spherical shell. Decay spectroscopy has not yet established single-particle states based on this orbital in ^{251}Md or ^{255}Lr. It should be noted that the intensity ratio $T(\Delta I = 1)/T(E2)$ is predicted to be larger for the $\pi 7/2^{+}[633]$ configuration with respect to the $\pi 7/2^{-}[514]$ case. Therefore $M1$ transitions should dominate below spin $\approx 16\hbar$, which does not favor their experimental observation.

The rotational bands in ^{251}Md and ^{255}Lr are overall well reproduced by theoretical calculations [264, 428, 433, 448, 469, 473, 488], in particular for the down-sloping orbital $\pi 1/2^{-}[521]$, which attracts great attention since it may close a hypothetical spherical shell gap at $Z = 114$. Some details, like possible alignment of the unfavored bands based on the $\pi 1/2^{-}[521]$ or $\pi 7/2^{-}[514]$ configuration[7], or the contribution of the $\pi j_{15/2}$ $1/2^{-}[770]$ orbital to the alignment proposed in [469, 475], are not confirmed. The reason why rotational bands in ^{251}Md and ^{255}Lr with the same s.p. configuration have very close moments of inertia certainly deserves further investigation [433, 489].

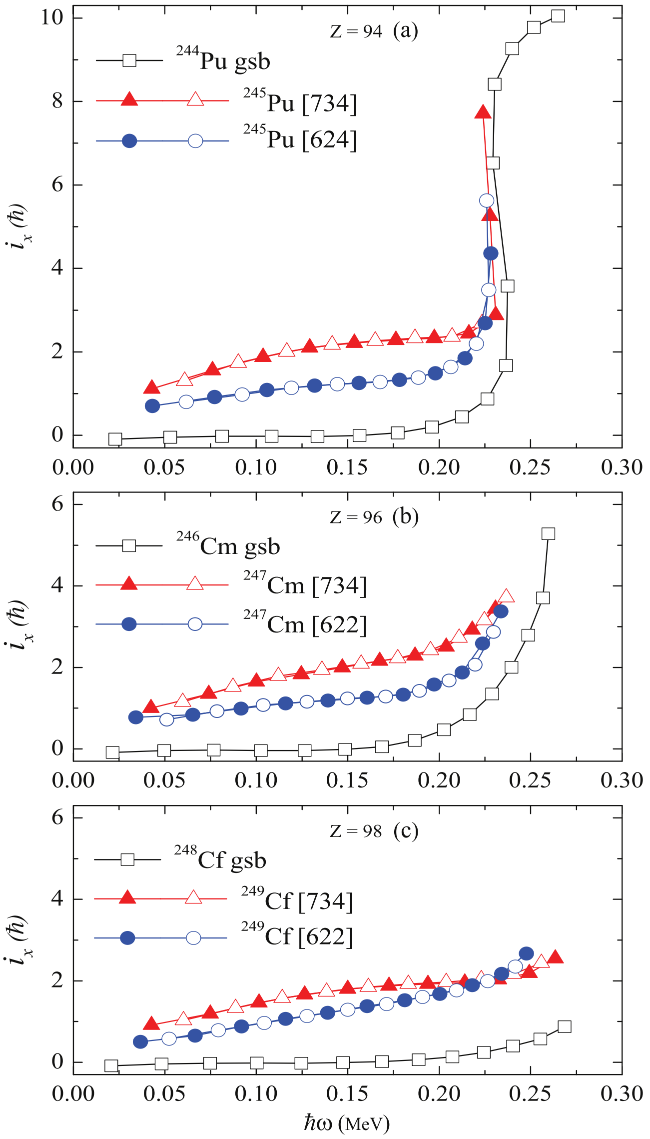

Figure 70. Alignment for the neutron-odd $N = 151$ isotones ^{245}Pu, ^{247}Cm and ^{249}Cf and for their $N = 150$ even–even neighbors. Reprinted from [393], Copyright 2014, with permission from Elsevier.

It should be noted that no high-spin rotational bands are known in proton-odd isotopes between ^{241}Am [391] and ^{251}Md [428]. Bridging the gap with data on Bk and Es isotopes would be valuable in order to obtain, for instance, information on the role of the $\nu j_{15/2}$ orbital in the alignment process. Overall, the role of this high-j orbital has not yet been

---

[7] Unfavored partners are those with angular momentum pointing backward with respect to rotation and therefore being first subject to alignment.

revealed experimentally, although theoretical calculations predict its substantial contribution.

General comments on theoretical calculations and their relations to experiment will be made in paragraph 4.1.

High-K bands

Following our discussion in sections 2.5.2 and 3.5 we are coming back to high-K states, their nature and rotational bands built on them. While a dozen of high-K 2qp states have been reported in the region from Cm to SHN, in only two cases so far high-spin states have been observed on top of them: ^{250}Fm [291] and ^{252}No [440]. Although high-K states have been already discussed in section 2.5.2 and in numerous review articles (just to quote the recent thorough compilation by Kondev *et al* [490]), we cannot overlook a brief overview of the band-head properties in the Fm–No region, since they are closely interrelated with the associated collective properties.

In the Hf region, numerous high-K isomers from 2- to 10-qp, and associated rotational bands have been observed. These studies have been shown to be very fertile, see e.g. [491] and the contribution by Walker and Xu in this focus issue [260]. We wish to make here a brief digression to remind (as mentioned by Kondev *et al* [490]), that an early work of Bohr and Mottelson in 1953 [64] was devoted in particular to the interpretation of rotational bands in ^{176}Hf fed by the decay of high-K states. The unexpected value of the moment of inertia triggered considerable theoretical developments.

Returning to the No region, decay spectroscopy techniques established a $K^\pi = 8^-$ character of the high-K isomers in ^{250}Fm and ^{252,254}No (see [289, 490] and references therein). For these isotopes, the 2qp configuration can either correspond to a proton or a neutron excitation. As shown in figure 68, a $K^\pi = 8^-$ state can be built by breaking a pair towards the configuration $\nu 7/2^+[624] \otimes \nu 9/2^-[734]$ or $\pi 7/2^-[514] \otimes \pi 9/2^+[624]$. In the $Z = 100$ Fm isotopes, a proton-pair breaking involves excitation across the $Z = 100$ deformed gap, which is energetically less favored as compared to $Z = 102$ No isotopes. Similarly, breaking a neutron pair in the $N = 150$ isotones (^{250}Fm, ^{252}No) leads to promoting a $\nu 7/2^+[624]$ neutron to the nearby $9/2^-[734]$ orbital, while in the $N = 152$ isotones (^{254}No) a neutron from each of these two orbitals has to be promoted across the $N = 152$ deformed gap. It is therefore expected that the $K^\pi = 8^-$ isomer corresponds to a neutron configuration in ^{250}Fm, a proton configuration in ^{254}No, and either proton or neutron in ^{252}No.

Comparison with theory allows us to continue the discussion on deformed shell gaps. All microscopic–macroscopic models converge toward the same predictions for $K^\pi = 8^-$ isomers (see table 4 of [432]): in ^{250}Fm the neutron 2qp state is lower in energy by 0.5–1 MeV compared to the 2qp proton excitation, as expected from the discussion above. In ^{252}No, 2qp proton and neutron $K^\pi = 8^-$ states are predicted to lie rather close in energy within 100–400 keV, the neutron configuration being always lower in energy. The situation is more controversial for ^{254}No, where models, sometimes with very similar ingredients, favour either a 2qp proton or a neutron excitation with energy differences as large as 1 MeV. There is no straightforward explanation for these discrepancies. As previously mentioned, from experimental evidence, the nature of the $K^\pi = 8^-$ isomer is also debated. From decay spectroscopy experiments, Herzberg *et al* [283], Tandel *et al* [284] and Heßberger *et al* [305] favor a 2qp proton configuration, while Clark *et al* [306] favor a neutron configuration.

As it would be expected, the predictions of EDF-based calculations are less consistent, since the deformed shell magic numbers $Z = 100$, $N = 152$ are not well reproduced by these models, which can in some cases significantly change the energy needed to break a pair across a (not reproduced) gap. This problem is found for calculations based on the Gogny [412, 440] or Skyrme [492] interactions. As discussed in section 3.7, there are large discrepancies in the predictions for the $\pi i_{13/2}$ spherical shell from which the $\pi 9/2^+[624]$ Nilsson orbital arises, which also contribute to the disagreement with experimental data.

A proper treatment of 2qp excitations is a very demanding task, including treatment of time reversal symmetry breaking, particle recoupling and blocking. The recoupling of K_1, K_2 states can lead to either $K_+ = K_1 + K_2$ or $K_- = |K_1 - K_2|$ excitations. According to the Gallagher–Moszkowski rule [441], states with parallel spins (K_+) are favored compared to anti-parallel spins (K_-), although there seem to be exceptions to this rule. Without a proper treatment, the K_+ and K_- states are degenerate. In microscopic–macroscopic calculations mentioned above, the residual spin-spin interaction is not systematically included. In EDF calculations based on the Gogny force [412, 440], breaking of the proper symmetry (namely 'z-symmetry' in this formalism) leads naturally to the K_+, K_- degeneracy being removed, with some exceptions to the Gallagher–Moszkowski rule. It is however not yet clear why such exceptions occur. This subject still needs to be explored and recoupling mechanisms should also be somehow included in calculations that do not take them into account.

Another possible way to improve modelization is to include beyond-mean-field effects e.g. vibrations, which are known to be relevant for 2qp states. This has been done in a few studies in the No region using phonon operators [493, 494], random phase approximation [495–497], or HFB configuration mixing [412].

This discussion shows that calculations of 2qp bandheads are a well debated topic with a rich underlying physics and several possible ways of improvement on the theoretical side.

Let us now discuss the rotational bands built on these high-K states. As discussed in section 3.5.3, these rotational bands were primarily analyzed to deduce the electromagnetic properties and, consequently, the nature of 2qp states. A discussion of their evolution as a function of the rotational frequency is instructive on its own. As a general rule, and following the discussion of rotational bands in odd isotopes, the presence of two unpaired nucleons reduces the pairing correlations and in this way contributes to a larger collectivity as compared to g.s. rotational bands in even–even nuclei and to those in odd nuclei. Since particle alignment is largely hindered, the moments of inertia are generally more stable as a function of rotation. This is indeed what is observed for

^{250}Fm and ^{254}No, as shown in figure 71. It can be seen that, the experimental kinematic moment of inertia (in red) is slowly raising, which indicates a smooth alignment. As shown by the calculations, the projection Ω of the total angular momentum along the symmetry axis is slowly decreasing. The K purity of the rotational band is therefore gradually lost, not only because of the alignment, but also because of the Coriolis mixing. At low rotational frequency the model calculations reproduce remarkably well the dynamic moment of inertia $\mathcal{J}^{(2)}$. For ^{252}No, there is an offset in the $\mathcal{J}^{(1)}$ moment of inertia of $\approx 10\hbar^2$ MeV^{-1} compared to ^{250}Fm, which is beyond any simple explanation. Since the two bands are interpreted as having the same neutron configuration, the effect can only be due to the protons. However, the Fm proton configuration exhibits deformed magicity, so lower pairing correlations and therefore a higher moment of inertia would be expected, while the opposite is observed experimentally. It is important to note that configuration-constrained total-routhian surface calculation performed by Fu *et al* [498] also fails to reproduce the offset. As expected from deformed gap considerations, the same calculations predict a higher $\mathcal{J}^{(1)}$ for the $K^{\pi} = 8^{-}$ band of ^{250}Fm compared to that of ^{252}No. Hence, we cannot rule out that the 2qp excitation in these two isotopes induces subtle polarization effects, which rearrange the proton configurations. Given the strong similarity between the level schemes and spectroscopic data for the two isotopes, there is no evidence for a rearrangement. Speculating on beyond-mean-field effects would be presumptuous at this stage.

The dynamic moments of inertia $\mathcal{J}^{(2)}$ in ^{250}Fm and ^{252}No both display a decrease at $\hbar\omega \approx 0.2$ MeV, which is not reproduced by calculations based on the D1S Gogny force [440]. This kind of anomaly in $\mathcal{J}^{(2)}$ corresponds usually to an adiabatic band crossing and is known as a Landau–Zener crossing[8]. Contrary to the backbending phenomenon, where the nucleus undergoes a 0qp to 2qp transition, this effect results from a smooth (adiabatic) interaction between states belonging to two different 2qp bands which have the same spin and parity and accidentally are close in energy. The most surprising fact is that both ^{250}Fm and ^{252}No experience the same phenomenon, although it is slightly less pronounced in ^{250}Fm. This similarity corroborates the same 2qp neutron configuration for both bands. A complete spectroscopy would possibly reveal the nature of the crossing bands, but in absence of such detailed data only speculations are possible. EDF calculations with the D1S force [440] do not provide any hints concerning the crossing or any other effect that could generate the dip in the $\mathcal{J}^{(2)}$. A detailed theoretical analysis has been performed by Fu *et al* using configuration-constrained total-routhian-surface calculations [498]. Although the model, without changing the parameters, does not reproduce the anomaly, the proximity of several other 2qp bands corroborates the crossing scenario, and a mixing with a $K^{\pi} = 7^{-}$ configuration is suggested. More than being just a curiosity, the band crossing reveals fine structure details still beyond deep understanding and the accuracy of current models.

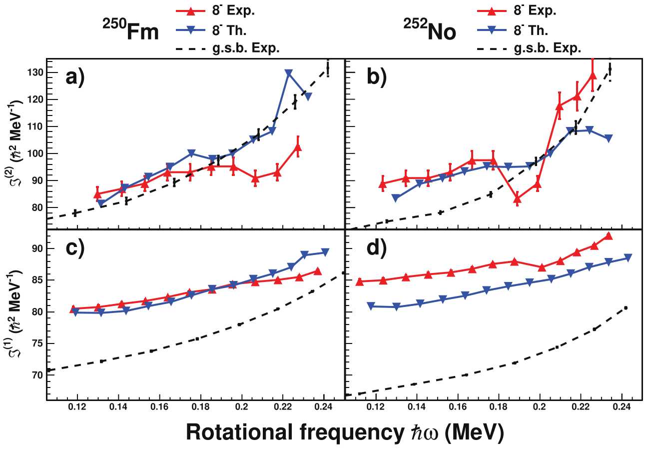

Figure 71. Dynamic (top) and kinematic (bottom) moment of inertia for ^{250}Fm (left) and ^{252}No (right). Experimental data for the g.s. are shown by a dotted line. The red (blue) curves correspond to experimental data (theoretical calculations) for the bands based on 2qp $K^{\pi} = 8^{-}$ excitations [440]. Theoretical calculations are performed using the HFB model and the D1S Gogny force.

Although ^{254}No has been the subject of the largest experimental efforts in this mass region, no rotational bands based on high-K states have been observed in this nucleus using prompt γ-ray spectroscopy. The question arises as to whether the 2qp configuration in ^{254}No is different to that in ^{250}Fm and ^{252}No, namely a $K^{\pi} = 8^{-}$ proton configuration would lead to more converted $\Delta I = 1$ transitions and therefore a lower γ-ray flux. This is actually not the case. As discussed above, the value of g_K for favored single states is 1(0) for $\pi(\nu)$ 2qp. Since $g_R \approx Z/A \approx 0.4$, the magnetic moment is of the same order of magnitude for both configurations. One possible hypothesis is that several 2qp states lie close in energy near the $K^{\pi} = 8^{-}$ state at ≈ 1.3 MeV, leading to a fragmented γ-ray de-excitation flux of high-K rotational bands.

In recent decay studies by Clark *et al* [306] and Heßberger *et al* [504], the first states of a high-K rotational band fed by an isomer at ≈ 3 MeV (likely a 4qp state) have been observed. While there is a large overlap between the transitions observed in the two experiments, the interpretations are different. Heßberger *et al* assign the sequence to a $K^{\pi} = 8^{-}$ proton band, whereas Clark *et al* propose a sequence built on a new $K^{\pi} = 10^{+}$ neutron excitation and by inference favor a neutron configuration for the $K^{\pi} = 8^{-}$ isomer. Clearly, more details and data are needed to clarify the situation. The question still arises why the rotational sequence observed by decay techniques has not been seen in prompt spectroscopy, which would allow, via a g_K measurement, to resolve the conflicting interpretations.

We have discussed in this paragraph only three isotopes: ^{250}Fm, ^{252,254}No. In lighter isotopes, several high-K isomers have been reported, but rotational bands built on top of them are only tentative. Using inelastic scattering, rotational bands based on a 2qp excitation has been reported in ^{244}Pu [437] and evidenced in ^{248}Cf [395, 505]. The isomer decay was

---

[8] Problem formulated in 1932 by Landau [499, 500], Zener [501], Stueckelberg [502] and Majorana [503].

observed by out-of-beam coincidence gating. It was, however, not possible to anchor the collective structures to the level scheme. Further, high-K isomeric states could be observed in ^{246,248}Cm [506] using the same technique, but rotational bands have not been reported. There is an experimental limitation in this case, since using a thick target prevents simultaneous decay spectroscopy at the focal plane of a spectrometer/separator.

Using fusion-evaporation reactions, no high-K rotational bands have been reported in Cm or Cf isotopes, and in general no high-spin studies have been published using these reactions. Recent measurements carried out at SHIP or RITU actually show a large drop of the cross section compared to Ca+Pb or Ca+Hg reactions [507, 508] which makes the study of high-K states challenging compared to the isotopes ^{250}Fm and ^{252}No.

4. Theory lessons and exotic phenomena

4.1. Discussion of the models

As discussed in the review, the agreement between spectroscopic data and theoretical predictions is rather good. We discussed in section 2 the isotopic/isotonic trend of single particle states, which is generally well reproduced within ≈300 keV. There are however some pathologies and exception to this rule: we mentioned the shortcomings of self-consistent approaches like EDF-based models in reproducing the deformed shell gaps $Z = 100$, $N = 152$, level ordering and level spacing for heavy nuclear species. On the contrary, all approaches agree on the doubly magic deformed character of ^{270}Hs ($Z = 108$, $N = 162$) although no experimental data are yet available to lend support on these predictions. As far as collective properties are concerned (see section 3), the moments of inertia are rather well reproduced using all approaches, except the few details discussed above.

Microscopic–macroscopic theory does apparently much better, with the crucial drawback that adjustment to data which is the key of this success, obscures the basic physics understanding. It is not our purpose to discuss the respective merits of both approaches. However, a survey of the literature calls for the following comments.

As far as single particle states are concerned much effort to improve the situation has been devoted to include beyond-mean-field effects, proper treatment of time-reversal symmetry breaking, particle recoupling, blocking, etc. in EDF-based calculations. Promising results have been achieved in a beyond mean-field approach by adding QVC to a relativistic field (RMF) model basis. After benchmarking the theory for light and medium mass nuclei, it has also been applied for heavier species up to $Z = 120$ isotopes [166, 509]. These calculations succeed in improving the reproduction of experimentally established single particle structures substantially, additionally in terms of the proper level spacing as can be seen in figure 72. In an application to SHN, predictions of this model trace the neutron and proton shell gaps for a sequence of even–even $Z = 120$ isotopes with neutron numbers $N = 172$, 176, 180 and 184. The model predicts that the proton shell gap remains robust for all four studied isotopes. For the neutron shell gap it suggests that it changes from $N = 172$ to 184 between ^{296}120 and ^{300}120 as can be seen in figure 73. This feature is in accordance with the general findings of self-consistent model approaches, suggesting for SHN a region of enhanced stability rather than pronounced and extended shell closures along isotopic and isotonic chains as observed in lighter nuclei. This was demonstrated e.g. by Bender *et al* [141] in 2001 for shell correction energies calculated for SHN comparing several HFB and RMF models.

In several studies mentioned above (see sections 3.6 and 3.7), in particular in the majority of microscopic–macroscopic approaches, pairing correlations are adjusted in order to better

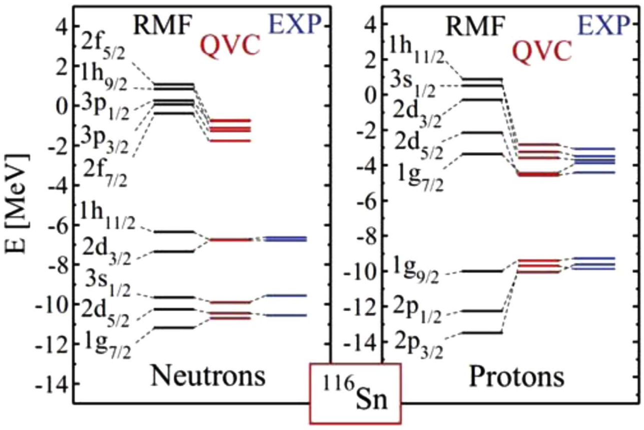

Figure 72. Reproduction of the experimental single quasiparticle spectrum of ^{116}Sn by relativistic mean field (RMF) calculations combined with quasiparticle vibrational coupling (QVC). Reprinted figure with permission from [166], Copyright (2012) by the American Physical Society.

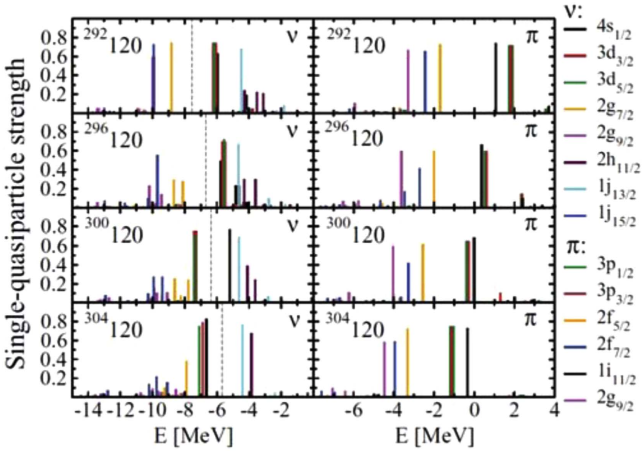

Figure 73. Development of single-quasiparticle strength distributions around the Fermi surface for the SHN ^{292,296,300,304}120 calculated using the QVC model. The proton shell gap $Z = 184$ remains robust throughout the whole isotope series (right panel), whereas the neutron energy gap changes from $N = 172$ to 184 between ^{296}120 and ^{300}120 (left panel). Reprinted figure with permission from [166], Copyright (2012) by the American Physical Society.

reproduce the moment of inertia or s.p. properties in the discussed mass region, see e.g. [264, 391, 394, 469, 471, 510]. It is satisfying that this results in a good reproduction of the moment of inertia, the alignment properties and the deformed shell gaps (with some parameters of the potential adjusted). The underlying reason for a need to decrease the pairing correlations (see e.g. [391, 394]) is however not clear and certainly deserves more investigations.

Modification of pairing has also been discussed in the frame of the EDF model, see e.g. [143, 353, 455, 473]. Bearing in mind that at the same time deformed shell gaps (and therefore a manifestation of pairing correlations) are not well described, it is perhaps premature to investigate such amendments in these models.

More generally, a discussion of fine details of the moments of inertia, pairing correlations or alignment frequencies may not be fully relevant as long as the deformed shell gaps are not well reproduced.

The role of high-order deformation like β_6 is investigated in several microscopic–macroscopic theoretical studies. It is argued that inclusion of this degree of freedom provides a better accuracy, e.g. alignment in $N = 151$ isotones [393] or the difference in the behavior between ^{252}No and ^{254}No [472], see also [160, 290, 351, 511–514]. In general, including as many degrees of freedom as possible leads to increasing accuracy of the results. In this context, there is a major difference between microscopic–macroscopic models and EDF-based ones since for the latter, the high-order deformations naturally emerge from the minimization procedure, if they are allowed by symmetry principles.

Proper treatment of time-reversal symmetry breaking should be taken into account in odd nuclei and 2qp states. This question is treated at different levels in the references mentioned above, but a discussion on this subject goes beyond the present review and is not specific to the heavy element region, see e.g. [473, 515] and references therein.

The role of octupole correlations has been mentioned above (sections 3.6 and 3.7) with its influence on the alignment process. Cranking calculations including this degree of freedom still need to be performed for the specific isotopes where the role of octupole correlations is suspected in order to investigate its possible role in delayed alignment.

Calculations of gyromagnetic factors or magnetic moments are rarely provided in theoretical studies. This quantity is however one of the basis for the single-particle assignment. Certainly, strong deviations with respect to simple models (see paragraph 3.1) are not expected. However it would be more satisfying to use a single theoretical framework rather than to mix some of them like in e.g. [440].

4.2. Exotic shapes and phenomena

In this paragraph we go through several predicted exotic phenomena that have not yet been confirmed experimentally. We will limit ourselves to phenomena related to collective features without prejudging their experimental observation.

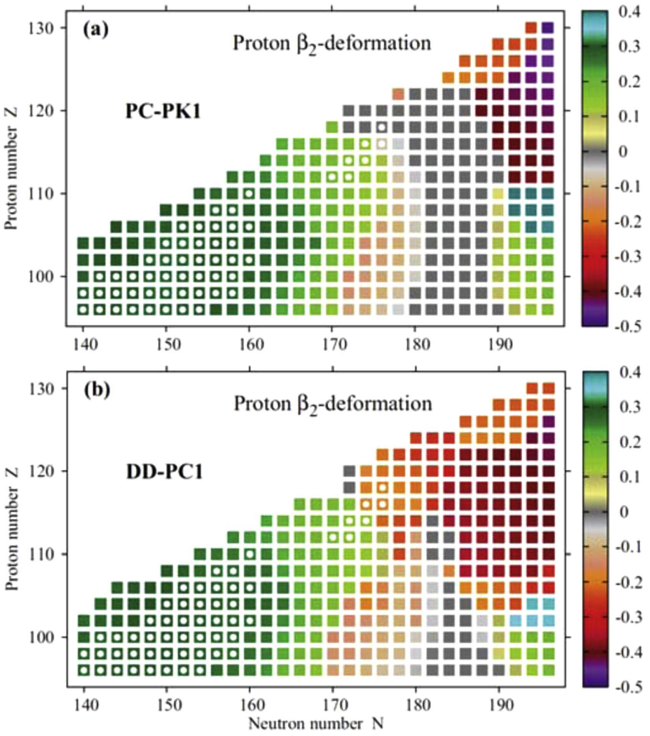

Figure 74. Quadrupole deformation (β_2) obtained from the two covariant energy density functionals PC-PK1 (left panel) and DD-PC1 (right panel) for even–even nuclei in the region $Z = 98$ to 130 and $N = 104$ to 196. Known nuclei are indicated by open circles. Reprinted figure with permission from [131], Copyright (2015) by the American Physical Society.

4.2.1. Oblate g.s. deformations. In a recent theoretical investigation Agbemava *et al* revisited the region of SHN [131]. They compare the predictions of EDF calculations, employing five different covariant EDFs which are known to have a good global performance [516, 517]. Treating in particular also nuclear deformation, they find for three of the functionals (NL3*, DD-ME2, and PC-PK1) spherical shapes for even–even nuclei around $Z = 120$ and $N = 184$. Two of them, however, (DD-PC1 and DD-MEδ) show the appearance of oblate shapes dominating the region. The two groups of functionals differ by their coupling schemes. The first group of three is based on density dependent meson-nucleon couplings, whereas the second group of two uses a point coupling scheme. In figure 74 the proton quadrupole deformations obtained for two of the five mentioned interactions, one of each group (DD-PC1, DD-Meδ), are shown. Usually, oblate shapes appear just before major shell fillings with hole(s) in orbitals which are down-sloping as a function of the deformation (low Ω member of a multiplet). The situation is different here with the prediction of oblate shapes both below and above the predicted spherical shell gap at $N = 184$. The reason for the occurrence of g.s. deformation in the region of SHN here is the behavior of SPLs as a function of deformation in a Nilsson picture. Nilsson diagrams calculated for the system ^{304}120 (figure 5 in [131]) show pronounced level density gaps at oblate shapes for $Z = 116$, 118 and 120. For neutrons the largest gap is found for $N = 178$ at $\beta_2 = -0.2$ to -0.3. It should be noted that the predominance of prolate versus oblate shapes along the nuclear chart is a longstanding problem in nuclear structure, already addressed by Bohr and Mottelson [69], see also the contribution of Arita in this focus issue [518].

Concerning the predictive power of the considered models the authors of [131] state that available experimental values are reproduced equally well for the different parametrizations, which makes a discrimination between the validity of the various functionals impossible. To this end, the accuracy achieved for the predictions has to be improved considerably. Additional experimental information on even–even nuclei, possibly covering a larger area of nuclides, can certainly help to benchmark theory here, particularly, in areas where large changes of deformation are seen in the calculation (see figure 74).

4.2.2. Octupole shapes. The observation of 2^- states in decay spectroscopy of e.g. $N = 150$ isotones provides evidence for octupole correlations. We previously mentioned (section 3.7) the role of octupole correlations in the delayed alignment of yrast or rotational bands at low excitation energy. The proper inclusion of octupole correlations (reflection-asymmetric shapes) in EDF-based models is subject of several recent studies, see e.g. [519, 520]. It has also been suggested that non-axial octupole correlations may appear at medium excitation energies [521]. Using the asymmetric shell model, Chen *et al* [522, 523] interpreted the 2^- states in ^{246,248}Cm, ^{250}Fm and ^{252}No and the first rotational states built on them as resulting from Y_{32} correlations. Using the cluster model, Shneidman *et al* [524] predict alternate parity bands corresponding to reflection-asymmetric shapes in the Cm–Rf isotopes at moderate excitation energy. In the limit of pure Y_{32} shapes, the deformation is of a tetrahedral type, which was predicted first to occur in nuclei in the late 1990s [525, 526], without a strong experimental evidence yet. The subject is however controversial in the VHN/SHN region [527–529].

4.2.3. Gamma-vibrational states. Gamma-vibrational 2^+ states have been reported in ^{246}Cm [530], ^{248}Cm [531, 532], ^{250}Cf [533], ^{252}Cf [534], ^{254}Fm [535] and ^{256}Fm [292] and discussed theoretically using different frameworks by Bès *et al* [536] (Nilsson single-particle model, quasi-particle and quasi-boson approximations), Ivanova *et al* [493] (phonon operators), Jolos *et al* [537] (quasiparticle-phonon model) and by Sun *et al* [538] (triaxial projected shell model). In the last reference, 2^+ states are also predicted at 0.6–0.8 MeV in ^{250,252}Fm and ^{252,254}No, although Jolos *et al* [537] calculate them at slightly higher excitation energies. These two approaches reproduce the experimental data rather well. However, evidence for the predicted 2^+ vibrational states has not yet been found in ^{250}Fm and ^{252,254}No, which calls for further effort on both, the experimental and the theoretical side.

4.2.4. Superdeformed shapes. Superdeformed (SD) shapes were first observed in 1961 in ^{241}Am [156] via an anomalously short fission lifetime of 14 ms. This result was a 'by-product' of SHE research in Dubna. Superdeformation was a very active topic in the 1970s, and many studies were performed in the actinide region, where these states are known as fission isomers. About 30 fission isomers were discovered in the Th–Bk region, see [408, 447]. A renewal in studies of very elongated shapes started in 1986 with the discovery of an SD band in ^{152}Dy extending up to $60\hbar$ [539], followed by an impressive number of results mainly in the $A \approx 60$, 80, 130, 150 and 190 mass regions. So far, around 400 SD bands or shape isomers have been discovered in $\approx$150 nuclei [540]. See also the contribution of Leoni and Lopez-Martens in this focus issue [541].

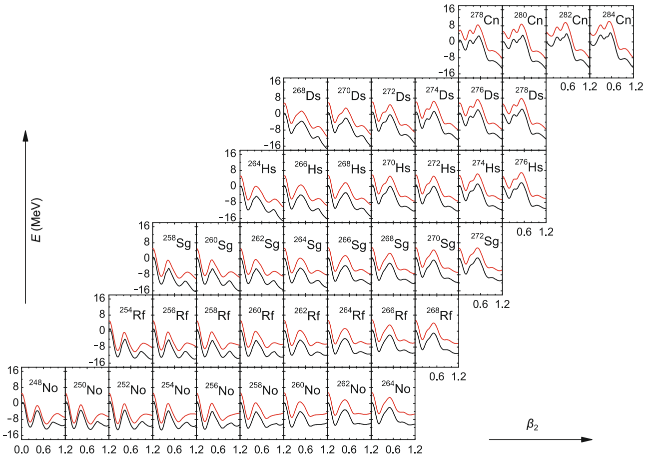

Figure 75. Potential energy as a function of the deformation for even–even No–Cn nuclei with (black) and without (red) octupole correlations. Superdeformed minima are predicted for the lightest No–Sg nuclei. Reprinted from [549]. CC BY 4.0.

A prolate superdeformed shape corresponds to a deformation parameter $\beta \approx 0.6$, or axis ratio 2:1. These shapes are stabilized by the level degeneracy and the associated gap. For a harmonic oscillator potential, the level degeneracy occurs for an oscillation frequency ratio $\omega_\perp : \omega_z = 2:1$, and more generally, degeneracies occur for integer ratios of oscillation frequencies $\omega_1 : \omega_2 : \omega_3$ along the principal axes. The presence of high-j orbitals from the $N + 2$ shell (super-intruder orbital) strongly polarizes nuclei toward SD shapes. The mechanism leading to high degeneracy and stabilization of SD shapes has been discussed by Bohr and Mottelson ([69], p 367-305, p 634-637), and several authors like Strutinsky *et al* [101] and Ragnarson [542]. Bohr and Mottelson ([69], p 578) also discuss the general features of shell effects in terms of the classic POT [543, 544] that allows to account for the basic nature of shell effects using semi-classical basics, see also the contributions of Arita [518] and Nakatsukasa *et al* in this focus issue [545]. This is a topic dear to Mottelson that he developed, as an example, in a lecture given at Les Houches in 1996 [100]. Note that in [69], reference is made to shape isomers only; the term 'superdeformation' being not yet used.

The island of experimentally observed shape isomers extends up to Bk, being the limit beyond which experimental studies become challenging. However, various recent model calculations predict possible prolate SD shapes in the region of Fm to $Z = 120$ isotopes [131, 412, 473, 546–549]. In general, SD shapes are predicted to be favored for the lightest isotopes in the Fm–Cn region, see for example figure 75. In very few cases, namely ^{242,244}Fm [412] and ^{248,250}Fm [548], the SD configuration is even expected to become the g.s. However, these states are not necessarily stable with respect to fission, as pointed out in [412]. Furthermore predictions have to be taken with care in the case where octupole deformations are not included, since they are known to decrease the fission barrier and possibly suppress superdeformed minima.

Moments of inertia of $\approx$160 $\hbar^2$ MeV^{-1} are predicted at low spin [412, 547, 548] for SD shapes in the No region. Because this value is much larger as compared to that for normal-deformed states, SD states may (like in other mass regions) become yrast at high angular momenta and therefore become experimentally accessible. This is for instance the case for ^{252,254}No, where SD bands are predicted to become yrast at $I \approx 24\ \hbar$ and $34\ \hbar$, respectively [547]. Although SD states in the No region are still speculative, it should be noticed that different models (PES, HFB with Skyrme or Gogny force) yield similar predictions. Experiments aiming at observation of these structures are obviously challenging. For the moment, only direct reactions have been used to study the Th-Bk fission isomer region, and access to high-spin states of shape isomers would only be possible using fusion-evaporation reactions, like in other SD mass regions.

Here we should also mention a (speculative) prediction of SD oblate states in the $Z = 114$ and $Z \geqslant 118$ regions [550–557] using RMF, HFB + Skyrme or Woods–Saxon models. It should be noted, however, that the calculations performed by Muntian and Sobiczewski using the Woods–Saxon model [558] do not support the prediction of Ren *et al* [551, 552] for $Z = 118$ isotopes, therefore casting some doubts on the above-mentioned predictions of oblate SD states.

5. Advances in experimental instrumentation

Technical and methodological development is mandatory for the progress of any scientific field. For the SHN research, the main limiting parameter for the advancement of the field are the ever lower cross sections being faced by the investigation of species with ever higher atomic number Z. In this section we present the technological efforts being presently pursued in the various laboratories regarding advanced facilities and detection devices in the first subsection and various new ideas regarding the methods of production of SHN and the experimental techniques to study them.

5.1. Future facilities and detection devices

New accelerator projects are presently on their way to being constructed, such as the SHE-factory at the FLNR in Dubna or SPIRAL2 at GANIL in Caen, or in planning as the cw-LINAC at GSI in Darmstadt. These developments are accompanied by the implementation of new separation and/or detection devices, like the AGFA gas-filled separator at ANL, the separator-spectrometer setup S^3 at SPIRAL2 or the γ-tracking arrays AGATA in Europe and GRETA in the USA. All these projects will be presented in this subsection.

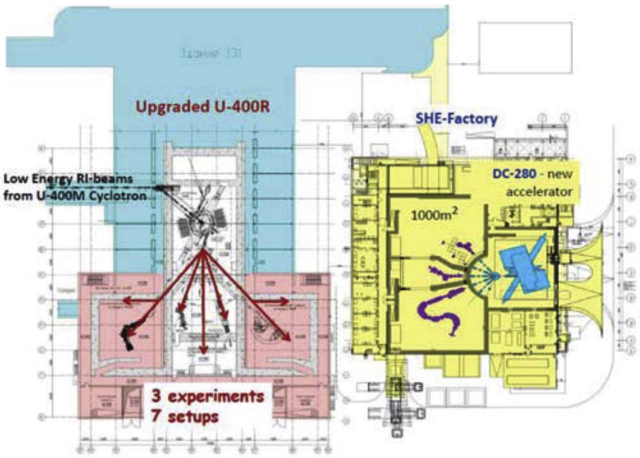

Figure 76. Overview of the FLNR accelerator facility of JINR, Dubna, including the SHE factory project presently under construction. Republished with permission of World Scientific, from [559]; permission conveyed through Copyright Clearance Center, Inc.

5.1.1. Dubna: The SHE-factory. In Dubna, Russia, the so called SHE-factory, one of the most promising projects for the progress in SHN research, will deliver very high intense beams devoted to the synthesis and spectroscopy of the heaviest elements [157, 560]. Aiming at highest production rates of SHE the facility is presently under construction at the FLNR of the JINR in Dubna. The heart of the SHE-factory is a new high intensity accelerator. The DC280 cyclotron is planned to deliver beams of 5–8 MeV/A at intensities of 10–20 particle μA. This dedicated facility is foreseen to operate 7000 h per year delivering a total dose of 1.3×10^{21} projectiles on target, a factor of $\approx$30 more than presently achievable. Assuming a state of the art separator and detection system, the facility should yield a total production of $\approx$5000 decay chains per year originating from SHN with typical production cross sections of 1–10 pb, thus allowing for a wide science program going beyond the pure production and including detailed spectroscopy of the decay properties of SHN. An overview of the project is given in figure 76.

The development of new separators is pursued in parallel [224]. A new 'universal' gas-filled separator DGFRS-II is being built for the synthesis and spectroscopy of SHN. It will have a $Q_vDQ_vQ_hD$ optics configuration. Compared to the DGFRS, a gain of a factor ≈ 3 in efficiency is expected. A pre-separator is foreseen for chemical and g.s. properties studies. At the focal plane, products will be stopped in a gas catcher and further transported to various apparatus for chemical analysis, mass measurement or laser spectroscopy. In this case the background suppression requirements are not as strict as compared to synthesis or spectroscopy experiments, which results in a simpler Q_vDQ_h design as shown in figure 77.

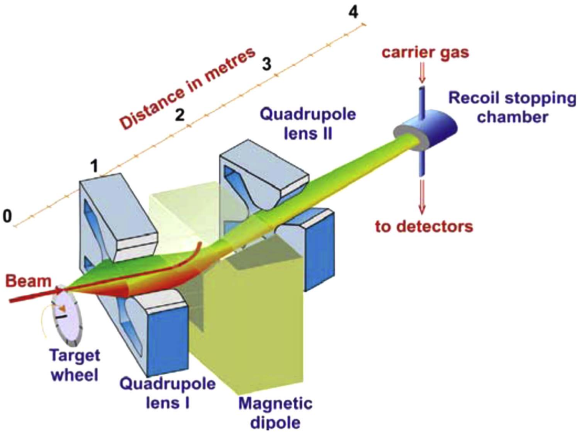

Figure 77. The pre-separator for the Dubna SHE-factory. Reprinted from [224], Copyright 2015, with permission from Elsevier.

5.1.2. *GANIL-SPIRAL2: S^3 and VAMOS-GFS.*

At GANIL, Caen, the S^3 vacuum Super Separator Spectrometer has been designed for the study of rare isotopes, synthesized using the very intense beams of the super conducting linear accelerator (SC LINAC 'LINAG').

In table 5 from [561] the expected beam intensities for a variety of ions are shown for the two phases of the project. In a first phase only an injector capable of accelerating ions with $A/Q = 3$ will be available which limits the beam intensities for heavier ions. With the injector foreseen for a second phase 'phase 1++' with $A/Q = 6$ or 7 capabilities, beam intensities of 10 pμA and more will be achieved also for ions with masses $A \gtrsim 40$.

The separator-spectrometer combination S^3 will combine large acceptance, high beam rejection and high mass resolving power of $\Delta M/M \approx 1/300$ for the spectroscopy and synthesis of a large panel of isotopes from $N \approx Z$ up to SHN. Its optics consists of a momentum achromat QQQDQQQ–QQQDQQQ followed by a mass spectrometer QQQEQQQ–QQQDQQQ: see figure 78. More details can be found in [223]. A transmission of ≈50% (≈20%) is expected for asymmetric (very asymmetric) reactions of Ca+Pb (Ne+U) type. The decay station known as SIRIUS (Spectroscopy and Identification or Rare Isotopes Using S^3) is designed for α, β, γ and CE spectroscopy of the implanted nuclei. Similar to devices like MoDSS and TASISPec described in section 2.3.2, however, using larger area silicon detectors, it will be made of a 10×10 cm^2 DSSD, an upstream tunnel of four 10×10 cm^2 1 mm thick Si pad detectors for the detection of α particles and fission fragments escaping from the implantation DSSD, and for electron spectroscopy. Gamma detection will be performed with Ge clover detectors of the EXOGAM or CLODETTE type. One or two tracker detectors placed upstream will provide a time of flight measurement and position for subsequent M/Q selection. These transmission detectors will additionally serve to distinguish between particles coming from upstream and signals from decays inside the DSSD.

Table 5. Beam intensities expected for the SC LINAC of SPIRAL2. Reproduced from [561]. CC BY 3.0.

Ion	Intensity (pμ(A)) $A/Q = 3$	Intensity (pμ(A)) $A/Q = 6$ or 7
^{16}O	216	375
^{19}F	57	50
^{36}Ar	35	40
^{40}Ar	5.8	30
^{48}Ca	2.5	15
^{58}Ni	2.2	10
^{84}Kr	0	20
^{124}Sn	0	10
^{139}Xe	0	10
^{238}U	0	2.5

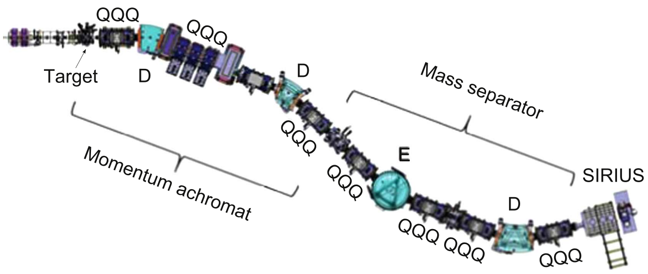

Figure 78. Schematic view of the S^3 Super Separator Spectrometer. The separator section is made of a momentum acromat with QQQDQQQ–QQQDQQQ optics. The second spectrometer section is a mass separator with QQQEQQQ–QQQDQQQ elements, followed by the decay station SIRUS. The length from the target point up to the focal plane is ≈30 m. Courtesy of the S^3 collaboration.

With this combination of the high intensity beams from the SC LINAC and the separation and spectroscopic capabilities of S^3+SIRIUS a variety of experiments are envisaged to study heavy and superheavy nuclei. Table 6 shows a selection of possible experiments which had been proposed by the scientific community interested in research at this new facility [175]. S^3 will considerably open the spectrum of decay studies not only in the region of SHN but also near ^{100}Sn with detailed spectroscopy, K-isomer studies, mass identification, reaction mechanism, etc. Detailed studies with cross sections down to the pb level will be possible. The expected count rates for the various measurement types are indicated for both phases (see above) of the project, based on the expected beam intensities as given in table 5.

Alternatively, it will be possible to study g.s. properties using the REGLIS setup (Rare Elements in Gas-Laser Ion Source and spectroscopy at S^3) [562] with the option to drive the ions into the DESIR hall (Désintégration, Excitation et Stockage des Ions Radioactifs = Decay, Excitation and Storage of Radioactive Ions) where various types of equipment will be available for e.g. mass measurement, collinear laser spectroscopy, etc.

Still at GANIL, the VAMOS-GFS project aims at upgrading the VAMOS vacuum spectrometer to a high-acceptance gas-filled

Table 6. Proposed nuclei for 'day 1' experiments at S^3 and for the phase 1++ when an injector with the capability to prepare ions with $A/Q = 6$ or 7 will be available at the SC LINAC presently under construction at the SPIRAL2 facility of GANIL. Courtesy of the S^3 collaboration.

Nuclide	Reaction	Feature	Cross-section (pbarn) (ER)	Rate (h^{-1})	# of events per 7 days
^{254}No	^{48}Ca+^{208}Pb	*K*-isomer	2×10^6	6×10^4	6×10^7
^{256}Rf	^{50}Ti+^{208}Pb	*K*-isomer	17×10^3	550	540.000
^{266}Hs	^{64}Ni+^{207}Pb	ER	15 (^{270}Ds)	0.34	285
^{266m}Hs	^{64}Ni+^{207}Pb	*K*-isomer	15 (^{270}Ds)	0.01	12.5
^{270}Ds	^{64}Ni+^{207}Pb	ER	15	0.45	380
^{270m}Ds	^{64}Ni+^{207}Pb	*K*-isomer	15 (^{270}Ds)	0.22	190
^{262}Sg	^{64}Ni+^{207}Pb	α-decay	15 (^{270}Ds)	0.02	25
^{276}Cn	^{70}Zn+^{207}Pb	*K*-Isomer	0.5 (^{277}Cn)	0.01	12.5
^{288}115	^{48}Ca+^{243}Am	ER	10	0.3	300
^{288}115	^{48}Ca+^{243}Am	*L* x-rays	10	1,8	1800

Table 7. Design parameters of the planned cw-LINAC configuration for SHN research at GSI/FAIR. Reproduced from [569]. CC BY 3.0.

Mass/charge	6/1
Frequency	217 MHz
Max. beam current	1 mA
Injection energy	1.4 MeV/*u*
Output energy	3.5–7.5 MeV/*u*
Output energy spread	± 3 keV/*u*
Length of acceleration	12.7 m
Sc CH cavities	9
Sc solenoids	7

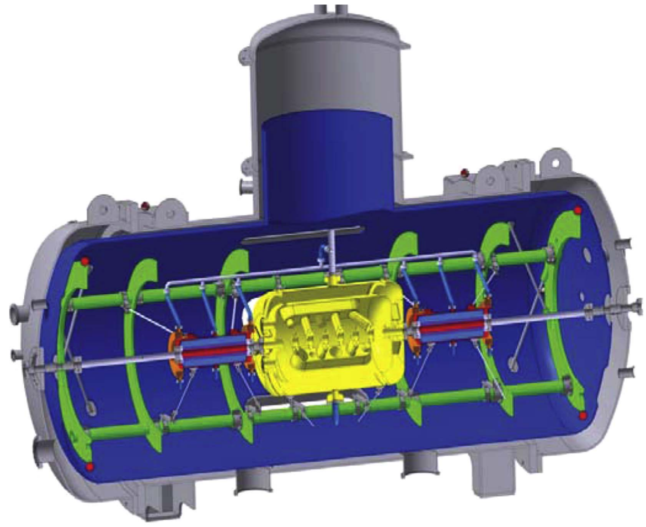

Figure 79. Scheme of the cw-LINAC Demonstrator with the CH-cavity (yellow) in its center in between two super conducting solenoids (red-orange). Reprinted from [569]. CC BY 3.0.

separator. The optics elements remain unchanged, therefore, it will have a Q_vQ_hD configuration with the possibility to choose different angles at the exit of the dipole (different bending angles) in order to optimize the performance as a function of the reaction kinematics. A test performed in 2009 validated the concept [563]: a transmission of ≈95% has been measured for the reaction ^{40}Ca + ^{150}Sm with a direct beam intensity larger than 10^{10}. A transmission × detection efficiency larger than 60% is expected for Ca+Pb like reactions using the 20 × 10 cm^2 MUSETT DSSD array [564]. VAMOS-GFS is intended to be coupled with AGATA [565], EXOGAM [566, 567] or the PARIS calorimeter [568].

5.1.3. The cw-LINAC project for GSI/FAIR. With the advent of the new facility FAIR at GSI, the existing GSI universal Linear Accelerator (UNILAC) will be adapted to the requirements of the new facility, losing its high duty cycle capabilities (presently 25%: 5 ms beam pulse length with a repetition rate of 50 Hz) which are essential for SHN research. As an injector for the synchrotrons of FAIR it will have in future short pulses at a low frequency of 1–3 Hz. As a consequence, a new dedicated accelerator project is presently under development. It will consist of a new superconducting 28 GHz full performance ECR ion source combined with an RFQ injection structure and a new continuous wave (cw) heavy ion LINAC. This high intensity/high duty cycle accelerator facility will serve for SHN research, with SHIP and TASCA, as well as material research, biophysics and plasma physics experiments at beam energies of several MeV. For more details of this project see [569], from which the design parameters of this machine are taken as listed in table 7.

A first linac demonstrator unit presently being tested at GSI is shown in figure 79 taken from [569]. It consists of a cryostat housing a superconducting CH-cavity in between two super conducting solenoids. The final complete cw-LINAC should have similar performance characteristics as the other two high intensity stable beam accelerator projects presently being constructed: the SHE-factory at FLNR in Dubna (see section 5.1.1) and the SC LINAC+S^3 at GANIL in Caen, France (see section 5.1.2).

5.1.4. AGFA at ANL. AGFA is the new Argonne Gas-Filled Analyzer [227]. It is a high acceptance gas-filled separator with a Q_vD configuration. According to simulations, a transmission × detection efficiency of ≈70% is expected for reactions of the Ca + Pb type. AGFA is intended to be coupled with GAMMASPHERE [359] in a first step and later with the GRETA γ-tracking array. AGFA will address the physics of VHN/SHN, proton-rich nuclei and the region around ^{100}Sn. In the nobelium region, a gain of a factor $\approx$5 in sensitivity is expected for AGFA and GAMMASPHERE compared to RITU and JUROGAM II, with the additional possibility to perform calorimetric measurements and to achieve a better coincidence efficiency. AGFA can also exploit the high-intense stable beams of the ATLAS accelerator for decay spectroscopy studies; a gain of a factor $\approx$100 is expected compared to the FMA using beam intensities up to 1 μA.

5.1.5. Gamma-ray tracking: AGATA and GRETA. While there are several ongoing projects of spectrometers/separators around the world, this is not the case for prompt γ arrays due to their high cost and complexity.

Increasing the prompt γ-ray efficiency and resolving power has always guided the design of new arrays. In the case of VHN/SHN studies, improving the energy resolution is not (yet) a priority while spectra are almost background-free. On the contrary the time selection is an important parameter to clean and isolate the γ-ray of interest from other background sources. Since the time-of-flight recoil dispersion exceeds the Ge detector time resolution, it is advantageous to measure the time with respect to the accelerator cycle (HF). However, Ge detectors have intrinsically a modest time resolution of $\approx$10 ns with little room for improvement. As discussed above, coincidence efficiency is important to build level schemes.

It should be noted that the coupling of the best prompt γ arrays with the most efficient spectrometers/separators is not necessarily realized not only for 'geographic' reasons, but also for practical reasons e.g. the target point of S^3 will be hardly compatible with a prompt array; the beam macro structure with its 20% duty cycle at SHIP is not suited for in-beam spectroscopy with its prompt count rate limitations, etc AGFA and VAMOS-GFS on the contrary are both intended (and to some extent designed) to be coupled with the state-of-the-art γ-tracking arrays GRETA and AGATA respectively, which will push down the detection limit to the sub-nb level for asymmetric reactions. As far as we are aware, the coupling of a high acceptance separator dedicated to very asymmetric reactions (Ne + U- like) with a high efficient prompt γ array is presently not foreseen.

As discussed in paragraph 3.4.1, the state-of-the-art Compton-suppressed arrays culminate in a photopeak efficiency of $\approx$10% at 1.3 MeV. AGATA and GRETA [565, 570], the new generation of Ge arrays are both based on the tracking concept and will have similar characteristics. The basic idea consists of building a Ge shell of over a hundred crystals. With this configuration and as soon as medium multiplicity cascades are emitted, the probability of Compton scattering between crystals (mostly adjacent) prevents individual γ-rays from being distinguished. The tracking principle is designed to determine the position and deposited energy for each interaction in the shell, which are subsequently analyzed by a tracking algorithm which traces back the original incident photon.

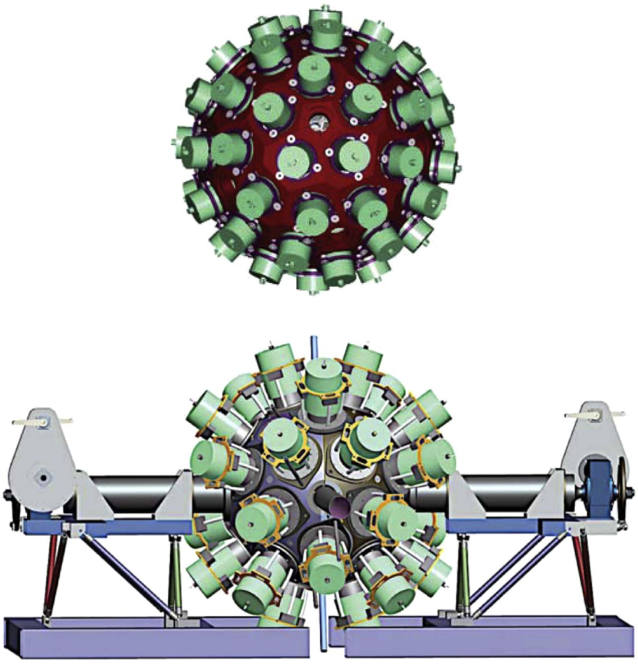

Figure 80. Design view of the 4π γ-tracking arrays AGATA (top) and GRETA (bottom). Courtesy of the AGATA and GRETA collaborations.

In order to determine the position of each interaction, the crystals are segmented in 6 slices and 6 sectors; corresponding to 36 segments for both AGATA and GRETA detectors. Since the corresponding position resolution is still not sufficient, the required resolution of few mm is achieved by pulse shape analysis of each segment's preamplifier signal. These signals are digitized typically at 100 MHz, 14 bits depth.

The AGATA and GRETA concepts are very similar. They are both based on hexagonal tapered crystals, ultimately 180 (120) packed in triples (quad) modules, corresponding to a total of 6480 (4320) segments for AGATA (GRETA), see figure 80. These configurations will result in a photopeak efficiency of $\approx$30% at 1 MeV for medium to high spin multiplicities. At the energies relevant for the study of VHN/SHN rotational bands, i.e. $E < 500$ keV, a higher efficiency of $\approx$40% is expected.

The implementation of the tracking concept has not only advantages in terms of photopeak and coincidence efficiency: the position resolution also provides a better angular resolution for Doppler correction. The determination of each interaction natively provides the possibility to perform polarimetry measurements. Also, the large detector coverage provides a calorimetric mode. Counting rate capabilities up to at least 50 kHz per crystal are possible thanks to the digital electronics.

Because of their complexity and cost, both GRETA (so far in its GRETINA early phase) and AGATA are built in evolutionary steps and are nomad between host laboratories to expand the physics panel. After a first implementation in

2011 at LBNL (in particular with the BGS), GRETINA moved at NSCL/MSU in 2012, then late 2013 to ANL, to NSCL in 2015, and back to ANL in 2017. AGATA was first installed at LNL from 2010 to 2011, at GSI in 2012 and 2013 and at GANIL since 2014 until 2019. Both physics cases of GRETA and AGATA include VHN/SHN research and a foreseen coupling with respectively AGFA and VAMOS-GFS.

It is possible to estimate the limits of sensitivity that can be reached using AGATA or GRETA coupled to the state of the art spectrometer or separator.

For the g.s. band of an even–even nucleus collecting ≈40% of the de-excitation flux, populated using a cold fusion-evaporation reaction ($A_{\mathrm{target}} = 208$, $500\,\mu\mathrm{g\,cm}^{-2}$ thick), a 100 pnA beam and 80% transmission for the residue, the total number of γ-rays collected in a two week long experiment is approximately $1.2\ 10^{12} \times \sigma$, with σ expressed in barn. If one assumes that 100 counts is the very minimum needed to observe a rotational band, the corresponding minimum cross section σ is 120 pb, i.e. Sg isotopes. As far as hot fusion-evaporation is concerned, a lower separator transmission of ≈20% can be assumed. The corresponding cross section limit is ≈600 pb, which corresponds to Rf isotopes. Without any technical breakthrough in the field, the prompt γ-ray study of the doubly magic deformed ^{270}Hs (cross section of ≈3 pb using the reaction ^{248}Cm + ^{24}Mg [571]) will be therefore out of reach.

Concerning odd nuclei, the de-excitation flux is more fragmented and γ–γ coincidences are valuable if not mandatory to disentangle a level scheme. We can roughly estimate that the cross section limit is 10 times higher compared to even–even nuclei, i.e. ≈1 nb for cold fusion-evaporation, corresponding to odd Sg isotopes. The spectroscopy of odd Db isotopes can also be envisaged using hot fusion-evaporation reactions.

5.2. Production and experimental techniques

Progress in science asks for new ideas and methods. Some of them considered presently for SHN research will be discussed in this subsection.

5.2.1. Isotope production. Without any exceptions, recent experiments on the spectroscopy of $Z \geqslant 100$ nuclei have been performed using fusion-evaporation reactions. These reactions have limitations in terms of cross-section and nuclei that can be accessed. Among the objectives of SHN research are the access to beta-stable nuclei, the production of nuclei around the doubly magic deformed ^{270}Hs at a substantial rate, and more generally of $N = 162$ isotopes, and finally to reach spherical magic isotopes.

Several new production mechanisms have been suggested to reach these goals. We will here briefly summarize those which might be relevant for spectroscopic studies.

Radioactive beams

It has been speculated since the 1990s that radioactive neutron-rich beams may be relevant for the synthesis of new SHE [572–574]. Details and references related to this question can be found in the comprehensive analysis of Loveland [575]. It has been as well speculated that using a neutron-rich beam may enhance the fusion-evaporation cross section. However, most theoretical estimates show that the cross section using these beams are at best similar compared to stable beams, see e.g. [575–583].

In order to estimate the production rates, it is important to take into account the fusion-evaporation cross sections, but also the predicted intensities of future radioactive beam facilities. An analysis of this problem has been performed by Hofmann [584] and later complemented by Loveland [575] using the expected intensities from the RIA facility. This project has been canceled in the meantime, but estimates can be scaled using intensities expected with other projects. In most cases, using cold asymmetric fusion reactions and a radioactive beam are not competitive with very asymmetric reactions and a stable beam. It is only using the most neutron-rich beams that new isotopes may be synthesized, with however production rates of less than 0.1 atom/day in the No region, with which spectroscopic studies will not be possible.

Symmetric reactions

Symmetric reactions have been suggested as an additional means to produce SHN, with the underlying objective of using neutron-rich Xe–Sn beams for synthesizing new isotopes. Predicted cross sections are however controversial [579, 581, 585–591]. Moreover, only an upper limit of 4 pb could be measured for the reaction ^{136}Xe + ^{136}Xe [592], while no event could be observed in the ^{124}Sn + ^{136}Xe reaction [593].

Multinucleon transfer reactions

As discussed above, a rather limited number of isotopes can be populated using fusion-evaporation reactions. An alternative to this process consists of using collisions above the Coulomb barrier up to ≈8 MeV/A, which can lead to the exchange of several nucleons between the projectile and the target, and therefore to access nuclei that cannot be populated using other means. These reactions are known in the literature either as multinucleon transfer (MNT) reactions, deep-inelastic collisions (DIC), deep-inelastic transfer (DIT), etc (for some authors MNT are considered as a particular case of deep-inelastic reactions while for others MNT reactions are intermediate between deep-inelastic and elastic collisions). For a recent review of the field see [594]. These reaction have been used since the 1970s to populate actinide elements, in particular on the right-side of the nuclear chart up to ^{256}Es, ^{257}Fm, ^{260}Md, ^{260}No, ^{262}Lr, see [595–597] and reference therein.

With MNT reactions, the production of the heaviest and most neutron-rich isotopes is favored using the heaviest target e.g. ^{248}Cm and a neutron-rich beam which favor the neutron flow between the projectile and the target e.g. ^{18}O, ^{48}Ca, ^{136}Xe, etc. In (multinucleon-)transfer reactions, the differential cross section is peaked around the grazing angle and broadens with the number of transferred nucleons. The nuclei of interest are therefore populated in a large angular and kinematic range which makes the use of a spectrometer positioned at the grazing angle rather inefficient, keeping also in mind that an on-line (A, Z) identification is a daunting task in this mass region. Experiments since the 1970s were

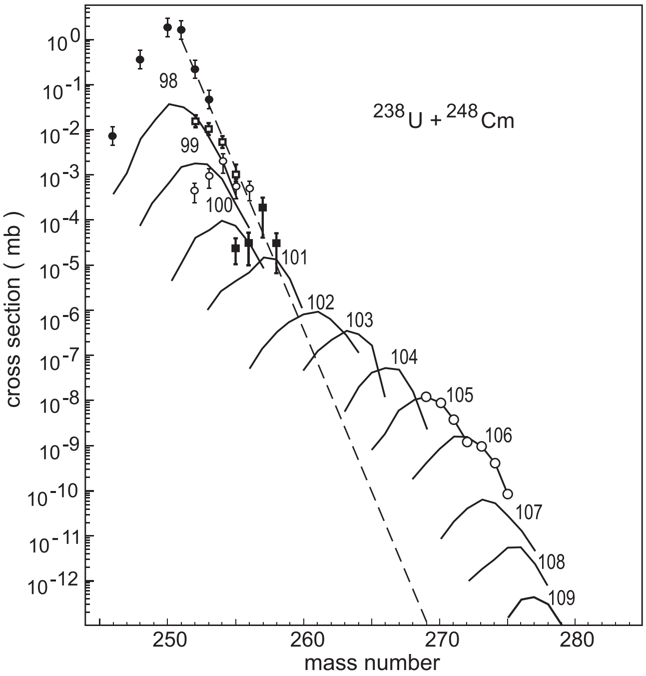

Figure 81. Cross section prediction using the collision of ^{238}U with ^{248}Cm at 800 MeV compared with experimental data from [598]. The dashed line corresponds to the trend expected without shell effects. Reprinted figure with permission from [581], Copyright (2008) by the American Physical Society.

therefore performed using radiochemical techniques, which have the advantage to integrate the production angles and to make the identification of long lived isotopes possible. Partly motivated by the search for the heaviest elements and new isotopes, the subject has been very fertile up to the 1980s.

There is a recent revival of interest for MNT reactions with calculations by Adamian *et al* [599] using the dinuclear system (DNS) concept and Zagrebaev *et al* [581, 600, 601] using Langevin-type dynamics. As shown in figure 81 taken from [581], the production of $Z = 106$ isotopes is predicted at the pb level, the increase of cross section compared to the exponential decrease as function of the mass being attributed to shell effects. Additionally promising is the prediction of substantial cross sections at forward angles [602] corresponding to head-on collisions.

More generally, the prediction by Adamian *et al* and Zagrebaev *et al* stimulated several new studies. On the theoretical side, calculations have been performed based on HFB [603–605], DNS [606], improved quantum molecular dynamics [607, 608] semi-classical description [609]. Experimental activities in this context are e.g. the study of the ^{238}U + ^{238}U collision using the VAMOS spectrometer [610], ^{160}Gd + ^{186}W using catcher foils [611], ^{197}Au + ^{232}Th using a superconducting solenoid time-of-flight spectrometer [612], ^{136}Xe + ^{208}Pb using the two-arm time-of-flight spectrometer CORSET [613], ^{136}Xe+^{198}Pt using VAMOS [614], ^{136}Xe + ^{208}Pb using GAMMASPHERE [615], and finally the investigation of a dedicated separator [616].

Recently, the ^{138}Xe + ^{238}U reaction has been studied using the γ ray detection arrays CLARA, AGATA and the PRISMA spectrometer at the grazing angle [617, 618]. Since only the beam-like products could be identified on an event-by-even basis, the selection of the heavy product (without decay-tagging possibility) turns out to be rather inefficient. However, new spectroscopic data have been obtained in ^{240}U: extension of the g.s. band and evidence for a $K^\pi = 0^-$ band interpreted as a collective octupole vibrational excitation [618].

Following calculations by Zagrebaev *et al*, the possibility to study MNT reactions using a zero degree separator was recently investigated at GSI with SHIP in a series of experiments using the reactions ^{58,64}Ni + ^{207}Pb [619], ^{48}Ca + ^{238}U [620] and ^{48}Ca + ^{248}Cm [621] at energies around the Coulomb barrier. Target-like nuclei were transmitted to the focal plane using the velocity filter capability of SHIP, and identified using their characteristic decay. The experiments demonstrate the effectiveness of a zero degree separator for the study of MNT reactions. It is important to note that the production of MNT close to zero degrees is not only a kinematic effect, but results from the reaction dynamics. Reaction channels down to ≈50 pb were measured and the new isotopes ^{216}U, ^{219}Np, ^{223,229}Am and ^{233}Bk could be observed in the ^{48}Ca + ^{248}Cm collisions. These experiments open interesting perspectives for decay and in-beam spectroscopy using MNT reactions, which will be inevitably developed in the future.

5.2.2. Lifetimes, electromagnetic moments, re-acceleration, direct reactions, etc.

As discussed in section 3.6, the electric quadrupole moment Q_{20} of deformed nuclei can be estimated in the No region via systematics of lifetimes as a function of the $E(2^+)$ energies ('Grodzin' and subsequent systematics) and relations between the electric quadrupole moment and the lifetime (23, 25). Even though these estimates are in good agreement with theoretical expectations, it would be valuable to measure the electric quadrupole moment more directly.

Lifetimes of collective states can be measured using the Recoil Distance Doppler Shift (RDDS) 'plunger' technique which is routinely used in conjunction with the R(D)T method. In the RDDS technique, a degrader is used to slow-down the recoils. The analysis as a function of the distance between the target and the degrader of the ratio of the partially shifted component (γ-ray emitted between the target and the degrader) and fully shifted component (γ-ray emitted after the degrader) provides the lifetime. RDDS experiments have been performed in conjunction with RITU down to the 40 μb level in ^{109}I using the symmetric reaction ^{58}Fe(^{54}Fe, $p2n$)^{109}I [622]. This case demonstrates that an experiment at the 2 μb level (^{254}No) should be feasible using a 1π tracking array, e.g. AGATA or GRETA coupled to a high transmission separator of the AGFA or VAMOS-GFS type. It should be noted that the presence of the degrader increases the angular dispersion of the recoils which has consequences for the separator transmission. Using inverse kinematics reactions would provide a better sensitivity, since the separator transmission would be higher and since the partially and fully shifted peaks are better separated. These reactions are however extremely challenging as far as the separator beam rejection is concerned.

The charge state plunger technique is an alternative for lifetime measurements [221]. This technique is based on the electronic conversion of low spin transitions. After conversion, the electronic structure is re-arranged with subsequent emission of x-rays, Auger and Koster–Croning electrons. As a consequence of Auger and Koster–Croning emission, the ion charge state increases. The principle is to place an 'equilibrium' or 'reset' foil after the target. If the transition occurs before the foil, it will reset the charge state to its initial value while in the opposite case the charge state will be higher. Analysis of the charge state distribution as of function of the distance between the target and the foil provides the (folded) lifetime of converted transitions. As mentioned in section 2.3, MARA is well suited for the implementation of this technique.

Mention should also be made of the conversion-electron detection using the recoil shadow method [222]. The principle is to screen the electron detection, which is at 90° with respect to the beam axis, using a mask placed between the target and the detection. Only electrons emitted after the mask can be detected. Converting the mask size into flight-time and changing its size subsequently enables measurement of the (folded) lifetime of converted transitions. Lifetimes at the sub-ns level can be measured in this way.

Coulomb excitation (Coulex) provides the most direct measurement of the electric quadrupole moment. Using the inverse kinematics reaction ^{48}Ca(^{208}Pb,2n)^{254}No, an energy of $\approx$3.1 MeV/A results for the residues. At this energy, the Coulomb excitation cross section on a Pb target is of $\approx$27, 11, 5 b for the 4^+, 6^+, 8^+ states, respectively [424]. However, a rather pure ^{254}No beam with a decent intensity of at least 10 ions s^{-1} should be delivered on the secondary target, which can only be achieved using a ^{208}Pb primary beam with an intensity at the pμA level, in conjunction with a high transmission separator with inverse kinematics capabilities. As far as we are aware, both requirements are not fulfilled by any existing or foreseen facility (the SC LINAC accelerator of SPIRAL2, Caen should provide in the future a pμA ^{208}Pb beam but the S^3 electric dipole is not suited for the high electric rigidities associated to inverse kinematics).

In lighter isotopes populated with higher cross section (via fusion-evaporation, transfer or eventually MNT), a re-acceleration of VHN/SHN can be envisaged. This is already possible at REX-ISOLDE up to at least Ra isotopes. An actinide beam factory would be beneficiary for Coulex experiments, but also for other techniques like direct reactions of the type $d(X, Y)p$ in inverse kinematics with the perspective to study nuclear structure and to measure spectroscopic factors via light particle spectroscopy.

In addition spectroscopic techniques used in other mass regions can also be transposed to the heaviest nuclei, provided that they are produced with sufficient yield, for instance time differential perturbed angular correlations in a magnetic field to measure the g-factors, atomic magnetic resonance [623], etc.

6. Conclusion and open questions

Pushing the frontiers of the nuclear landscape in the direction of mass and charge extremes has long been a driving subject of research. Since the 18th century, well before the quantum revolution, a considerable collection of literature has been devoted to the search and claim for new elements, see e.g. [624, 625]. With the discovery of the elementary constituents of atoms and the need to deploy energies, orders of magnitude larger than that of the chemical bonds, huge efforts have been devoted to build facilities and devices to transform, modify and probe nuclear matter. This corresponds to the 'big science' (r)evolution during and after the Second World War.

In the field of heavy elements several main directions were followed in parallel: (i) production of new elements and isotopes (ii) chemistry (iii) detailed spectroscopy of the heaviest possible atoms and nuclei. While these studies have important methodological differences, they basically require similar facilities and devices with the largest beam intensities, largest device transmission and selectivity, largest detection efficiency, fastest response, etc. Dedicated devices were specially designed for the SHN studies, just to cite SHIP at GSI, the DGFRS and VASSILISSA in Dubna, GARIS at RIKEN, and the BGS at LBNL. In the continuation of these efforts to continuously push the frontiers, new dedicated projects will soon be operational, namely the SHE factory in Dubna and the SC LINAC — S^3 combination at GANIL, Caen. This promises a wealth of new discoveries. The quest for the SHN island of stability is a tremendously difficult task; indeed, it is not even clear whether it will be ever possible to reach the corresponding isotopes. Spectroscopic information on the particular nuclear structure features of VHN and SHN can help to pave the path towards the superheavy species. It is crucial in characterizing this extreme form of nuclear matter. However, low production cross sections are also here an additional obstacle to go beyond the region of $Z \approx 100$ isotopes. The problem can be illustrated with the example of ^{254}No and ^{256}Rf, for which the production cross section drop by more than 2 orders of magnitudes from $\approx$2 μb to $\approx$10 nb.

Several prospects in the field of detailed spectroscopy have been discussed in this review. Advances and open question can be summarized as follows.

The study of single-particle states and low lying collective modes using decay spectroscopy is limited so far to production cross sections of few tens of pb, i.e. potentially $Z \approx 106$ at best. In the forthcoming years with new facilities, studies should reach the pb level corresponding to $Z \approx 116$ (Lv). In parallel, experimental developments should be made: for example target technologies should be developed in order to sustain the highest beam currents, experimental devices should be able to probe short lived nuclei or isomers in the sub μs range, etc.

The analysis of collective modes using prompt spectroscopy has recently reached the 10 nb limit. A new generation of Ge arrays based on digital electronics and/or γ tracking is being built, but it will be difficult to go beyond the nb limit ($Z \approx 106$) due to the rapid drop of the cross section and to the detector counting rate limitations. A technological breakthrough is therefore needed to overcome these limitations. Although only lighter nuclei can be accessed as with decay spectroscopy, the study of those deformed nuclei can provide information on heaviest nuclei through the down-sloping Nilsson orbitals. Prompt electron spectroscopy is still a recent tool for this region which certainly needs to be developed.

The exploration of K-isomers using either prompt or decay spectroscopy is a valuable approach for nuclear structure studies. Experimentally, their study is a ruse to observe states that would be hardly observed otherwise: the isomeric state itself but also those states fed by its decay. Their interpretation provide information on single particle states and in the case of high-K states with seniority larger than 2, they provide details of pairing correlations from zero to high rotational frequencies. Models also predict very long-lived isomers in the $Z \approx 110$ (Ds) region which are not only curiosities but also possible structures stabilizing SHN.

All spectroscopic data collected and interpreted are very promising ways to deduce in the next decades the location and properties of the island of stability. An intermediate milestone on this journey consists in making detailed studies around ^{270}Hs. All models agree on its deformed doubly magic character, but experimental data are needed to check the validity of the predictions. To reveal, how far this region of deformed nuclei extends, may help to anticipate the smoothness of the island of stability. In more heavy nuclei, the onset of sphericity will be a signal that one is approaching the island of stability.

Generally, experimental data feed the exchange with theory. Contrary to the lighter transfermiums, for the heavier SHN close to or on the island of stability, predictions can barely be compared because of the scarcity of isotopes and experimental data. As a consequence of the still very evident paucity of data, the question of the production of SHN in nature is still uncertain. While several assertions have been given in the past, it is now clear that there are too many uncertainties in the models (e.g. fission barrier height) to provide a sound answer.

The number of isotopes that can be accessed is modest due to the almost exclusive use of fusion-evaporation reactions and limited availability of beams and targets. Deep inelastic reactions provide probably the most promising and realistic way to extend the range of isotopes to be studied. Radioactive neutron-rich beams are potentially even more appealing but the needed intensities will probably not be available within at least one or two decades.

Techniques used in lighter mass regions are being- or need to be implemented in the VHN/SHN regions e.g. mass measurement, Coulomb excitation, direct reactions in inverse kinematics, laser spectroscopy (the ionization potential is a first step feeding the hope to measure nuclear moments in future), etc. The physics at the limits is not only a race towards the heaviest elements, but also towards details of nuclear structure features, precision measurements, g.s. property studies. The above-mentioned techniques, being presently under development or study, will provide complementary and extremely valuable information that, in particular, will feed the models. Here, nuclear physics also borrows advanced methods from adjacent fields such as atomic physics and chemistry.

On the theoretical side, many efforts have been devoted to SHN throughout the last half century. There is in general a good reproduction of spectroscopic data, but the main lesson of the last few years tells us that there is quite some room of improvement for EDF-based models, e.g. the non-reproduced $N = 152$, $Z = 100$ deformed magicity, the often occurring disagreement in level ordering or the generally too large level spacing. This in turn may cast doubts on some predictions of the SHN island of stability location and properties. The methodology and relevance of the models is however not subject of questioning on the basis of these experimental data. On the contrary the lesson is that the heaviest nuclei are more complex than expected and that there is a need to implement further effects, just to cite beyond mean-field correlations, and maybe to invent new still unsuspected paradigms.

Acknowledgments

We would like to thank all colleagues with whom we have been working on the topics discussed in this review, in particular A Chatillon, S Antalic, B Bally, M Bender, M Block, D Boilley, P Bonche, A Drouart, Th Duguet, PT Greenlees, S Heinz, S Hofmann, P-H Heenen, R-D Herzberg, FP Heßberger, J Khuyagbaatar, E Litvinova, AK Mistry, M Leino, A Lopez-Martens, J Piot, V Prassa, B Lu, P Reiter, M Sandzelius, J Sarén, H Savajols, M Schädel, D Seweryniak, B Sulignano, Ch Stodel, D Vretenar, the theory group from Bruyères-le-Châtel. We thank R Briselet, J Konki and B Sulignano for providing new data prior to publication, M Zielińska for Coulex calculations, M Zielińska and AK Mistry for a careful reading of the manuscript, and FP Heßberger for many fruitful discussions. One of us (DA) is supported by the European Commission in the framework of the CEA-EUROTALENT program.

ORCID

D Ackermann https://orcid.org/0000-0001-6284-1516
Ch Theisen https://orcid.org/0000-0002-8509-1022

References

[1] Becquerel H 1896 Sur les radiations émises par phosphorescence *C. R. Acad. Sci.* **122** 420–1
[2] Curie M and Curie P 1898 Sur une substance nouvelle radioactive contenue dans la pechblende *C. R. Acad. Sci.* **127** 175–8
[3] Curie P, Curie-Skodowska M and Bemont G 1898 Sur une nouvelle substance fortement radioactive contenue dans la pechblende *C. R. Acad. Sci.* **127** 1215
[4] Rutherford E 1899 Uranium radiation and the electrical conduction produced by it *Phil. Mag.* 5 **47** 109–63
[5] Rutherford E and Geiger H 1908 The charge and nature of the α-particle *Proc. R. Soc.* A **81** 162–73

[6] Becquerel A H 1900 Déviation du rayonnement du radium dans un champ électrique *C. R. Acad. Sci.* **130** 809–15

[7] Becquerel A H 1900 Note sur la transmission du rayonnement du radium au travers des corps *C. R. Acad. Sci.* **130** 979–84

[8] Rutherford E 1900 A radio-active substance emitted from thorium compounds *Phil. Mag.* 5 **49** 1–14

[9] Villard P 1900 Sur la réflexion et la réfraction des rayons cathodiques et des rayons déviables du radium *C. R. Acad. Sci.* **130** 1010–2

[10] Von Bayer O, Hahn O and Meitner L 1911 Über die β-strahlen des aktiven niederschlags des thoriums *Phys. Z.* **12** 1019

[11] Ellis C D 1921 The magnetic spectrum of the β-rays excited by γ-rays *Proc. R. Soc.* A **99** 261–71

[12] Ellis C D 1922 β-ray spectra and their meaning *Proc. R. Soc.* A **101** 1–17

[13] Hahn O 1921 Über ein neues radioaktives zerfallsprodukt im uran *Naturwissenschaften* **9** 84–84

[14] Rosenblum S 1929 Structure fine du spectre magnétique des rayons α du thorium C *C. R. Acad. Sci.* **188** 1401

[15] Hahn O and Strassmann F 1939 Über den nachweis und das verhalten der bei der bestrahlung des urans mittels neutronen entstehenden erdalkalimetalle *Naturwissenschaften* **27** 11–5

[16] Meitner L and Frisch O R 1939 Disintegration of uranium by neutrons: a new type of nuclear reaction *Nature* **143** 239–40

[17] Bohr N and Wheeler J A 1939 The mechanism of nuclear fission *Phys. Rev.* **56** 426–50

[18] Flerov and Petrjak 1940 Spontaneous fission of uranium *Phys. Rev.* **58** 89–89

[19] Wheeler J A 1955 Fission physics and nuclear theory *Proc. Int. Conf. on the Peaceful Uses of Atomic Energy* vol 2 *(Geneva)* pp 155–163, 220–229

[20] Wheeler J A 1955 Nuclear fission and nuclear stability *Niels Bohr and the Development of Physics* ed W Pauli *et al* (Oxford: Pergamon) pp 163–84

[21] Haxel O, Jensen J H D and Suess H E 1949 On the 'magic numbers' in nuclear structure *Phys. Rev.* **75** 1766–1766

[22] Mayer M G 1949 On closed shells in nuclei: II *Phys. Rev.* **75** 1969–70

[23] Mayer M G 1950 Nuclear configurations in the spin–orbit coupling model: I. Empirical evidence *Phys. Rev.* **78** 16–21

[24] Kragh H 2012 SHEs and the upper limit of the periodic table: early speculations *Eur. Phys. J.* H **38** 411–31

[25] Armbruster P 1996 Die synthese Überschwerer element *Spektrum der Wissenschaft* vol 12 (Heidelberg: Spektrum Verlag) pp 54–65

[26] Nilsson S G 1955 Binding states of individual nucleons in strongly deformed nuclei *Mat.-Fys. Medd.* **29** 16

[27] Scharff-Goldhaber G 1957 Nuclear physics *Nucleonics* **15** 123

[28] Armbruster P and Münzenberg G 2012 An experimental paradigm opening the world of SHEs *Eur. Phys. J.* H **37** 237–309

[29] Herrmann G 2014 Historical reminiscences: the pioneering years of SHEs research *The Chemistry of SHEs* (Berlin: Springer) pp 485–511

[30] Meldner H 1966 Predictions of new magic regions and masses for super-heavy nuclei from calculations with realistic shell model single particle Hamiltonians *Proc. Lysekil Symp. on Nucleides Far off the Stability line; Arkiv för Fysik* **36** 593

[31] Wong C Y 1966 Additional evidence of stability of the SHEs ^{310}126 according to the shell model *Phys. Lett.* **21** 688–90

[32] Sobiczewski A, Gareev F A and Kalinkin B N 1966 Closed shells for $Z > 82$ and $N > 126$ in a diffuse potential well *Phys. Lett.* **22** 500–2

[33] Myers W D and Swiatecki W J 1966 Nuclear masses and deformations *Nucl. Phys.* **81** 1

[34] Strutinsky V M 1967 Shell effects in nuclear masses and deformation energies *Nucl. Phys.* A **95** 420–42

[35] Strutinsky V M 1966 Microscopic caclulations of nucleon shell effects in the deformation energy of nuclei *Proc. Lysekil Symp. on Nucleides Far off the Stability Line; Arkiv för Fysik* **36** 629

[36] Nilsson S G, Nix J R, Sobiczewski A, Szymański Z, Wycech S, Gustafson C and Möller P 1968 On the spontaneous fission of nuclei with Z near 114 and N near 184 *Nucl. Phys.* A **115** 545–62

[37] Nilsson S G, Tsang C F, Sobiczewski A, Szymański Z, Wycech S, Gustafson C, Lamm I-L, Möller P and Nilsson B 1969 On the nuclear structure and stability of heavy and SHEs *Nucl. Phys.* A **131** 1–66

[38] Nilsson S G, Thompson S G and Tsang C F 1969 Stability of superheavy nuclei and their possible occurrence in nature *Phys. Lett.* B **28** 458–61

[39] Rost E 1968 Proton shell-model potentials for lead and the stability of superheavy nuclei *Phys. Lett.* B **26** 184–7

[40] Mosel U and Greiner W 1969 On the stability of superheavy nuclei against fission *Z. Phys.* **222** 261–82

[41] Grumann J, Mosel U, Fink B and Greiner W 1969 Investigation of the stability of superheavy nuclei around $Z = 114$ and $Z = 164$ *Z. Phys.* **228** 371–86

[42] Armbruster P 1985 On the production of heavy elements by cold fusion: the elements 106 to 109 *Annu. Rev. Nucl. Part. Sci.* **35** 135–94

[43] Flerov G N and Ter-Akopian G M 1985 SHEs *Treatise on Heavy-Ion Science* vol 4 (New York: Plenum Press) pp 331–99

[44] Seaborg G T and Loveland W D 1985 Transuranium nuclei *In Treatise on Heavy-Ion Science* vol 4 (New York: Plenum Press) pp 253–330

[45] Gol'danskii V I and Polikanov S M 1995 *The Transuranium Elements* (New York: Consultant Bureau) (https://doi.org/10.1007/978-1-4684-8381-9)

[46] Hofmann S 1998 New elements—approaching $Z = 114$ *Rep. Prog. Phys.* **61** 639–89

[47] Münzenberg G 1988 Recent advances in the discovery of transuranium elements *Rep. Prog. Phys.* **51** 57–104

[48] Armbruster P 2000 On the production of SHEs *Ann. Rev. Nucl. Part. Sci.* **0** 411–79

[49] Hofmann S and Münzenberg G 2000 The discovery of the heaviest elements *Rev. Mod. Phys.* **72** 733–67

[50] Hoffman D C, Ghiorso A and Seaborg G T 2000 *The Transuranium People: The Inside Story* (Singapore: World Scientific)

[51] Hofmann S 2002 *On Beyond Uranium: Journey to the End of the Periodic Table* (Boca Raton, FL: CRC Press)

[52] Armbruster P 2003 On the production of SHEs *C. R. Phys.* **4** 571–94

[53] Münzenberg G 2004 The structure of heavy nuclei—from lead to SHEs *Extended Density Functionals in Nuclear Structure Physics* (Berlin: Springer) pp 337–71

[54] Oganessian Y 2007 Heaviest nuclei from 48Ca-induced reactions *J. Phys. G: Nucl. Part. Phys.* **34** R165–242

[55] Hofmann S 2009 SHEs *The Euroschool Lectures on Physics with Exotic Beams, vol III* (Berlin: Springer) pp 203–52

[56] Hofmann S 2015 Super-heavy nuclei *J. Phys. G: Nucl. Part. Phys.* **42** 114001

[57] Oganessian Y T, Sobiczewski A and Ter-Akopian G M 2017 Superheavy nuclei: from predictions to discovery *Phys. Scr.* **92** 023003

[58] 2015 Special issue on superheavy elements *Nucl. Phys.* A **944** 1–690

[59] 2016 Proc. of the nobel symposium NS 160 chemistry and physics of heavy and SHEs *EPJ Web of Conf.* **131**

[60] Rainwater J 1950 Nuclear energy level argument for a spheroidal nuclear model *Phys. Rev.* **79** 432–4

[61] Bohr A 1951 On the quantization of angular momenta in heavy nuclei *Phys. Rev.* **81** 134–8

[62] Bohr A 1952 The coupling of nuclear surface oscillations to the motion of individual nucleons *Mat.-Fys. Medd.* **26** 14

[63] Bohr A and Mottelson B R 1953 Interpretation of isomeric transitions of electric quadrupole type *Phys. Rev.* **89** 316–7

[64] Bohr A and Mottelson B R 1953 Rotational states in even–even nuclei *Phys. Rev.* **90** 717–9

[65] Bohr A and Mottelson B R 1953 Collective and individual-particle aspects of nuclear structure *Mat.-Fys. Medd.* **27** 16

[66] Alaga G, Alder K, Bohr A and Mottelson B R 1955 Intensity rules for beta and gamma transitions to nuclear rotational states *Mat.-Fys. Medd.* **29** 9

[67] Bohr A and Mottelson B R 1955 Moments of inertia of rotating nuclei *Mat.-Fys. Medd.* **30** 1

[68] Bohr A and Mottelson B R 1969 *Nuclear Structure vol I* 1998, 1999, 2008, 1969

[69] Bohr A and Mottelson B R 1975 *Nuclear Structure vol II* 1998, 1999, 2008, 1975

[70] Bohr A and Mottelson B R 1974 Some current themes in nuclear research *Phys. Scr.* **10** 13

[71] Gamow G 1930 Mass defect curve and nuclear constitution *Proc. R. Soc.* A **126** 632–44

[72] Heisenberg M W 1984 Considérations théoriques générales sur la Structure du Noyau *Scientific Review Papers, Talks, and Books Wissenschaftliche Übersichtsartikel, Vorträge und Bücher* (Berlin: Springer) pp 179–225

[73] Weizsäcker V 1935 Zur theorie der kernmassen *Z. Phys.* **96** 431–58

[74] Bethe H A and Bacher R F 1936 Nuclear physics A. Stationary states of nuclei *Rev. Mod. Phys.* **8** 82–229

[75] Stuewer R H 1994 The origin of the liquid-drop model and the interpretation of nuclear fission *Perspect. Sci.* **2** 76–129

[76] Mottelson B R 1999 Why are nuclei described by independent particle motion? *Nucl. Phys.* A **649** 45c

[77] Vogel P 2000 Pairing and symmetry energy in $N \approx Z$ nuclei *Nucl. Phys.* A **662** 148–54

[78] Swiatecki W J 1994 Nuclear physics: Macroscopic aspects *Nucl. Phys.* A **574** 233–51

[79] Möller P, Nix J R, Myers W D and Swiatecki W J 1995 Nuclear g.s. masses and deformations *At. Data Nucl. Data Tables* **59** 185–381

[80] Pomorski K and Dudek J 2003 Nuclear liquid-drop model and surface-curvature effects *Phys. Rev.* C **67** 044316

[81] Pomorski K 2013 Fission-barrier heights in some newest liquid-drop models *Phys. Scr.* **2013** 014023

[82] Green A E S 1955 *Nuclear Physics* (New York: McGraw-Hill)

[83] Ragnarsson I and Nilsson S G 1995 *Shapes and Shells in Nuclear Structure* (Cambridge: Cambridge University Press) (https://doi.org/10.1017/CBO9780511563973)

[84] Nix J R 1967 The normal modes of oscillation of a uniformly charged drop about its saddle-point shape *Ann. Phys., NY* **41** 52–107

[85] Vandenbosch R and Huizenga J R 1973 *Nuclear Fission* (New York: Academic)

[86] Weigmann H and Theobald J P 1972 Evaluation of fission barrier parameters from near-barrier fission and isomeric half-life data *Nucl. Phys.* A **187** 305–13

[87] Dahlinger M, Vermeulen D and Schmidt K-H 1982 Empirical saddle-point and g.s. masses as a probe of the droplet model *Nucl. Phys.* A **376** 94–130

[88] Henning G *et al* 2014 Fission barrier of superheavy nuclei and persistence of shell effects at high spin: Cases of ^{254}No and ^{220}Th *Phys. Rev. Lett.* **113** 262505

[89] Holden N E and Hoffman D C 2000 Spontaneous fission half-lives for g.s. nuclide (technical report) *Pure Appl. Chem.* **72** 1525–62

[90] Swiatecki W J 1955 Systematics of spontaneous fission half-lives *Phys. Rev.* **100** 937–8

[91] Wapstra A H 1991 Criteria that must be satisfied for the discovery of a new chemical element to be recognized *Pure Appl. Chem.* **63** 879–86

[92] Cohen S, Plasil F and Swiatecki W J 1974 Equilibrium configurations of rotating charged or gravitating liquid masses with surface tension: II *Ann. Phys., NY* **82** 557–96

[93] Bartlett J H 1932 Structure of atomic nuclei *Phys. Rev.* **41** 370–1

[94] Bartlett J H 1932 Structure of atomic nuclei: II *Phys. Rev.* **42** 145–6

[95] Elsasser W M 1933 Sur le principe de Pauli dans les noyaux *J. Phys. Radium* **4** 549–56

[96] Elsasser W M 1934 Sur le principe de Pauli dans les noyaux —II *J. Phys. Radium* **5** 389–97

[97] Elsasser W M 1934 Sur le principe de Pauli dans les noyaux —III *J. Phys. Radium* **5** 635–9

[98] Guggenheimer K 1934 Remarques sur la constitution des noyaux atomiques—I *J. Phys. Radium* **5** 253–6

[99] Guggenheimer K 1934 Remarques sur la constitution des noyaux—II *J. Phys. Radium* **5** 475–85

[100] Mottelson B R 1998 Elementary features of nuclear structure *Trends in Nuclear Physics. 100 Years Later* ed H Nifenecker *et al* (Amsterdam: North-Holland) pp 25–121

[101] Strutinsky V M, Magner A G, Ofengenden S R and Døssing T 1977 Semiclassical interpretation of the gross-shell structure in deformed nuclei *Z. Phys.* A **283** 269–85

[102] Hartree D R 1928 The wave mechanics of an atom with a non-Coulomb central field: I. Theory and methods *Math. Proc. Camb. Phil. Soc.* **24** 89–110

[103] Hartree D R 1928 The wave mechanics of an atom with a non-Coulomb central field: II. Some results and discussion *Math. Proc. Camb. Phil. Soc.* **24** 111–32

[104] Hartree D R 1928 The wave mechanics of an atom with a non-Coulomb central field: III. Term values and intensities in series in optical spectra *Math. Proc. Camb. Phil. Soc.* **24** 426–37

[105] Fock V 1930 Näherungsmethode zur lösung des quantenmechanischen mehrkörperproblems *Z. Phys.* **61** 126–48

[106] Duerr H-P 1956 Relativistic effects in nuclear forces *Phys. Rev.* **103** 469–80

[107] Skyrme T H R 1956 The nuclear surface *Phil. Mag.* **1** 1043–54

[108] Vautherin D and Brink D M 1970 Hartree–Fock calculations with Skyrme's interaction *Phys. Lett.* B **32** 149–53

[109] Vautherin D, Veneroni M and Brink D M 1970 A Hartree–Fock calculation for the stability of super-heavy nuclei *Phys. Lett.* B **33** 381–4

[110] Dechargé J and Gogny D 1980 Hartree–Fock–Bogolyubov calculations with the D1 effective interaction on spherical nuclei *Phys. Rev.* C **21** 1568–93

[111] Davies K T R and McCarthy R J 1971 Brueckner–Hartree–Fock calculations of spherical nuclei in a harmonic-oscillator Basis: III. Renormalized calculations using the reid potential *Phys. Rev.* C **4** 81–97

[112] Köhler H S 1971 Nuclear masses, shell-model and superheavy nuclei: I *Nucl. Phys.* A **162** 385–406

[113] Bassichis W H and Kerman A K 1972 Note on self-consistent calculation of shell effects *Phys. Rev.* C **6** 370–2

[114] Rouben B, Pearson J M and Saunier G 1972 Hartree–Fock calculation of superheavy magic numbers *Phys. Lett.* B **42** 385–8

[115] Saunier G and Rouben B 1972 Superheavy Hartree–Fock Calculations *Phys. Rev.* C **6** 591–5

[116] Beiner M, Flocard H, Veneroni M and Quentin P 1974 On the stability of super-heavy nuclei: Some recent results of self-consistent calculations *Phys. Scr.* **10** 84

[117] Brack M and Quentin P 1974 Disappearance of shell effects at high excitation. self-consistent calculations at finite temperatures *Phys. Scr.* **10** 163

[118] Cusson R Y, Trivedi H P, Meldner H W, Weiss M W and Wright R E 1976 Self-consistent K-matrix-model calculation for finite and superheavy nuclei *Phys. Rev.* C **14** 1615–29

[119] Vallières M and Sprung D W L 1977 Hartree–Fock calculations of super-heavy nuclei *Phys. Lett.* B **67** 253–6

[120] Rouben B, Brut F, Pearson J M and Saunier G 1977 Superheavy Hartree–Fock calculations for magic numbers $Z = 126$ and 138 *Phys. Lett.* B **70** 6–8

[121] Kolb D 1977 Shell structure in the mass region $250 \leqq A \leqq 500$ *Z. Phys.* A **280** 143–7

[122] Tondeur F 1978 Extrapolation of a self-consistent energy density mass formula to the superheavy region and to the neutron drip line *Z. Phys.* A **288** 97–101

[123] Tondeur F 1980 Shell structure and stability of nuclei with $270 < A < 500$ and the possible existence of primordial superheavy nuclei *Z. Phys.* A **297** 61–71

[124] Berger J-F, Bitaud L, Decharge J, Girod M and Peru-Desenfants S 1996 Microscopic analysis of supeheavy elements and 66-78Ni with the Gogny force *Proc. Int. Workshop XXIV on Gross Properties of Nuclei and Nuclear Excitation (Hirschegg, Austria, 15–20, January 1996)* ed H Feldmeier *et al* (GSI) pp 43–55

[125] Gambhir Y K, Ring P and Thimet A 1990 Relativistic mean field theory for finite nuclei *Ann. Phys., NY* **198** 132–79

[126] Boersma H F 1993 Relativistic calculations of the superheavy nucleus $^{298}114$ *Phys. Rev.* C **48** 472–3

[127] Ćwiok S, Dobaczewski J, Heenen P-H, Magierski P and Nazarewicz W 1996 Shell structure of the SHEs *Nucl. Phys.* A **611** 211–46

[128] Rutz K, Bender M, Bürvenich T, Schilling T, Reinhard P-G, Maruhn J A and Greiner W 1997 Superheavy nuclei in self-consistent nuclear calculations *Phys. Rev.* C **56** 238–43

[129] Bürvenich T, Rutz K, Bender M, Reinhard P-G, Maruhn J A and Greiner W 1998 Superheavy nuclei in deformed mean-field calculations *Eur. Phys. J.* A **3** 139–47

[130] Bender M, Rutz K, Reinhard P-G, Maruhn J A and Greiner W 1999 Shell structure of superheavy nuclei in self-consistent mean-field models *Phys. Rev.* C **60** 034304

[131] Agbemava S E, Afanasjev A V, Nakatsukasa T and Ring P 2015 Covariant density functional theory: reexamining the structure of superheavy nuclei *Phys. Rev.* C **92** 054310

[132] Afanasjev A V and Frauendorf S 2005 Central depression in nuclear density and its consequences for the shell structure of superheavy nuclei *Phys. Rev.* C **71** 024308

[133] Wilson H A 1946 A spherical shell nuclear model *Phys. Rev.* **69** 538

[134] Wong C Y 1972 Bubble nuclei *Phys. Lett.* B **41** 451–4

[135] Beiner M and Lombard R J 1973 Bubble density distributions in spherical nuclei *Phys. Lett.* B **47** 399–404

[136] Dietrich K and Pomorski K 1997 On the shell structure of nuclear bubbles *Nucl. Phys.* A **627** 175–221

[137] Dietrich K and Pomorski K 1998 Stability of bubble nuclei through shell effects *Phys. Rev. Lett.* **80** 37–40

[138] Dechargé J, Berger J-F, Dietrich K and Weiss M S 1999 Superheavy and hyperheavy nuclei in the form of bubbles or semi-bubbles *Phys. Lett.* B **451** 275–82

[139] Yu Y, Bulgac A and Magierski P 2000 Shell correction energy for bubble nuclei *Phys. Rev. Lett.* **84** 412–5

[140] Mutschler A *et al* 2016 A proton density bubble in the doubly magic ^{34}Si nucleus *Nat. Phys.* **13** 152–6

[141] Bender M, Nazarewicz W and Reinhard P-G 2001 Shell stabilization of super- anmd hyperheavy nuclei without magic gaps *Phys. Lett.* B **515** 42–8

[142] Dobaczewski J, Afanasjev A V, Bender M, Robledo L M and Shi Y 2015 Properties of nuclei in the nobelium region studied within the covariant, Skyrme, and Gogny energy density functionals *Nucl. Phys.* A **944** 388–414

[143] Afanasjev A V, Khoo T L, Frauendorf S, Lalazissis G A and Ahmad I 2003 Cranked relativistic Hartree–Bogoliubov theory: Probing the gateway to superheavy nuclei *Phys. Rev.* C **67** 024309

[144] Agbemava S E, Afanasjev A V, Nakatsukasa T and Ring P 2015 Covariant density functional theory: reexamining the structure of superheavy nuclei *Phys. Rev.* C **92** 054310

[145] Schüler H and Schmidt T 1935 Über abweichungen des atomkerns von der kugelsymmetrie *Z. Phys.* **94** 457–68

[146] Heyde K and Wood J L 2016 Nuclear shapes: from earliest ideas to multiple shape coexisting structures *Phys. Scr.* **91** 083008

[147] Casimir H 1935 Über die hyperfeinstruktur des europiums *Physica* **2** 719–23

[148] Pauli W 1924 Zur frage der theoretischen deutung der satelliten einiger spektrallinien und ihrer beeinflussung durch magnetische felder *Naturwissenschaften* **12** 741–3

[149] Bohr N and Kalckar F 1937 On the transmutation of atomic nuclei by impact of material particles *Mat.-Fys. Medd.* **14** 10

[150] Townes C H, Foley H M and Low W 1949 Nuclear quadrupole moments and nuclear shell structure *Phys. Rev.* **76** 1415–6

[151] Burson S B, Blair K W, Keller H B and Wexler S 1951 The radiations from hafnium *Phys. Rev.* **83** 62–8

[152] Ghiorso A, Thompson S G, Higgins G H, Harvey B G and Seaborg G T 1954 Evidence for subshell at $N = 152$ *Phys. Rev.* **95** 293–5

[153] Wang M, Audi G, Wapstra A H, Kondev F G, MacCormick M, Xu X and Pfeiffer B 2012 The Ame2012 atomic mass evaluation *Chin. Phys.* C **36** 1603

[154] ENSDF: Evaluated Nuclear Structure Data File http://nndc.bnl.gov/ensdf

[155] Sobiczewski A and Pomorski K 2007 Description of structure and properties of superheavy nuclei *Prog. Part. Nucl. Phys.* **58** 292–349

[156] Polikanov S M, Druin V A, Karnaukhov V A, Mikheev V L, Pleve A A, Skobelev N K, Subbotin V G, Terakopyan G M and Fomichev V A 1962 Spontaneous fission with an anomalously short period: I *Sov. Phys.—JETP* **15** 1016–21

[157] Oganessian Y T and Utyonkov V K 2015 Superheavy nuclei from 48Ca-induced reactions *Nucl. Phys.* A **944** 62–98

[158] Chasman R R, Ahmad I, Friedman A M and Erskine J R 1977 Survey of single-particle states in the mass region $A > 228$ *Rev. Mod. Phys.* **49** 833–91

[159] Chasman R R and Ahmad I 1997 Nuclear structure at $A \sim 250$ and the stability of the SHEs *Phys. Lett.* B **392** 255–61

[160] Ćwiok S, Hofmann S and Nazarewicz W 1994 Shell structure of the heaviest elements *Nucl. Phys.* A **573** 356–94

[161] Ramirez E M *et al* 2012 Direct mapping of nuclear shell effects in the heaviest elements *Science* **337** 1207–10

[162] Muntian I, Patyk Z and Sobiczewski A 2003 Calculated masses of heaviest nuclei *Phys. At. Nuclei* **66** 1015–9

[163] Zhang W, Meng J, Zhang S Q, Geng L S and Toki H 2005 Magic numbers for superheavy nuclei in relativistic continuum Hartree–Bogoliubov theory *Nucl. Phys.* A **753** 106–35

[164] Muntian I, Hofmann S, Patyk Z and Sobiczewski A 2003 Properties of heaviest nuclei *Acta Phys. Pol.* B **34** 2073

[165] Wapstra A H, Audi G and Thibault C 2003 The AME2003 atomic mass evaluation: I. Evaluation of input data, adjustment procedures *Nucl. Phys.* A **729** 129–336

[166] Litvinova E V 2012 Quasiparticle-vibration coupling in a relativistic framework: shell structure of $Z = 120$ isotopes *Phys. Rev.* C **85** 021303(R)

[167] Greenlees P T *et al* 2012 Shell-structure and pairing interaction in superheavy nuclei: rotational properties of the $Z = 104$ nucleus ^{256}Rf *Phys. Rev. Lett.* **109** 012501

[168] Hofmann S *et al* 2007 The reaction ^{48}Ca + ^{238}U → ^{286}112* studied at the GSI-SHIP *Eur. Phys. J.* A **32** 251–60

[169] Düllmann C E *et al* 2010 Production and decay of element 114: high cross sections and the new nucleus ^{277}Hs *Phys. Rev. Lett.* **104** 252701

[170] Gates J M *et al* 2011 First SHEs experiments at the GSI recoil separator TASCA: the production and decay of element 114 in the ^{244}Pu(^{48}Ca,3-4n) reaction *Phys. Rev.* C **83** 054618

[171] Hofmann S *et al* 2012 The reaction ^{48}Ca. ^{248}Cm → ^{296}116* studied at the GSI-SHIP *Eur. Phys. J.* A **48** 62

[172] Khuyagbaatar J *et al* 2014 ^{48}Ca +^{249} Bk fusion reaction leading to element $Z = 117$: long-lived α-decaying ^{270}Db and discovery of ^{266}Lr *Phys. Rev. Lett.* **112** 172501

[173] Morita K *et al* 2012 New result in the production and decay of an isotope and ^{278}113 and of the 113th element *J. Phys. Soc. Japan* **81** 103201

[174] Asai M, Heßberger F P and Lopez-Martens A 2015 Nuclear structure of elements with $100 \leqslant Z \leqslant 109$ from alpha spectroscopy *Nucl. Phys.* A **944** 308–32

[175] Ackermann D 2015 Nuclear spectroscopy in nuclei with $Z \geqslant 110$ *Nucl. Phys.* A **944** 376–87

[176] Gamow G Z 1930 Fine structure of α-rays *Nature* **126** 397

[177] Black D H 1925 β ray spectra of thorium disintegration products *Proc. R. Soc.* A **109** 166–76

[178] Ahmad I, Friedman A M, Barnes R F, Sjoblom R K, Milsted J and Fields P R 1967 Decay of Fm^{253} *Phys. Rev.* **164** 1537–44

[179] Ahmad I, Porter F T, Freedman M S, Barnes R F, Sjoblom R K, Wagner F, Milsted J and Fields P R 1971 Energy Levels in Cf-251 via alpha decay of Fm-255 *Phys. Rev.* C **3** 390–407

[180] Ahmad I, Milsted J, Sjoblom R K, Lerner J and Fields P R 1973 Alpha decay of ^{251}Fm *Phys. Rev.* C **8** 737–44

[181] Ahmad I and Horwitz E P 1982 Alpha decay of $^{257}_{100}$ Fm *Nucl. Phys.* A **373** 434–44

[182] Bemis C E, Silva R J, Hensley D C, Keller O L, Tarrant J R, Hunt L D, Dittner P F, Hahn R L and Goodman C D 1973 x-ray identification of element 104 *Phys. Rev. Lett.* **31** 647–50

[183] Bemis C E, Dittner P F, Silva R J, Hahn R L, Tarrant J R, Hunt L D and Hensley D C 1977 Production, L x-ray identification, and decay of the nuclide ^{260}105 *Phys. Rev.* C **16** 1146–58

[184] Magill J, Pfennig G, Dreher R and Sóti Z 2015 *Karlsruher Nuklidkarte/Chart of the Nuclides* 9th edn (Eggenstein-Leopoldshafen: Nucleonica GmbH)

[185] Moseley H G J 1913 XCIII. The high-frequency spectra of the elements *London, Edinburgh, Dublin Phil. Mag. J. Sci.* **26** 1024–34

[186] Moseley H G J 1914 LXXX. The high-frequency spectra of the elements: II *London, Edinburgh, Dublin Phil. Mag. J. Sci.* **27** 703–13

[187] Heßberger F P *et al* 2009 Decay properties of neutron-deficient isotopes of elements from $Z = 101$ to $Z = 108$ *Eur. Phys. J.* A **41** 145–53

[188] Rudolph D *et al* 2013 Spectroscopy of element 115 decay chains *Phys. Rev. Lett.* **111** 112502

[189] Karol P J, Barber R C, Sherrill B M, Vardaci E and Yamazaki T 2016 Discovery of the elements with atomic numbers $Z = 113$, 115 and 117 (IUPAC technical report) *Pure Appl. Chem.* **88** 139–53

[190] Karol P J, Barber R C, Sherrill B M, Vardaci E and Yamazaki T 2016 Discovery of the element with atomic number $Z = 118$ completing the 7th row of the periodic table (IUPAC technical report) *Pure Appl. Chem.* **88** 155–60

[191] Theisen C, Lopez-Martens A and Bonnelle C 2008 Internal conversion and summing effects in heavy-nuclei spectroscopy *Nucl. Instrum. Methods Phys. Res.* A **589** 230–42

[192] Jones G D 2002 Detection of long-lived isomers in super-heavy elements *Nucl. Instrum. Methods Phys. Res.* A **488** 471–2

[193] Weale J W 1955 Alpha–gamma angular correlations and internal conversion measurements in ThCC” and ThC’D *Proc. Phys. Soc.* A **68** 35

[194] Hutchinson J M R 1967 Alpha-gamma angular correlations in three heavy odd-*A* nuclides *Phys. Rev.* **157** 1093–8

[195] Gerholm T R and Holmberg L 1971 Conversion electron correlations in nuclear structure research *Angular Correlations in Nuclear Disintegration: Proc. Int. Conf. on Angular Correlations in Nuclear Disintegration Delft (The Netherlands, 17–22 August 1970)* (Dordrecht: Springer) pp 120–56

[196] Jones G D, Hoare T H, Butler P A and White C A 1991 A compact apparatus for alpha—gamma , alpha -e K,L,M angular correlation and internal conversion coefficient measurements *J. Phys. G: Nucl. Part. Phys.* **17** 713

[197] Morss L R, Edelstein N M and Fuger J 2010 *The Chemistry of the Actinide and Transactinide Elements (Set 1–6): volumes 1–6* vol 1 (Dordrecht: Springer) (https://doi.org/10.1007/978-94-007-0211-0)

[198] Ichikawa S, Tsukada K, Asai M, Haba H, Sakama M, Kojima Y, Shibata M, Nagame Y, Oura Y and Kawade K 2002 Performance of the multiple target He/PbI2 aerosol jet system for mass separation of neutron-deficient actinide isotopes *Nucl. Instrum. Methods* B **187** 548–54

[199] Nagame Y *et al* 2003 Heavy element nuclear chemistry at JAERI *Phys. At. Nuclei* **66** 1131–6

[200] Asai M *et al* 2005 Experimental identification of spin-parities and single-particle configurations in ^{257}No and its α-decay daughter ^{253}Fm *Phys. Rev. Lett.* **95** 102502

[201] Türler A, Eichler R and Yakushev A 2015 Chemical studies of elements with $Z \geqslant 104$ in gas phase *Nucl. Phys.* A **944** 640–89

[202] Cohen B L and Fulmer C B 1958 Fission-fragment mass separator and the nuclear charge distribution of fission fragments of a single mass *Nucl. Phys.* **6** 547–60

[203] Bohr N 1940 Scattering and stopping of fission fragments *Phys. Rev.* **58** 654–5

[204] Leino M 1997 In-flight separation with gas-filled systems *Int. Conf. on Electromagnetic Isotope Separators and Techniques Related to Their Applications; Nucl. Instrum. Methods Phys. Res.* B **126** 320–8

[205] Leino M 2003 Gas-filled separators—an overview *14th Int. Conf. on Electromagnetic Isotope Separators and Techniques Related to their Applications; Nucl. Instrum. Methods Phys. Res.* **204** 129–37

[206] Tsyganov Y S 1999 The Dubna gas-filled recoil separator: status and developments *J. Phys. G: Nucl. Part. Phys.* **25** 937

[207] Morita K *et al* 1992 RIKEN isotope separator on-line GARIS/IGISOL *Nucl. Instrum. Methods* B **70** 220–5

[208] Ninov V, Gregorich K E and McGrath C A 1998 The Berkeley gas-filled separator *AIP Conf. Proc.* **455** 704–7

[209] Leino M *et al* 1995 Gas-filled recoil separator for studies of heavy elements *Nucl. Instrum. Methods* B **99** 653–6

[210] Sarén J, Uusitalo J, Leino M and Sorri J 2011 Absolute transmission and separation properties of the gas-filled recoil separator RITU *Nucl. Instrum. Methods Phys. Res.* A **654** 508–21

[211] Zhang Z Y *et al* 2013 A gas-filled recoil separator, SHANS *16th Int. Conf. on ElectroMagnetic Isotope Separators and Techniques Related to their Applications (Matsue, Japan, 27 December 2012); Nucl. Instrum. Methods Phys. Res.* B **317** 315–8

[212] Semchenkov A *et al* 2008 The transactinide separator and chemistry apparatus TASCA at GSI-optimization of ion-optical structures and magnet designs *Nucl. Instrum. Methods* B **266** 4153–61

[213] Münzenberg G, Faust W, Hofmann S, Armbruster P, Güttner K and Ewald H 1979 The velocity filter SHIP and a separator of unslowed heavy ion fusion products *Nucl. Instrum. Methods* **161** 65–82

[214] Grévy S *et al* 2002 Production of super heavy elements at GANIL: present status and perspectives *J. Nucl. Radiochem. Sci.* **3** 9–12

[215] Yeremin A, Malyshev O, Popeko A, Chepigin V, Svirikhin A, Lopez-Martens A, Hauschild K, Dorvaux O, Gall B and Gehlot J 2015 First experimental tests of the kinematic separator SHELS (separator for heavy element spectroscopy) *EPJ Web Conf.* **86** 00065

[216] Yeremin A V *et al* 2015 Experimental tests of the modernized VASSILISSA separator (SHELS) with the use of accelerated ^{50}Ti ions *Phys. Part. Nuclei Lett.* **12** 43–7

[217] Popeko A G *et al* 2016 Separator for heavy element spectroscopy—velocity filter SHELS *Proc. 17th Int. Conf. on Electromagnetic Isotope Separators and Related Topics (EMIS2015) (Grand Rapids, MI, USA, 11–15 May 2015); Nucl. Instrum. Methods Phys. Res.* B **376** 140–3

[218] Spolaore P, Larson J D, Signorini C, Beghini S, Xi-Kai Z and Hou-Zhi S 1985 A recoil mass spectrometer for the XTU tandem at LNL *Nucl. Instrum. Methods Phys. Res.* A **238** 381–92

[219] Davids C N, Back B B, Bindra K, Henderson D J, Kutschera W, Lauritsen T, Nagame Y, Sugathan P, Ramayya A V and Walters W B 1992 Startup of the fragment mass analyzer at ATLAS *Nucl. Instrum. Methods Phys. Res.* B **70** 358–65

[220] Sarén J *et al* 2008 The new vacuum-mode recoil separator MARA at JYFL *Proc. 15th Int. Conf. on Electromagnetic Isotope Separators and Techniques Related to their Applications; Nucl. Instrum. Methods Phys. Res.* B **266** 4196–200

[221] Ulfert G, Habs D, Metag V and Specht H J 1978 Lifetime measurements of nuclear levels with the charge plunger technique *Nucl. Instrum. Methods* **148** 369–79

[222] Backe H, Richter L, Willwater R, Kankeleit E, Kuphal E, Nakayama Y and Martin B 1978 In-beam spectroscopy of low energy conversion electrons with a recoil shadow method—a new possibility for subnanosecond lifetime measurements *Z. Phys.* A **285** 159–69

[223] Déchery F *et al* 2015 Toward the drip lines and the superheavy island of stability with the super separator spectrometer S3 *Eur. Phys. J.* A **51** 66

[224] Popeko A G 2016 On-line separators for the dubna SHEs factory *Proc. 17th Int. Conf. on Electromagnetic Isotope Separators and Related Topics (EMIS2015) (Grand Rapids, MI, USA, 11–15 May 2015); Nuclear Instrum. Methods Phys.* B **376** 144–9

[225] Leino M *et al* 1995 Gas-filled recoil separator for studies of heavy elements *Nucl. Instrum. Methods Phys. Res.* B **99** 653–6

[226] Madhavan N *et al* 2010 Hybrid recoil mass analyzer at iuac—first results using gas-filled mode and future plans *Pramana* **75** 317–31

[227] Seweryniak D 2013 Status and plans for recoil separators for experiments with intense stable beams from ATLAS *16th Int. Conf. on ElectroMagnetic Isotope Separators and Techniques Related to their Applications (Matsue, Japan, 27 December 2012); Nucl. Instrum. Methods* B **317** 274–6

[228] Block M *et al* 2010 Direct mass measurements above uranium bridge the gap to the island of stability *Nature* **463** 785–8

[229] Block M *et al* 2013 Direct mass measurements of the heaviest elements with penning traps *Int. J. Mass Spectrom.* **349** 94–101

[230] Ackermann D 2011 Investigation of ^{270}Ds and its decay products *GSI Sci. Rep. 2010* GSI Report 2011-1 GSI p 200

[231] Sewtz M *et al* 2003 Resonance ionization spectroscopy of fermium $(Z = 100)$ *Spectrochim. Acta* B **58** 1077–82

[232] Laatiaoui M *et al* 2016 Atom-at-a-time laser resonance ionization spectroscopy of nobelium *Nature* **538** 495–8

[233] Chhetri P *et al* in preparation

[234] Sato T K *et al* 2015 Measurement of the first ionization potential of lawrencium, element 103 *Nature* **520** 209–11

[235] Ghiorso A, Nitschke J M, Alonso J R, Alonso C T, Nurmia M, Seaborg G T, Hulet E K and Lougheed R W 1974 element 106 *Phys. Rev. Lett.* **33** 1490–3

[236] Hofmann S, Faust W, Münzenberg G, Reisdorf W, Armbruster P, Güttner K and Ewald H 1979 Alpha decay studies of very neutron deficient isotopes of Hf, Ta, W, and Re *Z. Phys.* A **291** 53–70

[237] Hofmann S, Münzenberg G, Hesseberger F P and Schött H J 1984 Detector system for investigation of proton radioactivity and new elements at SHIP *Nucl. Instrum. Methods Phys. Res.* **223** 312–8

[238] Ackermann D, Heßberger F P, Hoffmann J, Kurz N, Maurer J, Mistry A K, Piot J, Vostinar M and Wieczorek P 2015 MoDSS—a compact mobile decay spectroscopy set-up for the investigation of heavy and superheavy nuclei after separation *GSI Sci. Rep. 2014* GSI Report 2015-1 GSI p 169

[239] Mistry A K 2016 Decay spectroscopy at SHIP using a new focal plane detection system *GSI Sci. Rep. 2015* GSI-Report 2016-1 GSI p 109

[240] Anne R and Mueller A C 1992 LISE 3: a magnetic spectrometer—Wien filter combination for secondary radioactive beam production *Nucl. Instrum. Methods Phys. Res.* B **70** 276–85

[241] Andersson L-L *et al* 2010 TASISpec—a highly efficient multi-coincodence spectrometer for nuclear structure investigations of the heaviest elements *Nucl. Instrum. Methods Phys. Res.* A **622** 164–70

[242] Page R D *et al* 2003 The GREAT spectrometer *14th Int. Conf. on Electromagnetic Isotope Separators and Techniques Related to their Applications; Nucl. Instrum. Methods Phys. Res.* B **204** 634–7

[243] Gates J M *et al* 2015 Decay spectroscopy of element 115 daughters: $^{280}\mathrm{Rg} \rightarrow {}^{276}\mathrm{Mt}$ and $^{276}\mathrm{Mt} \rightarrow {}^{272}\mathrm{Bh}$ *Phys. Rev.* C **92** 021301(R)

[244] Hauschild K *et al* 2006 GABRIELA: a new detector array for γ-ray and conversion electron spectroscopy of transfermium elements *Nucl. Instrum. Methods Phys. Res.* A **560** 388–94

[245] Hauschild K *et al* to be published

[246] Sarmiento L G, Andersson L-L and Rudolph D 2012 A Geant4 simulation package for the TASISpec experimental detector setup *Nucl. Instrum. Methods* A **667** 26–31

[247] Geiger H and Nuttal J M 1911 The ranges of the α particles from various radioactive substances and a relation between range and period of transformation *Phil. Mag.* 6 **22** 613–21

[248] Gamow G 1929 Zur quantentheorie der atomzertrümmerung *Z. Phys.* **52** 510–5

[249] Bothe W and Fränz H 1927 Atomzertrümmerung durch α-strahlen von polonium *Z. Phys.* **43** 456–65

[250] Bothe W and Fränz H 1928 Atomtrümmer, reflektierte α-teilchen und durch α-strahlen erregte röntgenstrahlen *Z. Phys.* **49** 1–26

[251] Geiger H 1922 Reichweitenmessungen an α-strahlen *Z. Phys.* **8** 45–57

[252] Poenaru D N, Gherghescu R A and Carjan N 2007 Alpha-decay lifetimes semiempirical relationship including shell effects *Europhys. Lett.* **77** 62001

[253] Qi C, Andreyev A N, Huyse M, Liotta R J, Van Duppen P and Wyss R 2014 On the validity of the Geiger–Nuttall alpha-decay law and its microscopic basis *Phys. Lett.* B **734** 203–6

[254] Loveland G T, Morrissey D J and Seaborg G T 2005 *Modern Nuclear Chemistry* (New York: Wiley) (https://doi.org/10.1002/0471768626)

[255] Sobiczewski A, Muntian I and Patyk Z 2001 Problem of 'deformed' superheavy nuclei *Phys. Rev.* C **63** 034306

[256] Krappe H J and Pomorski K 2012 *Theory of Nuclear Fission* (Berlin: Springer) (https://doi.org/10.1007/978-3-642-23515-3)

[257] Smolańczuk R, Skalski J and Sobiczewski A 1995 Spontaneous-fission half-lives of deformed superheavy nuclei *Phys. Rev.* C **52** 1871–80

[258] Heßberger F P 2017 Spontaneous fission properties of SHEs *Eur. Phys. J.* A **53** 75

[259] Walker P M and Dracoulis G G 1999 Energy traps in atomic nuclei *Nature* **399** 35–40

[260] Walker P M and Xu F R 2016 High-K isomerism in rotational nuclei *Phys. Scr.* **91** 013010

[261] Löbner K E G 1968 Systematics of absolute transition probabilities of K-forbidden gamma-ray transitions *Phys. Lett.* B **26** 369–70

[262] Dracoulis G D, Walker P M and Kondev F G 2016 Review of metastable states in heavy nuclei *Rep. Prog. Phys.* **79** 076301

[263] Herzberg R-D and Greenlees P T 2008 In-beam and decay spectroscopy of transfermium nuclei *Prog. Part. Nucl. Phys.* **61** 674–720

[264] Zhang Z-H, He X-T, Zeng J-Y, Zhao E-G and Zhou S-G 2012 Systematic investigation of the rotational bands in nuclei with $Z \approx 100$ using a particle-number conserving method based on a cranked shell model *Phys. Rev.* C **85** 014324

[265] Bender M, Bonche P, Duguet T and Heenen P-H 2003 Skyrme mean-field study of rotational bands in transfermium isotopes *Nucl. Phys.* A **723** 354–64

[266] Parkhomenko A and Sobiczewski A 2005 Neutron one quasi-particle states of heaviest nuclei *Acta Phys. Pol.* B **36** 3115–37

[267] Asai M, Tsukada K, Haba H, Ichikawa T, Toyoshima A, Ishii T, Nagame Y, Nishinaka I, Kojima Y and Sueki K 2011 Neutron one-quasiparticle states in ^{251}Fm$_{151}$ populated via the α decay of ^{255}No *Phys. Rev.* C **83** 014315

[268] Heßberger F P *et al* 2016 Alpha- and EC-decay measurements of ^{257}Rf *Eur. Phys. J.* A **52** 192

[269] Asai M *et al* 2013 g.s. configuration of the $N = 157$ nucleus ^{259}No *Phys. Rev.* C **87** 014332

[270] Hatsukawa Y *et al* 1989 Alpha decay properties of light einsteinium isotopes *Nucl. Phys.* A **500** 90–110

[271] Moody K J *et al* 1993 Decay properties of heavy mendelevium isotopes *Nucl. Phys.* A **563** 21–73

[272] Gan Z-G *et al* 2001 A new alpha-particle-emitting isotope ^{259}Db *Eur. Phys. J.* A **10** 21–5

[273] Heßberger F P *et al* 2001 Decay properties of neutron-deficient isotopes ^{256,257}Db, ^{255}Rf, ^{252,253}Lr *Eur. Phys. J.* A **12** 57–67

[274] Gan Z-G *et al* 2004 New isotope ^{265}Bh *Eur. Phys. J.* A **20** 385–7

[275] Chatillon A *et al* 2006 Spectroscopy and single-particle structure of the odd-Z heavy elements ^{255}Lr and ^{251}Md and ^{247}Es *Eur. Phys. J.* A **30** 397–411

[276] Heßberger F P *et al* 2005 Energy systematics of low lying nilsson levels in odd-mass einsteinium isotopes *Eur. Phys. J.* A **26** 233–9

[277] Hauschild K *et al* 2008 High-K and $t_{1/2} = 1.4(1)$ ms and isomeric state in ^{255}Lr *Phys. Rev.* C **78** 021302(R)

[278] Antalic S *et al* 2008 Decay studies of neutron-deficient lawrencium isotopes *Eur. Phys. J.* A **38** 219–26

[279] Qian J *et al* 2009 Spectroscopy of ^{257}Rf *Phys. Rev.* C **79** 064319

[280] Antalic S *et al* 2009 Studies of neutron-deficient mendelevium isotopes at SHIP *Eur. Phys. J.* A **43** 35–44

[281] Heßberger F P *et al* 2012 Alpha-gamma decay studies of ^{253}No and ist daugher products ^{253}Md and ^{249}Fm *Eur. Phys. J.* A **48** 75

[282] Parkhomenko A and Sobiczewski A 2004 Proton one quasi-particle states of heaviest nuclei *Acta Phys. Pol.* B **35** 2447–71

[283] Herzberg R-D *et al* 2006 Nuclear isomers in SHEs as stepping stones towards the island of stability *Nature* **442** 896–9

[284] Tandel S K *et al* 2006 K isomers in ^{254}No: probing single-particle energies and pairing strength in the heaviest nuclei *Phys. Rev. Lett.* **97** 082502

[285] Xu F, Zhao E and Wyss P W R 2004 Enhanced stability of superheavy nuclei due to high-spin isomerism *Phys. Rev. Lett.* **92** 252501

[286] Hoff R W, von Egidy T, Lougheed R W, White D H, Börner H G, Schreckenbach K, Barreau G and Warner D D 1984 Levels of ^{244}Cm populated by the beta decay of 10 h ^{244}Am^{g} and 26 min ^{244}Am^{m} *Phys. Rev.* C **29** 618–22

[287] Hansen P G, Wilsky K, Baba C V K and Vandenbosch S E 1963 Decay of an isomeric state in Cm244 *Nucl. Phys.* **45** 410–6

[288] Multhauf L G, Tirsell K G and Meyer R A 1976 Collective excitations in ^{246}Cm and the decay of ^{246}Am^{m} *Phys. Rev.* C **13** 771–89

[289] Herzberg R-D and Cox D M 2011 Spectroscopy of actinide and transactinide nuclei *Radiochim. Acta* **99** 441–57

[290] Liu H L, Walker P M and Xu F R 2014 Favored configurations for four-quasiparticle K isomerism in the heaviest nuclei *Phys. Rev.* C **89** 044304

[291] Greenlees P *et al* 2008 High-K structure in ^{250}Fm and the deformed shell gaps at $N = 152$ and $z = 100$ *Phys. Rev.* C **78** 021303(R)

[292] Hall H L, Gregorich K E, Henderson R A, Lee D M, Hoffman D C, Bunker M E, Fowler M M, Lysaght P, Starner J W and Wilhelmy J B 1989 β -delayed fission from ^{256}Es^{m} and the level scheme of ^{256}Fm *Phys. Rev.* C **39** 1866–75

[293] Peterson D *et al* 2006 Decay modes of ^{250}No *Phys. Rev.* C **74** 014316

[294] Sulignano B *et al* 2007 Identification of a K isomer in ^{252}No *Eur. Phys. J.* A **33** 327

[295] Jeppesen H B *et al* 2009 Multi-quasiparticle states in ^{256}Rf *Phys. Rev.* C **79** 031303(R)

[296] Ackermann D 2012 Discovery of a K-isomer in ^{266}Hs *GSI Sci. Rep. 2011* GSI Report 2012-1 GSI p 208

[297] Ackermann D *et al* to be published

[298] Hofmann S *et al* 2001 The new isotope ^{270}110 and its decay products ^{266}Hs and ^{262}Sg *Eur. Phys. J.* A **10** 5–10

[299] Reiter P *et al* 1999 g.s. band and deformation of the $Z = 102$ isotope ^{254}No *Phys. Rev. Lett.* **82** 509–12

[300] Leino M *et al* 1999 In-beam study of ^{254}No *Eur. Phys. J.* A **6** 63–9

[301] Reiter P *et al* 2000 Entry distribution, fission barrier, and formation mechanism of $^{254}_{102}$ No *Phys. Rev. Lett.* **84** 3542–5

[302] Herzberg R-D *et al* 2001 Spectroscopy of transfermium nuclei: $^{252}_{102}$No *Phys. Rev.* C **65** 014303

[303] Butler P A *et al* 2002 Conversion electron cascades in $^{254}_{102}$No *Phys. Rev. Lett.* **89** 202501

[304] Leppänen A P *et al* 2006 Recoil-fission tagging of the transfermium nucleus ^{252}No *Eur. Phys. J.* A **28** 301–6

[305] Heßberger F P *et al* 2010 Decay studies of K isomers in ^{254}No *Eur. Phys. J.* A **43** 55

[306] Clark R M *et al* 2010 High-K multi-quasiparticle states in ^{254}No *Phys. Lett.* B **690** 19–24

[307] Heßberger F P *et al* 2016 Investigation of electron capture decay of ^{258}Db and α decay of ^{258}Rf *Eur. Phys. J.* A **52** 328

[308] Heßberger F P *et al* 2006 Alpha-gamma decay studies of ^{255}Rf and ^{251}No and and ^{247}Fm *Eur. Phys. J.* A **30** 561–9

[309] Heßberger F P *et al* 2006 Alpha-gamma decay studies of ^{255}No *Eur. Phys. J.* A **29** 165–73

[310] Antalic S *et al* 2011 Isomeric states in ^{253}No and ^{253}Fm *Eur. Phys. J.* A **47** 62

[311] Heßberger F P 2007 Nuclear structure investigations in the region of superheavy nuclei *Phys. At. Nuclei* **70** 1445–51

[312] David H M *et al* 2015 Decay and fission hindrance of two- and four-quasiparticle K isomers in ^{254}Rf *Phys. Rev. Lett.* **115** 132502

[313] Prassa V, Lu B-N, Nikšić T, Ackermann D and Vretenar D 2015 High-K isomers in transactinide nuclei close to $N = 162$ *Phys. Rev.* C **91** 034324

[314] Walker P M, Dracoulis G D, Byrne A P, Fabricius B, Kibedi T, Stuchbery A E and Rowley N 1994 Multi-quasiparticle and rotational structures in ^{179}W: Fermi alignment, the K-selection rule and blocking *Nucl. Phys.* A **568** 397–444

[315] Alder K, Bohr A, Huus T, Mottelson B and Winther A 1956 Study of nuclear structure by electromagnetic excitation with accelerated ions *Rev. Mod. Phys.* **28** 432–542

[316] Ford J L C, Stelson P H, Bemis C E, McGowan F K, Robinson R L and Milner W T 1971 Precise Coulomb excitation $B(E2)$ values for first 2^+ states of the actinide nuclei *Phys. Rev. Lett.* **27** 1232–4

[317] Bemis C E, McGowan F K, Ford J L C, Milner W T, Stelson P H and Robinson R L 1973 $E2$ and $E4$ transition moments and equilibrium deformations in the actinide nuclei *Phys. Rev.* C **8** 1466–80

[318] Raman S, Nestor C W JR. and Tikkanen P 2001 Transition probability from the ground to the first-excited $2+$ state of even–even nuclides *At. Data Nucl. Data Tables* **78** 1–128

[319] Pritychenko B, Birch M, Horoi M and Singh B 2014 B(E2) evaluation for transitions in even-even nuclei *Nucl. Data Sheets* **120** 112–4

[320] Pritychenko B Reduced transition probabilities or B(2; $0+ \rightarrow 2+$) values, National Nuclear Data Center http://nndc.bnl.gov/be2/

[321] Hasse R W and Myers W D 1988 *Geometrical Relationships of Macroscopic Nuclear Physics* (Berlin: Springer) (https://doi.org/10.1007/978-3-642-83017-4)

[322] Poenaru D and Greiner W 1996 *Handbook of Nuclear Properties* (Oxford: Clarendon)

[323] Ton H, Beens W, Roodbergen S and Blok J 1970 Lifetimes of $2+$ and $4+$ rotational states in heavy doubly even nuclei *Nucl. Phys.* A **155** 235–44

[324] Martin M J 2014 Nuclear data sheets for $A = 248$ *Nucl. Data Sheets* **122** 377–409

[325] Ower H *et al* 1982 Structure of high-spin states in ^{232}Th, ^{234}U and ^{236}U *Nucl. Phys.* A **388** 421–44

[326] Simon R S, Devito R P, Emling H, Kulessa R, Brianon C and Lefebvre A 1982 Rotational band crossings in ^{232}Th *Phys. Lett.* B **108** 87–90

[327] Grosse E *et al* 1981 Collective rotation of ^{238}U at high spins *Phys. Scr.* **24** 337

[328] Spreng W *et al* 1983 First observation of backbending in an actinide nucleus *Phys. Rev. Lett.* **51** 1522–5

[329] Piercey R B *et al* 1981 Anomalous behavior of high-spin states in ^{248}Cm *Phys. Rev. Lett.* **46** 415–9

[330] Czosnyka T, Cline D, Hasselgren L, Wu C Y, Diamond R M, Kluge H, Roulet C, Hulet E K, Lougheed R W and Baktash C 1986 E2 properties of the SHEs band in ^{248}Cm *Nucl. Phys.* A **458** 123–36

[331] Hackman G *et al* 1998 High-spin properties of octupole bands in ^{240}Pu and ^{248}Cm *Phys. Rev.* C **57** R1056–9

[332] Cresswell A J *et al* 1995 Population of collective bands in Dy isotopes using heavy ion induced transfer reactions *Phys. Rev.* C **52** 1934–9

[333] Wu C Y, Simon M W, Cline D, Davis G A, Macchiavelli A O and Vetter K 1998 Production and spectroscopy of the neutron-rich nucleus ^{166}Dy *Phys. Rev.* C **57** 3466–9

[334] Takai H *et al* 1988 Population of high spin states by quasi-elastic and deep inelastic collisions *Phys. Rev.* C **38** 1247–61

[335] Lee I Y *et al* 1997 Study of neutron-rich nuclei using deep-inelastic reactions *Phys. Rev.* C **56** 753–9

[336] Cocks J F C *et al* 2000 Multi-nucleon transfer reactions as a tool for spectroscopy of heavy nuclei *J. Phys. G: Nucl. Part. Phys.* **26** 23

[337] Cocks J F C *et al* 1999 Spectroscopy of Rn, Ra and Th isotopes using multi-nucleon transfer reactions *Nucl. Phys.* A **645** 61–91

[338] James A N, Morrison T P, Ying K L, Connell K A, Price H G and Simpson J 1988 Microsecond mass separation of heavy compound nucleus residues using the Daresbury recoil separator *Nucl. Instrum. Methods Phys. Res.* A **267** 144–52

[339] Simon R S, Schmidt K H, Heßberger F P, Hlavac S, Honusek M, Münzenberg G, Clerc H G, Gollerthan U and Schwab W 1986 Evidence for nuclear shape coexistence in ^{180}Hg *Z. Phys.* A **325** 197–202

[340] Paul E S *et al* 1995 In-beam γ-ray spectroscopy above ^{100}Sn using the new technique of recoil decay tagging *Phys. Rev.* C **51** 78–87

[341] Greenlees P T *et al* 1998 First observation of excited states in ^{226}U *J. Phys. G: Nucl. Part. Phys.* **24** L63

[342] Nitschke J M, Leber R E, Nurmia M J and Ghiorso A 1979 Observations in the reaction of two magic nuclei: ^{208}Pb and ^{48}Ca *Nucl. Phys.* A **313** 236–50

[343] Türler A *et al* 1988 Determination of the partial electron capture- and spontaneous-fission half-lives of ^{254}No *Z. Phys.* A **331** 363–4

[344] Gäggeler H W *et al* 1989 Cold fusion reactions with ^{48}Ca *Nucl. Phys.* A **502** 561–70

[345] Yeremin A V *et al* 2003 The upgrade of the kinematic separator VASSILISSA-experimental results and plans *Phys. At. Nuclei* **66** 1042–52

[346] Taylor R B E *et al* 1999 γ decay of excited states in ^{198}Rn identified using correlated radioactive decay *Phys. Rev.* C **59** 673–81

[347] Ćwiok S, Pashkevich V V, Dudek J and Nazarewicz W 1983 Fission barriers of transfermium elements *Nucl. Phys.* A **410** 254–70

[348] Möller P, Nix J R and Swiatecki W J 1987 Calculated fission properties of the heaviest elements *Nucl. Phys.* A **469** 1–50

[349] Staszczak A, Piat S and Pomorski K 1989 Influence of the pairing vibrations on spontaneous fission probability *Nucl. Phys.* A **504** 589–604

[350] Bhandari B S and Bendardaf Y B 1992 Systematics of the deduced fission barriers for the doubly even transactinium nuclei *Phys. Rev.* C **45** 2803–18

[351] Patyk Z and Sobiczewski A 1991 g.s. properties of the heaviest nuclei analyzed in a multidimensional deformation space *Nucl. Phys.* A **533** 132–52

[352] Egido J L and Robledo L M 2000 Fission barriers at high angular momentum and the SHEs rotational band of the nucleus ^{254}No *Phys. Rev. Lett.* **85** 1198–201

[353] Duguet T, Bonche P and Heenen P-H 2001 Rotational properties of ^{252,253,254}No: influence of pairing correlations *Nucl. Phys.* A **679** 427–40

[354] Laftchiev H, Samsœn D, Quentin P and Piperova J 2001 Hartree–Fock–Bogoliubov calculations of the rotational band of the very heavy ^{254}No nucleus *Eur. Phys. J.* A **12** 155–9

[355] Zajac K, Próchniak L, Pomorski K, Rohozinski S G and Srebrny J 2001 Collective quadrupole excited states in actinide and transuranic nuclei *Acta Phys. Pol.* B **32** 681–4

[356] Lee I-Y, Deleplanque M A and Vetter K 2003 Developments in large gamma-ray detector arrays *Rep. Prog. Phys.* **66** 1095

[357] Eberth J and Simpson J 2008 From Ge(Li) detectors to gamma-ray tracking arrays—50 years of gamma spectroscopy with germanium detectors *Prog. Part. Nucl. Phys.* **60** 283–337

[358] Riley M A, Simpson J and Paul E S 2016 High resolution gamma-ray spectroscopy and the fascinating angular momentum realm of the atomic nucleus *Phys. Scr.* **91** 123002

[359] Lee I-Y 1990 The GAMMASPHERE *Nucl. Phys.* A **520** c641–55

[360] Simpson J 1997 The euroball spectrometer *Z. Phys.* A **358** 139–43

[361] Duchêne G, Beck F A, Twin P J, de France G, Curien D, Han L, Beausang C W, Bentley M A, Nolan P J and Simpson J 1999 The clover: a new generation of composite Ge detectors *Nucl. Instrum. Methods Phys. Res.* A **432** 90–110

[362] Shepherd S L *et al* 1999 Measurements on a prototype segmented clover detector *Nucl. Instrum. Methods Phys. Res.* A **434** 373–86

[363] Sharpey-Schafer J F and Simpson J 1988 Escape suppressed spectrometer arrays: a revolution in γ-ray spectroscopy *Prog. Part. Nucl. Phys.* **21** 293–400

[364] Greenlees P T *et al* 2003 In-beam spectroscopy at the RITU gas-filled recoil separator *Eur. Phys. J.* A **20** 87–92

[365] Pakarinen J *et al* 2014 The SAGE spectrometer *Eur. Phys. J.* A **50** 53

[366] Lazarus I *et al* 2001 The GREAT triggerless total data readout method *IEEE Trans. Nucl. Sci.* **48** 567–9

[367] Piot J *et al* 2012 In-beam spectroscopy with intense ion beams: evidence for a rotational structure in ^{246}Fm *Phys. Rev.* C **85** 0413015(R)

[368] Anderson J T *et al* 2012 A digital data acquisition system for the detectors at gammasphere *2012 IEEE Nuclear Science Symp. and Medical Imaging Conf. (NSS/MIC)* pp 1536–40

[369] Greenberg J S and Vincent P 1985 High-energy atomic physics–experimental *Treatise on Heavy-Ion Science: vol 5 High-Energy Atomic Physics* (Boston, MA: Springer) pp 139–421

[370] Van Klinken J, Feenstra S J, Wisshak K and Faust H 1975 Mini-orange spectrometers for in- and off-beam observation of conversion electrons *Nucl. Instrum. Methods* **130** 427–41

[371] Aengenvoort B *et al* 1998 Conversion-electron gamma-ray coincidence spectroscopy of superdeformed ^{135}Nd *Eur. Phys. J.* A **1** 359–64

[372] Coz Y L *et al* 2000 Evidence of multiple shape-coexistence in ^{188}Pb *EPJ Direct* **1** 1–6

[373] Metlay M P, Saladin J X, Lee I Y and Dietzsch O 1993 The ICEBall: a multiple element array for in-beam internal conversion electron spectroscopy *Nucl. Instrum. Methods Phys. Res.* A **336** 162–70

[374] Ketelhut S *et al* 2014 Simulated performance of the in-beam conversion-electron spectrometer, SPICE *Nucl. Instrum. Methods Phys. Res.* A **753** 154–63

[375] Paris P, Liang C F and Legrand B 1995 Gradient-field electron guides for conversion electron studies *Nucl. Instrum. Methods Phys. Res.* A **357** 398–405

[376] Męczyński W *et al* 1998 Gamma-spectroscopy of the ^{199}At nucleus with the recoil filter detector *Eur. Phys. J.* A **3** 311–2

[377] Kankaanpää H *et al* 2004 In-beam electron spectrometer used in conjunction with a gas-filled recoil separator *Nucl. Instrum. Methods Phys. Res.* A **534** 503–10

[378] Butler P A, Jones P M, Cann K J, Cocks J F C, Jones G D, Julin R and Trzaska W H 1996 Electron spectroscopy using a multi-detector array *Nucl. Instrum. Methods Phys. Res.* A **381** 433–42

[379] Herzberg R D *et al* 2009 Structure of rotational bands in ^{253}No *Eur. Phys. J.* A **42** 333–7

[380] Bastin J E *et al* 2006 In-beam gamma ray and conversion electron study of ^{250}Fm *Phys. Rev.* C **73** 024308

[381] Sorri J *et al* 2016 Determination of absolute internal conversion coefficients using the SAGE spectrometer *Nucl. Instrum. Methods Phys. Res.* A **812** 24–32

[382] Mistry A K *et al* 2017 In-beam study of ^{253}No using the SAGE spectrometer *Eur. Phys. J.* A **53** 24

[383] Ishii T, Shigematsu S, Asai M, Makishima A, Matsuda M, Kaneko J, Hossain I, Ichikawa S, Kohno T and Ogawa M 2005 In-beam γ-ray spectroscopy of ^{240}U using the (^{18}O, ^{16}O) reaction *Phys. Rev.* C **72** 021301(R)

[384] Ishii T *et al* 2006 g.s. band of the neutron-rich transuranium nucleus ^{250}Cm$_{154}$ *J. Phys. Soc. Japan* **75** 043201

[385] Makii H *et al* 2007 Z dependence of the $N = 152$ deformed shell gap: in-beam γ-ray spectroscopy of neutron-rich ^{245,246}Pu *Phys. Rev.* C **76** 061301(R)

[386] Ishii T *et al* 2007 In-beam γ-ray study of the neutron-rich nuclei ^{240}U, ^{246}Pu, and ^{250}Cm produced by the (^{18}O, ^{16}O) reaction *Phys. At. Nuclei* **70** 1457–61

[387] Ishii T *et al* 2008 Observation of high-j quasiparticle states in ^{249}Cm by in-beam γ-ray spectroscopy using heavy-ion transfer reactions *Phys. Rev.* C **78** 054309

[388] Takahashi R *et al* 2010 In-beam γ-ray spectroscopy of ^{248,250,252}Cf by neutron-transfer reactions using a Cf target *Phys. Rev.* C **81** 057303

[389] Ishii T *et al* 2007 g.s. bands of neutron-rich ^{236}Th and ^{242}U nuclei and implication of spherical shell closure at $N = 164$ *Phys. Rev.* C **76** 011303(R)

[390] Wang X *et al* 2009 Structure of ^{240}Pu: evidence for octupole phonon condensation? *Phys. Rev. Lett.* **102** 122501

[391] Saleem K A *et al* 2004 Alignments in the odd-proton actinides ^{237}Np and ^{241}Am *Phys. Rev.* C **70** 024310

[392] Saleem K A 2002 *PhD Thesis* Illinois Institute of Technology

[393] Hota S S *et al* 2014 $N = 151$ Pu, Cm and Cf nuclei under rotational stress: role of higher-order deformations *Phys. Lett.* B **739** 13–8

[394] Tandel S K *et al* 2010 Rotational bands in odd-A Cm and Cf isotopes: exploring the highest neutron orbitals *Phys. Rev.* C **82** 041301(R)

[395] Hota S S 2012 Spectroscopy of neutron-rich Pu, Cm and Cf nuclei via inelastic and transfer reactions *PhD Thesis* University of Massachusetts Lowell

[396] Qiu Y *et al* to be published

[397] Nica N 2005 Nuclear data sheets for $A = 252$ *Nucl. Data Sheets* **106** 813–34

[398] Humphreys R D *et al* 2004 In-beam electron spectroscopy of ^{226}U and ^{254}No *Phys. Rev.* C **69** 064324

[399] Ketelhut S 2010 Rotational structures and high-K isomerism in ^{248,250}Fm *PhD Thesis* University of Jyväskylä

[400] Rubert J, Piot J, Asfari Z, Gall B J P, Ärje J, Dorvaux O, Greenlees P T, Koivisto H, Ouadi A and Seppälä R 2012 First intense isotopic titanium-50 beam using MIVOC method *Nucl. Instrum. Methods Phys. Res.* B **276** 33–7

[401] Arnould M, Goriely S and Takahashi K 2007 The r-process of stellar nucleosynthesis: astrophysics and nuclear physics achievements and mysteries *Phys. Rep.* **450** 97–213

[402] Goriely S and Pinedo G M 2015 The production of transuranium elements by the *r*-process nucleosynthesis *Nucl. Phys.* A **944** 158–76

[403] Dubray N, Goutte H and Delaroche J-P 2008 Structure properties of ^{226}Th and ^{256,258,260}Fm fission fragments: mean-field analysis with the Gogny force *Phys. Rev.* C **77** 014310

[404] Möller P and Randrup J 2015 Calculated fission-fragment yield systematics in the region $74 \leqslant Z \leqslant 94$ and $90 \leqslant N \leqslant 150$ *Phys. Rev.* C **91** 044316

[405] Sadhukhan J, Nazarewicz W and Schunck N 2016 Microscopic modeling of mass and charge distributions in the spontaneous fission of ^{240}Pu *Phys. Rev.* C **93** 011304(R)

[406] Baran A, Kowal M, Reinhard P-G, Robledo L M, Staszczak A and Warda M 2015 Fission barriers and probabilities of spontaneous fission for elements with $Z \geqslant 100$ *Nucl. Phys.* A **944** 442–70

[407] Britt H C, Cheifetz E, Hoffman D C, Wilhelmy J B, Dupzyk R J and Lougheed R W 1980 Fission barriers for ^{255}Es, ^{256}Es, and ^{255}Fm *Phys. Rev.* C **21** 761(R)–763(R)

[408] Bjørnholm S and Lynn J E 1980 The double-humped fission barrier *Rev. Mod. Phys.* **52** 725–931

[409] Wagemans C 1991 *The Nuclear Fission Process* (Boca Raton, FL: CRC Press)

[410] Itkis M G, Vardaci E, Itkis I M, Knyazheva G N and Kozulin E M 2015 Fusion and fission of heavy and superheavy nuclei (experiment) *Nucl. Phys.* A **944** 204–37

[411] Bonneau L, Quentin P and Samsœn D 2004 Fission barriers of heavy nuclei within a microscopic approach *Eur. Phys. J.* A **21** 391–406

[412] Delaroche J-P, Girod M, Goutte H and Libert Structure J 2006 properties of even–even actinides at normal and super deformed shapes analysed using the Gogny force *Nucl. Phys.* A **771** 103–68

[413] Möller P, Sierk A J, Ichikawa T, Iwamoto A, Bengtsson R, Uhrenholt H and Åberg S 2009 Heavy-element fission barriers *Phys. Rev.* C **79** 064304

[414] Kowal M, Jachimowicz P and Sobiczewski A 2010 Fission barriers for even–even superheavy nuclei *Phys. Rev.* C **82** 014303

[415] Warda M and Egido J L 2012 Fission half-lives of superheavy nuclei in a microscopic approach *Phys. Rev.* C **86** 014322

[416] Namboodiri M N, Chulick E T, Natowitz J B and Kenefick R A 1975 Production of Ca, Ga, and Br nuclei having angular momenta equal to or greater than the calculated liquid drop limit *Phys. Rev.* C **11** 401–9

[417] Bass R 1977 Nucleus–nucleus potential deduced from experimental fusion cross sections *Phys. Rev. Lett.* **39** 265–8

[418] Henning G 2012 Stability of transfermium elements at high spin : mesuring the fission barrier of ^{254}No *PhD Thesis* Université Paris-Sud

[419] Lü H, Marchix A, Abe Y and Boilley D 2016 KEWPIE2: A cascade code for the study of dynamical decay of excited nuclei *Comp. Phys. Comm.* **200** 381–99

[420] Zagrebaev V I *et al* NRV: low energy nuclear knowledge base http://nrv.jinr.ru/nrv/

[421] Zubov A S, Sargsyan V V, Adamian G G and Antonenko N V 2011 Population of g.s. rotational bands of superheavy nuclei produced in complete fusion reactions *Phys. Rev.* C **84** 044320

[422] Czosnyka T, Cline D and Wu C Y 1983 *Bull. Am. Phys. Soc.* **28** 745

[423] Czosnyka T, Cline D and Wu C Y GOSIA User's Manual http://slcj.uw.edu.pl/gosia/

[424] Zielińska M 2016 private communication

[425] Reiter P *et al* 2005 Structure of the odd-*A*, shell-stabilized nucleus $^{253}_{102}$No *Phys. Rev. Lett.* **95** 032501

[426] Heßberger F P *et al* 1997 Spontaneous fission and alpha-decay properties of neutron deficient isotopes $^{257-253}$104 and ^{258}106 *Z. Phys.* A **359** 415–25

[427] Herzberg R-D *et al* 2002 In-beam spectroscopy of ^{253,254}No *Eur. Phys. J.* A **15** 205–8

[428] Chatillon A *et al* 2007 Observation of a rotational band in the odd-Z transfermium nucleus $^{251}_{101}$Md *Phys. Rev. Lett.* **98** 132503

[429] Asai M, Haba H, Sato N, Kasamatsu Y, Kaji D, Morimoto K and Morita K 2011 α fine-structure spectroscopy for ^{255g,m}Lr *RIKEN Accelerator Progress Report 2010* **vol 44** p 22

[430] Briselet R *et al* to be published

[431] Chatillon A 2005 Spectroscopie des transfermium impairs en protons: la structure du noyau de ^{251}Md *PhD Thesis* Université Claude Bernard—Lyon I

[432] Theisen C, Greenlees P T, Khoo T-L, Chowdhury P and Ishii T 2015 In-beam spectroscopy of heavy elements *Nucl. Phys.* A **944** 333–75 special issue on SHEs

[433] Ketelhut S *et al* 2009 γ-ray spectroscopy at the limits: first observation of rotational bands in ^{255}Lr *Phys. Rev. Lett.* **102** 212501

[434] Jeppesen H B *et al* 2009 High-*K* multi-quasiparticle states and rotational bands in $^{255}_{103}$Lr *Phys. Rev.* C **80** 034324

[435] Sandzelius M 2015 private communication

[436] Cox D M and GEANT4 A 2014 Simulation of the SAGE spectrometer and its first application to ^{255}Lr *PhD Thesis* University of Liverpool

[437] Hota S S *et al* 2016 Population and decay of a $K^{\pi} = 8^{-}$ two-quasineutron isomer in ^{244}Pu *Phys. Rev.* C **94** 021303(R)

[438] Ghiorso A, Nurmia M, Harris J, Eskola K and Eskola P 1971 Defence of the berkeley work on alpha-emitting isotopes of element 104 *Nature* **229** 603–7

[439] Ghiorso A, Eskola K, Eskola P and Nurmia M 1973 Isomeric states in ^{250}Fm and ^{254}No *Phys. Rev.* C **7** 2032–6

[440] Sulignano B *et al* 2012 Investigation of high-*K* states in ^{252}No *Phys. Rev.* C **86** 044318

[441] Gallagher C J 1962 Coupling of angular momenta in two-particle states in deformed even–even nuclei *Phys. Rev.* **126** 1525–31

[442] Harris S M 1965 Higher order corrections to the cranking model *Phys. Rev.* **138** B509–13

[443] Baktash C, Nazarewicz W and Wyss R 1993 On the question of spin fitting and quantized alignment in rotational bands *Nucl. Phys.* A **555** 375–407

[444] Holmberg P and Lipas P O 1968 A new formula for rotational energies *Nucl. Phys.* A **117** 552–60

[445] Grodzins L 1962 The uniform behaviour of electric quadrupole transition probabilities from first 2+ states in even–even nuclei *Phys. Lett.* **2** 88–91

[446] Raman S, Nestor C W, Kahane S and Bhatt K H 1989 Predictions of $B(E2; 0_1^+ \rightarrow 2_1^+)$ values for even–even nuclei *At. Data Nucl. Data Tables* **42** 1–54

[447] Thirolf P G and Habs D 2002 Spectroscopy in the second and third minimum of actinide nuclei *Prog. Part. Nucl. Phys.* **49** 325–402

[448] Bender M, Heenen P-H and Reinhard P-G 2003 Self-consistent mean-field models for nuclear structure *Rev. Mod. Phys.* **75** 121–80

[449] Stone J R, Guichon P A M, Reinhard P G and Thomas A W 2016 Finite nuclei in the quark-meson coupling model *Phys. Rev. Lett.* **116** 092501

[450] Raeder S to be published

[451] Ćwiok S, Heenen P-H and Nazarewicz W 2005 Shape coexistence and triaxiality in the superheavy nuclei *Nature* **433** 705–9

[452] Bender M and Heenen P-H 2013 Structure of superheavy nuclei *J. Phys.: Conf. Ser.* **420** 012002

[453] Kortelainen M, McDonnell J, Nazarewicz W, Reinhard P-G, Sarich J, Schunck N, Stoitsov M V and Wild S M 2012 Nuclear energy density optimization: large deformations *Phys. Rev.* C **85** 024304

[454] Kortelainen M *et al* 2014 Nuclear energy density optimization: shell structure *Phys. Rev.* C **89** 054314

[455] Shi Y, Dobaczewski J and Greenlees P T 2014 Rotational properties of nuclei around ^{254}No investigated using a spectroscopic-quality skyrme energy density functional *Phys. Rev.* C **89** 034309

[456] Litvinova E V and Afanasjev A V 2011 Dynamics of nuclear single-particle structure in covariant theory of particle-vibration coupling: from light to superheavy nuclei *Phys. Rev.* C **84** 014305

[457] Afanasjev A V and Shawaqfeh S 2011 Deformed one-quasiparticle states in covariant density functional theory *Phys. Lett.* B **706** 177–82

[458] Tarpanov D, Dobaczewski J, Toivanen J and Carlsson B G 2014 Spectroscopic properties of nuclear skyrme energy density functionals *Phys. Rev. Lett.* **113** 252501

[459] Mottelson B R and Valatin J G 1960 Effect of nuclear rotation on the pairing correlation *Phys. Rev. Lett.* **5** 511–2

[460] Johnson A, Ryde H and Sztarkier J 1971 Evidence for a 'singularity' in the nuclear rotational band structure *Phys. Lett.* B **34** 605–8

[461] Johnson A, Ryde H and Hjorth S A 1972 Nuclear moment of inertia at high rotational frequencies *Nucl. Phys.* A **179** 753–68

[462] Stephens F S and Simon R S 1972 Coriolis effects in the yrast states *Nucl. Phys.* A **183** 257–84

[463] Bengtsson R and Frauendorf S 1979 Quasiparticle spectra near the yrast line *Nucl. Phys.* A **327** 139–71

[464] Diebel M and Mosel U 1981 Cranking-HFB calculations of the yrastline for the nuclei ^{232}Th, ^{234,236,238}U,^{248}Cm *Z. Phys.* A **303** 131–4

[465] Egido J L and Ring P 1982 Is there backbending in the actinides? *J. Phys. G: Nucl. Phys.* **8** L43

[466] Dudek J, Nazarewicz W and Szymański Z 1982 Possible existence of backbending in actinide nuclei *Phys. Rev.* C **26** 1708–11

[467] Wiedenhöver I *et al* 1999 Octupole correlations in the Pu isotopes: from vibration to static deformation? *Phys. Rev. Lett.* **83** 2143–6

[468] He X T and Re Z Z 2008 Particle-number conserving treatment for the SHEs bands in even–even transfermium nuclei *Int. J. Mod. Phys.* E **17** 208–18

[469] He X T, Ren Z Z, Liu S X and Zhao E G 2009 Influence of high-j intruder orbitals in odd mass transfermium nuclei ^{253}No and ^{251}Md *Nucl. Phys.* A **817** 45–60

[470] Al-Khudair F, Long G-L and Sun Y 2009 Competition in rotation-alignment between high-j neutrons and protons in transfermium nuclei *Phys. Rev.* C **79** 034320

[471] Zhang Z-H, Zeng J-Y, Zhao E-G and Zhou S-G 2011 Particle-number conserving analysis of rotational bands in ^{247,249}Cm and ^{249}Cf *Phys. Rev.* C **83** 011304(R)

[472] Liu H L, Xu F R and Walker P M 2012 Understanding the different rotational behaviors of ^{252}No and ^{254}No *Phys. Rev.* C **86** 011301(R)

[473] Afanasjev A V and Abdurazakov O 2013 Pairing and rotational properties of actinides and superheavy nuclei in covariant density functional theory *Phys. Rev.* C **88** 014320

[474] Zhang Z-H, Meng J, Zhao E-G and Zhou S-G 2013 Rotational properties of the superheavy nucleus ^{256}Rf and its neighboring even–even nuclei in a particle-number-conserving cranked shell model *Phys. Rev.* C **87** 054308

[475] He X-T, Zhang Z-H, Zeng J-Y, Zhao E-G, Ren Z-Z, Scheid W and Zhou S-G 2014 Rotation and alignment of high-j orbitals in transfermium nuclei *EPJ Web Conf.* **66** 02045

[476] Afanasjev A V 2014 Microscopic description of rotation: from SHEss to the extremes of ultra-high spin *Phys. Scr.* **89** 054001

[477] Frauendorf S and Pashkevich V V 1984 Quasiparticles in pear-shaped rotating nuclei *Phys. Lett.* B **141** 23–7

[478] Hamamoto I 1976 Band crossing in the cranking model *Nucl. Phys.* A **271** 15–28

[479] Braid T H, Chasman R R, Erskine J R and Friedman A M 1971 (d, p) and (d, t) studies of the actinide elements: II. ^{243}Cm, ^{245}Cm, ^{247}Cm, and ^{249}Cm *Phys. Rev.* C **4** 247–62

[480] Ahmad I, Greene J P, Moore E F, Kondev F G, Chasman R R, Porter C E and Felker L K 2005 Energy levels of ^{251}Cf populated in the α decay of $^{255}_{100}$Fm and EC decay of $^{251}_{99}$Es *Phys. Rev.* C **72** 054308

[481] Ahmad I and Chasman R R 2009 Neutron single-particle states above the $N = 164$ subshell in $^{251}_{98}$Cf and $^{249}_{96}$Cm studied by neutron transfer reactions *Phys. Rev.* C **80** 064315

[482] Daniels W R, Hoffman D C, Lawrence F O and Orth C J 1968 Decay of ^{245}Pu *Nucl. Phys.* A **107** 569–80

[483] Ahmad I, Yates S W, Sjoblom R K and Friedman A M 1979 Proton states in ^{247}Bk excited by ^{246}Cm(α, t) reaction and ^{247}Cf (electron capture) and ^{251}Es α decays *Phys. Rev.* C **20** 290–7

[484] Ahmad I, Friedman A M, Chasman R R and Yates S W 1977 Proton orbital $1/2^-$ [521] and the stability of SHEs *Phys. Rev. Lett.* **39** 12–5

[485] Dewberry R A, Kouzes R T, Naumann R A, Lanier R G, Börner H G and Hoff R 1983 The ^{249}Bk$(p, t)^{247}$Bk reaction *Nucl. Phys.* A **399** 1–10

[486] Erskine J R, Kyle G, Chasman R R and Friedman A M 1975 Study of ^{249}Bk, ^{241}Am, and ^{231}Pa with proton transfer reactions *Phys. Rev.* C **11** 561–79

[487] Ahmad I, Sjoblom R K, Friedman A M and Yates S W 1978 Proton states in the $Z = 99$ nucleus ^{251}Es excited by ^{251}Fm electron capture decay and ^{250}Cf(α, t) reaction *Phys. Rev.* C **17** 2163–75

[488] Afanasjev A V, Abusara H, Litvinova E and Ring P 2011 Spectroscopy of the heaviest nuclei (theory) *J. Phys.: Conf. Ser.* **312** 092004

[489] Chatillon A *et al* 2005 Spectroscopy of the odd transfermium ^{251}Md and ^{255}Lr nuclei using γ, electron and α spectroscopy *Exotic Nuclei Exon2004* (Singapore: World Scientific) (https://doi.org/10.1142/9789812701749_0029)

[490] Kondev F G, Dracoulis G D and Kibédi T 2015 Configurations and hindered decays of isomers in deformed nuclei with $A > 100$ *At. Data Nucl. Data Tables* **103–104** 50–105

[491] Dracoulis G D 2013 Isomers nuclear structure and spectroscopy *Phys. Scr.* **2013** 014015

[492] Heenen P-H 2015 private communication

[493] Ivanova S P, Komov A L, Malov L A and Solovev V G 1976 Two-quasiparticle and single-phonon states of even–even deformed nuclei in the region of the actinides *Sov. J. Part. Nucl. Phys.* **7** 175

[494] Soloviev V G and Siklos T 1964 Energies of strongly deformed even nuclei in the range $228 \leqq A \leqq 254$ *Nucl. Phys.* **59** 145–58

[495] Robinson A P *et al* 2008 $K^{\pi} = 8^-$ isomers and $K^{\pi} = 2^-$ octupole vibrations in $N = 150$ shell-stabilized isotones *Phys. Rev.* C **78** 034308

[496] Jolos R V, Malov L A, Shirikova N Y and Sushkov A V 2011 Structure of some low lying two-quasiparticle and collective states in nuclei with $Z \sim 100$ considered in the quasiparticle phonon model *J. Phys. G: Nucl. Part. Phys.* **38** 115103

[497] Solov'ev V G, Sushkhov A V and Shirikova N Y 1991 Description of nonrotational states of ^{250}Cf and ^{256}Fm *Sov. J. Part. Nucl.* **54** 748

[498] Fu X M, Xu F R, Jiao C F, Liang W Y, Pei J C and Liu H L 2014 Irregularity in $K^{\pi} = 8^-$ rotational bands of $N = 150$ isotones *Phys. Rev.* C **89** 054301

[499] Landau L D 1932 Zur theorie der energieubertragung: I *Phys. Z. Sowjetunion* Engl. trans. in collected papers of L D Landau (Pergamon, New York, 1965) **1** 88

[500] Landau L D 1932 Zur theorie der energieubertragung: II *Phys. Z. Sowjetunion* **2** 46 Engl. trans. in collected papers of L D Landau, (Pergamon, New York, 1965)

[501] Zener C 1932 Non-adiabatic crossing of energy levels *Proc. R. Soc.* A **137** 696–702

[502] Stueckelberg E C G 1932 Theorie der unelastischen stsse zwischen atomen *Helv. Phys. Acta* **5** 369

[503] Majorana E 2008 Atomi orientati in campo magnetico variabile *Il Nuovo Cimento* **9** 43–50

[504] Heßberger F P *et al* 2009 Decay studies of K isomers in ^{254}No *Eur. Phys. J.* A **43** 55–66

[505] Chowdhury P *et al* 2011 Spectroscopy of neutron-rich Pu nuclei *AIP Conf. Proc.* **1377** 13–7

[506] Chowdhury P 2010 Isomers in heavy deformed nuclei *Proc. DAE Symp. on Nucl. Phys.* vol 55, p I3

[507] Khuyagbaatar J *et al* 2010 The new isotope ^{236}Cm and new data on ^{233}Cm and ^{237,238,240}Cf *Eur. Phys. J.* A **46** 59–67

[508] Konki J and Sulignano B 2016 private communication

[509] Afanasjev A V and Litvinova E 2015 Impact of collective vibrations on quasiparticle states of open-shell odd-mass nuclei and possible interference with the tensor force *Phys. Rev.* C **92** 044317

[510] Nerlo-Pomorska B, Pomorski K and Bartel J 2011 Rotational states and masses of heavy and superheavy nuclei *Phys. Rev.* C **84** 044310

[511] Muntian I, Patyk Z and Sobiczewski A 2001 Are superheavy nuclei around ^{270}Hs really deformed? *Phys. Lett.* B **500** 241–6

[512] Patyk Z and Sobiczewski A 1991 Main deformed shells of heavy nuclei studied in a multidimensional deformation space *Phys. Lett.* B **256** 307–10

[513] Liu H L, Xu F R, Walker P M and Bertulani C A 2011 Effects of high-order deformation on high-*K* isomers in superheavy nuclei *Phys. Rev.* C **83** 011303(R)

[514] Zamfir N V, Hering G, Casten R F and Paul P 1995 Hexadecapole deformations in actinide and trans-actinide nuclei *Phys. Lett.* B **357** 515–20

[515] Pototzky K J, Erler J, Reinhard P G and Nesterenko V O 2010 Properties of odd nuclei and the impact of time-odd mean fields: a systematic Skyrme–Hartree–Fock analysis *Eur. Phys. J.* A **46** 299–313

[516] Agbemava S E, Afanasjev A V, Ray D and Ring P 2014 Global performance of covariant energy density functionals: SHEs observables of even–even nuclei and the estimate of theoretical uncertainties *Phys. Rev.* C **89** 054320

[517] Zhang Q-S, Niu Z-M, Li Z-P, Yao J-M and Meng J 2014 Global dynamical correlation energies in covariant density functional theory: cranking approximation *Front. Phys.* **9** 529–36

[518] Arita K 2016 Nuclear shell structures in terms of classical periodic orbits *Phys. Scr.* **91** 063002

[519] Robledo L M and Bertsch G F 2011 Global systematics of octupole excitations in even–even nuclei *Phys. Rev.* C **84** 054302

[520] Robledo L M and Butler P A 2013 Quadrupole-octupole coupling in the light actinides *Phys. Rev.* C **88** 051302(R)

[521] Zhao J, Lu B-N, Zhao E-G and Zhou S-G 2012 Nonaxial-octupole Y_{32} correlations in $N = 150$ isotones from multidimensional constrained covariant density functional theories *Phys. Rev.* C **86** 057304

[522] Chen Y-S, Sun Y and Gao Z-C 2008 Nonaxial-octupole effect in superheavy nuclei *Phys. Rev.* C **77** 061305(R)

[523] Chen Y S and Gao Z C 2008 Triaxial reflection asymmetric shell model *Int. J. Mod. Phys.* E **17** 146–58

[524] Shneidman T M, Adamian G G, Antonenko N V and Jolos R V 2006 Possible alternative parity bands in the heaviest nuclei *Phys. Rev.* C **74** 034316

[525] Takami S, Yabana K and Matsuo M 1998 Tetrahedral and triangular deformations of $Z = N$ nuclei in mass region $A \sim$ 60–80 *Phys. Lett.* B **431** 242–8

[526] Dudek J, Goźdź A, Schunck N and Miśkiewicz M 2002 Nuclear tetrahedral symmetry: possibly present throughout the periodic table *Phys. Rev. Lett.* **88** 252502

[527] Mazurek K, Dudek J, Góźdź A A, Curien D, Kmiecik M and Maj A 2009 New nuclear stability islands of octahedral and tetrahedral shapes *Acta Phys. Pol.* A **40** 731–5

[528] Jachimowicz P, Rozmej P, Kowal M, Skalski J and Sobiczewski A 2011 Test of tetrahedral symmetry for heavy and superheavy nuclei *Int. J. Mod. Phys.* E **20** 514–9

[529] Chen Y S and Gao Z-C 2010 Tetrahedral instability in superheavy nuclei *10th Int. Conf. on Nucleus-Nucleus Collisions (NN2009); Nucl. Phys.* A **834** 378c–380c

[530] Multhauf L G, Tirsell K G, Morrow R J and Meyer R A 1971 Levels of ^{246}Cm from the β^--decay sequence ^{246}Pu(11 days)^{246m}Am(25 min)^{246} Cm *Phys. Rev.* C **3** 1338–51

[531] Thompson R C, Huizenga J R and Elze T W 1975 Collective states in ^{230}Th, ^{240}Pu, ^{244}Pu, and ^{248}Cm excited by inelastic deuteron scattering *Phys. Rev.* C **12** 1227–35

[532] Yates S W, Friedman A M and Ahmad I 1975 Octupole states in ^{246}Cm and ^{248}Cm populated by inelastic deuteron scattering *Phys. Rev.* C **12** 795–800

[533] Ahmad I, Friedman A M and Yates S W 1980 Vibrational states in ^{250}Cf excited by the (d, d') reaction *Phys. Rev.* C **21** 874–8

[534] Fields P R, Ahmad I, Barnes R F, Sjoblom R K and McHarris W C 1973 Nuclear spectroscopic studies of ^{252}Es *Nucl. Phys.* A **208** 269–86

[535] Ahmad I, Diamond H, Milsted J, Lerner J and Sjoblom R K 1973 Alpha-decay of 39.3 h ^{254m}Es isomer *Nucl. Phys.* A **208** 287–301

[536] Bès D R, Federman P, Maqueda E and Zuker A 1965 Properties of the γ-vibrational state *Nucl. Phys.* **65** 1–20

[537] Jolos R V, Shirikova N Y and Sushkov A V 2012 Neutron number dependence of the energies of the γ-vibrational states in nuclei with $Z \sim 100$ and the manifestation of pseudospin symmetry *Phys. Rev.* C **86** 044320

[538] Sun Y, Long G-L, Al-Khudair F and Sheikh J A 2008 γ-vibrational states in superheavy nuclei *Phys. Rev.* C **77** 044307

[539] Twin P J *et al* 1986 Observation of a discrete-line superdeformed band up to $60\hbar$ in ^{152}Dy *Phys. Rev. Lett.* **57** 811–4

[540] Singh B, Zywina R and Firestone R B 2002 Table of superdeformed nuclear bands and fission isomers: third edn (October 2002) *Nucl. Data Sheets* **97** 241–592

[541] Leoni S and Lopez-Martens A 2016 Rotation of warm nuclei and superdeformation *Phys. Scr.* **91** 063009

[542] Ragnarsson I, Nilsson S G and Sheline R K 1978 Shell structure in nuclei *Phys. Rep.* **45** 1–87

[543] Gutzwiller M C 1971 Periodic orbits and classical quantization conditions *J. Math. Phys.* **12** 343–58

[544] Balian R and Bloch C 1972 Distribution of eigenfrequencies for the wave equation in a finite domain: III. Eigenfrequency density oscillations *Ann. Phys., NY* **69** 76–160

[545] Nakatsukasa T, Matsuyanagi K, Matsuzaki M and Shimizu Y R 2016 Quantal rotation and its coupling to intrinsic motion in nuclei *Phys. Scr.* **91** 073008

[546] Staszczak A, Dobaczewski J and Nazarewicz W 2006 Fission barriers of superheavy nuclei in the Skyrme–Hartree–Fock model *Int. J. Mod. Phys.* E **15** 302–10

[547] Shi-Jie Z and Fu-Rong X 2008 Shape coexistence of superheavy nuclei *Chin. Phys.* C **32** S2 152

[548] Shi-Jie Z, Fu-Rong X, Cen-Xi Y and Chong Q 2009 Alignments in the nobelium isotopes *Chin. Phys.* C **33** 107

[549] Wang H, Liu H, Xu F and Jiao C 2012 Investigation of octupole effects in superheavy nuclei with improved potential-energy-surface calculations *Chin. Sci. Bull.* **57** 1761–4

[550] Bengtsson R, Larsson S E, Nilsson S G and Ragnarsson I 1975 Alternative regions of metastable heavy and SHEs directly accessible in heavy-ion reactions *Phys. Lett.* B **55** 6–10

[551] Ren Z and Toki H 2001 Superdeformation in the newly discovered SHEs *Nucl. Phys.* A **689** 691–706

[552] Ren Z 2002 Shape coexistence in even–even superheavy nuclei *Phys. Rev.* C **65** 051304(R)

[553] Ahmad S, Bhuyan M and Patra S K 2012 Properties of $Z = 120$ nuclei and the α-decay chains of the ^{292,304}120 isotopes using relativistic and nonrelativistic formalisms *Int. J. Mod. Phys.* E **21** 1250092

[554] Patra S K, Bhuyan M, Mehta M S and Gupta R K 2009 Superdeformed and hyperdeformed states in $Z = 122$ isotopes *Phys. Rev.* C **80** 034312

[555] Jachimowicz P, Kowal M and Skalski J 2011 Superdeformed oblate superheavy nuclei *Phys. Rev.* C **83** 054302

[556] Hong-Liang L 2013 Oblate superdeformed high-K states in superheavy nuclei *Commun. Theor. Phys.* **60** 577

[557] Próchniak P and Staszczak A 2013 Superdeformed oblate superheavy nuclei in the self-consistent approach *Acta Phys. Pol.* A **44** 287–92

[558] Muntian I and Sobiczewski A 2004 Superdeformed SHEs of superheavy nuclei? *Phys. Lett.* B **586** 254–7

[559] Oganessian Y 2013 Synthesis of the heaviest nuclei at FLNR: main results and prospects *Proc. Int. Symp. on Exotic Nuclei EXON-2012 (Vladivostok, Russia, 16 October 2012)* ed Y E Penionzhkevich and Y G Sobolev (Singapore: World Scientific) pp 483–98

[560] Dmitriev S, Mikhail M I and Yuri Y O 2016 Status and perspectives of the dubna SHEs factory. *EPJ Web Conf.* **131** 08001

[561] Petit E and on behalf of the SPIRAL2 collaboration 2016 Status report on the SPIRAL2 facility at GANIL *Proc. NA-PAC2016 (Chicago, IL, USA)* TUA1IO02 accepted

[562] Ferrer R *et al* 2013 In gas laser ionization and spectroscopy experiments at the superconducting separator spectrometer (S3): conceptual studies and preliminary design *16th Int. Conf. on ElectroMagnetic Isotope Separators and Techniques Related to their Applications (Matsue, Japan, 27 December 2012); Nucl. Instrum. Methods Phys. Res.* B **317** 570–81

[563] Schmitt C *et al* 2010 New gas-filled mode of the large-acceptance spectrometer VAMOS *Nucl. Instrum. Methods Phys. Res.* A **621** 558–65

[564] Theisen C *et al* 2014 Musett: a segmented Si array for recoil-decay-tagging studies at VAMOS *Nucl. Instrum. Methods Phys. Res.* A **747** 69–80

[565] Akkoyun S *et al* 2012 AGATA-advanced gamma tracking array *Nucl. Instrum. Methods Phys. Res.* A **668** 26–58

[566] Azaiez F and Korten W 1997 EXOGAM: a γ-ray spectrometer for nuclear structure studies at SPIRAL *Nucl. Phys. News* **7** 21–5

[567] Simpson J *et al* 2000 The EXOGAM array: a radioactive beam gamma-ray spectrometer *Acta Phys. Hung. New Ser. Heavy Ion Phys.* **11** 159–88

[568] Maj A *et al* 2009 The PARIS project *Acta Phys. Pol.* A **40** 565–75

[569] Barth W A, Clemente G, Dahl L A, Mickat S, Schlitt B and Vinzenz W 2011 Future heavy ion linacs at GSI *Proc. IPAC2011* pp 2550–2 Number WEPS031 (jacow.org)

[570] Lee I-Y and Simpson J 2010 AGATA and GRETA: the future of gamma-ray spectroscopy *Nucl. Phys. News* **20** 23–8

[571] Türler A *et al* 2003 On the decay properties of ^{269}Hs and indications for the new nuclide ^{270}Hs *Eur. Phys. J.* A **17** 505–8

[572] Iljinov A S, Mebel M V and Cherepanov E A 1990 The possibilities of synthesizing heavy elements with radioactive nuclear beams *Proc. 1st Int. Conf. on Radioactive Nuclear Beams* pp 289–98

[573] Hussein M S 1991 A viable route to the production of SHEs: low-energy fusion of very neutron-rich nuclei *Nucl. Phys.* A **531** 192–204

[574] Münzenberg G 1998 Synthesis and investigation of SHEs: perspectives with radioactive beams *Phil. Trans. R. Soc.* A **356** 2083–104

[575] Loveland W 2007 Synthesis of transactinide nuclei using radioactive beams *Phys. Rev.* C **76** 014612

[576] Adamian G G, Antonenko N V and Scheid W 2000 Isotopic dependence of fusion cross sections in reactions with heavy nuclei *Nucl. Phys.* A **678** 24–38

[577] Adamian G G, Antonenko N V and Scheid W 2004 Isotopic trends in the production of superheavy nuclei in cold fusion reactions *Phys. Rev.* C **69** 011601(R)

[578] Adamian G G, Antonenko N V and Scheid W 2004 Possibilities of synthesis of new superheavy nuclei in actinide-based fusion reactions *Phys. Rev.* C **69** 044601

[579] Aritomo Y 2007 Possibility of synthesizing a doubly magic superheavy nucleus *Phys. Rev.* C **75** 024602

[580] Feng Z-Q, Jin G-M, Li J-Q and Scheid W 2007 Formation of superheavy nuclei in cold fusion reactions *Phys. Rev.* C **76** 044606

[581] Zagrebaev V and Greiner W 2008 Synthesis of superheavy nuclei: a search for new production reactions *Phys. Rev.* C **78** 034610

[582] Smolańczuk R 2010 Synthesis of transactinide nuclei in cold fusion reactions using radioactive beams *Phys. Rev.* C **81** 067602

[583] Bao X J, Gao Y, Li J Q and Zhang H F 2015 Theoretical study of the synthesis of superheavy nuclei using radioactive beams *Phys. Rev.* C **91** 064612

[584] Hofmann S 2001 Synthesis of SHEs using radioactive beams and targets *Prog. Part. Nucl. Phys.* **46** 293–302

[585] Aritomo Y, Wada T, Ohta M and Abe Y 1997 Diffusion mechanism for synthesis of SHEs *Phys. Rev.* C **55** R1011–4

[586] Denisov V Y 2001 Production of SHEs in symmetric reactions *Prog. Part. Nucl. Phys.* **46** 303–5

[587] Świątecki W J, Siwek-Wilczyńska K and Wilczyński J 2005 Fusion by diffusion: II. Synthesis of transfermium elements in cold fusion reactions *Phys. Rev.* C **71** 014602

[588] Siwek-Wilczyńska K, Skwira-Chalot I and Wilczyński J 2007 Role of mass asymmetry in fusion of super-heavy nuclei *Int. J. Mod. Phys.* E **16** 483–90

[589] Mandaglio G, Nasirov A K, Curciarello F, De Leo V, Romaniuk M, Fazio G and Giardina G 2012 Processes in massive nuclei reactions and the way to complete fusion of reactants. what perspectives for the synthesis of heavier SHEs? *EPJ Web Conf.* **38** 01001

[590] Choudhury R K and Gupta Y K 2014 Revisiting the symmetric reactions for synthesis of super-heavy nuclei of *Phys. Lett.* B **731** 168–72

[591] Cap T, Siwek-Wilczyńska K and Wilczyński J 2014 No chance for synthesis of super-heavy nuclei in fusion of symmetric systems *Phys. Lett.* B **736** 478–81

[592] Oganessian Y T *et al* 2009 Attempt to produce the isotopes of element 108 in the fusion reaction ^{136}Xe + ^{136}Xe *Phys. Rev.* C **79** 024608

[593] Avez B *et al* 2011 Study of ^{124}Sn + ^{136}Xe fusion-evaporation: analysis of a rare-event experiment (arXiv:1111.2913)

[594] Corradi L, Pollarolo G and Szilner S 2009 Multinucleon transfer processes in heavy-ion reactions *J. Phys. G: Nucl. Part. Phys.* **36** 113101

[595] Magda M T and Leyba J D 1992 Production of heavy elements by transfer of massive clusters *Int. J. Mod. Phys.* E **01** 221–47

[596] Kratz J V, Schädel M and Gäggeler H W 2013 Reexamining the heavy-ion reactions ^{238}U + ^{238}U and ^{238}U + ^{248}Cm and actinide production close to the barrier *Phys. Rev.* C **88** 054615

[597] Kratz J V, Loveland W and Moody K J 2015 Syntheses of transuranium isotopes with atomic numbers $Z \leqslant 103$ in multi-nucleon transfer reactions *Nucl. Phys.* A **944** 117–57 special issue on SHEs

[598] Schädel M *et al* 1982 Actinide production in collisions of ^{238}U with ^{248}Cm *Phys. Rev. Lett.* **48** 852–5

[599] Adamian G G, Antonenko N V and Zubov A S 2005 Production of unknown transactinides in asymmetry-exit-channel quasifission reactions *Phys. Rev.* C **71** 034603

[600] Zagrebaev V I, Oganessian Y T, Itkis M G and Greiner W 2006 Superheavy nuclei and quasi-atoms produced in collisions of transuranium ions *Phys. Rev.* C **73** 031602(R)

[601] Zagrebaev V I and Greiner W 2013 Production of heavy trans-target nuclei in multinucleon transfer reactions *Phys. Rev.* C **87** 034608

[602] Zagrebaev V I and Greiner W 2011 Production of heavy and superheavy neutron-rich nuclei in transfer reactions *Phys. Rev.* C **83** 044618

[603] Kedziora D J and Simenel C 2010 New inverse quasifission mechanism to produce neutron-rich transfermium nuclei *Phys. Rev.* C **81** 044613

[604] Simenel C, Golabek C and Kedziora D J 2011 Actinide collisions for QED and SHEs with the time-dependent Hartree–Fock theory and the Balian–Vénéroni variational principle *EPJ Web Conf.* **17** 09002

[605] Sekizawa K and Yabana K 2013 Time-dependent Hartree–Fock calculations for multinucleon transfer processes in ^{40,48}Ca + ^{124}Sn, ^{40}Ca + ^{208}Pb, and ^{58}Ni + ^{208}Pb reactions *Phys. Rev.* C **88** 014614

[606] Feng Z-Q, Jin G-M and Li J-Q 2009 Production of heavy isotopes in transfer reactions by collisions of ^{238}U + ^{238}U *Phys. Rev.* C **80** 067601

[607] Tian J, Wu X, Zhao K, Zhang Y and Li Z 2008 Properties of the composite systems formed in the reactions of ^{238}U + ^{238}U and ^{232}Th + ^{250}Cf *Phys. Rev.* C **77** 064603

[608] Zhao K, Wu X and Li Z 2009 Quantum molecular dynamics study of the mass distribution of products in 7.0A MeV ^{238}U + ^{238}U collisions *Phys. Rev.* C **80** 054607

[609] Yanez R and Loveland W 2015 Predicting the production of neutron-rich heavy nuclei in multinucleon transfer reactions using a semi-classical model including evaporation and fission competition, GRAZING-F *Phys. Rev.* C **91** 044608

[610] Golabek C *et al* 2010 Investigation of deep inelastic reactions in ^{238}U + ^{238}U at Coulomb barrier energies *Eur. Phys. J.* A **43** 251–9

[611] Loveland W, Vinodkumar A M, Peterson D and Greene J P 2011 Synthesis of heavy nuclei using damped collisions: a test *Phys. Rev.* C **83** 044610

[612] Barbui M *et al* 2011 Search for heavy and superheavy systems in ^{197}Au + ^{232}Th collisions near the Coulomb Barrier *J. Phys.: Conf. Ser.* **312** 082012

[613] Kozulin E M *et al* 2012 Mass distributions of the system ^{136}Xe + ^{208}Pb at laboratory energies around the Coulomb barrier: a candidate reaction for the production of neutron-rich nuclei at $N = 126$ *Phys. Rev.* C **86** 044611

[614] Watanabe Y X *et al* 2015 Pathway for the production of neutron-rich isotopes around the $N = 126$ shell closure *Phys. Rev. Lett.* **115** 172503

[615] Barrett J S *et al* 2015 ^{136}Xe + ^{208}Pb reaction: a test of models of multinucleon transfer reactions *Phys. Rev.* C **91** 064615

[616] Dvorak J, Block M, Düllmann C E, Heinz S, Herzberg R-D and Schädel M 2011 IRiS exploring new frontiers in neutron-rich isotopes of the heaviest elements with a new inelastic reaction isotope separator *Symp. on Radiation Measurements and Applications (SORMA) XII 2010; Nucl. Instrum. Methods Phys. Res.* A **652** 687–91

[617] Vogt A *et al* 2015 Light and heavy transfer products in ^{136}Xe + ^{238}U multinucleon transfer reactions *Phys. Rev.* C **92** 024619

[618] Birkenbach B *et al* 2015 Spectroscopy of the neutron-rich actinide nucleus ^{240}U following multinucleon-transfer reactions *Phys. Rev.* C **92** 044319

[619] Comas V F, Heinz S, Hofmann S, Ackermann D, Heredia J A, Heßberger F P, Khuyagbaatar J, Kindler B, Lommel B and Mann R 2013 Study of multi-nucleon transfer reactions in ^{58,64}Ni + ^{207}Pb collisions at the velocity filter SHIP *Eur. Phys. J.* A **49** 112

[620] Heinz S and Beliuskina O 2014 Deep inelastic transfer reactions a new way to exotic nuclei? *J. Phys.: Conf. Ser.* **515** 012007

[621] Devaraja H M *et al* 2015 Observation of new neutron-deficient isotopes with in multinucleon transfer reactions *Phys. Lett.* B **748** 199–203

[622] Procter M G *et al* 2011 Anomalous transition strength in the proton-unbound nucleus *Phys. Lett.* B **704** 118–22

[623] Goodman L S, Diamond H and Stanton H E 1975 Nuclear and atomic moments and hyperfine-structure parameters of ^{253}Es and ^{254m}Es *Phys. Rev.* A **11** 499–504

[624] Karpenko V 1980 The discovery of supposed new elements: two centuries of errors *Ambix* **27** 77–102

[625] Fontani M, Costa M and Orna M V 2014 *The Lost Elements: The Periodic Table's Shadow Side* (Oxford: Oxford University Press)

[626] Stavsetra L, Gregorich K E, Dvorak J, Ellison P A, Dragojevic I, Garcia M A and Nitsche 2009 Independent Verification of Element 114 Production in the 48Ca+242Pu Reaction *Phys. Rev. Lett.* **103** 132502